STAR Collaboration Decadal Plan

The STAR Collaboration

December, 2010

Contents

Chapter 1

Executive Summary

Remarkable discoveries have been made at RHIC. During the first six years of RHIC, we found that the dense QCD matter created in relativistic heavy-ion collisions demonstrates very strong collective flow characteristic of a strongly-coupled liquid, rather than the weakly-coupled gas of quarks and gluons that had been expected. In fact, the shear viscosity to entropy ratio is so low that it has been dubbed the "perfect liquid". The observation of substantial jet quenching is an exciting result, indicating that the matter is virtually opaque to energetic quarks and gluons. Even heavy-quark hadron yields are strongly suppressed. Differences in the yields and flow of baryons vs. mesons have provided evidence for partonic collectivity and led to the completely unexpected conclusion that hadron formation at intermediate transverse momenta proceeds via constituent quark coalescence. Polarized proton collisions show that the large-rapidity transverse single-spin asymmetries that had been seen at lower energies persist to RHIC energies where, in contrast to the lower energy results, the cross sections can be explained by perturbative QCD.

The discoveries have continued during the past four years. STAR has identified anti-hypertriton production in Au+Au collisions, the first ever observation of an anti-hypernucleus. Azimuthal charged-particle correlations have been observed in Au+Au collisions that may arise from local strong parity violation in the dense medium. Measurements of the correlations between non-photonic electrons and hadrons in p+p collisions have been combined with results for non-photonic electron R_{AA} to provide indications that even hadrons containing b-quarks are suppressed in central Au+Au collisions. Jet-like correlations have identified several novel features in heavy-ion collisions relative to p+p, including the near-side "ridge" that may probe the early state of the collisions. Polarized p+p collisions have set the most precise constraints to date on the polarization of the gluons in the proton. New global analyses which include the RHIC results indicate that the integrated contribution to the proton spin from gluons in the momentum range $0.05 < x < 0.2$ is small. The observation of a dramatic broadening of forward π^0-π^0 correlations in d+Au collisions provides the clearest indication to date that the onset of gluon saturation is accessible at RHIC. Related theoretical developments point to a potential connection between gluon saturation and the "ridge". Additional new research areas have been opened by the first reconstruction of full jets in relativistic heavy-ion collisions by STAR, the beginning of the RHIC Beam Energy Scan, and the first observation of W-boson production in polarized p+p collisions.

These discoveries set the stage for the future research opportunities at RHIC. The STAR Collaboration has identified the following key questions that we believe will drive RHIC science during the coming decade:

- What are the properties of the strongly-coupled system produced at RHIC, and how does it thermalize?
- Are the interactions of energetic partons with QCD matter characterized by weak or strong coupling? What is the detailed mechanism for partonic energy loss?
- Where is the QCD critical point and the associated first-order phase transition line?
- Can we strengthen current evidence for novel symmetries in QCD matter and open new avenues?
- What other exotic particles are created at RHIC?
- What is the partonic spin structure of the proton?
- How do we go beyond leading twist and collinear factorization in perturbative QCD?
- What is the nature of the initial state in nuclear collisions?

The STAR detector - with its combined large acceptance capabilities for tracking, calorimetry, and particle identification - is ideally suited to answer these questions in the coming years. Recent upgrades, including DAQ1000 and the barrel Time-of-Flight system, have already begun to position STAR for these upcoming studies. Essentially the entire STAR physics program is built around the Time Projection Chamber (TPC). It will be crucial to ensure that it remains fully operational. Studies to date of the TPC aging are inconclusive. If future measurements indicate the necessity, STAR has the capability to rewire the TPC read-out sectors in order to extend the TPC lifetime for another decade.

Additional upgrades to STAR will nonetheless be needed to address these questions. Measurements of identified hadrons containing heavy quarks, both open (D^0 and Λ_c) and hidden (J/ψ and $\Upsilon(1s, 2s, 3s)$), will play key roles in exploring the properties of the strongly-coupled system, thermalization, and the mechanism for partonic energy loss. The Heavy Flavor Tracker (HFT) and Muon Telescope Detector (MTD) will be essential for these measurements. Upgrades to both the trigger and data acquisition system will also be required to answer several of the heavy-ion questions.

Upgrades will also be necessary to take advantage of the opportunities presented by p+p and p+A collisions at RHIC. The Forward GEM Tracker is required for STAR measurements of the anti-quark polarization in the proton. The addition of a Forward Hadron Calorimeter will extend STAR measurements of quark helicity and transversity distributions to the strange quark sector. A second phase Roman pots upgrade will permit a high-sensitivity search for glueballs. Upgrades to the Forward Meson Spectrometer to provide e/h and γ/π^0 discrimination, together with the addition of forward tracking and particle identification, will be critical to explore the origins of the large transverse spin asymmetries and the partonic structure of heavy nuclei.

The extraordinary flexibility of the RHIC facility will play a crucial role in answering these questions, as the questions will require detailed investigations of many different colliding systems over a broad range of nucleon-nucleon center-of-mass energies. The increase in heavy-ion luminosity made available by the RHIC-II upgrade, as well as increases in proton luminosity, will also play crucial roles because several of the most discriminating measurements involve rare probes. During the next few years, we will focus our studies of dense QCD matter on those observables, such as non-photonic electrons and $\Upsilon \rightarrow e^+e^-$, that profit the most from the small amount of material currently in the central region of STAR, as well as those, such as γ+jet, that will require multiple RHIC years to achieve the required statistical precision in both the A+A and reference p+p systems. In parallel, our spin physics program will focus primarily on polarized p+p collsions at $\sqrt{s}$=500 GeV to explore the polarization of the anti-quarks in the proton and extend our understanding of gluon polarization to lower x, through di-jet and γ+jet measurements. The middle years of the decade will be devoted primarily to the new opportunties that will be made available by the addition of the HFT and MTD to STAR. This is also the time that we expect to perform phase II of the RHIC Beam Energy Scan if the results from Runs 10 and 11 indicate that the QCD critical point is experimentally accessible at RHIC. During the latter part of the decade, STAR will exploit the new capabilities made available with the upgraded forward instrumentation to perform sensitive, high-precision measurements, such as Drell-Yan and direct photon production, in both polarized p+p collisions and in p+A collisions. The latter will require dedicating at least an entire RHIC year to asymmetric collision measurements. The STAR Collaboration believes the existing results from d+Au collisions clearly justify dedicating the beam time necessary to explore the low-x partonic structure of both light and heavy nuclei and the onset of gluon saturation using p+A collisions, the most discriminating probe of this physics currently attainable at RHIC.

A new era is beginning in relativistic heavy-ion physics with the turn-on of the LHC. As the new energy frontier, the LHC is going to teach us a great deal about the dense matter created in relativistic heavy-ion collisions. Nonetheless, RHIC will remain essential in order to address these key questions fully. A detailed, quantitative understanding of the properties of the strongly-coupled system is going to require investigation over a range of beam energies and species. Many important measurements are likely to be much easier to interpret at the lower RHIC energies because of the reduced backgrounds. For example, Υ production is almost entirely "primordial" at RHIC, whereas a significant fraction of Υ production at the LHC will likely arise from recombination, analogous to J/ψ production at RHIC. The response of the medium to a jet probe is another example. Other important measurements will be complementary. For example, most jets at RHIC above transverse momenta of $\sim$30 GeV/c involve light quarks. In contrast, gluons will dominate the jet yields at the LHC at essentially all accessible transverse momenta. RHIC will remain unique in many ways. If the indications to date are borne out, forward measurements at RHIC will provide access to the onset of gluon saturation, whereas most LHC phenomena will be deep in the saturation domain. The onset region is particularly important to elucidate the dynamics that lead to saturation. RHIC is the only facility that can seek out the QCD critical point using collider detectors, which involve significantly reduced systematic uncertainties when comparing results at different beam energies. And RHIC, of course, is the world's only polarized hadron collider.

Regarding the further future, the STAR Collaboration has recognized that the capabilities of

the existing mid-rapidity detectors are very well suited for important measurements in e+p and e+A collisions by eSTAR during the early phase of eRHIC. These measurements will build on the knowledge that we gain about the partonic structure of the nucleon and nuclei during the coming decade. They will require the addition of tracking, triggering, and particle identification capabilities on the east side of STAR. During the next few years, R&D will be required to identify the optimum technology for the particle momenta of interest.

Table 1.1 provides an overview of the measurements that STAR anticipates performing to address these compelling physics questions. In this Decadal Plan, we expand on the physics questions raised above, identify the crucial measurements needed to address them, and indicate how such measurements will be enabled through our proposed plan of detector upgrades over the next decade.

Table 1.1: Some of the measurements that we anticipate performing to address the key questions, and the upgrades that will make those measurements possible. Measurements are only specified in the first time period during which they will be possible. In many cases, they will continue into later time periods. Abbreviations: 'corr' for correlations, 'NPE' for non-photonic electrons, 'CNM' for cold nuclear matter, '(SI)DIS' for (semi-inclusive) deep-inelastic scattering, 'F-F' for forward-forward.

	Near term (Runs 11–13)	Mid-decade (Runs 14–16)	Long term (Runs 17–)
Colliding systems	p+p, A+A	p+p, A+A	p+p, p+A, A+A, e+p, e+A
Upgrades	FGT, FHC, RP, DAQ10K, Trigger	HFT, MTD, Trigger	Forward Instrum, eSTAR, Trigger
(1) Properties of sQGP	Υ, $J/\psi \to ee$, m_{ee}, v_2	Υ, $J/\psi \to \mu\mu$, Charm v_2, R_{CP}, Charm corr, Λ_c/D ratio, μ-atoms	p+A comparison
(2) Mechanism of energy loss	Jets, γ-jet, NPE	Charm, Bottom	Jets in CNM, SIDIS, c/b in CNM
(3) QCD critical point	Fluctuations, correlations, particle ratios	Focused study of critical point region	
(4) Novel symmetries	Azimuthal corr, spectral function	$e-\mu$ corr, $\mu-\mu$ corr	
(5) Exotic particles	Heavy anti-matter, glueballs		
(6) Proton spin structure	W A_L, jet and di-jet A_{LL}, intra-jet corr, $(\Lambda+\bar{\Lambda})$ D_{LL}/D_{TT}		$\bar{\Lambda}$ D_{LL}/D_{TT}, polarized DIS, polarized SIDIS
(7) QCD beyond collinear factorization	Forward A_N		Drell-Yan, F-F corr, polarized SIDIS
(8) Properties of initial state			Charm corr, Drell-Yan, J/ψ, F-F corr, Λ, DIS, SIDIS

Chapter 2

What is the nature of QCD matter at the extremes?

Five of the key questions that the STAR Collaboration has identified for the coming decade grow out of the successes and surprises that have come from the first 10 years of A+A studies at RHIC:

- What are the properties of the strongly-coupled system produced at RHIC, and how does it thermalize?
- Are the interactions of energetic partons with QCD matter characterized by weak or strong coupling? What is the detailed mechanism for partonic energy loss?
- Where is the QCD critical point and the associated first-order phase transition line?
- Can we strengthen current evidence for novel symmetries in QCD matter and open new avenues?
- What other exotic particles are created at RHIC?

In this chapter, we discuss why we believe these are the compelling questions that will drive future measurments in A+A collisions at RHIC, and how we intend to answer them.

2.1 What are the properties of the strongly-coupled system produced at RHIC, and how does it thermalize?

Prior to RHIC operation, it was already clear that, near the predicted parton-hadron phase boundary at T_c of about 170 MeV, the QCD medium is located far into the non-perturbative regime. Lattice QCD methods were developed to take account of this awareness. However, their equilibrium predictions were, at first, not suitable to address the questions of collisional dynamics. This resulted in a wide initial application of theoretical methods inspired by the well explored perturbative QCD methods. Within this theoretical framework, the medium is essentially pictured as a free gas of partons. This point of view was fundamentally challenged by completely new insights provided by the RHIC results: the QGP state of matter created at RHIC possesses distinct non-perturbative properties, for example the features of a "near perfect liquid", of extremely small viscosity over entropy density ratio. Despite the success of the ideal hydrodynamic description of medium evolution, thermalization of the medium created at RHIC and its equation of state remain among the critical open questions demanding further exploration by both experimentalists and theorists. Equilibration of a partonic medium is argued to be not the only approach successful in description of the medium space-time evolution [1, 2]; and if thermalization is indeed achieved, the extent of equilibration and the time-scale for establishing thermalization still pose a challenge for understanding of the medium's evolution.

Resolving these open questions would constitute an important step towards a detailed understanding of the nature of QCD matter. RHIC's "perfect liquid" provides an exciting testing ground for theoretical development. Viscous three-dimensional hydrodynamic models are now replacing initial ideal aproximations. The application of string theory may now become experimentally testable. In AdS/CFT the weak coupling of string theory is dual to the strong-coupling limit of quantum field theory [3]. For heavy-ion physics, this provides an alternative method to Lattice QCD to solve problems in the strongly coupled regime analytically.

Although the implications of this discovery to other fields are under investigation, remarkable connections are already emerging. For example, in condensed matter physics, strongly interacting systems, like the super-cooled state of lithium 6 and clean undoped graphene [4], have been found to behave like a "perfect fluid" [5]. The tools that are familiar to our field, including hydrodynamics and collision-dominated transport theory, are also crucial to understand the evolution of these other systems.

2.1.1 What do we know now and what do we want to know further?

Among the experimental results from RHIC supporting thermalization there are the following three prominent categories: collective behavior in the bulk sector, constituent quark scaling at intermediate transverse momentum, and jet-medium interactions manifested in the jet-related studies.

In the bulk sector, the transverse momentum spectra of identified hadrons, their radial and elliptical flow and relative production rates are all consistent with an equilibrium description of the partonic matter. The measured hadron abundances are found consistent with chemical equilibration at a temperature of $T_{ch} = 164 \pm 4$ MeV [6, 7], Fig. 2.1. This temperature obtained from statistical

model fits is close to the critical temperature predicted for the QCD phase transition, and represents a lower limit on the thermalization temperature. Additionally, considerable enhancement of relative multi-strange baryon yields, compared to p+p measurements at the same energy and lower energies A+A results, are of particular importance. The statistical model fits to the semi-central and central 200 GeV Au+Au data including strange and multi-strange hadron species indicate saturation of the strangeness. The successful description of relative abundances of non-strange and strange hadrons is consistent with thermalization of the partonic degrees of freedom in the light-flavor (u, d and s) sector. The success of statistical models implies that hadron production is statistical in nature, and in the light of the observed strangeness saturation in semi-central and central Au+Au collisions, it is argued to provide evidence of thermalization occuring at least in the vicinity of the QCD parton-hadron coexistence line [6].

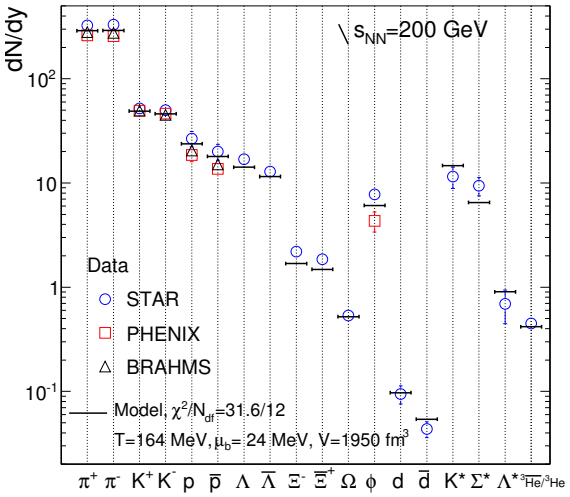

Figure 2.1: Midrapidity hadron yields measured at the RHIC top energy of $\sqrt{s_{NN}} = 200$ GeV in comparison to statistical model fits (excluding resonances) [6, 7]. The fit parameters are $T_{ch} = 164 \pm 4$ MeV, $\mu_B = 24 \pm 2$ MeV.

Mass-dependent modifications of spectral shapes are found to be consistent with a collective radial velocity field [8]. Early work on characterizing the transverse momentum distributions for various hadrons within the hydrodynamically-inspired model [9] with two parameters, T_{kin} and β, describing random (thermal) and collective components, has been recently expanded by the non-equilibrium Tsallis fits [10, 11]. Tsallis fits describe simultaneously the transverse momentum spectra of a wide variety of identified hadron species, and indicate a strong increase of radial flow velocity with event multiplicity from zero in 200 GeV p+p collisions to $0.47c$ in central Au+Au collisions [10]. Additionally, the fit results show the evolution of the system from a highly non-equilibrated state in p+p collisions towards nearly complete thermalization in central Au+Au collisions. A hardening of the transverse mass spectra has been also observed for strange and multi-strange hadrons (Ξ, Ω, ϕ), that are expected to be less sensitive to the hadronic phase of the collision due to low hadronic interaction cross-sections [12, 13]. Even for the most central collisions,

the temperature that best describes the spectra for multi-strange ϕ and Ω at kinetic freeze-out is found to be close to the chemical freeze-out temperature T_{ch} shown above (albeit with large uncertainties), and thus the amount of radial flow extracted from such fits could reflect that built up pre-hadronization. The strength of radial flow for non-strange hadrons extracted from the fits is found to be the same as that of multistrange hadrons from the fit [14]. It has been argued in the same work that hadronic phase scattering doesn't produce collective radial flow, and is insufficient to maintain the system in equilibrium. The consequence of hadronic scatterings in the later phase of the collision is that the copiously produced light hadrons are driven away from thermal equilibrium, appearing less thermalized at the end of the hadronic phase than at its beginning. The resulting large off-equilibrium effect for light (non-strange) hadrons does not contribute to an increase of the radial flow, and might provide a natural explanation for two apparent contradictory observations of different flow velocities for non-strange and (multi)strange hadrons from Blast-wave model [15, 16] and ideal hydrodynamics [17]. Hydrodynamic and Tsallis descriptions of spectral shapes seem to support the idea of a thermalized medium, however, alternative descriptions are also possible. For example, the observed changes of the spectral shapes can be also attributed to the interplay of the soft and hard components, e.g. influence of the hard and semi-hard scattering extending to low p_T [18].

Additionally, transverse momentum spectra dependences with respect to the reaction plane are among the most important results from RHIC, which can support the idea of collectivity and thermalization. The azimuthal momentum space anisotropy of hadron production is extracted in terms of coefficients of an azimuthal Fourier decomposition of particle spectra, where the second harmonic coefficient, v_2, is referred to as elliptic flow. Elliptic flow is considered to be particularly sensitive to the early stages of the collisions due to self-quenching effects [19, 20], and thus provides an experimental tool for probing early collision times.

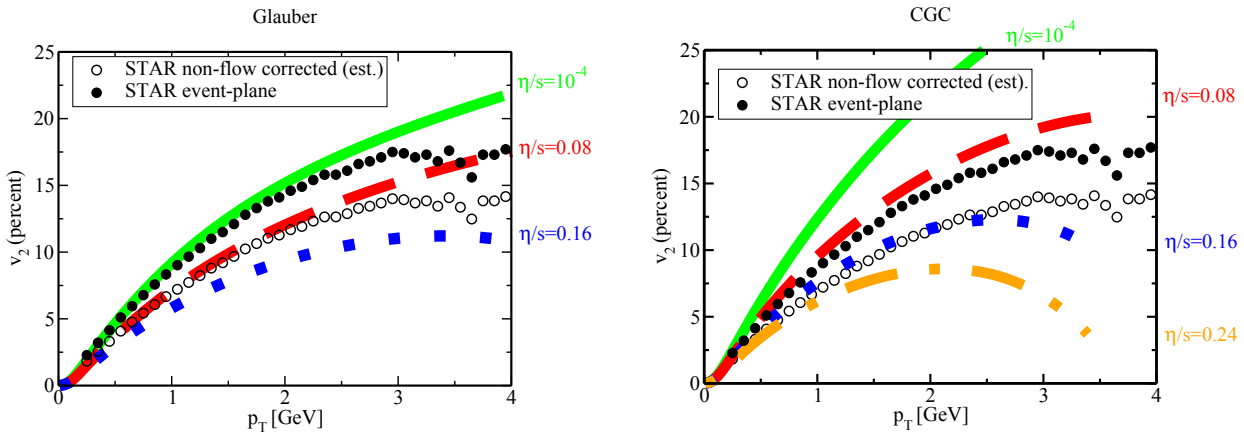

Figure 2.2: Comparison between data and a calculation of a viscous hydrodynamical model [26] under Glauber-type (left) and CGC-type initial conditions (right) assuming different η/s.

Early theoretical works based on ideal hydrodynamics have provided reasonable accounts for

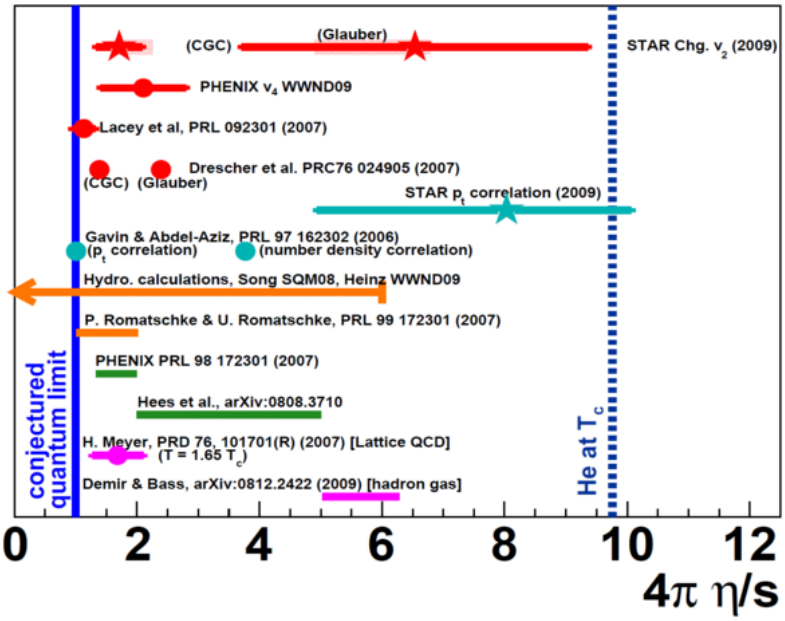

Figure 2.3: Collection of η/s calculations [28], where red indicates results based on flow measurements, cyan for results based on fluctuation measurements, orange for results based on hydrodynamic calculations, green for estimation based on heavy flavor measurements, and magenta for other calculations.

magnitude, mass and transverse momentum dependences of elliptic flow [21, 22], suggesting the attainment of local thermal equilibrium at an early stage in these collisions. The (approximate) applicability of ideal hydrodynamics led to claims [23, 24] that in near-central collisions at RHIC the elliptic flow has reached the ideal hydrodynamic limit, unlike in all investigations at lower energy. However, the input parameters, e.g. the initial energy density distribution, the freeze-out temperature, etc., were chosen such that the models could describe the data. It was later realized that the uncertainties from initial conditions, equation of state, hadronic rescattering effects, and non-zero viscosity [25, 26] can have significant impact on the model predictions. Figure 2.2 shows a viscous-hydrodynamical model calculation of elliptic flow [26] together with a comparison with the data under Glauber-type as well as Color-Glass-Condensate initial conditions. An η/s close to the quantum limit [27] for a strongly coupled medium is required to describe the data. This is consistent with other constraints on η/s [28] as shown in Fig. 2.3. Although the derived value from different calculations cover a large range, most are below the η/s of superfluid states of helium, indicating the creation of "perfect liquid" at RHIC. Until recently, hydrodynamical models required a very short (< 1 fm) thermalization time, but possible mechanisms of such early thermalization were not explicitly addressed by the models. Such strict constraints on thermalization time cannot be fulfilled with perturbative QCD scatterings and require some additional yet-undefined non-perturbative mechanisms. In recent years the developments of hybrid hydrodynamic models [29], consisting of a transverse-hydrodynamic stage followed by perfect-fluid hydrodynamics, provided a

possible description of the soft sector observables without assumption of a very fast thermalization time.

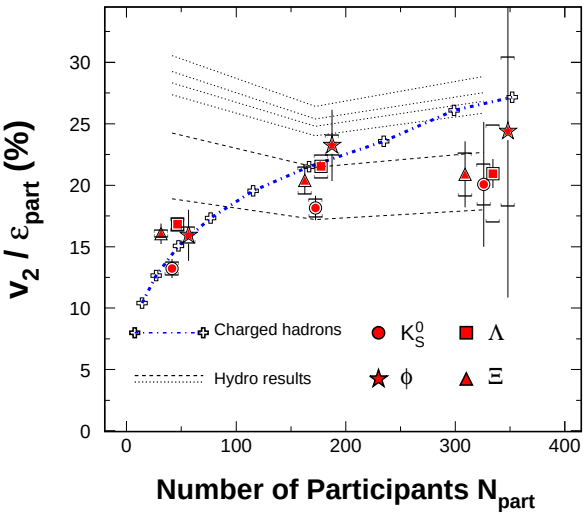

Figure 2.4: Centrality dependence of v_2/ϵ_{part} versus number of participants for charged hadrons (crosses), K^0_S(circles), ϕ (stars), $\Lambda + \bar{\Lambda}$ (squares) and ($\Xi + \bar{\Xi}$ (triangles) from 200 GeV Au+Au collisions [32]. Ideal hydrodynamic model calculations from [33].

We note that the agreement of ideal hydro calculations with the integrated v_2 measurements is at about the 30% level. The remaining discrepancy could be attributed to an incomplete thermalization of the medium or to an earlier transition to the hadronic phase. Both scenarios require further experimental and theoretical exploration. Despite recent advances in hydrodynamic modeling of the medium at RHIC, which now incorporate full 3-dimensional evolution, non-zero viscosity in the partonic phase and hadron transport treatment for the hadronic stage, detailed descriptions of available measurements of the Fourier coefficients remains challenging, particularly the rapidity dependence of $v_2(y)$ [30, 31], the growing discrepancy between $v_2(p_T)$ and the perfect-liquid prediction at higher momenta, the centrality dependence of the v_2-to-eccentricity ratio (see Fig. 2.4, [32, 33]), and the relative strength of the v_4 and v_2 components. These features of the experimental data may find a natural explanation in non-equilibrium treatments of the collision evolution [1, 2]. For example, in an out-of-equilibrium scenario the strength of v_2 and v_4 will depend on the number of scatterings, and thus on the system size and particle density, with the expected relationship $v_4/v_2^2 > 1/2$, while ideal hydrodynamic calculations expect $v_4/v_2^2 = 1/2$.

Other experimental results, such as the measurements of angular pair-correlations in the soft sector (below 2 GeV/c), might be also suggesting appreciable non-thermal soft hadron emission even in the most central RHIC collisions. The remnants of jet-like features [34] in angular correlations on relative pseudo-rapidity ($\eta_\Delta = \eta_1 - \eta_2$) and azimuth ($\phi_\Delta = \phi_1 - \phi_2$) shown in Fig. 2.5, after removal of first and second Fourier components, affect a significant fraction (10-30%) of measured

hadrons. Hard scatterings responsible for such correlations in p+p events, are expected in heavy ion collisions, however, in the fully equilibrated medium at freeze-out such initial state correlations are expected to be washed out.

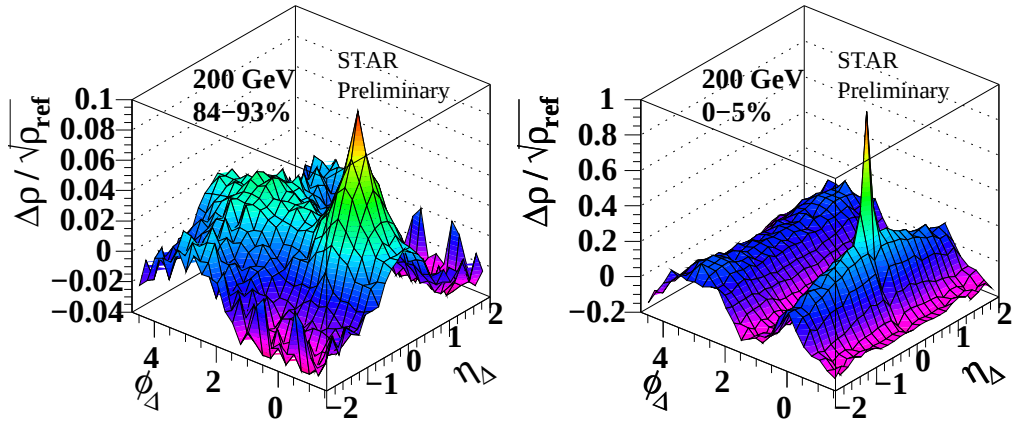

Figure 2.5: Evolution of autocorrelation structures measured by STAR for $0.15 < p_T < 2.0$ GeV/c charged hadrons from peripheral (left) to central (right) Au+Au collisions at 200 GeV.

At higher transverse momentum values, $1.5 < p_T < 5$ GeV/c, recombination models [35, 36, 37] have found great success in describing experimental measurements of particle yields and flow. In these models, the idea of thermalized medium once again plays central role: hadron production proceeds via coalescence of constituent quarks with presumed thermal spectra and collective transverse velocity distributions. Particularly, the saturation of the elliptic flow values for baryons and mesons at intermediate p_T, enhanced relative production of baryons far exceeding expectations from p+p collisions, and specific patterns in the nuclear modification factors for identified hadrons, all are consistent with expectations from coalescence (for review see [38]).

Constituent quark scaling features in these observables, especially in identified v_2 measurements, led to claims that quark recombination might be the relevant hadronization mechanism through-out both the soft and intermediate-p_T sectors [39]. When elliptic flow v_2 is plotted versus transverse kinetic energy $(m_{\mathrm{T}} - m_0)$, both divided by the number of constituent quarks (n_q), the v_2 for all identified particles below $(m_{\mathrm{T}} - m_0)/n_q \sim 1$ GeV/c^2 follows a universal curve. This scaling behavior as shown in Fig. 2.6 is considered as evidence for the existence of partonic degrees of freedom during the Au + Au collision process at 200 GeV. It is very hard to explain this observed pattern in a scenario where only hadronic matter exists throughout the interaction, whereas the hypothesis of coalescence of hadrons from de-confined quarks offers a ready explanation. Figure 2.6 right panel shows the most recent results on multi-strange hadron v_2 in Au+Au collisions at RHIC [40]. Comparing with the results for light-quark hadrons, one can see that the strange hadrons show the similar scaling properties further confirming the conclusion of the partonic collectivity developed in high-energy nuclear collisions at RHIC. In addition, multi-strange particles have relatively low hadronic interaction cross sections, therefore the elliptic flow measurements for ϕ and Ω particles are the most promising probes of the early stages of the collision.

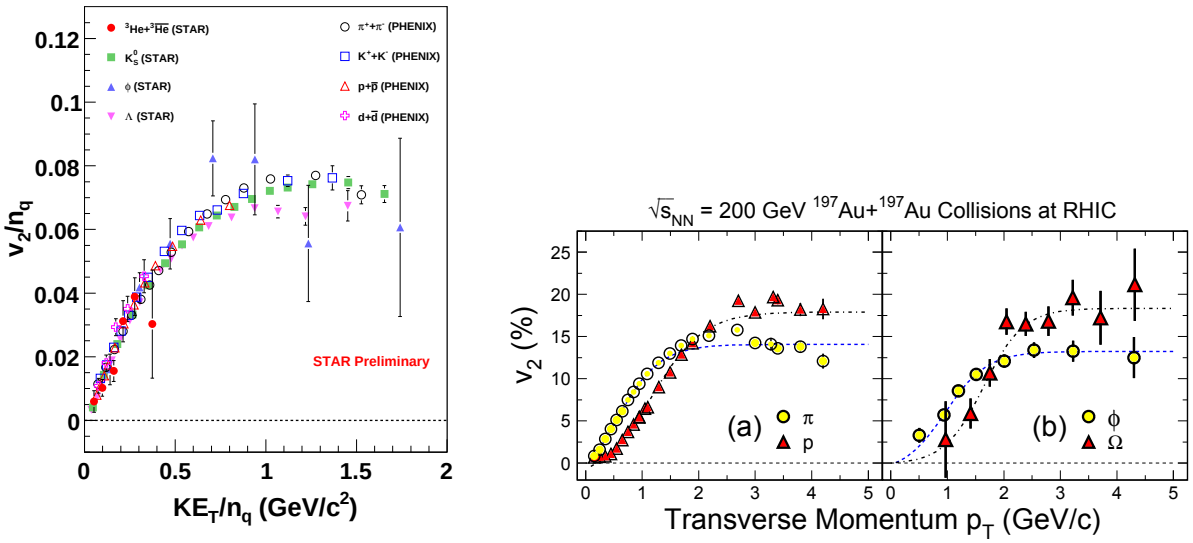

Figure 2.6: Left Plot: Number of quark scaled v_2 as a function of the scaled transverse kinetic energy. Right plot: The event anisotropic parameter v_2 for (a) light quark hadrons and (b) strange quark hadrons. The data are from the minimum bias Au+Au collisions at $\sqrt{s_{\rm NN}} = 200$ GeV. The figure is taken from [40].

It remains unclear if another set of experimental observations, a jet-like signal in the di-hadron angular correlation that is found to accompany all sorts of identified triggers, can be simultaneously described within a coalescence approach. Introduction of the "soft+hard" recombination into the concept might be an answer to this challenge; however the details of the trigger and centrality dependencies are not yet worked-out. The strength of the correlation signals, similar for all particle trigger particle types, is at odds with modest fragmentation contributions expected from coalescence model fits to the data [16]. An additional stumbling block resulted from the experimental reports of jet-like peaks associated with Ω and ϕ triggers that were not expected in the early model prediction, as recombination of thermal quarks was expected to be the dominant production mechanism for Ω and ϕ. This led to the idea of phantom jets [41], which could not be tested experimentally yet due to lack of statistics.

The jet-like peaks observed in the angular correlations of hard hadron triggers and soft associated hadrons [42] also lead one to question the complete thermalization of the medium, as those remnants of early-time hard scatterings had to survive the thermalization process. However, the comparisons between p+p and different centrality bins of Au+Au collisions have shown that soft ($0.15 < p_T < 4.0$ GeV/c) associated hadrons, balancing a high-p_T trigger on the opposite side, exhibit progressive broadening of the distribution in the azimuthal angle and a softer p_T spectrum. In Fig. 2.7 the centrality dependence of $\langle p_T \rangle$ for associated away-side hadrons is compared with the

inclusive charged hadron distribution. The mean transverse momentum of hadrons associated with high p_T triggers progressively decreases with increasing centrality, while inclusive hadrons show increase of $\langle p_T \rangle$. Despite ambiguities of the two-component approach used for the separation of the jet-like signal and underlying background, the observed trend suggest that a hard parton traversing the medium makes substantial progress toward thermalization, making the thermalization of the medium itself even more plausible.

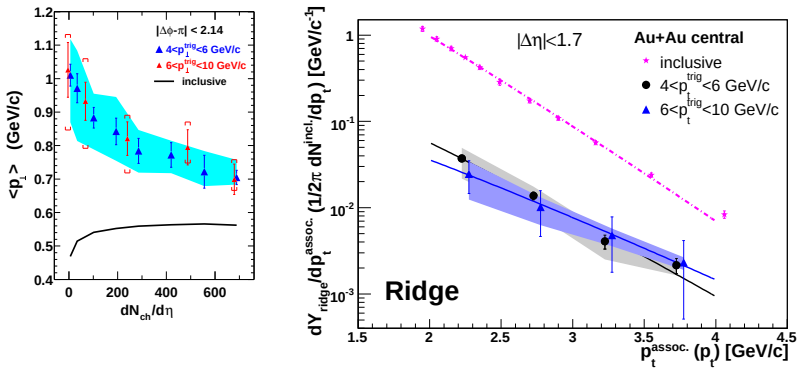

Figure 2.7: (left)Away-side associated hadron $\langle p_T \rangle$ distribution for $4 < p_T^{trig} < 6$ and $6 < p_T^{trig} < 10$ GeV/c. (right) Ridge p_T spectrum in central Au+Au collisions for particles associated with triggers selected between 4 and 6 GeV/c and 6 and 10 GeV/c. The dash-dotted line is the inclusive hadron spectrum from central Au+Au collisions.

Recent studies [43] of correlation structure details on the same side of the high-p_T trigger yielded a novel picture that, in contrast with p+p and d+Au events, the same-side correlation in central Au+Au collisions consists of two distinct components a small angle jet-like peak, consistent with expectations of in-vacuum jet fragmentation, and a long-range $\Delta\eta$ correlation, the ridge, that exhibits properties similar to the bulk. Multiple mechanisms are proposed to explain this experimental observation: CGC color-flux tubes, gluon radiation, momentum kick model, medium heating and hadronization by quark recombination, and others [44]. The longitudinal extent of the ridge suggests an early formation time, constraining significantly applicability of a wide range of the models, and providing a new tool to study medium evolution and possible thermalization. The detailed studies of correlation shapes and yields, extending to higher p_T, where fragmentation would dominate the hadron production, together with particle identification for both trigger and associate hadrons, should provide the information critical for understanding the mechanisms of jet-medium interactions and possible thermalization of parton energy.

2.1.2 What measurements do we need?

Measurement of Heavy Quark Production

To understand the degree of thermalization and gain insights into in-medium energy loss mechanisms STAR plans to measure the cross-sections and transverse momentum spectra of hadrons

with open and hidden heavy flavor. Due to their large masses, the charm and bottom quarks are predominantly produced via hard scattering in the initial stage of the high-energy heavy-ion collision, and thermalization (if at all) would be only partial or substantially delayed compared to that of the light-flavored hadrons. These spectra can serve as a sensitive tool to probe the in-medium rescattering and interactions responsible for thermalization.

Within the realm of statistical models, the use of particle yield ratios for charmed hadrons will allow to test if the apparent thermal equilibrium supported by the light-flavor sector measurements extends even to quarks with masses considerably higher than T_c. It has been suggested that, in the presence of a deconfined QGP phase, heavy hadrons with multiple heavy quarks (J/ψ, B_C) will be enhanced compared to the hadrons with a single heavy quark [45, 46]. Other works [47] expect considerable shift of the yield from D to D_S in a chemically equilibrated source.

Direct measurements of hadrons containing heavy quarks will also allow to better understand the unexpectedly large suppresion of heavy flavor jets, currently measured through their semileptonic decay electrons (non-photonic electrons), which pose a serious challenge to our understanding of parton energy loss. These kind of measurements will be discussed in detail in the following section. Such measurements will not be possible until the commissioning or completed installation of the Heavy Flavor Tracker (HFT), Muon Telescope Detector (MTD), and full RHIC-II luminosities.

The HFT upgrade will enable STAR to directly reconstruct charmed hadrons (D^0, D^+, D_S, Λ_c) using the displaced vertices of their decay products. In addition, distance-of-closest-approach (DCA) cuts will allow the statistical separation of D from B mesons in the non-photonic electron spectra. The MTD will allow us to overcome the difficulties encountered in electron-related analysis through using the corresponding muon channels. In the following we highlight some of the measurements that can be done when all upgrades are available.

Measurement of Heavy Quark Flow

An important prospective measurement is the elliptic flow of D mesons down to very low p_T. If the charm quark flow is directly established, it will signify frequent re-scatterings in the medium, thus probing the high degree of thermalization of the light quarks. Figure 2.8 illustrates the sensitivity of the prospective elliptic flow measurement, estimated for 500M minimum bias Au+Au collisions at 200 GeV using 5 nb^{-1} of RHIC delivered luminosity, together with the prediction from a transport model [48] assuming charm quarks have identical partonic elliptic flow as that of the light quarks (red), as well as when charm quarks do not flow (green). The right panel of Fig. 2.8 shows the projection for elliptic flow of charm decay and bottom decay electrons with 500 million minimum-bias Au+Au collisions. This event sample is in between the minimum and maximum luminosity RHIC-II is expected to deliver in one 12-week run. High precision measurements of the high-p_T charm decay electron v_2 and, especially, that of bottom decay electrons over the entire p_T region will require an accumulated data sample from multiple RHIC-II Au+Au runs. The combined analysis of the D-meson spectra, v_2 distribution, and ratios will allow us to test charm quark collectivity and the thermodynamic nature of the created medium.

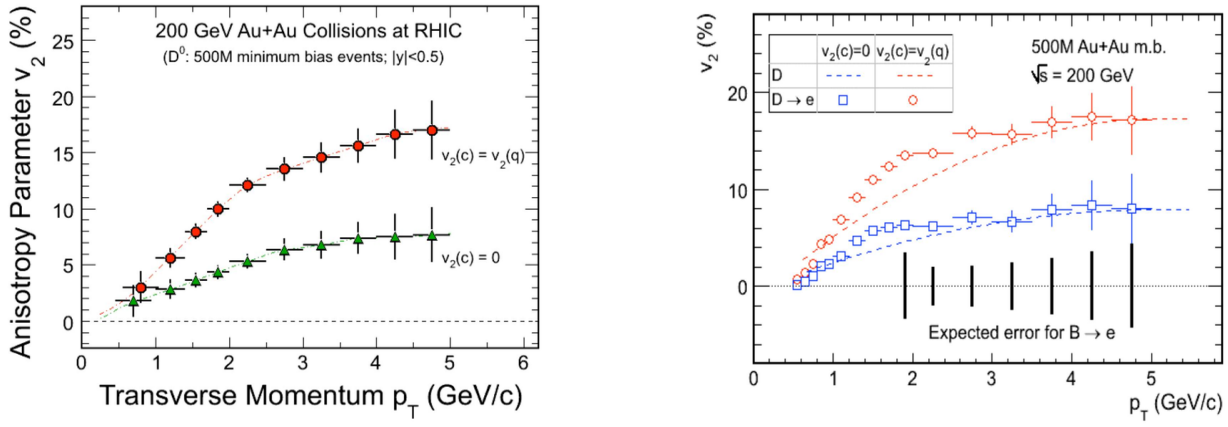

Figure 2.8: (Left panel) Projected uncertainty in D^0 elliptic flow measurement with 500 million minimum-bias events recorded by HFT+TPC in the cases when charm quarks do not flow (green) and when charm quarks have the same size of flow as that of light quarks (red). (Right panel) Projected uncertainty in the elliptic flow measurements for charm decay electrons (open symbols) in the same two scenarios as in the left panel, as well as the expected uncertainty for the measurement of bottom decay electrons (black lines).

Study of Multi-parton Coalescence through Λ_c/D^0

In central Au+Au collisions at RHIC, a baryon to meson enhancement has been observed in the intermediate p_T region ($2 < p_T < 6$ GeV/c). This is explained by a hadronization mechanism involving collective multi-parton coalescence rather than independent vacuum fragmentation. The success of the coalescence approach implies deconfinement and the development of collectivity of the light quarks prior to hadronization. Since Λ_c is the lightest charmed baryon and its mass is not far from that of the D^0 meson, a similar pattern of baryon to meson enhancement is expected in the charm sector. Λ_c/D^0 enhancement can also be a signature of a strongly coupled quark-gluon plasma since the heavier particle gets a larger boost from the strongly coupled medium. Furthermore, the Λ_c has a small semi-leptonic branching ratio, so the interpretation of non-photonic electron R_{AA} may need to be revisited if the Λ_c yield is enhanced substantially in central Au+Au collisions. Therefore, it would be very interesting to measure R_{CP} of Λ_c baryons and compare it to R_{CP} of D^0 mesons. With the HFT, STAR will be able to identify Λ_c baryons and to perform a measurement of R_{CP}.

Figure 2.9 shows the projected Λ_c/D^0 measurements with 2 billion minimum-bias events, corresponding to 20 nb^{-1} delievered luminosity, in the cases of zero enhancement and the same enhancement as for Λ/K^0_s. We will need to accumulate multiple runs at RHIC-II to obtain good accuracy in this measurement.

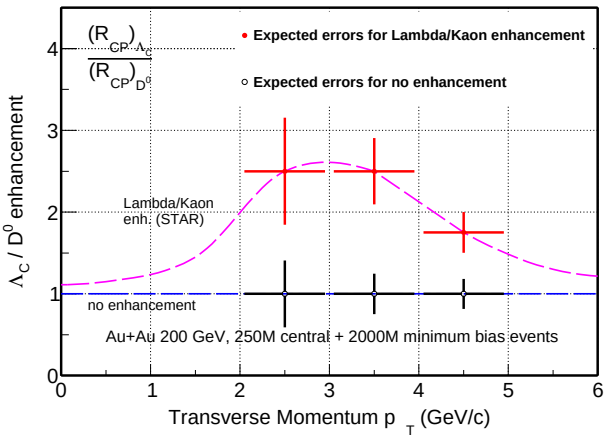

Figure 2.9: Statistical errors of the Λ_c/D^0 ratio for the case of no enhancement (black) and of Λ/K^0_s-like enhancement (red) with 2 billion minimum-bias events.

Measurement of Heavy Quarkonia Production

Heavy quarkonia production was predicted to be significantly suppressed in QGP due to Debye screening effects [49]. The screening is quantified by the Debye length, which is a function of the temperature. When the temperature is high enough so that the screening length is smaller than the size of a meson, the primordial quarkonia will dissolve. The abundance of the various heavy quarkonia states also adds important features to the signature. Since different meson states have different sizes and masses while the screening length decreases with increasing temperature, one would expect to observe a sequential melting of different meson states.

Later progress in the field has made the picture much more complicated. In the strongly coupled system, dissociation due to hard gluon scattering instead of the screening effect could be the main reason for heavy quarkonia suppression. The observed signal is now thought to be a combination of dissociation and recombination effects due to the large number of charm quarks in a Au+Au collision at RHIC [50]. On the other hand, Lattice QCD calculations indicate that J/ψ will not melt until above $2T_c$, whereas the study using potential models combined with pQCD shows all quarkonia except $\Upsilon(1S)$ dissolve at a temperature less than $1.5T_c$ [51]. Therefore, relative yields of various quarkonium species can serve as a probe for the medium temperature. Additionally, these measurements could help gain a better understanding of the surprising experimental results showing a similar R_{AA} suppression level for J/ψ at the SPS and at RHIC [52], despite an order of magnitude difference in collision energies. This leads to the model arguing that the observed suppression comes solely from the absence of feed-down from χ_c and ψ', due to the melting of these two mesons.

To reveal the actual mechanism of heavy quarkonia production in the strongly coupled medium, we need high precision measurement on all species of heavy quarkonia, including J/ψ, ψ', χ_c and Υ(1S+2S+3S) in a broad p_T range. Compared to the other quarkonia, Υ is a cleaner probe since it is much less affected by the recombination and disassociation due to hadronic co-movers. The

Muon Telescope Detector upgrade will allow us to measure Υ through its dimuon decay channel with much better mass resolution (Fig. 2.10) compared to that of the dielectron decay channel. With RHIC-II luminosity, we expect to reconstruct 169K J/ψ and 2500 Υ from 300 pb^{-1} of p+p collisions, and 630K J/ψ and 9300 Υ from 26 nb^{-1} of Au+Au collisions [53, 54]. The success of these measurements relies on the high luminosity from RHIC-II and the installation of the MTD.

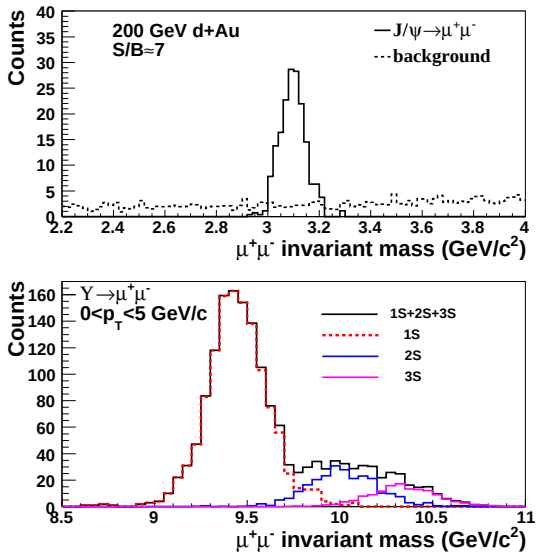

Figure 2.10: Expected di-muon invariant mass distribution for J/ψ in d+Au collisions (top panel). Invariant mass distribution of di-muon from Υ decays for $p_T < 5$ GeV/c (bottom panel).

Figure 2.11 shows the expected uncertainty of $\Upsilon(1S) \rightarrow e^+e^-$ R_{AA} measurements with 20 nb^{-1} delivered Au+Au collisions and 100 pb^{-1} delivered p+p collisions. We will be able to clearly separate Υ 1S, 2S and 3S through the dimuon channel, as shown in the lower panel of Fig. 2.10. Figure 2.12 shows the expected uncertainty of $\Upsilon(1S) \rightarrow \mu^+\mu^-$ R_{AA} measurements with a RHIC delivered luminosity of 20 nb^{-1} in Au+Au collisions and 300 pb^{-1} in p+p collisions. We can achieve reasonable accuracy on Υ(1S) measurements with one 12-week RHIC-II run with maximum luminosity, but we will need the accumulated data from multiple RHIC-II runs in order to have precise results other Υ states, as well as on differential measurements such as p_T-dependent Υ production measurements. Similar measurements are planned in the $J/\psi \rightarrow e^+e^-$ and $J/\psi \rightarrow \mu^+\mu^-$ channels, as discussed in the following section.

Heavy Quarkonia Flow

The amount of J/ψ elliptic flow is an important test of the recombination mechanism for J/ψ production. The large v_2 observed in non-photonic electron production at low p_T indicates strong collectivity of charm quarks during the evolution of the medium. The fraction of J/ψ produced from charm quark recombination should have large v_2 as well, while primordial J/ψ, if they survive

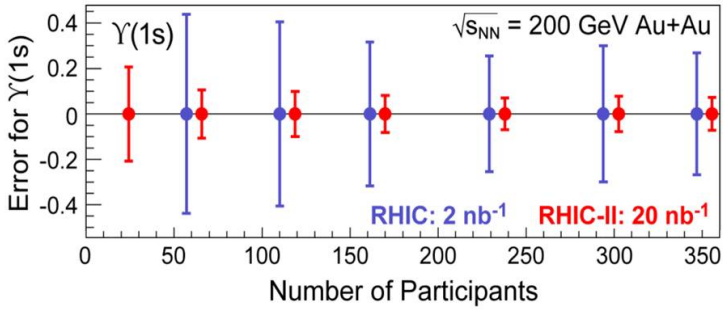

Figure 2.11: Projected uncertainty of $\Upsilon(1S) \rightarrow e^+e^-$ as a function of N_{part} with RHIC delivered luminosity of 20 nb^{-1} Au+Au collisions and 100 pb^{-1} p+p collisions (red), as well as the one with 2 nb^{-1} Au+Au collisions(blue).

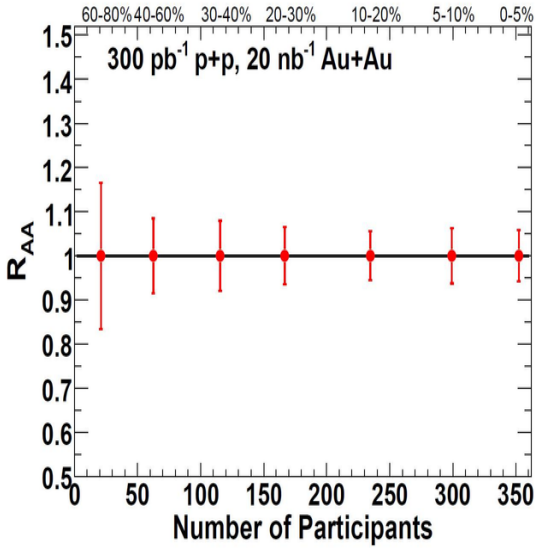

Figure 2.12: Projected uncertainty of $\Upsilon \rightarrow \mu^+\mu^-$ R_{AA} measurement with a RHIC delivered luminosity of 20 nb^{-1} in Au+Au collisions and 300 pb^{-1} in p+p collisions.

the strong interaction with the medium constituents, will have a small amount of flow coming from the variation of the amount of absorption geometrically. Figure 2.13 shows the expected uncertainty of J/ψ v_2 measurement in minimum-bias Au+Au collisions with one 12-week RHIC-II run with maximum luminosity in the case when charm quarks are fully thermalized. A high precision measurement will need data accumulated from multiple RHIC-II runs.

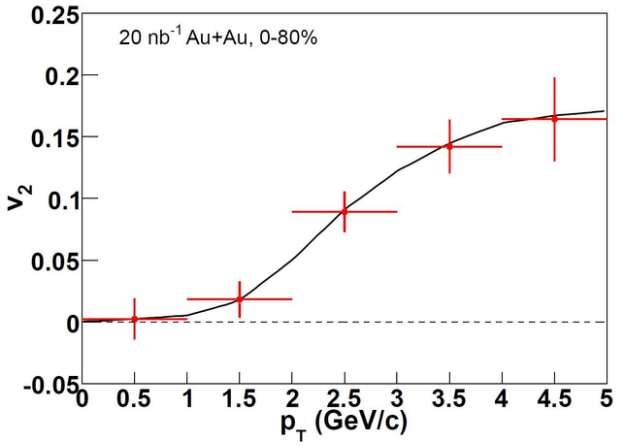

Figure 2.13: Projected uncertainty of $J/\psi \rightarrow \mu^+\mu^-$ elliptic flow measurement, assuming complete thermalization of charm quarks, with 20 nb^{-1} RHIC-II delivered luminosity.

Hydrogenlike muonic atoms as a measure of thermal lepton distribution at RHIC

Muonic atoms with muons captured by protons or nuclei have been studied over many decades, and have become a precision tool for fundamental physics such as determining nuclear shapes and masses. However, muonic atoms with the nuclear core replaced by more exotic particles (pions, kaons or antiprotons) are rarely produced. These hydrogenlike muonic atoms are $\mu - \pi$, $\mu - K$ and $\mu - \overline{p}$ (antimatter muonic hydrogen). To date, only one such object, a $\mu - \pi$ system, has been observed, in 1976 by Coombes et al. [55] (33 events) at BNL and in 1982 by Aronson et al. [56] (320 events) at FermiLab. In these experiments, the atoms were formed from K_L decay. A high-intensity kaon beam in which the decay products muon and pion are formed at low relative momentum are necessary conditions for formation and observation. The apparent production rate of 4×10^{-7} per K_L is consistent with a prediction from the wave-function overlap at zero separation computed using only the Coulomb interaction. We propose a more direct route, taking advantage of the large number of thermal muons and hadrons produced in a relativistic heavy ion collision to produce new kinds of exotic atoms and detect them in STAR, using their relative yields to determine conditions at early stages in the collisions.

Mel Schwartz was the first to propose measuring the distributions of exotic atoms formed by binding a directly produced lepton to one of the charged hadrons emerging from the final state of a nuclear collision. The idea is not just to discover the exotic atoms, but also to measure the thermal electromagnetic emission from the QGP via a direct measurement of the single muon

spectrum. Measurements in this range are capable of probing thermal electromagnetic emission processes in an initial plasma with a temperature of a couple of hundred MeV, as argued by Baym and others [57]. The soft leptons produced in the early evolution of Au+Au collisions at RHIC are difficult to measure because of the large number of charged particles created in the collisions, which eventually decay to muons weakly. The exotic atoms are produced by hadrons and thermal muons or muons from resonance decay (e.g. $\rho \rightarrow \mu\mu$), which co-exist right around freeze-out. In contrast, muons from weak or electromagnetic decays are produced far from the collision zone, and can not combine with the charged hadrons. The exception is the case of K_L decay. However, K_L, with its small branching ratio to $\mu - \pi$, will make negligible contribution to the total $\mu - \pi$ yield within the STAR detector. In addition, production from other atoms ($\mu - K$ and $\mu - \overline{p}$) will provide a unique signal for the formation of such atoms from the collisions. Detailed rate estimates were carried out by Baym et al. [57] and by Kapusta and Mocsy [58], showing sensitivity to initial momentum distributions and particle densities. Since the collision zone at freeze-out is on the order of 10 fm in dimension while the size of the formed atoms is of hundreds of Fermi, only the wave functions of the atom's s states at the origin contribute to the formation probability.

$$\frac{dN_{atom}}{dyd^2p_{T,atom}} = 8\pi^2\zeta(3)\alpha^3{m^2}_{red}\frac{dN_h}{dyd^2p_{T,h}}\frac{dN_l}{dyd^2p_{T,l}} \tag{2.1}$$

Equation 2.1 shows that the yield of atoms is directly proportional to the yield of hadrons and leptons in the collision event. The factor is dominated by the QED fine structure constant α^3 or 4×10^{-7}. The copiously produced hadrons and muons in relativistic heavy-ion collisions make it a unique system to produce such exotic atoms as antimatter muonic hydrogen. Baym provided an estimate for the integrated yield of 10^{-5} $\mu - \pi$ atoms in one unit of rapidity per central Au+Au collision. This means that STAR samples about 10,000 such events when saving 500 million central Au+Au collision events to tape. Kapusta and Mocsy extended the calculation to p_T spectra, and estimated about 10^{-5} $\mu - \pi$ atoms at $p_T \simeq 1 \pm 0.5$ GeV/c per central Au+Au collision. In both calculations, the hadrons and muons are assumed to be from a thermal distribution, and the muon yield is estimated to be a factor of 5000 ($1/\alpha^2$) lower than the pion yield. To obtain a more accurate estimate of the rate, we use the measured $\pi^{\pm}$, kaon and proton spectra from STAR data, and scale the pion down by a factor of $(\alpha/\alpha_s)^2 = (1/1700)$ as a substitution for the unmeasured single muon spectrum.

Figure 2.14 shows the invariant spectra of $\mu - \pi$, $\mu - K$, and $\mu - \overline{p}$. The $\mu - \pi$ spectrum is very similar to the prediction from Kapusta and Mocsy, while our other spectra are significantly higher than their calculation. This is mainly due to the different estimate of other hadron spectra and low-p_T muon yields they used. We emphasize that the estimates are to provide the order of magnitude for a feasibility study. This serves as guidance for the physics program, and isn't intended to be a very vigorous theoretical prediction. The actual yields will be measured experimentally and provide a first-hand single muon spectra. These atoms are created in the collisions as neutral particles. They travel from the collision vertex through the vacuum to the beam pipe wall, where the material in the beam pipe dissociates them into muon and hadron. In the STAR detector with its Solenoidal magnetic field, the charged muon and hadron are bent in different directions entering the TPC. The signature of these atoms would be a V0 decay vertex at the beam pipe with a muon

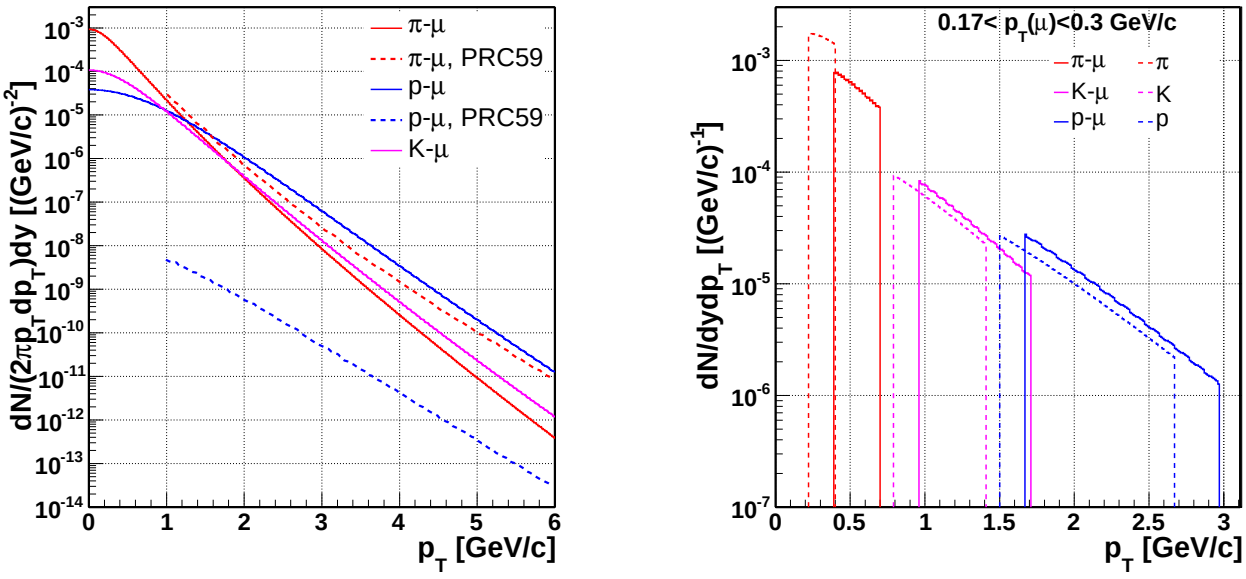

Figure 2.14: Left Panel: muonic atom yields from our estimate and from Kapusta [58]; right panel: muonic atom yields with muon momentum at $0.17 < p_T < 0.30$ GeV/c.

and a hadron carrying opposite charge. To observe these atoms, we would need the following: a) Dissociation of the atoms in detector material before the detector tracking and identification of the hadron and muon. It has been calculated by Prasa [59] that 0.01 inch of aluminum foil is sufficient to dissociate the atoms. This has been validated experimentally by Aronson in 1982. The aluminum foil is equivalent in terms of radiation length (0.3%) to our beryllium beam pipe. b) Muon identification at the appropriate momentum. With the combination of TPC dE/dx and TOF, STAR can cleanly identify muons at low momentum ($0.17 < p_T < 0.3$ GeV/c), as shown in Fig. 2.15. This will cover three different ranges of momenta of $0.4 < p_T < 0.7$ GeV/c, $0.9 < p_T < 1.7$ GeV/c and $1.7 < p_T < 2.9$ GeV/c for $\mu - \pi$, $\mu - K$, $\mu - \overline{p}$ respectively. In these ranges, the pion, kaons and protons are exactly within the TOF identification comfort zone. Muons can also be identified by the MTD at higher momentum ($p_T >$ 1.5 GeV/c), as also shown in Fig. 2.15. This means we will be able to identify $\mu - \pi$ at $p_T >$ 3 GeV/c. For $\mu - K$ and $\mu - \overline{p}$, the corresponding atom momentum is too high for its rate to be experimentally accessible.

Based on the muon identification range discussed in the above section, we can project the spectrum ranges for all three species of atoms. Figure 2.14 shows the corresponding atom and its daughter hadron p_T ranges when the muons are identified at $0.17 < p_T < 0.3$ GeV/c with TPC dE/dx and TOF. Table 2.1 shows the p_T ranges of all three types of atoms and their daughters identifiable by STAR with appreciable rates. For example, the antimatter muonic hydrogen production rate is about 2 candidates in one unit of rapidity in a million central Au+Au collisions. The TPC tracking and identification efficiency is on the order of 50%. In a data sample of 500M central events, we will have 500 such candidates. The $\mu - \pi$ atoms are produced at an order of magnitude higher rate in the low momentum range. These measurements provide three different

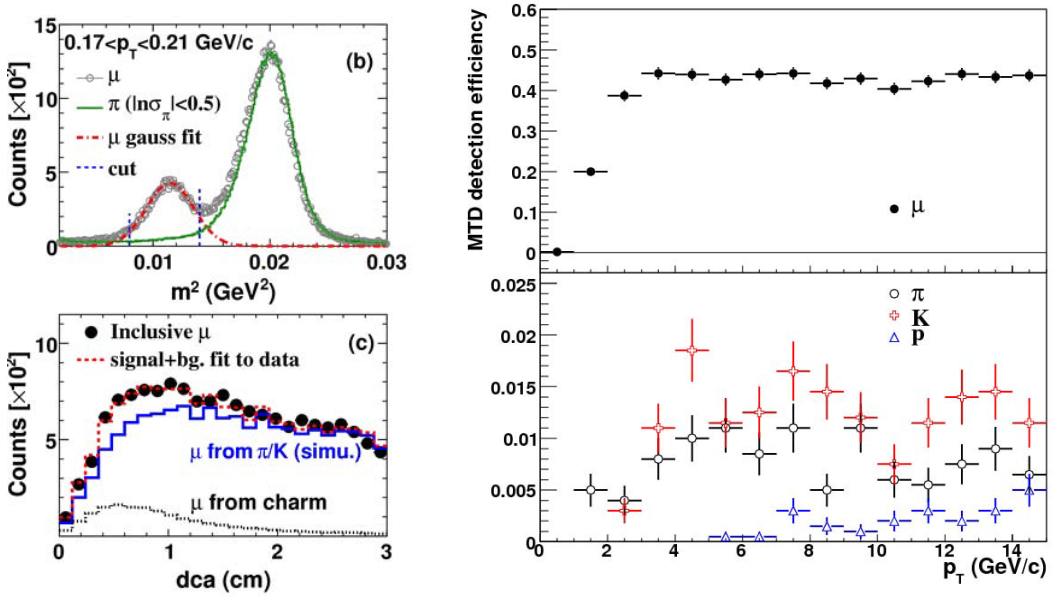

Figure 2.15: Left panels: muon identification at STAR with TPC dE/dx and TOF; Right panel: muon idenfitication and efficiency (top) compared to hadron efficiency (bottom) using Barrel Muon Telescope Detector.

Atom	μ p_T (GeV/c)	Hadron p_T	Atom p_T	dN/dy
$\mu - \pi$	[0.17,0.3]	[0.22,0.4]	[0.39,0.7]	9×10^{-5}
$\mu - K$	[0.17,0.3]	[0.8,1.4]	[0.97,1.7]	1×10^{-5}
$\mu - \overline{p}$	[0.17,0.3]	[1.5,2.7]	[1.7,3.0]	4×10^{-6}
$\mu - \pi$	> 1.5	> 2	> 3.5	3×10^{-9}

Table 2.1: Transverse momentum ranges for muonic atoms accessible to STAR.

measurements of the direct muon yields at low momentum. The yields of atoms at higher momentum are much lower, and the MTD trigger will greatly enhance the candidates to tape for offline reconstruction. The RHIC-II luminosity projection is about 60 KHz Au+Au hadronic interactions, which translates into 6000 Hz of central Au+Au collisions. In a 12 week run, that will produce about 100 $\mu - \pi$ atoms with muons at $p_T > 1.5$ GeV/c that are accessible to MTD trigger.

It may be possible to identify the atoms using the V0 topology without muon identification. However, the background is unknown, and more studies need to be done on this.

The available luminosity delivered to STAR is much higher than the STAR DAQ rate. For central Au+Au collisions (top 10%), the expected rate is 6000 Hz. With a MTD trigger [53], the rate can be reduced by an order of magnitude. This is more or less the full bandwidth STAR TPC is projected to handle for all the events. The daughter pion and muon from the atom have similar

momenta, and will often stay within a single TPC sector. To reduce the effective TPC rate, we propose to read out only the TPC sector associated with the MTD hit. This reduces not only the TPC effective rate by a factor of 24, but also the data volume and offline computing resources correspondingly. With this design, we will be able to take all the luminosity available to us for this physics topic.

In summary, RHIC provides a unique environment for producing and detecting new particles. The measurements outlined in this document not only provide potential discoveries of new particles but also a unique tool for probing the properties of sQGP.

Study Conical Emission through heavy flavor probes

The broad and double-peaked away-side di-hadron correlation with high-p_T trigger particles (see Figure 2.16) [60] is one of the surprising findings in relativistic heavy-ion collisions at RHIC. Three-particle correlations reveal off-diagonal structures in Au+Au data for the away-side correlated hadrons [61] (see Figure 2.17). Two leading scenarios are debated to describe the data. In one, it is argued that the triangular flow (v_3) from the initial fluctuations in the overlap geometry can account for the observation [62]. The other physics mechanism is supersonic Mach-cone shock waves, which can be generated by via energy deposition by fast moving partons in the dense medium. If Mach-cone shock waves are indeed the underlining physics mechanism, how the measured opening angle is affected by the medium dynamics and how one could extract the medium's speed of sound from three-particle correlations are the inevitable next questions. It is therefore important to measure conical emission induced by heavy flavor hadrons through 3-particle correlations to further understand the properties of the strongly coupled medium. The golden signature for the Mach cone is the velocity dependence of the conical emission angle. This requires heavy flavor correlation measurements at different p_T .

Based on the experience of the published charged hadron three-particle correlations [61], we will need at least 500k charm or bottom leading particles (D^0) to do a good 3-particle measurement. Utilizing the total cross section predicted by FONLL for $c\overline{c}$ ($256\mu b$) and $b\overline{b}$ ($1.87\mu b$) and the predicted p_T spectra in p+p collisions, taking into account the branching ratio as well as realistic efficiency estimates, we obtain a rough estimate of the RHIC delivered luminosity needed for this measurement in each heavy quark p_T bin as shown in Table 2.2.

Table 2.2: Estimates of the RHIC delivered luminosity needed for the heavy quark induced conical emission measurement for each heavy quark p_T bin.

p_T (GeV/c)	lum for charm (nb^{-1})	lum for bottom (nb^{-1})
3-4	2.5	35
4-5	10	50
5-6	25	80
$\geq$6	50	50

We clearly need the luminosity accumulated from multiple RHIC-II runs to carry on this im-

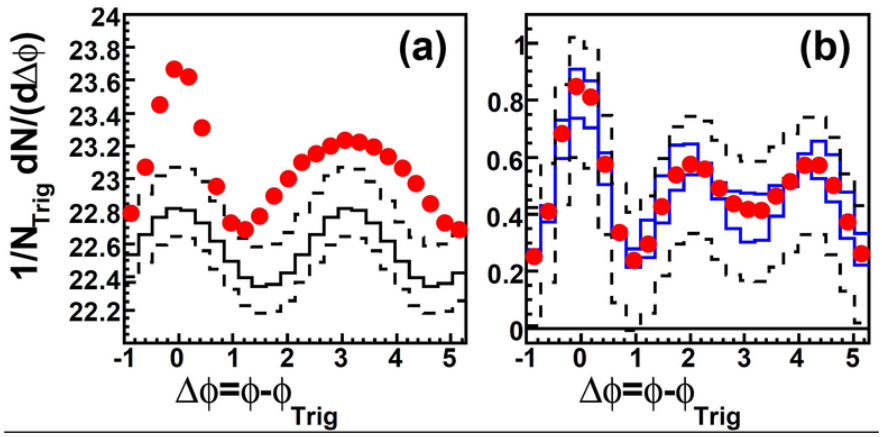

Figure 2.16: (left panel) Raw two-particle correlation signal (data points), anisotropic flow background (solid histogram), and background normalization systematic uncertainty (dashed histograms). (right panel) Background-subtracted two-particle correlation and systematic uncertainties due to background normalization (dashed histograms) and flow (blue histograms)

.

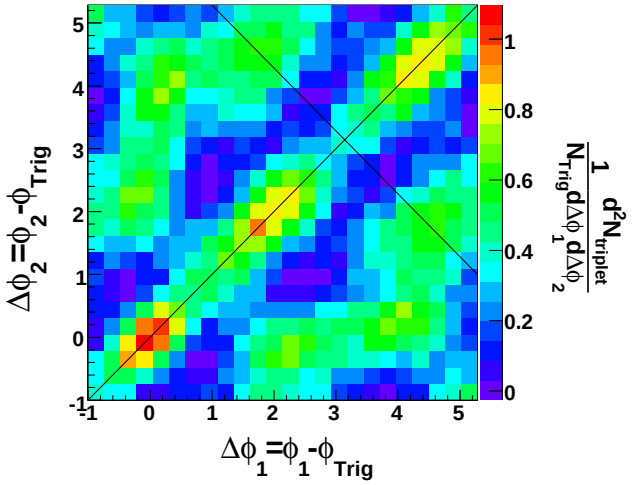

Figure 2.17: Background-subtracted three-particle correlations in ZDC-triggered central 12% Au+Au collisions at 200 GeV.

portant measurement.

Studying the Ridge through Jet-Hadron and Direct Photon - Hadron Correlations

The origin of the long-range correlation in pseudorapidity observed in Au+Au collisions is not yet understood. Whether it comes from jet-medium interactions or it is part of the bulk matter is still an open question. To unambiguously determine if the near-side ridge is caused by partonic energy loss or not, one can utilize jet-hadron correlations where instead of a trigger particle a fully reconstructed jet is used, to see if long-range $\Delta\eta$ correlations are present. A natural next step would be to study the jet shape of fully reconstructed jets to see if the jet structure is elongated in pseudorapidity. Furthermore on can "turn off" partonic energy loss by looking at near-side direct gamma - hadron correlations. If in these correlations a ridge structure is visible it would strongly suggest that the ridge is a bulk phenomena rather than a consequence of partonic energy loss. Overall, combing these measurements will help to further constrain the origin of the near-side ridge in heavy-ion collisions. We will be able to do this study with the current detector configuation and the high luminosity provided by RHIC-II upgrade.

2.2 What is the detailed mechanism for partonic energy loss?

To extend our understanding of the properties of the hot and dense medium produced at RHIC, it is essential to elucidate further our knowledge of the mechanisms by which highly energetic partons, produced in the early stages of the collisions, interact with the medium, and lose to it substantial amounts of their energy. The question, "what is the detailed mechanism for partonic energy loss?", is multi-faceted, requiring us to determine the answers to the following questions:

1. Is the mechanism predominantly collisional or radiative? Beyond this, at what energy scale can the coupling between the parton and the medium be described perturbatively, as opposed to via strong coupling methods?

2. Does the mechanism depend on the parton type?

3. Does the energy loss depend on the partonic energy and/or velocity?

To answer these questions, we need to establish further how the deposited energy is redistributed into the surrounding medium, and what is the path length dependence of the energy loss.

2.2.1 What do we know now?

The phenomenon of jet quenching was definitively established in the first three RHIC runs, with the observation of strongly quenched single-hadron [63] distributions and di-hadron correlations [64] in the most central Au+Au collisions but not in d+Au collisions, as shown in Fig. 2.18.

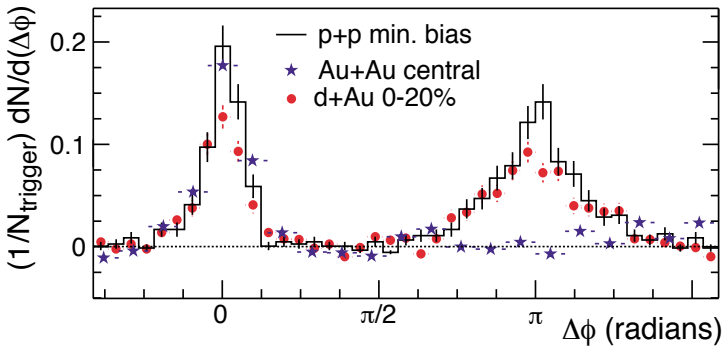

Figure 2.18: Dihadron correlations for p+p, d+Au, and central Au+Au collisions at $\sqrt{s_{NN}} = 200$ GeV [65].

At this point the energy loss was thought to be dominated by induced gluon radiation [66, 67]. If this were the case, then heavy flavor partons should exhibit only a very small energy loss due to the "dead-cone" effect [68]. However, R_{AA} measurements made with non-photonic electrons indicate that the heavy flavor suppression is very similar to that of light quarks and gluons [69, 70]. This led to the understanding that collisional energy loss was also significant, especially for charm and

bottom quarks. However, to date the magnitude of the non-photonic electrons suppression cannot be reproduced unless it is assumed they are all the decay products of charm. In p+p data STAR measurements have shown that at 7 GeV/c the $e_b/(e_b + e_c)$ ratio is ~0.5 [71], which, combined with non-photonic electron R_{AA}, indicates a significant amount of B meson energy loss at high p_T. Detailed bottom to charm meson measurements have not yet been made for Au+Au collisions and, therefore, the individual high-p_T suppression rates have not yet been measured. The measurement of these particles will be possible with the completion of the HFT and MTD upgrades, and these results are a specific focus of STAR over the next decade.

Leading particle measurements suffer from a number of limitations. First, leading hadrons come from a mixture of parent quarks and gluons. Second, as a fragmentation product, the energy of a hadron is not a perfect proxy for the energy of the parent parton. While, due to the steeply falling jet energy spectrum, the leading hadron frequently carries a significant fraction of the parent parton energy, such a trigger ultimately samples a wide range of partonic energies.

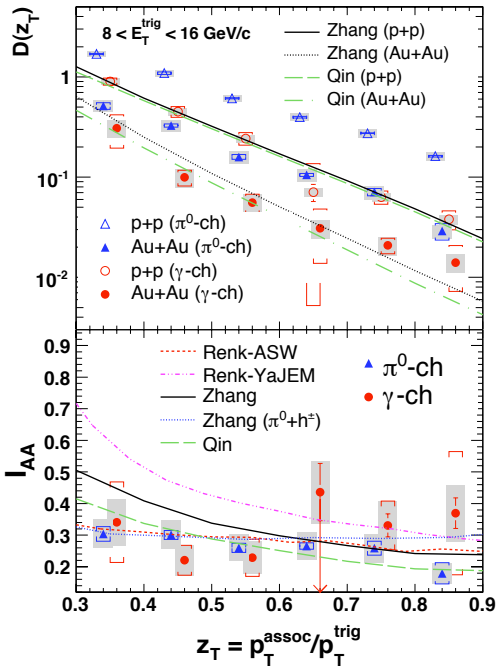

Figure 2.19: Top: The z_T of the away-side associated-particle yields from π^0- (triangles) and γ_{dir}-hadron (circles) correlations in p+p (open symbols) and 0-10% Au+Au (closed symbols) at $\sqrt{s_{NN}}$ = 200 GeV. Bottom: I_{AA} as a function of z_T for γ_{dir} (circles) and π^0 triggers (triangles). Boxes show the z_T-correlated systematic errors, and brackets show the point-to-point systematic errors. The bin centers are shifted for clarity. Data are compared to theoretical calculations [72].

The gamma-jet process potentially provides access to the underlying scattered parton's energy. By using a direct photon (γ_{dir}) as a tag, the kinematics can be largely resolved. Measurements of the distribution of particles from the jet opposite, in $\Delta\phi$, to the tagged photon reveals how

much energy was lost, and how it was redistributed, by the colored parton as it traversed the medium. First attempts to study γ_{dir}-hadron and compare to π^0-hadron correlations have been made. Since photons have no color or charge and are therefore not expected to interact with the medium, such comparative analyses can also be used to study the path-length dependence of the partonic energy loss. The use of γ_{dir} as the trigger instead of a π allows us to probe deeper into the medium, reducing the interaction length of the away-side jet. However, with the precision of current measurements, over the momentum range of the associated and trigger particles currently accessible to such analyses at STAR, no obvious difference in the suppression, measured via I_{AA}, is observed when γ_{dir} or π^0 are used as triggers, as shown in Fig. 2.19 [72]. The reach and precision of further measurements will be discussed later in this section.

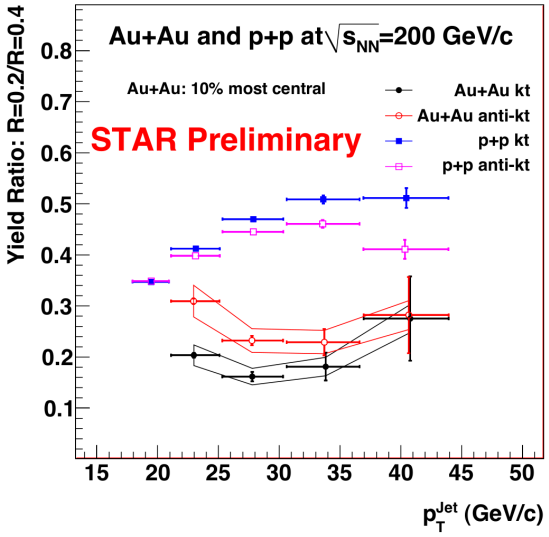

Figure 2.20: Ratio of the jet spectra reconstructed using resolution parameters of R=0.2 and R=0.4 for p+p and central Au+Au collisions at $\sqrt{s_{NN}}$ = 200 GeV [73].

Another method to limit the uncertainty in the partonic energy is through the full reconstruction of jets in heavy ion collisions. Beyond producing a far better proxy for the energy of the parent parton than a leading hadron, this technique allows one to trace the evolution of energy flow in directions both longitudinal and transverse to the direction of the parent parton. STAR has recently had success in performing full jet reconstruction in Au+Au collisions, via the use of the FastJet package [74, 75, 76] and novel background subtraction techniques.

Figure 2.20 shows the ratio of the reconstructed jet spectra when using a resolution parameter of R=0.2 compared to R=0.4 for p+p and Au+Au collisions. As expected the p+p data rise with increasing jet p_T due to the increase in the collimation of the jet fragmentation. The Au+Au ratio is very different indicating significant redistribution of the jet fragments. This analysis is supplemented by jet-hadron correlations. Such correlations require that the anti-k_T jet finding

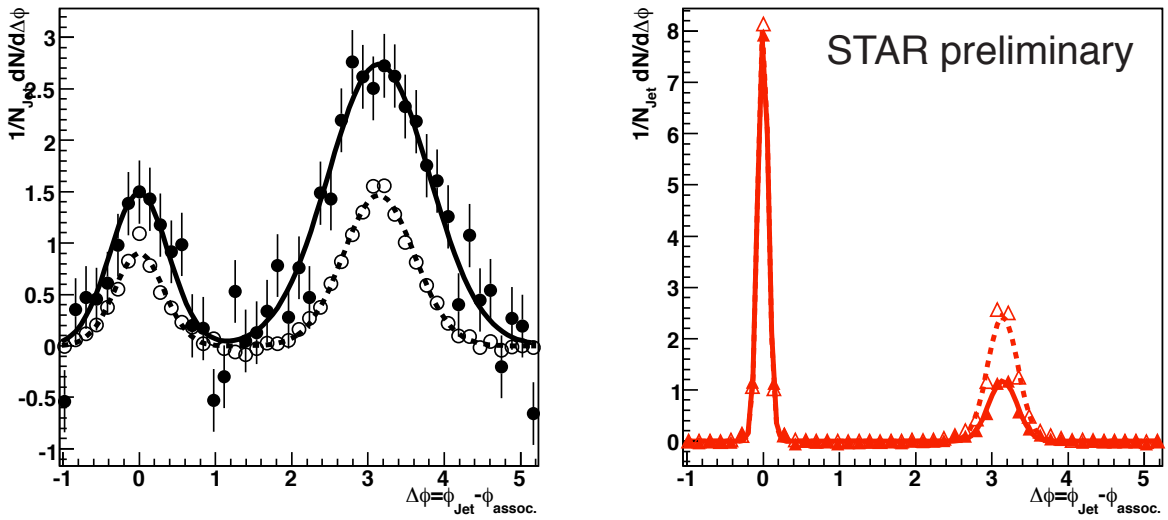

Figure 2.21: Jet-hadron correlations for R=0.4 for p+p (open symbols) and central Au+Au (closed symbols) collisions at $\sqrt{s_{NN}}$ = 200 GeV [77]. Left: $0.2 < p_T^{associated} < 1.0$ GeV/c. Right: $p_T^{associated} > 2.5$ GeV/c. Trigger jet selection described in the text. Curves are Gaussian fits.

algorithm locates a jet-like energy cluster with a summed energy greater than 20 GeV when only particles with momenta greater than 2 GeV/c are considered. The trigger jet also includes a high tower, with neutral E_T greater than 5.5 GeV. In this way a highly biased jet sample is selected such that in Au+Au collisions this "trigger" jet is likely to have been emitted without interacting with the medium. The direction of this trigger jet is used as the axis with which to study the $\Delta\phi$ correlation of all the other charged particles in the event. Figure 2.21 shows these correlations for central Au+Au and p+p collisions for associated particle p_T of $0.2 < p_T < 1.0$ GeV/c and $p_T > 2.5$ GeV/c. It is clear that the jet-like correlation on the away-side, although significantly suppressed for high $p_{T,assoc}$, has the same width in Au+Au as in p+p. However, the same conclusion does not hold for low $p_{T,assoc}$. In this case both the width of the Au+Au correlation and the number of particles involved are significantly increased. The lost partonic energy re-emerges as numerous low-p_T particles with a more diffuse correlation with respect to the initial partonic direction, but a correlation is preserved. These studies show that, while the energy is radiated over a wider cone in heavy ion collisions than in p+p collisions, a large fraction of the energy can be recovered, and detailed measurements can be made, on a statistical level, about the energy flow of parton energy loss.

The picture that emerges from the study of 2+1 particle correlations is that when a second high p_T particle is demanded in the away-side of the $\Delta\phi$ correlation, both the near- and away-side peaks in Au+Au collisions correspond in width and magnitude to those observed in p+p [78]. This suggests that asking for high-p_T, or high-z, fragments from a jet in central A-A collisions biases the jet towards surface emission and/or not interacting with the hot and dense medium. A

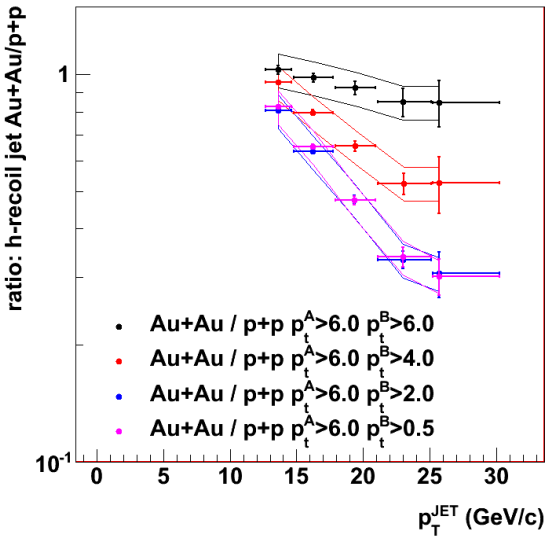

Figure 2.22: The ratio of hadron-jet correlations for Au+Au/p+p collisions at $\sqrt{s_{NN}}$= 200 GeV as a function of reconstructed jet p_T [73].

similar effect can be deduced by studying hadron-jet correlations. In this analysis a high energy Barrel Electromagnetic Calorimeter (BEMC) tower signal, most likely a neutral pion, is selected as the trigger particle. The energy spectrum of the recoiling reconstructed jet at $|\Delta\phi - \pi| < 0.4$ to this trigger is recorded in both p+p and central Au+Au. The yields in p+p and Au+Au are normalized to the trigger hadron pair. The ratio of the normalized away-side jet spectra is shown in Fig. 2.22 for three recoil jet leading particle p_T thresholds. As this threshold is increased the ratio Au+Au/p+p also increases. This means that for this selection the probability of finding an away-side jet of a fixed energy is similar in Au+Au to that of p+p collisions, i.e. in Au+Au collisions these cuts select a very similar jet population per di-hadron trigger as for p+p. This suggests that the partonic energy loss of the away-side jet is decreased, which in turn indicates that asking for a highly energetic near-side and away-side hadronic fragment biases towards non-interacting/surface jets. When the p_T threshold is reduced, as shown by the blue data points in Fig. 2.22, the ratio is far below unity and drops significantly with jet p_T, suggesting a substantial redistribution of the jet energy in Au+Au collisions.

In both p+p and Au+Au collisions a biased data sample was collected by requiring that each event had at least one BEMC tower recording a transverse energy of at least 5.5 GeV. First the anti-k_T algorithm with R=0.4 was run on these data with a lower p_T threshold for both neutral and charged particles of 2 GeV/c. A "trigger" jet was identified as jet with $p_T > 20$ GeV/c that included the triggered tower, and the jet algorithm was re-run with the particle momentum p_T threshold reduced to 0.2 GeV/c. Recoil jets were detected as those with $|\Delta\phi| > 2.74$ radians with respect to the "trigger" jet. Due to the momentum cut on the particles and the fact that the BEMC

only accurately responds to neutral particles, the "trigger" jet has a highly biased fragmentation towards high-z neutral particles. The recoil jet does not suffer from such a bias. In Au+Au events this bias towards high-z fragments also means that the jet is highly likely to come from the surface of the medium and/or pass through the medium without interactions. The recoil jet is therefore biased towards longer path lengths and is more likely to lose significant energy in the medium. The black points in the left plot of Fig. 2.23 show the per trigger corrected reconstructed "recoil" jet spectrum from p+p data. The magenta points are for the corrected reconstructed jets from the 0-20% most central Au+Au data. The correction in Au+Au data is via unfolding, which accounts for background fluctuations to allow for a fair comparison to the p+p spectrum. If one assumes that 100% of the recoil jets in the STAR acceptance are identified in both Au+Au and p+p, the two spectra should be identical if the binary scaling of hard scattered partons holds. There is considerable evidence from the integrated yield of heavy flavor particles and the R_{AA} of high-p_T photons that this is the case. There is a distinct lack of "recoil" jets at a given energy compared to p+p. If, however, a fixed energy loss of 8 GeV is assumed for all measured "recoil" jets and this is artificially added to each jet, the spectra become very similar, red points in Fig. 2.23. It can be seen from the right plot of Fig. 2.23, which shows the ratio of the shifted Au+Au to the p+p recoil spectra that this is not exact, but under such a scenario a maximal path length energy loss of 7-8 GeV/c outside of R=0.4 is indicated. This is similar to the energy outside of R=0.4 for the away-side jet that is calculated via summing of the large angle energy depositions in the jet-hadron correlations of Fig. 2.21.

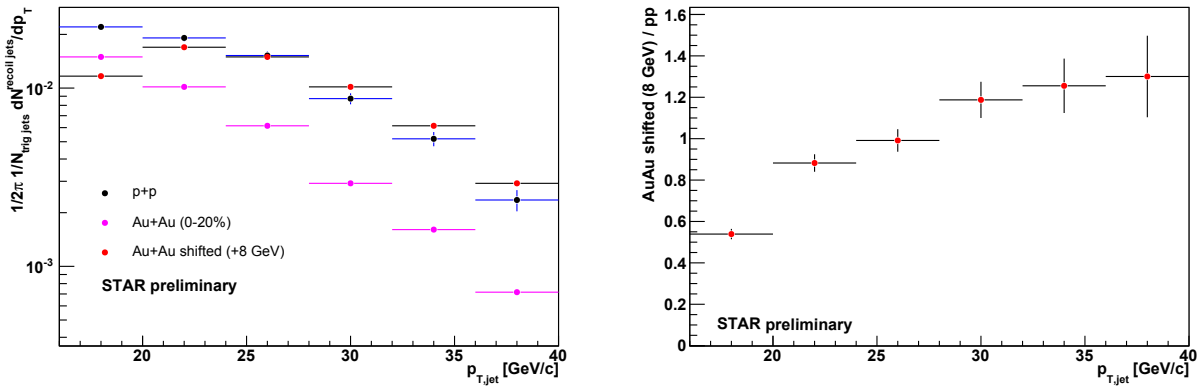

Figure 2.23: Left: The recoil jet spectra (R=0.4) for p+p and Au+Au collisions and for Au+Au collisions when the jet energy is shifted by 8 GeV. Right: The ratio of the recoil jet spectra after shifting the Au+Au spectrum. See text for further details.

2.2.2 What measurements do we need to perform to answer the question?

Since the first jet quenching measurements, the understanding of the phenomenon has advanced, but to this day attempts to quantify the properties of the medium differ by orders of magnitude

between different theoretical approaches [79, 80]. The TechQM collaboration [81] began the process of resolving this issue, and the JET collaboration [82] will continue this work with the goal to produce a solid and complete calculational framework with which to interpret the data.

One functional way to quantify partonic energy loss is via the modification of the fragmentation function. However, in order to interpret leading particle measurements, the theoretical approaches need to fold in the parton type, the underlying partonic spectrum, the vacuum fragmentation function and the fluctuations in the energy loss, together with fluctuations in the geometry of the matter probed, in the process of which a number of approximations need to be made. Different theoretical treatments make different choices about these approximations. Because of these different choices, from the same data different approaches produce dramatically different properties of the matter probed. Experimentally, the way forward is to limit the choices that theories make. New techniques will become available with the higher luminosity at RHIC-II, and with the advent of the LHC, which move beyond leading particle measurements and have high statistical precision and will help to constrain this theoretical space.

While further refinement of calculations involving perturbative techniques will continue, a major alternative picture for energy loss has emerged in recent years, which utilizes strong coupling techniques rooted in the AdS/CFT framework (for a recent overview, see [83]). This picture takes a fundamentally different view of the energy loss process: rather than treating the parton as a perturbative probe of a perhaps strongly coupled medium, it treats the entire process as strongly coupled. The strongly coupled theory makes specific predictions about the length dependence of and the fragmentation cascade due to the energy loss process, which differ markedly from those of the weakly coupled theory. The new techniques and measurements outlined below will allow for detailed tests of these predictions, to establish whether, and, if so, at what energy scale, the treatment of energy loss via strong coupling is merited.

While first attempts at γ-hadron measurements have been made with the STAR detector, Fig. 2.19, these suffer from limited reach due to limited luminosity. High precision measurements can be made with the existing STAR detector and projected RHIC-II luminosities by the middle of the decade, for parton p_T out to 15 GeV/c. Figure 2.24 shows projected uncertainties for the suppression of hadrons recoiling from a 15 GeV photon with fractional energy $z_T = 0.25$ as a function of year, with projected luminosities. Predictions from different theoretical approaches are also shown. At RHIC energies, for this photon energy, backgrounds from fragmentation photons are limited and backgrounds from π^0 fragmentation are small enough to be treatable. These backgrounds become more intractable for fixed photon energy as $\sqrt{s_{NN}}$ increases, so measurements at this photon energy are best made at RHIC energies. Reach to larger p_T would require major upgrades to the STAR Barrel Electromagnetic Calorimeter, and higher luminosity to make precision measurements.

Studies of the path length dependence of partonic energy loss have already been attempted via di-hadron correlations with respect to the reaction plane, but further sensitivity can be gained by utilizing the full jet reconstruction analysis. If the fraction of energy lost is dependent on the distance the parton travels through the plasma, an effective v_2 should emerge for reconstructed jets. Preliminary analysis indicates that this is so, but more detailed studies are needed to ensure that the jet fragmentation products are not affecting the calculated reaction plane angle. To complete

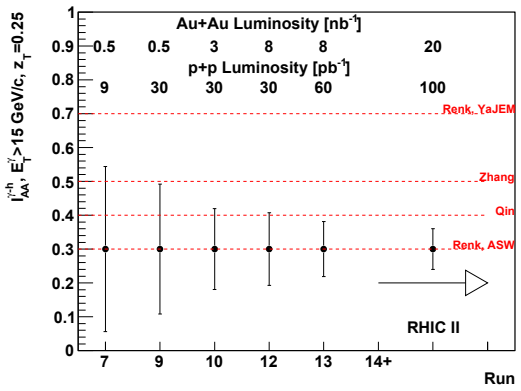

Figure 2.24: Projection of statistical uncertainties in the ratio between central Au+Au and p+p of away-side yield of hadrons associated with a trigger direct photon, $I_{AA}^{\gamma-h}$, as a function of RHIC run and increasing cumulative luminosity sampled. The lines show predictions for this ratio. (Renk-YaJEM and Renk-ASW [84, 85], Zhang [86], Qin[87])

this study, RHIC-II luminosities are needed to ensure that sufficient statistics are available for the more peripheral collisions.

A different method to study the path length dependence of the partonic energy loss is to exploit the fact that uranium is a prolate nucleus. Even in central collisions the overlap region of some of the collisions will be elliptical, and one can study the energy loss of jets in and out of the event-plane where jet production is maximal. An added bonus is that the energy density of U+U collisions at $\sqrt{s_{NN}} = 200$ GeV is predicted to be greater than that of Au+Au, so the jet quenching effects may be more dramatic. Two weeks of collisions at design luminosity gives 120 μb^{-1}. With this luminosity, assuming a 300 Hz DAQ rate and 50% up-time one can expect to record 55M 0-30% central events which would allow one to measure jets out to 40 GeV/c. This would allow us to take a first look at the data from these collisions; however, more data would be needed to make a detailed analysis with respect to the reaction plane.

The recent success of full jet finding in the heavy-ion environment has made it possible to probe in more detail how the lost partonic energy emerges. However, these studies are only just beginning, and much remains to be done. While there are clear indications of jet broadening due to partonic interactions with the medium, a much deeper understanding is needed. To this end sub-jet analyses and jet-shape studies (both integral and differential) are needed as a function of jet energy. STAR also intends to utilize the recently completed ToF to allow for a particle dependent study of the correlated energy.

It has also recently been suggested that the "ridge" and "mach-cone" phenomena reported at RHIC could be due to correlated particle production due to v_3, or triangular flow. One can study this claim in more detail by using jet-finding algorithms to identify jets and looking at the jet-hadron correlations in both $\Delta\phi$ and $\Delta\eta$. The use of the jet-finder to identify triggers reduces the number of spurious random triggers that are more likely to be part of the bulk. If the ridge

and "mach-cone" are bulk phenomena, and not associated with the jet, such measurements should result in a large reduction of these correlations.

The major issue with these measurements is the trigger. The simplest trigger, a high tower in the BEMC, is also the most biased, preferentially selecting those jets with the most highly collimated energy profile and the least modified fragmentation function. Measurements have been made with minimum bias, or central, triggers which are simpler to interpret than triggered data sets. These do not rely on the calorimeter to set an energy scale, and so introduce no bias on the jet fragmentation, but cannot sample the full luminosity provided by RHIC. Upgrades to the trigger are necessary to allow for an intermediate step. As is currently done in p+p collisions, one would trigger on a cluster of electromagnetic energy in a 0.4×0.4 $\eta \times \phi$ patch in the BEMC, but with boundaries that can move, rather than the fixed boundaries that exist in the current trigger system. This trigger has the potential to recover from much of the collimation bias in the high tower trigger.

With this trigger upgrade, detailed studies of jet properties for jet E_T from approximately 20 GeV to 50 GeV will be possible, where the lower limit is set by fluctuations in the underlying event (of average energy approximately 45 GeV for a jet radius of 0.4 at $\sqrt{s_{NN}} = 200$ GeV) and the upper limit placed by luminosity considerations. While measurements at lower jet energy are best done at RHIC energies due to the lower underlying event, higher E_T jet measurements are best done at higher energies than RHIC can provide. However, it is currently thought that jet measurements at the LHC can only be performed in Pb-Pb collisions for jet $E_T >\sim 50$ GeV/c. As mentioned an outstanding question of vital importance to the theoretical simulation of partonic energy loss is if the lost energy is a constant for all partonic energies or fractional. It is currently predicted to depend logarithmically on the parton's energy. It is therefore important to push the STAR measurements to as high jet energies as possible to connect with the up-coming data from the LHC. Only by combining the two data-sets will the reach in jet energy be sufficient to answer this important point. It is estimated that there are 0.01 jets per million central Au+Au events with energies of 50 GeV/c. A minimum of 100 jets are needed at this p_T to make a study of the energy loss, i.e. 700M central events will have to be recorded by STAR. This requires RHIC-II luminosities. The data collected in Run 10 will also be studied to investigate in more detail the trigger biases created for such highly energetic jets when the BEMC high tower and/or jet patch triggers are used. If the trigger bias can be understood for some analyses, such triggers can be used to collect more data, since at RHIC-II luminosities STAR cannot record all the central events delivered.

At RHIC-II luminosities the charge distortions in the TPC are significant, affecting, even after off-line corrections, the momentum resolution for charged particles with very small sagitta (i.e. high p_T). Hence, the question of whether the 50 GeV/c jet energies can be resolved by STAR with sufficient accuracy has arisen, or is the installation of barrel hadronic calorimetry necessary to measure such highly energetic jets? To this end preliminary studies have been performed to simulate the expected charged particle irresolution at high p_T and see its effect on the reconstructed jet spectra. STAR's recently recorded 500 GeV p+p data suggest that, at 30 GeV/c, the charged track momentum resolution is $\sigma_k/k \sim 0.3$. This high luminosity data set involved charge distortions similar to those anticipated in the heavy-ion RHIC-II era. The left plot of Fig. 2.25 shows the effect of this

reduced resolution on the detector level jet energy spectrum when PYTHIA's fragmentation and energy spectrum are assumed. The black dashed curve is the particle level PYTHIA jet spectrum, the solid blue curve is the particle level reconstructed jet spectrum when nominal resolutions are assumed for the charged and neutral particles. The magenta curve includes a smearing of 30% for charged particles with $p_T > 15$ GeV/c, as suggested by the analysis of the 500 GeV p+p data. As expected there is a significant flattening of the jet spectrum at high p_T. This effect is emphasized in the right plot of Fig. 2.25, where the ratios of the reconstructed smeared and unfolded jet spectrum to that of the particle level PYTHIA one are given. When the track momentum resolution, and hence the jet energy resolution, are well known the true particle level spectrum can be obtained via unfolding, the black and blue curves in the right plot of Fig. 2.25. However, this requires a good determination of the momentum resolution as a function of particle p_T. This should be possible with the increased statistics for single tracks from the data set needed to make the jet measurements. The magenta curve in the right plot of Fig. 2.25 shows the results of unfolding the magenta curve on the left plot with the jet energy resolutions derived from the nominal particle momentum resolution, which is $\sigma_k/k = 0.0053p_T + 0.005$.

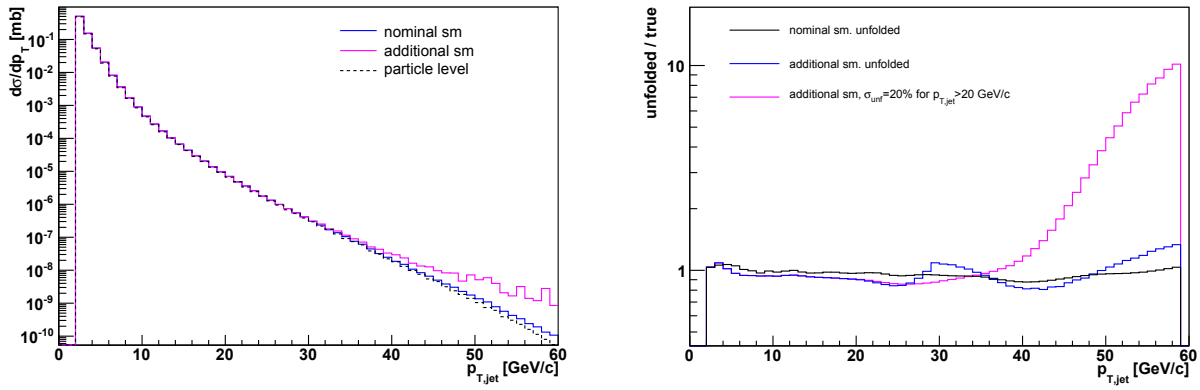

Figure 2.25: The effect of applying various momentum resolutions for the charged tracks within the jet. PYTHIA's minbias spectrum and fragmentation functions are assumed. The anti-k_T jet finding algorithm was used with a resolution parameter of R=0.4. Left: The particle level reconstructed jet spectra. Right: The ratio to the particle level jet spectrum of the reconstructed jet spectra after unfolding when various charged particle momentum resolutions are assumed. See text for further detail.

If detailed momentum resolution measurements cannot be made, the particle level jet spectrum can still be resolved by placing an upper cut on the p_T of the charged tracks used in the analysis. Figure 2.26 shows the same PYTHIA simulations but this time with a variety of cuts placed on the maximum value of the charged particles' transverse momenta. While the jet spectrum is shown at the particle level, the track cut was placed at the detector level to account for the effects of momentum resolution. It can be seen that for an upper cut of 20-30 GeV/c the jet loss is less than 10% at jet energies of 50 GeV/c. This loss will be further reduced in the Au+Au analyses due to the quenching of high p_T particles by the medium.

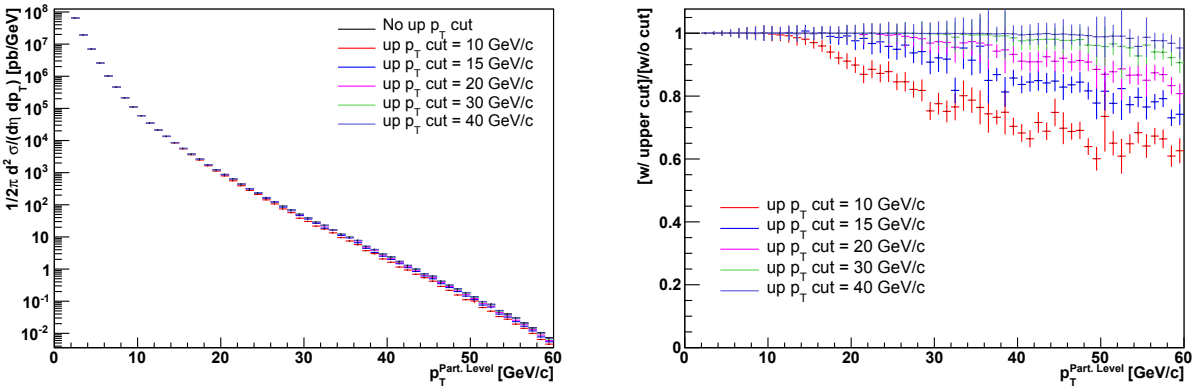

Figure 2.26: The effect of placing an upper p_T cut on the charged tracks within the jet assuming PYTHIA's minbias spectrum and fragmentation. The anti-k_T jet finding algorithm was used with a resolution parameter of R=0.4. Left: the particle level jet spectra after applying various upper p_T cuts. Right: The ratio of the particle jet spectra. See text for further detail.

A further axis in the space of jet quenching is provided by partonic identity. While it is difficult to disentangle light quarks from gluons, especially in a heavy ion environment, charm and bottom can be easily tagged by the existence of a charmed or bottom hadron in the final state. Due to their large masses the charm and bottom quarks are predominantly produced via hard scattering in the initial stage of the high-energy heavy-ion collision. The final state spectra can therefore serve as a sensitive tool to probe in-medium rescattering and interactions responsible for thermalization. STAR plans to measure the cross-sections and transverse momentum spectra of hadrons with open and hidden heavy flavor.

At p_T relevant to RHIC collisions, around 10 GeV/c, both charm and bottom are slow probes, with $\beta\gamma$ of the order of 1-10, which has been predicted to lead to weaker gluon Bremsstrahlung via the "dead cone" effect. Other sources of partonic energy loss, such as elastic scattering, have a different dependence on parton velocity than Bremsstrahlung, and also have a different pathlength dependence. The ability to vary parton velocity and momentum independently, in the hard regime, therefore enables one to disentangle the various mechanisms in play when a parton loses energy.

Leading particle measurements will be enabled by the Heavy Flavor Tracker, which can cleanly identify and fully reconstruct the kinematics of charmed hadrons. Figure 2.27 show the estimated D^0 significance of the $K\pi$ invariant mass as a function of p_T for 500M central Au+Au collisions. In this figure the HFT is used to identify the secondary vertex, and the combined TPC/TOF PID used to identify the K and π. Though these channels are not triggerable, the estimated reach in D^0 reconstruction is to 10 GeV/c in a RHIC year, well into the $\beta\gamma$ where charm becomes mainly a way to tag a light quark. At these high p_T, measurements of the nuclear modification factor, R_{AA}, will provide new insights into medium properties. Figure 2.28 shows the projected uncertainty of R_{CP} of D^0 mesons reconstructed through their $K\pi$ decay channel using 500 M minimum-bias events at $|vertex_z| \leq 5$cm using HFT. Here we assume that the suppression for heavy quarks is the same as that of light quarks. Taking into account the STAR duty factor (50%), the efficiency

of the $vertex_z$ cut (20%), 50 kHz collision rates at RHIC-II, and assuming 500 Hz bandwidth for minimum-bias trigger, this corresponds to 5 nb^{-1} delivered Au+Au collisions, which is in between the minimum (3.3 nb^{-1}) and maximum (21 nb^{-1}) luminosity RHIC-II is expected to deliver in a 12-week run [88].

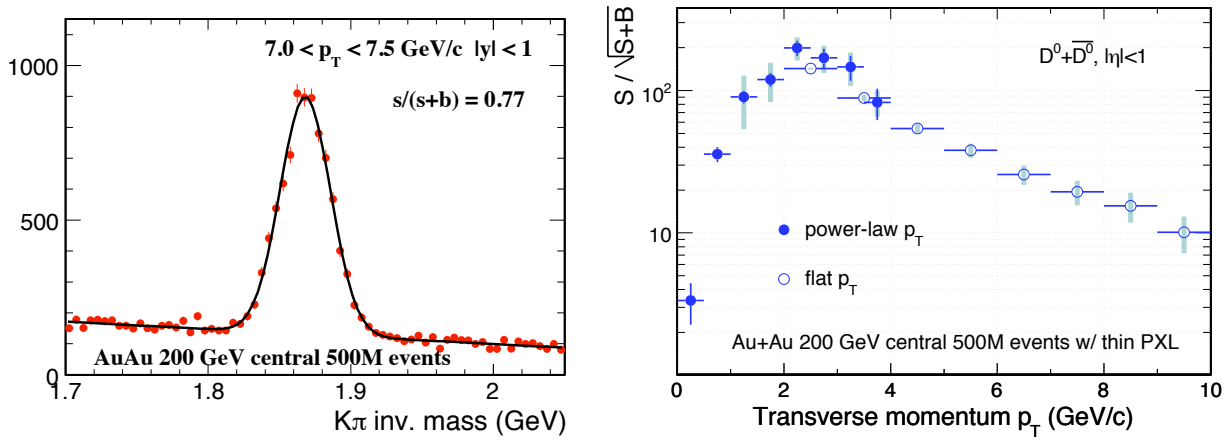

Figure 2.27: The estimated D^0+$\bar{D}^0$ reconstruction significance for 500M central Au+Au collisions at $\sqrt{s_{NN}}$ = 200 GeV using the HFT. Left : The invariant mass distribution for 7 < D^0+$\bar{D}^0$ < 7.5 GeV/c. Right: As a function of D^0+$\bar{D}^0$ p$_T$.

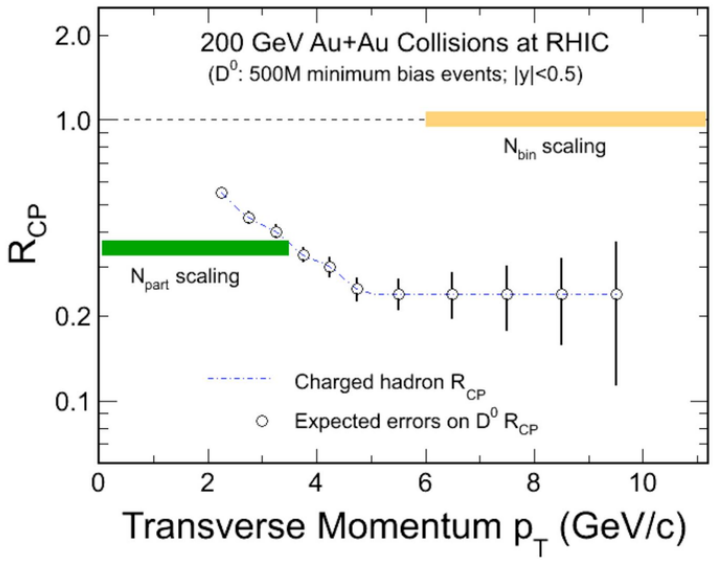

Figure 2.28: Uncertainty for the R_{CP} measurement as a function of p_T with 500 million minimum-bias Au+Au collisions.

As compared to leptonic measurements, direct open charm reconstruction removes one step in the ambiguous decay chain from a lepton to a hadron to a parton, at each point of which information is lost. This makes the interpretation of correlation measurements cleaner. Since in elementary collisions, heavy quarks fragment hard, leading particle measurements with heavy quarks provide much better proxies for the partonic kinematics than such measurements with light quarks, though the possibility of reconstruction of tagged heavy quark jets is worth further study. An interesting first study will be to measure the near-side correlation of hadrons with respect to the reconstructed charm meson, and look for evidence of the emitted soft gluons as the heavy parton passed through the medium.

The non-photonic electron spectra are dominated by semileptonic decays from charm and bottom mesons. Using a high precision direct measurement of charm in their hadronic decay channels, we will be able to evaluate the charm contribution to the non-photonic electon spectra and obtain the pure bottom yield. We can also statistically distinguish electrons from charm and bottom decay electrons taking into account the different life times of charm and bottom mesons. The left panel of Figure 2.29 shows the projection of the ratio of bottom decay electron over the total non-photonic electron yield using the latter method. The projection of the low p_T measurements is represented by the open circles using data from 50 million central Au+Au collisions. The projection of high p_T measurements is represented by the closed circles, using high-tower trigger sampling from 500 μb^{-1} Au+Au collisions at $|vertex_z| \leq 5$ cm, corresponding to 5 nb^{-1} RHIC delivered luminosity. The right panel of the figure shows the projection on the R_{CP} measurements for electrons from charm (red) and bottom (blue) decays with the same amount of delivered luminosity as in the left panel. Measurements at $p_T \leq 3$ GeV/c with the assumed luminosity are of excellent precision, while at high p_T, we need to accumulate data from more than one full RHIC-II Au+Au run to obtain the desired high precision results.

pQCD models including both radiative and collisional energy loss predict that heavy quark R_{AA} increases as a function of p_T in the very high p_T region, while AdS/CFT models expect the R_{AA} to slightly decrease with p_T [89]. One of the measurements proposed to distinguish between these two scenarios is the ratio of R_{AA}^{charm} over R_{AA}^{bottom} as a function of p_T. Figure 2.30 shows the predicted results of this ratio at RHIC from both pQCD and AdS/CFT models. The magnitudes as well as the trends as a function of the p_T are dramatically different. However, this specific prediction has limitations in its applicability, as denoted by the brackets in the figure. Depending on the strength of the interaction, it may be necessary to integrate luminosity over a number of years at RHIC, and to extend the calculation to take into account higher order corrections, in order to make a quantitative comparison between theory and experiment.

An alternative way to perform the crucial measurement of B meson production is through $B \rightarrow J/\psi + X$ decays. The J/ψ is produced via two channels, direct J/ψ, including feed down from other charmonia states, and $B \rightarrow J/\psi + X$. The B meson decay channel is the only known way to produce a displaced J/ψ, and hence bottom can be unambiguously disentangled from the more copious charm. The effective longer lifetime of daughter J/ψ from the B make it cleanly distinguishable from that of the primary particle. This displaced decay vertex can be identified offline via the high position resolution of the HFT and used to filter out J/ψ from B decays by setting a cut on the "pseudo-$c\tau$", which is an experimental approximation of the actual $c\tau$. The

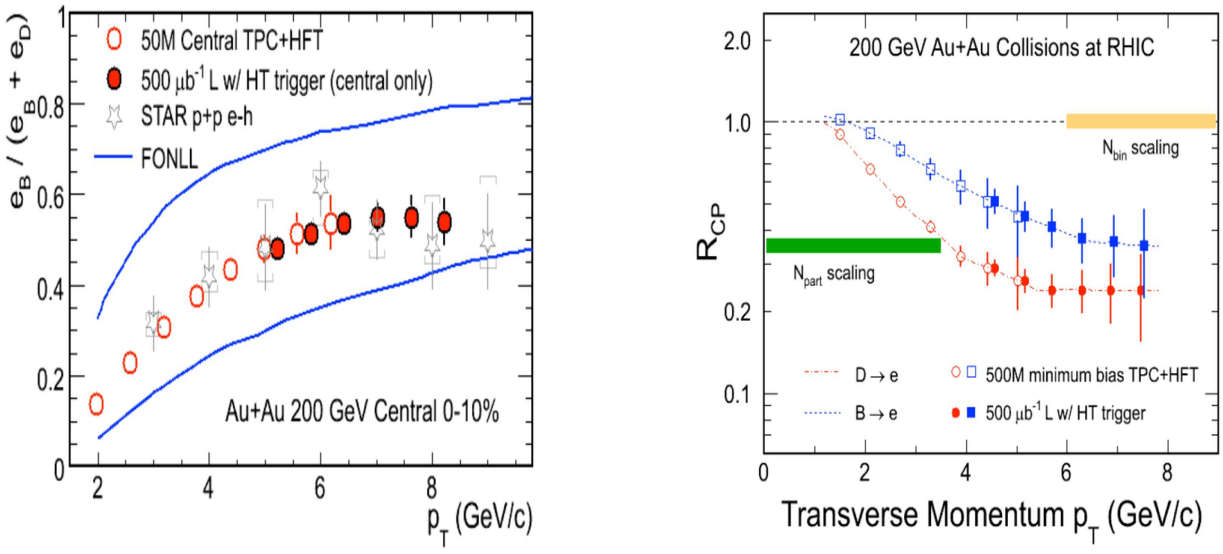

Figure 2.29: (left panel) The (B→e)/NPE ratio as a function of p_T. Expected errors are estimated for 50 million Au+Au central events (open circles) and 500 μb^{-1} sampled luminosity with a high tower trigger (closed circles). Open stars represent preliminary results from 200 GeV p+p collisions through electron-hadron correlation. (Right panel) Nuclear modification factor R_{CP} of electrons from D meson and B meson decays. Expected uncertainties are estimated for 500 M Au+Au minimum-bias events (open symbols) and 500 μb^{-1} sampled luminosity with a high-tower trigger at $|vertex_z| \leq 5$ cm (filled symbols), corresponding to 5 nb^{-1} RHIC delivered luminosity.

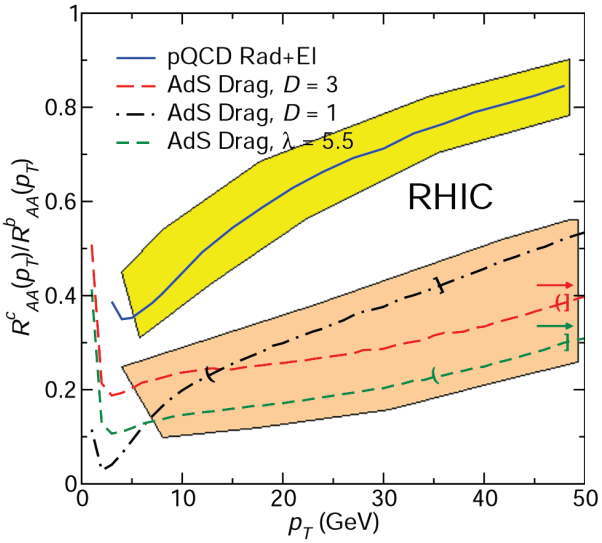

Figure 2.30: Prediction of $R_{AA}^{charm}/R_{AA}^{bottom}$ from AdS/CFT and pQCD with a range of input parameters at RHIC.

pseudo-$c\tau$ is defined as $\overrightarrow{L} \cdot p_T^{J/\psi}/|p_T^{J/\psi}| \cdot |M^{J/\psi}/|p_T^{J/\psi}|$, where $\overrightarrow{L}$ is the path length between the J/ψ production location and collision vertex, $M^{J/\psi}$ is the J/ψ mass and $p_T^{J/\psi}$ is the J/ψ p_T. The left panel of the Figure 2.31 shows the pseudo-$c\tau$ distributions for prompt and B-decay $J/\psi \rightarrow e^+e^-$ in central Au+Au collisions, where pileup effects in the HFT detector are included. As shown in the right panel of Figure 2.31, by requiring a pseudo-$c\tau$ larger than 700 μm, we can reject almost all of the background while keeping a clean sample of B-decay J/ψ with about 20% efficiency. The power of this measurement is to provide a clean sample of B-decay J/ψ to study bottom production.

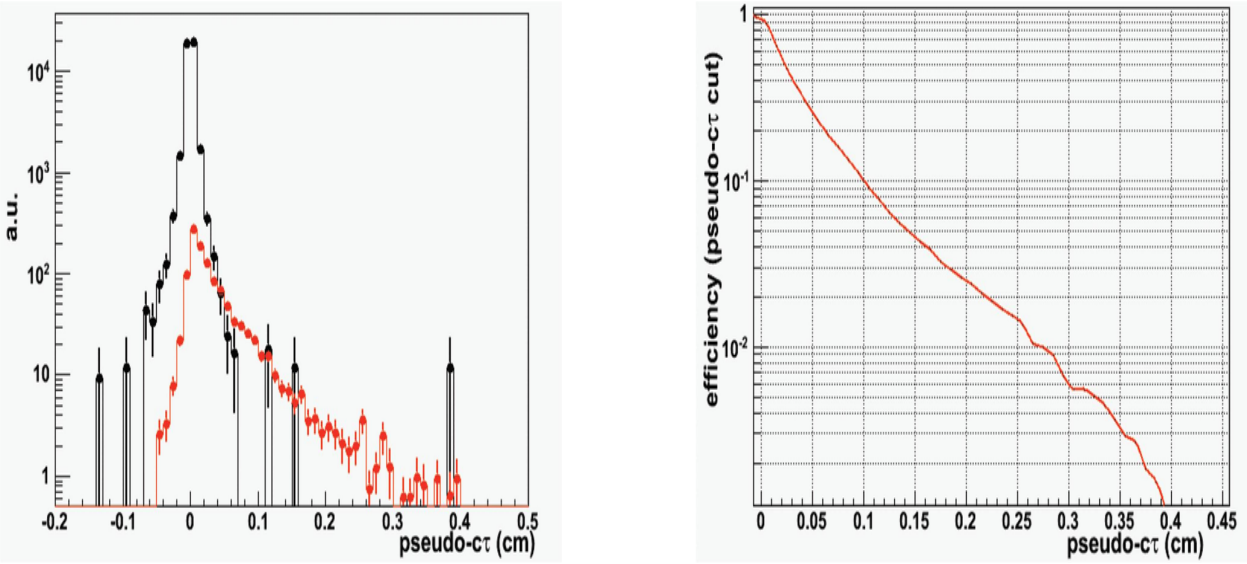

Figure 2.31: Left panel: pseudo-$c\tau$ distributions for direct and B-decay $J/\psi \rightarrow e^+e^-$ in central Au+Au collisions after including HFT PIXEL detector pile-up effects. The black and red histograms are from direct and B-decay $J/\psi \rightarrow e^+e^-$, respectively. The right panel shows the efficiency under different pseudo-$c\tau$ cuts for B-decay $J/\psi \rightarrow e^+e^-$.

The $p_T^{J/\psi}$ is required to be larger than 1.25 GeV/c, so that the pseudo-$c\tau$ is close to the actual B meson $c\tau$. This represents a serious challenge to the STAR data acquisition system, with its current maximum bandwidth of 1 kHz. If we can identify a way to trigger on the two TPC sectors that contain the decay electrons, the DAQ10K upgrade will allow us to circumvent the rate limitation. In this case, a 12-week RHIC-II run with maximum delivered luminosity will provide 2700 and 1700 events in Au+Au and p+p collisions, respectively. To obtain good precision in differential measurement, accumulated data from multiple RHIC-II runs is needed. In the muon channel, the MTD upgrade adds the capability to trigger on the decay products of the J/ψ via the channel $B \rightarrow J/\psi \rightarrow \mu\mu + X$, with rate sufficiently small to fit into the trigger bandwidth. Beside not being limited by the trigger bandwidth, this channel has advantages in determining pseudo-$c\tau$, since a muon is less affected by interactions with the detector material than an electron. This will enable us to set a lower cut on the pseudo-$c\tau$ and obtain a higher signal.

In addition, since the mass of the J/ψ is so close to that of the B, its momentum can also be

used as a good approximation for the original B momentum, as illustrated in Fig. 2.32. This is not the case when non-photonic electrons or muons are used, as shown in Fig. 2.33. This correlation makes the interpretation in terms of b quark energy loss significantly clearer for the $B \rightarrow J/\psi$ channel than for semi-leptonic decays.

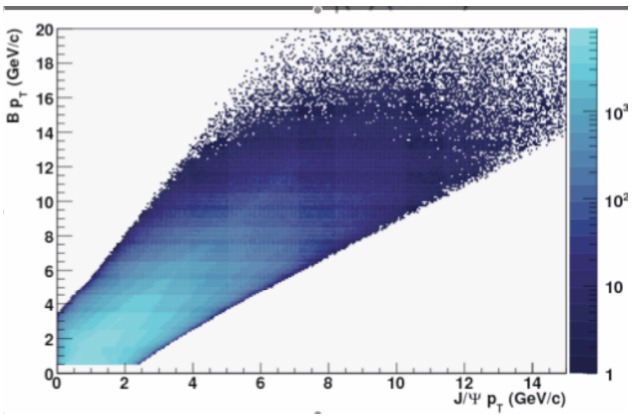

Figure 2.32: The correlation between the J/ψ p_T and the B meson p_T.

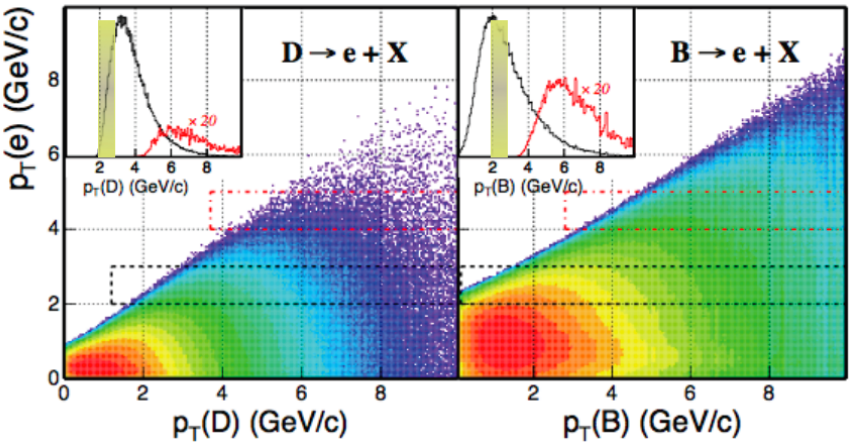

Figure 2.33: The correlation between the electron/muon p_T and the heavy flavor particle p_T for left: D mesons and right: B mesons.

Figure 2.34 shows the expected uncertainty in $J/\psi \rightarrow e^+e^-$ (left panel) and $J/\psi \rightarrow \mu^+\mu^-$ (right panel) R_{AA}. The $J/\psi \rightarrow e^+e^-$ projection is from 5 nb^{-1} sampled luminosity in Au+Au collisions and 200 pb^{-1} sampled luminosity in p+p collisions, luminosities achievable in the first part of this decade. The $J/\psi \rightarrow \mu^+\mu^-$ projection is from 20 nb^{-1} delivered luminosity in Au+Au collisions, the maximum luminosity a 12-week RHIC-II run can provide in the middle of the decade, along with 300 pb^{-1} delivered luminosity in p+p collisions.

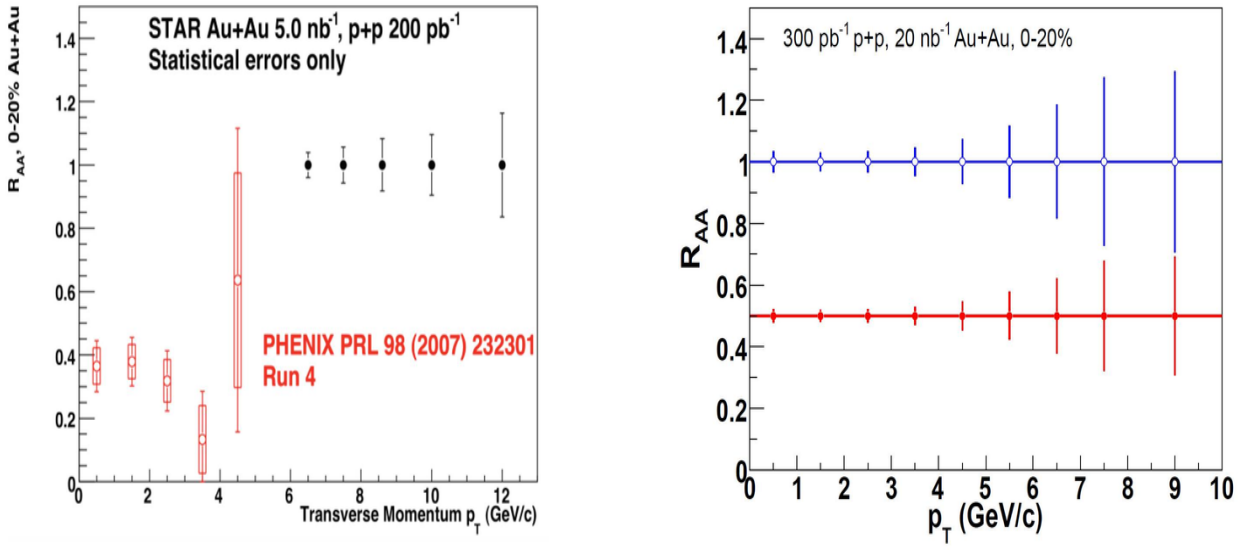

Figure 2.34: (Left panel) Projected uncertainty of $J/\psi \to e^+e^-$ R_{AA} measurement at high p_T in the case when $R_{AA} = 1$, with a sampled luminosity of 5 nb^{-1} in Au+Au and 200 pb^{-1} in p+p collisions. (Right panel) Projected uncertainty of $J/\psi \to \mu^+\mu^-$ R_{AA} measurement at high p_T in the cases when $R_{AA} = 1$ (blue) and 0.5 (red), with a RHIC delivered luminosity of 20 nb^{-1} in Au+Au and 200 pb^{-1} in p+p collisions.

2.3 Where is the QCD critical point and the associated first-order phase transition line?

2.3.1 Status of the QCD Phase Diagram

Physical systems undergo phase transitions when external parameters such as the temperature (T) or a chemical potential (μ) are changed. A phase diagram provides intrinsic knowledge about the structure of the matter under study. It tells us how matter organizes itself under external conditions into various degrees of freedom. The theory of strong interactions, Quantum Chromodynamics (QCD), predicts that nuclear matter at high temperature and/or density makes a transition from a state where quarks and gluons are confined and chiral symmetry is broken to a state where quarks and gluons are de-confined and chiral symmetry is restored. QCD has several conserved quantities: baryon number, electric charge, and strangeness. Each of these is associated with a chemical potential. As a result, the QCD phase diagram is four-dimensional. $\mu_{\rm Q}$ and $\mu_{\rm S}$ are relatively small compared to $\mu_{\rm B}$ (baryonic chemical potential). The temperature T and $\mu_{\rm B}$ are shown in a typical QCD phase diagram. Experimentally, large parts of the phase diagram can be covered by varying the beam energy. Both the temperature and baryon potential parameters, T and $\mu_{\rm B}$, vary as the function of the beam energy. This strategy is followed by several experimental programs such as those at RHIC at BNL, SPS at CERN, FAIR at GSI and NICA at JINR. Among these, the experiments at RHIC have obtained definitive evidence of matter where quarks and gluons are the relevant degrees of freedom [90]. Most of the experiments at RHIC were carried out at center-of-mass energy ($\sqrt{s_{\rm NN}}$) of 200 GeV, where the baryon chemical potential is small and a cross-over is expected according to lattice QCD predictions [91]. Experiments at lower collision energies will study the rest of the QCD phase diagram.

Theoretically, finite temperature lattice QCD calculations at zero baryon chemical potential suggest a cross-over above a critical temperature, $T_{\rm c}$, of about 170 to 190 MeV from a system with hadronic degrees of freedom to a system where the relevant degrees of freedom are quarks and gluons. At large $\mu_{\rm B}$, several QCD-based calculations find the quark-hadron phase transition to be of first order. Going towards the smaller $\mu_{\rm B}$ region, the point in the QCD phase plane (T vs. $\mu_{\rm B}$) where the first order phase transition ends is the QCD Critical Point (CP) [92, 93]. The focus in the coming decade will be on attempts to locate the CP both experimentally and theoretically. Current theoretical calculations are highly uncertain about the location of the CP. This is primarily because lattice QCD calculations at finite $\mu_{\rm B}$ face numerical challenges.

The experimental plan is to vary the center of mass energy ($\sqrt{s_{\rm NN}}$) of heavy-ion collisions to scan the phase plane and, at each energy, search for signatures of the CP that might survive the evolution of the system [94]. This program has started and the first phase of the STAR experimental program at RHIC is expected to be completed in 2010-2011, as summarized in Table 2.3. The second phase of the Beam Energy Scan (BES) program at RHIC will depend on the results from the first phase. Finer steps in the beam energies or $\mu_{\rm B}$ and T, with focused analyses, are envisioned. From the collider side, electron cooling will need to be installed in order to increase the luminosity if the current measurements find the low energy region is the most promising. We anticipate that the second phase of this program will be carried out in the period of 2014-2015.

We envisage different ways to approach the BES analysis. We search for direct evidence for a CP,

Table 2.3: Collision energy and corresponding chemical potential μ_B. The data are taken from [95].

$\sqrt{s_{NN}}$ (GeV)	μ_B (MeV)
5	550
7.7	410
11.5	300
18	230
27	151
39	112

Table 2.4: Physics goals, some experimental measurements, and required detectors.

Physics	Experimental Measurements	Detectors
Critical Point	Net-protons and net-charge higher moments Fluctuations in K/π, p/π, $\langle p_T \rangle$ Light nuclei cluster multiplicity distributions	TPC, FTPC, TOF
Phase Transition and Phase Boundary	Heavy quark collectivity (e.g., J/ψ v_2, ...) Di-lepton spectra and v_2 vs. mass and p_T NCQ scaling of v_2 Net-proton and net-kaon higher moments Dynamical charge correlations for LPV Azimuthally-sensitive HBT	TPC, FTPC, TOF, HFT
Exotics	Light nuclei, strangelets Di-lepton spin alignment in high mass region, including J/ψ	TPC, TOF, EMCAL, HLT

we look for signs of the existence of a phase boundary, and we study exotic phenomena that may be related to a phase transition. Table 2.4 lists the three possibilities, the related measurements, and the STAR detector components that are critical to those measurements. For a more complete list of measurements, we refer the readers to a more detailed description in STAR BES documents [96, 97].

The exploration of the QCD phase diagram, schematically shown in the left of Fig. 2.35 [94], is the center piece of the RHIC Physics Program. The phase diagram shows information about the location of the phase boundary between the hadron gas (HG, light blue) and the quark-gluon plasma (QGP, navy).

Figure 2.35 right plot depicts our current understanding of the QCD phase diagram. According to Lattice QCD calculations, there is a cross over close to $\mu_B = 0$. The critical temperature for such a transition is also shown; the range reflects the uncertainties in the theoretical calculations. The figure also shows temperatures at various stages in heavy-ion collisions as a function of μ_B (at different $\sqrt{s_{NN}}$). The μ_B values are estimated at chemical freeze-out. The initial temperatures

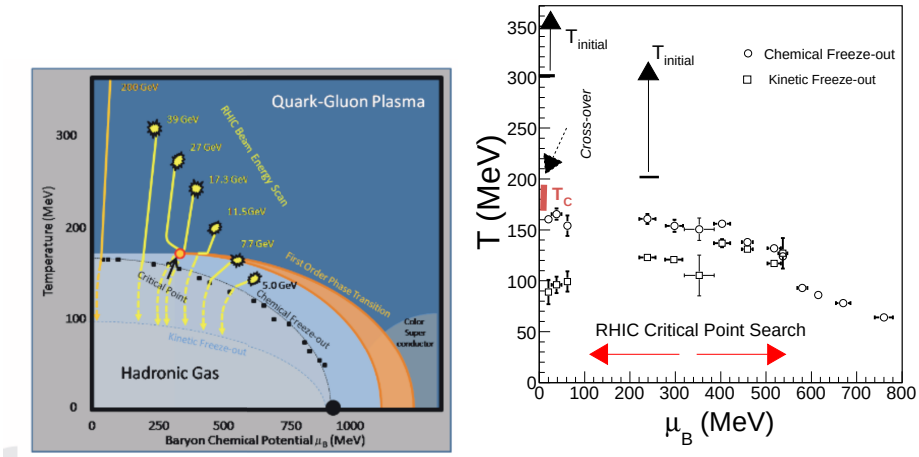

Figure 2.35: Left-plot: Schematic representation of the QCD Phase Diagram. The location of the critical point, the separation between the 1st-order transition and chemical freeze-out, and the focusing of the event trajectories towards the critical point are chosen to illustrate plausible possibilities. The plot is taken from [96]. Right-plot: Current understanding of the QCD phase diagram [98]. Open circles and squares represent the chemical and kinetic freeze-out parameters (T and $\mu_{\rm B}$) in high-energy nuclear collisions, respectively. Horizontal arrows are the RHIC beam energy scan range.

($T_{\rm initial}$) achieved at top RHIC and SPS energies are obtained from models that explain the direct photon measurements from the PHENIX experiment at RHIC and from the WA98 experiment at SPS [99]. From these models, which assume that thermalization is achieved in the collisions within a time between 0.1-1.2 fm/c, the $T_{\rm initial}$ extracted is greater than 300 MeV and 200 MeV at RHIC and at SPS, respectively. The $T_{\rm ch}$ and $T_{\rm kin}$ values extracted from particle ratios and $p_{\rm T}$ spectra of various hadrons, respectively, using models assuming thermal equilibrium are also shown. Most QCD-based model calculations suggest that the phase transition at large $\mu_{\rm B}$ is of first order. The horizontal arrows in the figure indicate the region that will be covered by the beam energy scan program.

What information is missing and needs to be addressed in this decade:

- The location of the QCD Critical Point and evidence for 1st order phase transition
- Establishing the trajectory of the QCD phase boundary.

2.3.2 Search for the QCD Critical Point and Phase Transition Line

Strategy to Locate the Critical Point

The critical point search component of the BES program requires a careful choice of experimental observables and the steps in μ_B for this experimental driven approach to locate CP. A non-monotonic dependence of observables sensitive to CP on $\sqrt{s_{NN}}$ and an increase of long-wavelength or low-momentum number fluctuations should become apparent only near the critical point. For example, the rise and then fall of this signal as μ_B increases should allow us to ascertain the (T,μ_B) coordinates of the critical point. Note that the magnitude of these non-monotonic excursions, as well as the probability that they will survive the final state interactions, is difficult to predict. Fortunately for the experiments, there may not be a need for the system's evolution trajectory to pass precisely through the critical point in the (T,μ_B) plane to see the signatures, as some hydrodynamic calculations show that the critical point attracts trajectories [100]. In such a case, if the trajectory misses the critical point by 100 MeV along the μ_B axis, the signatures are expected to persist. Note, however, that this attraction is not generic, and relies on specific features of the equation of state near the critical point [97]. Available lattice QCD calculations suggest the μ_B region of influence around CP would be around 100 MeV [101].

A Possible Observable

The earliest suggestion was based on the fact that fluctuations of energy in a canonical ensemble would grow without bound at the CP. The net energy in a restricted part of the phase space of a fireball would vary from one event to another (all other variables being held constant or controlled) because of thermodynamic fluctuations. The suggestion was to observe the variance of energy from one event to another. However, this has a problem that there may be small fluctuations in the variables that have to be held constant, and all such fluctuations will add to the variance [102]. These other fluctuations taken together could swamp the signal. There then followed attempts to look at variables which were sensitive only to dynamical fluctuations. However, their relationship to thermodynamics remains unclear.

The STAR experiment has recently developed a new observable, which can be used to look for critical point fluctuations at RHIC. In a thermal system, the correlation length (ξ) diverges at the CP. ξ is related to various moments of the distributions of conserved quantities such as net-baryons, net-charge, and net-strangeness. Finite size and time effects in heavy-ion collisions put constraints on the values of ξ. A theoretical calculation suggests $\xi \sim$ 2-3 fm for heavy-ion collisions at RHIC. It was recently shown that higher moments of distributions of conserved quantities, measuring deviations from a Gaussian, have a sensitivity to CP fluctuations that is greater than that of variance (σ^2), due to a stronger dependence on ξ. As discussed in [94], the numerator of the skewness (S) goes as $\xi^{4.5}$ and kurtosis (κ) goes as ξ^7. In addition, crossing of the phase boundary can manifest itself by a change of sign of skewness as a function of energy density [103]. Furthermore, the lattice calculations and QCD-based models have shown that moments of net-baryon distributions are related to baryon number susceptibilities. The product $\kappa\sigma^2$, related to the ratio of fourth order to second order susceptibilities, shows a large deviation from unity near the CP. Due to the connection between the ratios of the susceptibilities and the high order correlation function, one

can make a direct comparison between the quantities from experiment and lattice calculations. Experimentally measuring event-by-event net-baryon numbers is difficult. However, the net-proton multiplicity distribution can serve as a reasonable replacement. Theoretical calculations have shown that net-proton fluctuations reflect the singularity of the charge and baryon number susceptibility, as expected at the CP [94].

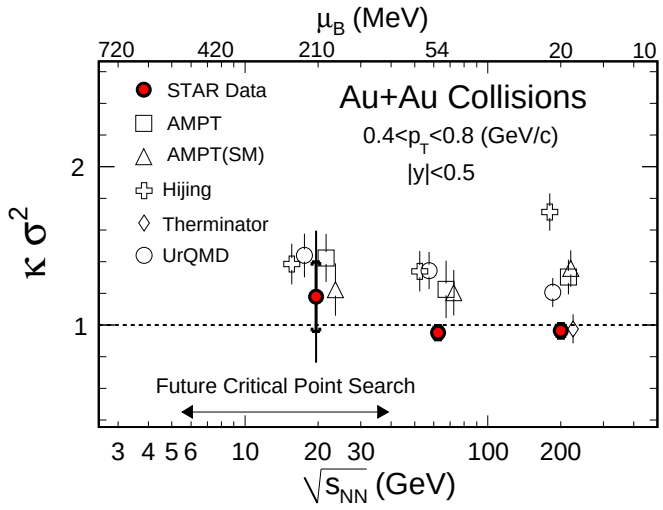

Figure 2.36: Energy and baryon-chemical potential dependence of $\kappa\sigma^2$ for net-protons, compared to several model calculations that do not include a CP. Experimental and model results are shown as filled symbols and open symbols, respectively. Figure taken from [104].

Figure 2.36 shows the recent experimental results on the energy dependence of $\kappa\sigma^2$ for net-protons, compared to several model calculations that do not include a CP. Also shown at the top of Fig. 2.36 are the $\mu_{\rm B}$ values corresponding to the various $\sqrt{s_{\rm NN}}$. Within the experimental statistics, we have not yet observed any non-monotonic beam energy dependence [104]. The results, $\kappa\sigma^2$, from three collision energies are consistent with unity that could imply that the system is thermalized with a small value of correlation length. The results from non-CP models are constants as a function of $\sqrt{s_{\rm NN}}$ and have values between 1-2. The result from the thermal model is exactly unity. Within the ambit of the models studied, the observable changes little with changes in non-CP physics (such as collective expansion and particle production) at the various energies studied. From comparisons to models and the lack of non-monotonic dependence of $\kappa\sigma^2$ on $\sqrt{s_{\rm NN}}$ studied, we conclude that there is no indication from our measurements for a CP. Clearly the data taken in year 2010 and proposed in year 2011 will be crucial to bridge the gap in baryon chemical potential regions to search for the CP in the QCD phase diagram. Lattice QCD provides predictions for these ratios. Away from the CP the fireball is expected to come to thermal equilibrium, and the lattice results should agree with observations. Near the critical point the fireball will fall out of equilibrium because of critical slowing down [105], and hence the lattice results would not describe the data. If

a non-monotonic behavior of the $\kappa\sigma^2$ is seen, then it will be clear that the system has passed or is close to the CP.

Strategy to Identify the Phase Transition/Phase Boundary

To determine if the matter no longer crossed a partonic phase, one can look for the turn-off of new phenomena that have been established at top RHIC energy and are associated with QGP signatures. If our current understanding of RHIC physics and these signatures is correct, a turn-off must be observed in several signatures at lower beam energies. Such corroboration among several observables is an essential part of the *unfinished business* for the discovery of quark-gluon-plasma. There are several such observables, including jet-quenching, number of constituent quark scaling in anisotropy flow v_2, ϕ-meson v_2, and possible local parity violation. Here we discuss three of the observables that STAR has identified as essential drivers of our plan to probe the QCD phase boundary.

Constituent-quark-number scaling of v_2, indicating partonic degrees of freedom

When elliptic flow v_2 is plotted versus transverse kinetic energy $(m_{\rm T} - m_0)$, both divided by the number of constituent quarks (n_q), the v_2 for all identified particles below $(m_{\rm T} - m_0)/n_q \sim 1$ GeV/c^2 falls on a universal curve. This scaling behavior, as shown in Fig 2.6, is considered to be evidence for the existence of partonic degrees of freedom in the medium resulting from Au + Au collisions at 200 GeV. Turn-off of the scaling at a given beam energy (characterized by a T and $\mu_{\rm B}$) would indicate these events remain on the hadronic side of the phase boundary.

Figure 2.6 right panel shows the most recent results on non-strange and multi-strange hadron v_2 in Au+Au collisions at RHIC [106]. The elliptic flow measurements for the multi-strange particles with their low hadronic interaction cross sections are the most promising probes of the early stages of the collision. Absence of large v_2 for such hadrons compared to those from other lighter hadrons will hold the key to understanding the phase boundary.

Dynamical charged hadron azimuthal correlations

The STAR experiment at RHIC has recently measured dynamical charged hadron azimuthal correlations based on a 3-particle correlation technique [107]. The results from Au+Au collisions at $\sqrt{s_{\rm NN}} = 200$ GeV at mid-rapidity for $0.15 < p_{\rm T} < 2$ GeV/c for same charged and opposite charged hadrons with respect to the reaction plane (characterized by the third particle) are shown in Fig. 2.37. The observable, $\langle\cos(\phi_{\rm a}+\phi_{\rm b}-2\Psi_{\rm RP})\rangle$, represents the difference between azimuthal correlations projected onto the direction of the angular momentum vector and correlations projected onto the collision event plane. As shown in the figure, the difference between the same charge and opposite charge correlations could not be explained by models such as HIJING and UrQMD and by incorporating realistic values for the elliptic flow in such simulations. The signal seems to be consistent with the predictions of the existence of meta-stable domains in the QCD vacuum, which lead to Local Parity Violation (LVP) and are expected to be produced in ultra-relativistic heavy-ion collisions [107].

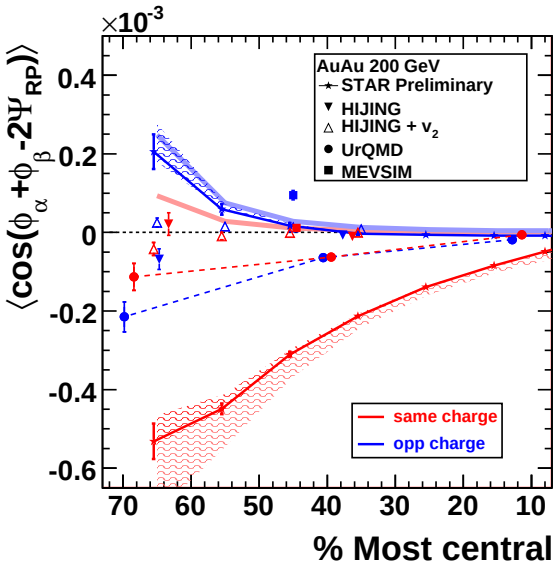

Figure 2.37: $\langle\cos(\phi_a+\phi_b-2\Psi_{RP})\rangle$ results from 200 GeV Au+Au collisions are compared to calculations with event generators HIJING (with and without an elliptic flow afterburner), URQMD (connected by dashed lines), and MEVSIM. Thick lines represent HIJING reaction-plane-independent background. Taken from [107].

For such a phenomena, where the massless quarks can change their chirality due to interactions with gluon fields, there could be separation of positive charges from negative charges along the direction of the angular momentum of the collision as a result of large magnetic fields reached in the collisions (especially in non-central collisions). (See Sect. 2.4 for further discussion of this "Chiral Magnetic Effect".) De-confinement allows for the possibility of quarks traveling over distances greater than nucleonic scales, and chiral symmetry restoration is essential, because a chiral condensate will tend to erase any asymmetry between the number of right- and left-handed fermions. The observable presented is parity-even, making it susceptible to physical processes not related to parity violation effects. If the observations are related to LPV, then the parity violation is itself a de-confinement signal that we expect to turn-off at some point if we go down low enough in energy.

Interferometry

By studying interferometry as a function of beam energy we can infer the energy density of the medium produced at the last re-scattering of the hadrons. The source dimensions, or homogeneity regions, as determined via HBT encode different information. R_{side} only contains information about the spatial extension, while R_{out} holds spatial and temporal data. The ratio R_{out}/R_{side} can therefore reveal the emission duration of the source. It has been predicted that for a first order phase transition, this ratio should become much greater than unity due to a stalling in the emission

during the phase transition [109]. Measurements of R_{out}, R_{side} and R_{long} as a function of collision energy have been studied in great detail, and no major jumps in R_{out}/R_{side} are observed.

However, momentum spectra and anisotropy tell only half of the story of collective flow. The bulk response of the system has a non-trivial structure in both space and time. Just as the p_T-dependence of azimuthally-integrated HBT radii gives access to the geometric substructure generated by radial flow (e.g. [110]), HBT measured relative to the standard second-order event plane gives access to the spatial analogs of directed and elliptic flow [110, 111], and contains important information not accessible in momentum space alone. These measurements can be sensitive to a softening in the equation of state, related to a first-order phase transition or even a rapid crossover.

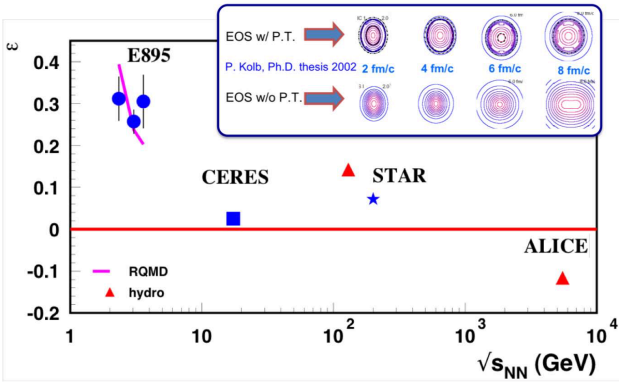

Figure 2.38: Freeze-out anisotropy from 2nd-order oscillations of HBT radii shown as a function of collision energy. Inset shows hydrodynamic evolution of the source shape for an equation of state with (upper) and without (lower) softening due to finite latent heat [112]. Taken from [97].

The collision energy dependence of the freeze-out anisotropy, extracted from 2nd order oscillations of HBT radii, is shown in Fig. 2.38. The suggestive non-monotonic behavior in the data between $\sqrt{s_{NN}} = 5 - 30$ GeV may be caused by the changing of the equation of state [112].

2.3.3 Advantages of RHIC/STAR

Uniform and large acceptance

One of the big advantages of experiments at RHIC compared to those at SPS is the uniform acceptance for each hadron species over all the beam energies studied. These can be seen from the rapidity vs. transverse momentum acceptance distributions for pions, kaons and protons shown in Fig. 2.39, obtained using the STAR TPC+TOF at 7.7 GeV, 39 GeV and 200 GeV Au+Au collisions. A common acceptance for identified hadrons at all beam energies is important for event-by-event type fluctuation studies and for interpretation of the physics results. These results show that the data taken by the STAR experiment can be used to deliver the physics goals discussed in this section.

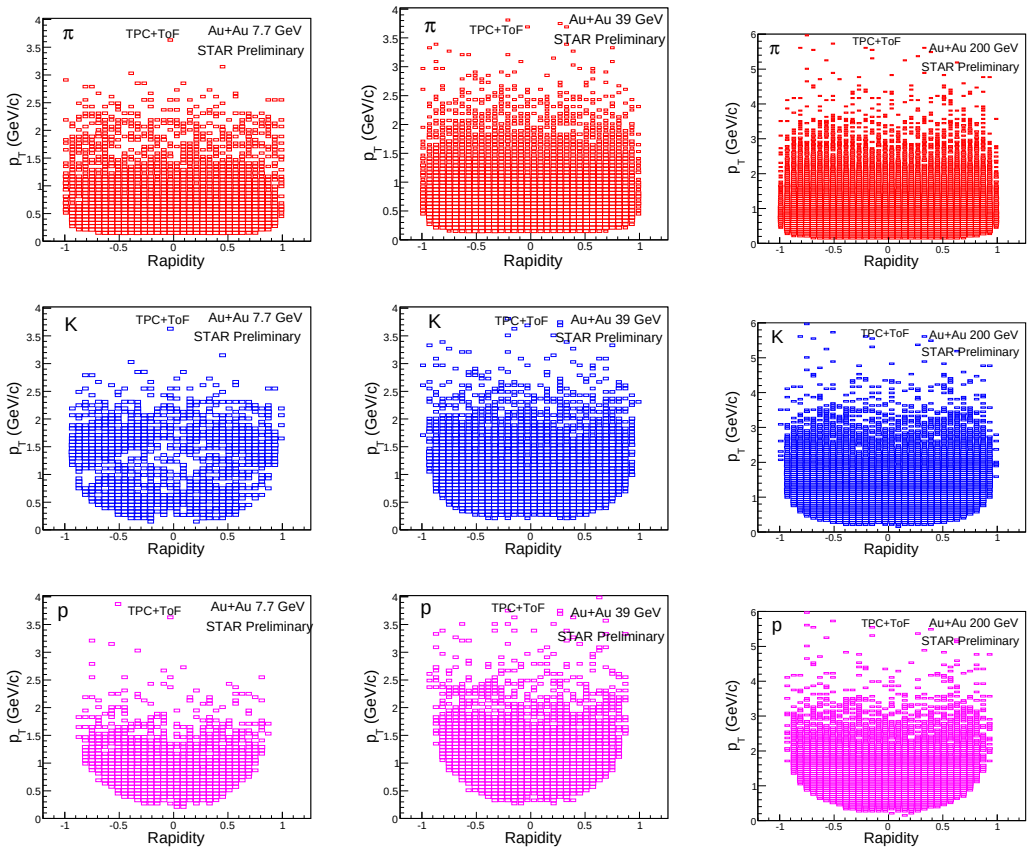

Figure 2.39: Particle acceptance represented in p_{T} versus rapidity for collisions at $\sqrt{s_{\mathrm{NN}}}$ =7.7 GeV (left plots), 39 GeV (middle plots) and 200 GeV (right plots).

Excellent particle identification

In year 2010 the particle identification capabilities in STAR got a boost by the successful completion of the full barrel TOF. For physics analyses like those addressing NCQ scaling, high order correlations and fluctuations due to the critical point, and obtaining the freeze-out parameters, it is important to have a good measurement of particle identification over the large acceptance in STAR. Figure 2.40 shows the enhanced particle identification capabilities with the TOF in STAR in Run 10 for Au+Au collisions at 39 and 7.7 GeV. The top panels represent $1/\beta$ vs. rigidity, while the bottom panels show the dE/dx distributions. One can see that the momentum reach for identifying the various hadrons has increased significantly with the newly completed TOF system in STAR.

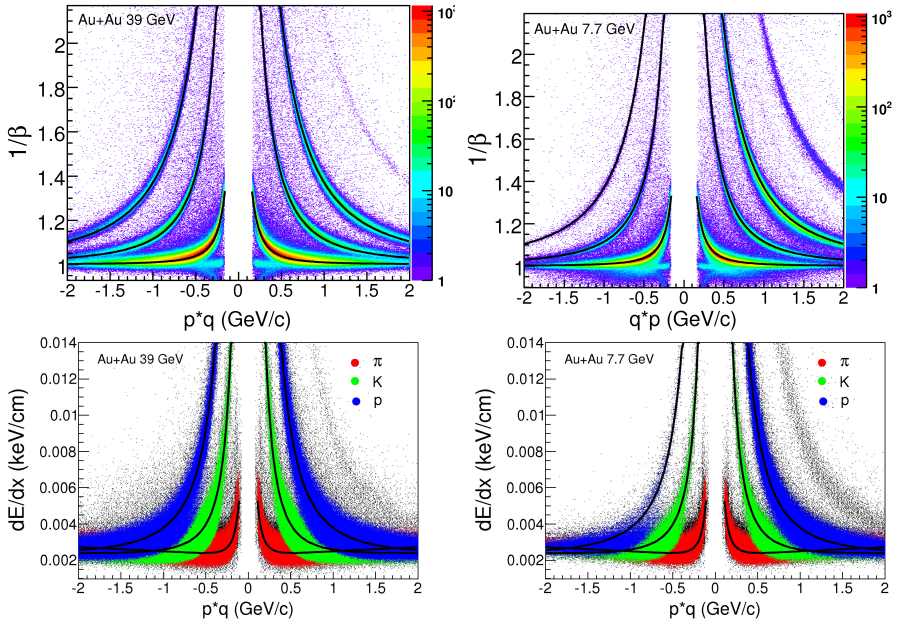

Figure 2.40: Top and bottom panels show $1/\beta$ and specific energy dE/dx, respectively, as a function of rigidity from STAR data for Au+Au collisions at 39 GeV (left) and 7.7 GeV (right).

2.3.4 Next steps

If evidence for CP is found, subsequent phases of BES running should be carried out. The first exploration phase, now underway, was proposed as a few steps in $\sqrt{s_{\rm NN}}$ (or $\mu_{\rm B}$) to narrow down to an area of interest for further study (see Table 2.3 for the beam energies and corresponding $\mu_{\rm B}$ values [95]). In the future, we intend to use smaller steps in $\mu_{\rm B}$ within the region of interest to verify and trace the possible effect of focusing and to pin down more precisely the location and properties of the critical point.

2.4 Can we strengthen current evidence for novel symmetries in QCD matter and open new avenues?

2.4.1 Local Parity Violation

Local parity violation (LPV) in strong interactions [113, 114] may well prove to be one of the most important and enduring discoveries from RHIC since the initial round of evidence related to the strongly interacting Quark Gluon Plasma. Reference [113], the first refereed paper laying out the case for this new physics, was featured as an "Editor's Suggestion" in PRL, and a press conference to announce the discovery at the April 2010 APS meeting in Washington DC resulted in a large number of press stories worldwide, including a detailed article in The New York Times. It is beyond question that any physics discovery with this kind of impact warrants an extensive program of further verification, amplification and further detailed study during the coming decade.

There are still many open questions related to the non-trivial structure of the QCD vacuum. The generation of mass from spontaneous chiral symmetry breaking, and topological solutions (instantons, sphalerons) are relevant to this discussion [115, 116]. The observation of event-by-event local parity violation in strong interactions lends support to current theoretical understanding, and has an immediate impact, not just on relativistic heavy ion physics, but on all spheres of physics touched by QCD (high energy physics, astrophysics, cosmology, etc.). This area of experimental investigation offers unique insights into non-perturbative QCD.

The observation of a local parity-violating signal assumes the following chain of circumstances. In non-central heavy-ion collisions, a large orbital angular momentum vector (L) exists at 90° to the reaction plane, leading to an exceptionally intense localized magnetic field ($\sim 10^{15}$ T, due to the net charge of the system). If the system is deconfined, there can be strong parity-violating domains, and different numbers of quarks of left- and right-handed helicity, leading to preferential emission of like-sign charged particles along L. The phenomenon is sometimes called the Chiral Magnetic Effect (CME) [117, 118], and has been studied in lattice QCD calculations [119, 120, 121].

In the azimuthally anisotropic emission of particles,

$$\frac{dN_{\pm}}{d\phi} \propto 1 + 2a_{\pm}\sin(\phi - \Psi_{RP}) + ...$$

the coefficient a represents the size of the parity-violating signal, and the remaining terms (not shown explicitly) are the familiar ones with coefficients v_n for directed and elliptic flow, etc. However, the coefficient a averages to zero when integrated over many parity-violating domains in many events. In the presence of parity violation, a non-zero average signal can be obtained by forming a correlation between pairs of emitted particles relative to the reaction plane. The observed results [113, 114] are consistent with the expected signal for local parity violation, especially the centrality dependence. There are caveats attached to this observation – the expected parity violation is parity-odd, whereas the only accessible observable to measure it is parity-even, which means that effects not related to parity violation (e.g., jets and resonances) can contribute to the measured signal. It has been shown that there is no known background, or effect predicted by existing event-generating models, that could account for the observed signals [113, 114]. A challenge that remains

to be addressed in the future is to demonstrate the observation of CME without any significant reliance on models to rule out possible background effects.

Future Directions

One of the next logical steps in the investigation of CME will present itself when central uranium-uranium data with good statistical significance become available, which can be anticipated in the second and subsequent RHIC runs with uranium beams. The crucial factor in CME is the extremely intense magnetic field, while the background phenomena with a potential to confuse the signal arise from elliptic flow. In non-central collisions of spherical nuclei such as Au + Au, it is not easy to disentangle these two effects, and they both always increase and decrease together as the available parameter space is explored. Central U + U collisions open up a unique opportunity to escape from this undesirable pattern. Specifically, in the so-called body-body [122] configuration of central U + U, where the major axes of the two deformed nuclei are parallel to each other and perpendicular to the beam axis, then we can expect the elliptic flow effects to remain finite while the strong magnetic field will vanish [123, 124].

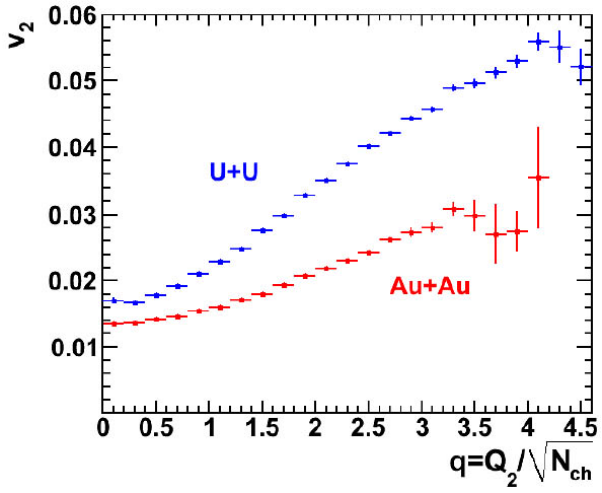

Figure 2.41: Elliptic flow versus q, the magnitude of the second-order event plane flow vector normalized by charged particle multiplicity, in a Monte Carlo Glauber simulation of central collisions.

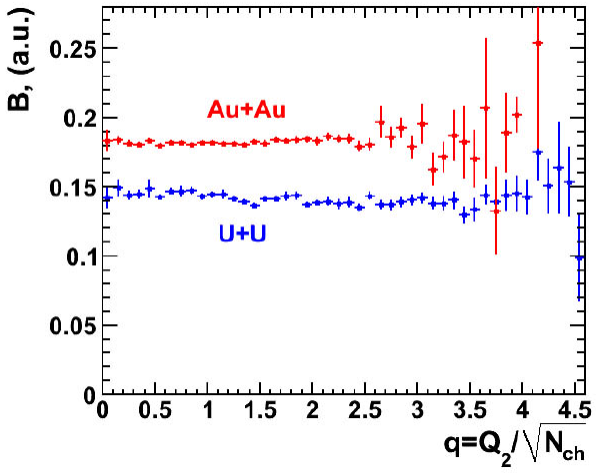

Figure 2.42: Simulated CME magnetic field, in arbitrary units, versus q, the magnitude of the second-order event plane flow vector normalized by charged particle multiplicity, in a Monte Carlo Glauber simulation of central collisions.

The above of course refers to the ideal case of perfectly selected body-body configurations at zero impact parameter. However, simulations demonstrate that with plausible cuts to select the desired U + U configuration, there will still be a substantial and improved ability to disentangle magnetic effects from elliptic flow [124]. Figures 2.41 and 2.42 show elliptic flow and magnetic field **B** versus q, the normalized magnitude of the flow vector for the second-order event plane, for a sample of Monte Carlo events from a Glauber model where only very central events have been

included, based on the simulated signal in the Zero Degree Calorimeters. One noteworthy finding is that while v_2 is strongly correlated with q as expected, the simulated magnetic field is independent of q. This means that the correlation observable used to detect the LPV phenomenon would remain constant with q if the signal is a true chiral magnetic effect, whereas it would increase with q by a measurable amount if flow-related background effects are still present [124]. Figure 2.41 might give the impression that Au + Au collisions allow the same study to be carried out, but in fact, U + U offers a significant improvement. First, the percentage change in v_2 for U + U is about double that for Au + Au. Second, the variation in elliptic flow shown in Fig. 2.41 is mostly due to fluctuations in the initial-state spatial eccentricity in the case of Au + Au, which are still not well understood. In contrast, for U + U, the variation in elliptic flow is mostly due to variation in the orientation of the deformed nuclei at the moment of collision and are not subject to a similar uncertainty [124].

Another promising avenue for future research in the same area is a comparison of measurements in isobaric systems like ${}^{96}_{44}$Ru + ${}^{96}_{44}$Ru and ${}^{96}_{44}$Ru + ${}^{96}_{40}$Zr and ${}^{96}_{40}$Zr + ${}^{96}_{40}$Zr [123, 124]. One expects very similar elliptic flow in these systems. The magnetic field is proportional to Z and the CME signal goes like Z^2. Therefore, the observed CME signal should change by about 20% between these isobaric systems, a level that is easily measurable [123, 124]. Other possible isobaric systems may involve a smaller relative change in Z^2 but can offer an offsetting advantage in terms of more spherical nuclei. In addition, isobaric experiments at RHIC will provide a new approach to the study of initial conditions, and will offer insights into, for example, baryon stopping and the mechanism for imparting directed flow at ultrarelativistic energies. The FOPI collaboration has already used comparisons of Ru + Ru with Zr + Ru to investigate stopping at SIS energies [125, 126].

The data from Run 10 at RHIC are the basis for a partial and very preliminary study of the beam energy dependence of LPV, and subsequent RHIC runs are expected to add data for continuing the beam energy scan program [127]. The energy scan has the potential to open up new physics related to chiral magnetism, since LPV is generally accepted as needing deconfinement to happen [118]. So apart from its very high intrinsic importance, with implications well beyond heavy ion physics, LPV is a deconfinement signal that we expect to turn-off at some point if we scan down low enough in energy. Keeping in mind that the duration of the intense magnetic field becomes longer as the beam energy is lowered, it is plausible that the LPV signal will increase steadily as we scan down, and then reverse its trend more abruptly upon passing a threshold energy for deconfinement [123]. On the other hand, the known background effects are expected to have a quite different energy dependence. At the time of writing, there remains a pressing need for theoretical calculations of the energy dependence of chiral magnetism, so that quantitative predictions can be generated.

To date, we have no experimental guidance regarding the size of the local parity-violating domains of chiral magnetism, but this line of investigation will be increasingly feasible during coming RHIC runs as statistics improve and as the particle ID capabilities of STAR are upgraded. Using a variety of multiparticle correlation techniques, a promising approach would be to compare cluster sizes for charged and neutral particles. The latter would be largely unaffected by the intense magnetic field and would be very useful for characterizing the background effects [123].

Since the 1970s, it has been known that clusters, each including two to three charged particles, play an important role in multiparticle production at high energies [128]. In the context of the non-perturbative phenomena and phases of QCD, where the concepts of instantons and sphalerons are

introduced [129], it has been suggested that there could be a connection between the aforementioned clusters and sphalerons. This idea in principle could be explored in any experiment involving multi-particle production, but a particularly promising proposed test involves double Pomeron exchange [130] in pp2pp phase II running at STAR [131]; more details on this physics and on the pp2pp hardware can be found in the following section and Chap. 4, respectively. The special advantage of this proposed test arises from the very clean environment of pp2pp compared with typical heavy ion reactions; there will only be one cluster per event and the kinematics are very well defined [123].

2.4.2 Dilepton measurements and chiral symmetry restoration

One of the conditions necessary for the observation of Local Parity Violation (LPV) is the existence of Chiral Symmetry Restoration, where quarks are at their current mass and approximate chiral symmetry [117, 132]. In fact, chiral symmetry restoration has been actively searched for since the beginning of the field of relativistic heavy-ion physics. In the vacuum, hadrons have chiral partners ($[\pi, \sigma]$, $[\rho, a_1]$, $[K, \kappa]$). However, their masses are very different due to chiral symmetry breaking. This difference is expected to disappear when chiral symmetry is restored. The expectation is for the in-medium properties of the chiral partners to approach each other and for the particles as hadrons to disappear when the medium, which the hadrons are part of, goes from hadronic gas through the chiral phase transition, deep into the QGP. There are two possible consequences: dropping mass and broadening [132, 133]. A well-known observable is the excitation of the in-medium spectral function of vector mesons. The ρ meson is very promising in this regard because it decays to dileptons with very short lifetime (~ 1 fm/c). This provides the best opportunity to observe the in-medium effect on the vector meson through its dilepton decay when the decay can occur in the same location, while the modified spectral function is present with the in-medium effect. Additional information on the nature of the emitting source can be obtained from the momentum and azimuthal dependence of the spectral function. It has been argued that the dilepton spectra in the intermediate mass range (IMR) directly relate to the thermal radiation of the QGP [133, 134]. Regardless of whether the QGP radiation or hadronic decays dominate the IMR dilepton emission, the IMR enhancement detects the matter at a temperature close to T_c and provides a stringent constraint on the spectral function of hadrons close to T_c [135].

In the last few years, RHIC and SPS have made significant advances in measuring the dilepton yields relevant to the ρ spectral function [136, 137, 138]. NA60/SPS [136] has measured the dimuon spectrum around the ρ invariant mass in In+In collisions at $\sqrt{s_{NN}} = 17$ GeV; see Fig. 2.43. A ρ spectral distribution was observed, and the NA60 analysis supports the scenario of the ρ width broadening and is not consistent with a dropping mass. Furthermore, the transverse-momentum spectra as a function of dimuon invariant mass were analyzed [139]. The inverse-slope parameter of the p_t spectrum increases from low mass to around 1 GeV/c^2 and decreases from there to the J/ψ mass, as seen in Fig. 2.44. The increase at low mass is presumably due to the contribution from hadronic decays at the late stage of the evolution with large radial flow, while the subsequent decrease is interpreted as due to partonic radiation at an earlier stage where radial flow has not been fully developed.

RHIC provides a larger collision system with much higher energy. It is important to have a consistent picture between the experimental data and the expected energy dependence from models

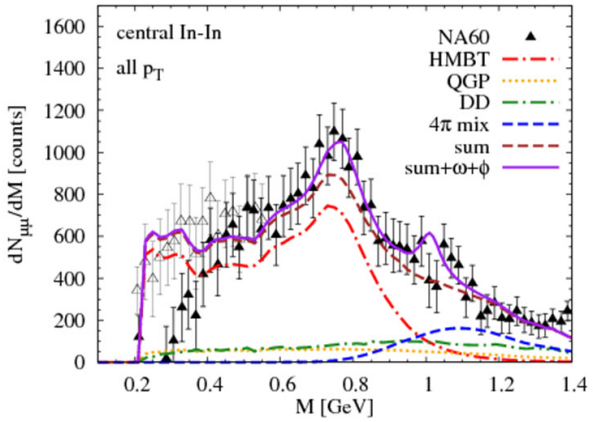

Figure 2.43: The dimuon invariant mass measured by NA60 in indium-indium collisions at the SPS. The measurements are well described by a cocktail where there is in-medium broadening of the ρ mass.

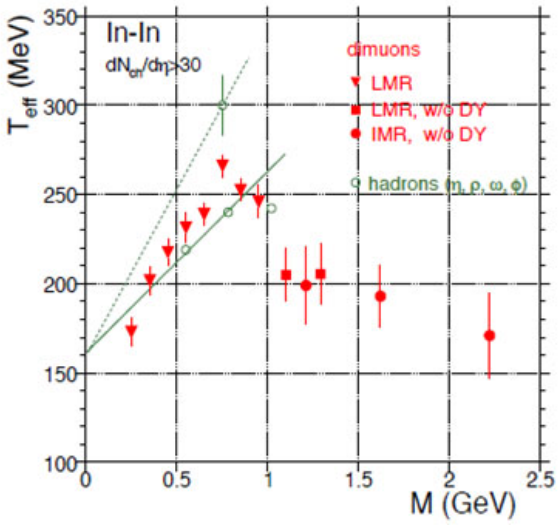

Figure 2.44: Transverse momentum inverse slope versus dimuon invariant mass in In+In collisions measured by NA60 at the SPS.

which explain the SPS data. Models by Rapp *et al.* [133, 134] show that the dileptons from the in-medium hadronic decays have little dependence on the collision energy, since the total baryon and antibaryon density is more or less independent of the collision energy, while the dileptons from the QGP thermal radiation increase significantly, due to the increasing energy density and temperature at the earlier stage, and the increasing duration of the QGP.

PHENIX [138] has provided the first measurement of dielectron spectra in minimum-bias Au+Au collisions at RHIC. Although future measurements with the upgraded Hadron-Blind Detector (HBD) will greatly improve statistics and reduce the combinatoric background, the current result shows a broad enhancement at a dielectron invariant mass of around 0.5 GeV/c^2 at low momentum, and the effect disappears at high transverse momentum [138]. This result seems not to be compatible with what was observed at SPS. Study of these effects at different energies between SPS and RHIC will clarify the situation.

STAR has started the dilepton program with the upgraded Time-of-Flight system for electron identification [140] and the future upgrade of the Muon Telescope Detector (MTD) for muon identification at midrapidity [53]. Figure 2.45 shows a Monte Carlo simulation of a cocktail dielectron spectrum in the STAR detector, using GEANT. Figure 2.46 shows the preliminary dielectron invariant mass spectrum from Run 9 minbias p+p collisions at $\sqrt{s_{NN}} = 200$ GeV. This represents about 100M minbias events. A data sample of 350M minbias and 250M central Au+Au collisions has been collected in Run 10, which is equivalent to a factor of a few thousands more dielectron pairs than in Run 9 p+p collisions. This should provide a high-precision measurement of the low-

invariant mass and low-p_t dilepton spectra. This result (together with PHENIX) should provide a more conclusive measurement around ρ mass range, and determine whether there is a smooth evolution from SPS to RHIC. The result should guide us toward a clear picture of what needs to be done over the next few years.

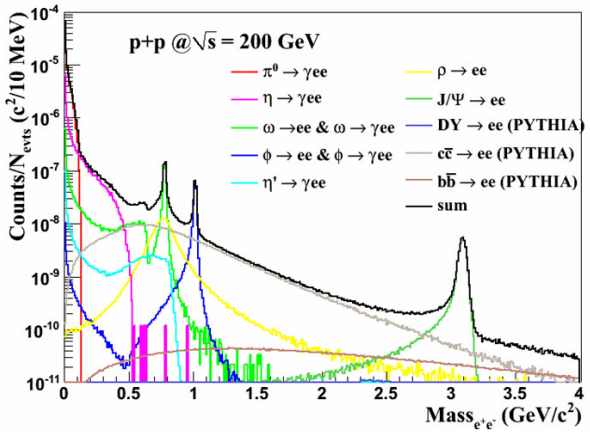

Figure 2.45: A GEANT-based Monte Carlo calculation of the background cocktail for STAR's dielectron invariant mass in p+p collisions at 200 GeV.

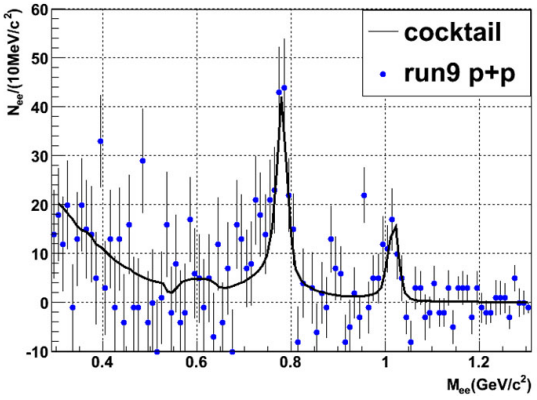

Figure 2.46: The dielectron invariant mass measured by STAR in p+p collisions at 200 GeV.

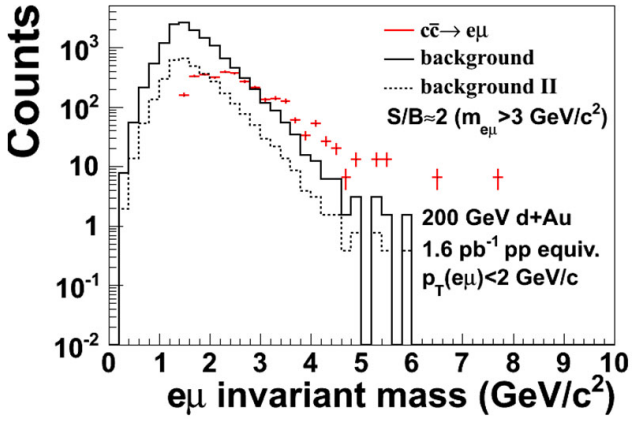

Figure 2.47: Projected $e\mu$ invariant mass in various scenarios based on data from MTD prototype tests (see text).

Unfortunately, the increased dominance of correlated charm decays in the IMR is sensitive not only to the total charm cross section, but also to the charm momentum spectrum, and thus to the charm thermalization and energy loss [134]. NA60 Collaboration at SPS used dimuons to study

the IMR mass range, and provided evidence for the production of thermal-like muon pairs with masses above 1 GeV/c^2 in In+In collisions [141]. The charm contribution was studied using the displaced vertex in a fixed target reference frame. At RHIC, both the charm contribution and the thermal radiation are expected to increase relative to what was observed at SPS [134]. Although the upgraded inner tracker (HFT) will provide a precise measurement of charm spectra and elliptic flow, a measurement of the correlation of $c\bar{c}$ is still challenging if not impossible. On the other hand, the MTD upgrade, in addition to the existing electron identification in STAR, will provide $e\mu$ correlations for a much-needed independent measurement of the heavy-flavor contribution to the dileptons. Figure 2.47 shows the $e\mu$ invariant mass for a realistic estimate of background muons from data taken with a prototype MTD module during d+Au collisions in Run 8. This shows that in the mass range accessible by the MTD ($M_{e\mu} >\sim 1$ GeV/c^2), the signal-to-background ratio is quite good for a definite measurement of the $e\mu$ correlation. Due to the uncertainty in the background level, Fig. 2.47 also presents two background studies made possible by preliminary data from the prototype MTD. The background would be subtracted statistically by the like-sign combinations, and the uncertainty in the background level at this point doesn't propagate to the systematic uncertainty of the final $e-\mu$ correlation measurements.

Over the next decade, STAR will have a strong program for studying the properties of hadronic and partonic matter using dileptons. The unique capability of measuring dielectron, dimuon and $e\mu$ correlations at midrapidity in the same detector, along with the flexibility of the RHIC facility, provide an unprecedented opportunity for accessing signatures of possible chiral symmetry restoration. This work will also be complementary to the study of Local Parity Violation, since chiral symmetry restoration is believed necessary for LPV.

2.4.3 Rare Decays

Rare processes like leptonic decays of hadrons provide possible observables in searching for traces of New Physics beyond the standard model [142, 143, 144, 145]. These decays usually involve electromagnetic or weak couplings which can be calculated to high accuracy. The LHC is aiming at a direct observation of the Higgs and physics beyond the Standard Model (SM). Precision measurements at low energy target deviations of observables from the SM prediction as indirect evidence of coupling from the New Physics to the rare process [142]. Observations exist that point at discrepancies between SM predictions and experimental observations. To mention a few [142]: (g-2) measurements [146], a 3.3σ higher branching ratio for $\pi^0 \to e^+e^-$ than SM prediction [147]; observation of 3 events of a possible intermediate neutral particle in $\Sigma^+ \to p\mu\mu$ [148].

RHIC provides a unique opportunity for searching for New Physics beyond Standard Model with rare decays of hadrons. The high luminosity and high multiplicity in nucleus-nucleus collisions produce copious hadrons of interest for the rare decay process. With the upgrades to the detectors and Data Acquisition System (DAQ), the STAR Collaboration has positioned itself with high rate capability and excellent lepton identification at low momentum to search for the rare decays from copiously produced hadrons. The pseudoscalar mesons (for example, η or η') are particularly interesting since their decay to e^+e^- pairs is suppressed by $\alpha^2(10^{-4})$ and helicity conservation due to the small electron mass ($r^2 = (m_e/m_P)^2 \simeq 10^{-6}$). Couplings from Physics beyond the SM can increase this branching ratio significantly [142].

R_0	Unitary Bound	CLEO bound	CLEO+OPE [10]	[20]	Experiment
$R_0(\pi^0 \to e^+e^-) \times 10^8$	≥ 4.69	$\geq 5.85 \pm 0.03$	6.23 ± 0.12	6.26	7.49 ± 0.38[1]
$R_0(\eta \to \mu^+\mu^- \times 10^6$	≥ 4.26	$\leq 6.23 \pm 0.12$	5.12 ± 0.27	4.64	5.8 ± 0.8[16]
$R_0(\eta \to e^+e^-) \times 10^9$	≥ 1.78	$\geq 4.33 \pm 0.02$	4.60 ± 0.09	5.24	$\leq 2.7 \times 10^4$[15]
$R_0(\eta' \to \mu^+\mu^-) \times 10^7$	≥ 1.35	$\leq 1.44 \pm 0.01$	1.364 ± 0.010	1.30	
$R_0(\eta' \to e^+e^-) \times 10^{10}$	≥ 0.36	$\geq 1.121 \pm 0.004$	1.178 ± 0.014	1.86	

Table 2.5: This table provides the predictions and experimental results.

The conventional theory for the pseudoscalar meson (P) decays to a lepton pair [149] provides a formula for the branching ratio (B.R.):

$$B(P \to l^+l^-) = B(P \to \gamma\gamma)2\alpha^2 r^2 \sqrt{1-4r^2}(|X|^2 + |Y|^2)$$

Where X and Y are imaginary and real parts of the decay amplitudes. This results in $B(\eta \to \mu^+\mu^-) > 4.4 \times 10^{-6}$, and is compatible with the experimentally measured B.R., $B(\eta \to \mu^+\mu^-) = (5.7 \pm 0.8) \times 10^{-6}$. In a similar fashion, the dielectron channel can be predicted in SM with good precision: $\frac{B(\eta \to e^+e^-)}{B(\eta \to \mu^+\mu^-)} = 4.05 \times 10^{-4}$. And the B.R. is then 2.3×10^{-9}. Any unknown process present in the di-electron channel can enhance this B.R.

The combination of STAR's TPC and TOF with 2π coverage at mid-rapidity provides excellent electron identification and high mass resolution at low momentum. In addition, the EMC surrounding the TPC and TOF system provides additional trigger capabilities and electron identification at high transverse momentum. In central Au+Au collisions, the π^0, η, and Σ yields are roughly 600, 60 and 60 per collision that fall in the acceptance; these yields are more than two orders of magnitude higher than that in p+p collisions. STAR's annual data collection is expected to be in the order of 500 million central Au+Au collisions. This means that we have annual yields of 3×10^{11}, 3×10^{10}, and 3×10^{10} of π^0, η, and Σ respectively.

In Run 9 (2009), STAR had installed 75% of the full TOF system and took data in p+p collisions; in Run 10, the full TOF system was installed for Au+Au collisions at various energies. Figure 2.48 shows the simulations of electron-pair invariant mass with inputs from Tsallis fits to the measured hadron spectra and with decay form factors and kinematics from PYTHIA. The simulation is with the Run 9 detector configuration. This is the cocktail of the expected di-electron distribution.

The preliminary data of electron-pair invariant mass (M_{ee}) has been analyzed from 100 million minimum-bias p+p collisions. The spectrum shown in Fig. 2.49 is after like-sign background subtraction. The cocktail can describe the data reasonably well without the $\eta \to e^+e^-$ decay channel as shown by the black curve. The pink peak is the $\eta \to e^+e^-$ with the upper limit from the PDG [150]. The best fit is a factor of 5 below the PDG limit of 2.5×10^{-5}. A 90% confidence level will provide an upper limit about an order of magnitude better than the current world data.

This shows the promise of our program to search for rare decays of hadrons in relativistic heavy-ion collisions at STAR. With the high hadron yields to tape, high efficiency for electrons at low momentum and high mass resolution, STAR provides a unique tool for such a program in the years

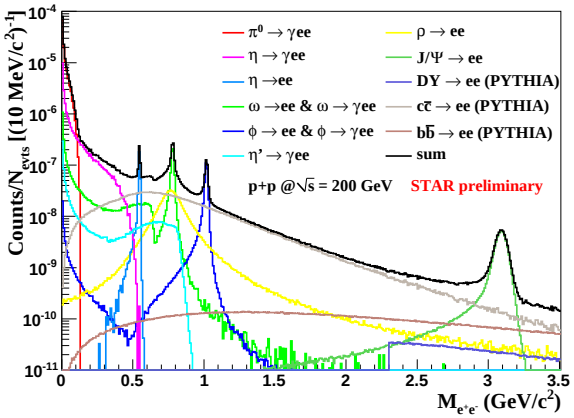

Figure 2.48: M_{ee} simulation for dielectron production in minbias p+p collisions at $\sqrt{s} = 200$ GeV. The cocktail is from a combination of data and PYTHIA with decay form factors and branching ratios. The $\eta \to e^+e^-$ branching ratio has been set to the upper limit from the PDG.

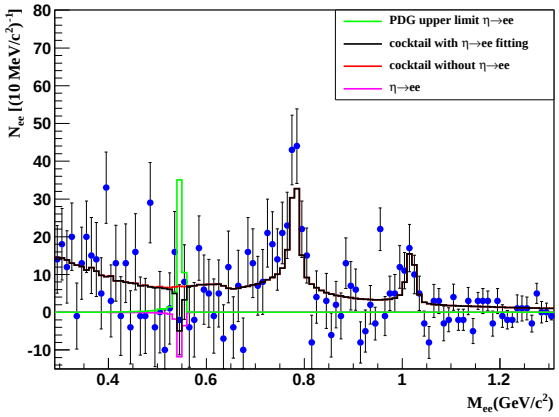

Figure 2.49: M_{ee} data for dielectron production in minbias p+p collisions at $\sqrt{s} = 200$ GeV in FY2009 with 75% TOF installed. The $\eta \to e^+e^-$ branching ratio is from the upper limit in PDG.

to come. More studies are needed to assess the feasibility of other di-electron channels such as $\pi^0 \to e^+e^-$ and $\eta' \to e^+e^-$.

Another example of future searches for rare decays involves $\Sigma^+ \to p\mu^+\mu^-$ and $\Sigma^+ \to pe^+e^-$. The $\Sigma^+ \to pe^+e^-$ B.R. is predicted to be $\leq 7 \times 10^{-6}$ by the calculation of the ratio of $\Sigma^+ \to pe^+e^-/\Sigma \to p\gamma$ [145]. Furthermore, it is predicted that $1/120 > (\Sigma^+ \to p\mu^+\mu^-)/(\Sigma^+ \to pe^+e^- > 1/1210$. The HyperCP Collaboration has reported the first evidence of the $\Sigma^+ \to p\mu^+\mu^-$ decay channel with 3 events. The narrow range of di-muon invariant mass from those events also indicates that the decay proceeds via an intermediate neutral particle as depicted in Fig. 2.50 [148]. The B.R.

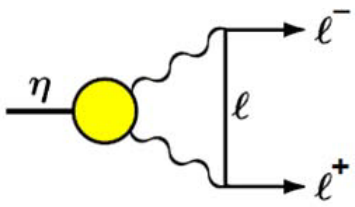

Figure 2.50: Rare $\eta \to l^+l^-$ decay diagram.

of the observation is at the level of 10^{-7}. The confirmation of detection of this otherwise unknown neutral particle will have significant impact on physics. With the Heav-Flavor Tracker and the Muon Telescope Detector upgrades coupled with the large sample of Σ^+ and its anti-particle at an annual yield of 3×10^{10}, STAR has the ability to not only confirm or rule out this observation, but also to be able to measure the $\Sigma^+ \to pe^+e^-$ decay channel, given the large B.R. of 8×10^{-6}. Simulations are on-going with the HFT+ MTD detectors to obtain a sensitivity analysis.

2.5 What other exotic particles are created at RHIC?

2.5.1 Discoveries of the heaviest antimatter and antihypernuclei

Searching for A=4,5 antimatter

Understanding the asymmetry of anti-matter and matter is one of the frontiers of modern physics. Nuclei are abundant in the universe, but anti-nuclei with A≥2 haven't been found in nature. Relativistic heavy ion collisions, simulating the condition at the early universe, provide an environment with abundant antinucleons and antihyperons and produce antinuclei and antihypernuclei by coalescing them together. This offers the first opportunity for discovery of antihypernuclei and heavier antinuclei having A>2 [151]. The antialpha particle ($\bar{\alpha}$) is next in line with A=-4. With the dataset taken during Run 10, we expect to find about 10 antialpha particles in the data sample to tape of 250 million central and 350 million minbias Au+Au collisions. The next stable antimatter nucleus would be A=6 (^6He,^6Li). However, the penalty factor [152] on the production rate for an additional antinucleon is about 1500 as shown in Fig. 2.51. This means that the A=6 antinuclei are produced at a rate 2×10^6 lower than that of an A=4 antialpha particle. Unless production mechanisms or collider technology change dramatically, it is unlikely that A=6 antinuclei can be produced in collider or fixed-target experiments. It has been argued that a more economic way of producing heavier antimatter and/or nuclear matter containing large amount of strange quark contents is through excitation of complex nuclear structure from the vacuum [153] or through strangeness distillation from a QGP [154, 155, 156]. An enhanced deviation from the usual large penalty factor with increasing atomic mass number (A) would be an exciting indication of a new production mechanism.

The heaviest antimatter that can be produced and detected with a tracking detector in high-energy accelarators are likely to be A=4 or 5 unstable antinuclei: $^4\overline{He} * \rightarrow \bar{t} + \bar{p}$, $^4\overline{Li} \rightarrow ^3\overline{He} + \overline{p}$, $^5\overline{Li} \rightarrow ^4\overline{He} + \overline{p}$. The possible annual total event sample at STAR in a 12-week period (total live time of 4.4×10^6 s) with RHIC-II luminosity (50KHz Au+Au minbias collisions) is $\sim 2 \times 10^{11}$. STAR is expected to write to tape $\sim 10^9$ events annually. Therefore, a new trigger scheme coupled to a high-rate DAQ is important to take advantage of the luminosity available for these discoveries. We propose to use a trigger based on EMC high-towers with a threshold of $E_T > 2.5$ GeV/c, which provides a rejection of about five for minbias Au+Au collisions and also provides the location of the TPC sector containing the tracks of the antimatter candidates. The EMC trigger efficiency is shown in Fig. 2.52 and is quite high ($> 60\%$) since antimatter annihination deposits large amounts of energy in the EMC. Reading a single TPC sector increases the DAQ rate by $\sim$ 24 through reduced data volume. We refer to Chap. 4 for the details about the DAQ10K project.

Probing baryon-strangeness correlation with hypernuclei

Since the coalescence process (or statistical production) for formation of hypernuclei and antihypernuclei requires that nucleons or antinucleons and hyperons or anti-hyperons be produced in proximity in phase space, hypernucleus and antihypernucleus production are sensitive to correlations of the coordinate and momentum space distributions of nucleons and hyperons [157]. Equilibrium between these two species is one of the signatures of QGP formation, which also results in higher

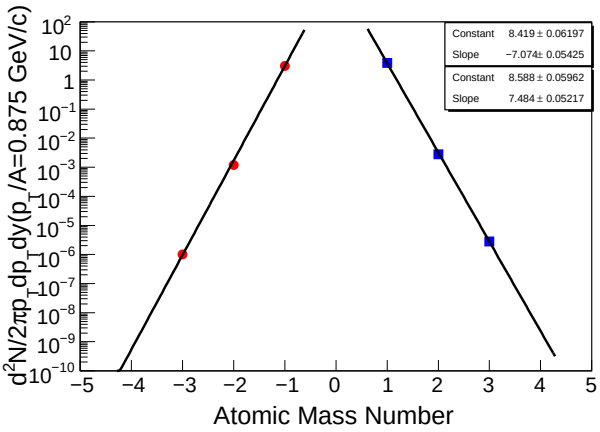

Figure 2.51: Differential invariant yields of nuclei and antinuclei as a function of atomic mass number in central Au+Au collisions at $\sqrt{s_{NN}} = 200$ GeV. The penalty factor for producing light nuclei in 200 GeV Au+Au collisions is $\sim$1300. That for anti-nuclei is $\sim$1700.

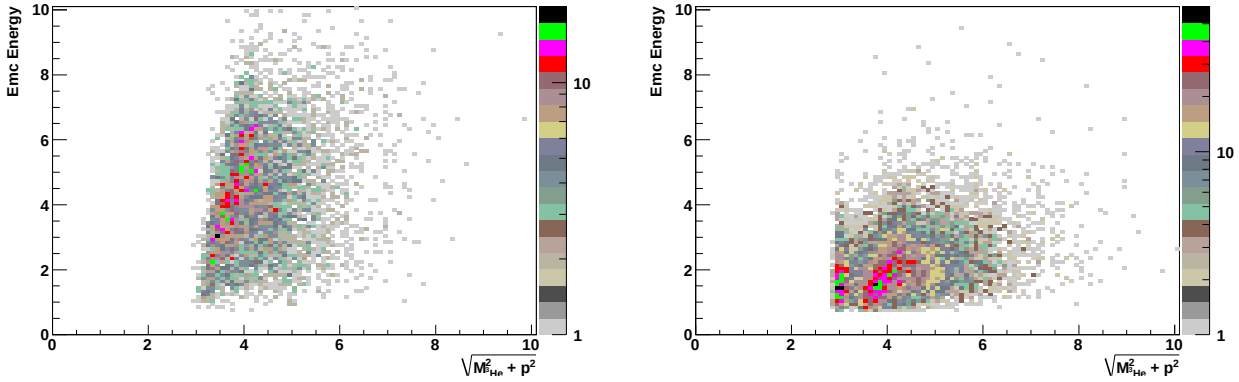

Figure 2.52: Left panel: $^3\overline{He}$ EMC energy vs TPC $\sqrt{m^2+p^2}$. Right panel: same for ^3He.

hypernucleus and antihypernucleus yields. Similarly, the hypertriton yield can be compared to the yields of helium and tritons which have the same atomic mass number.

Thermal models can predict not only the simple hadron production, but also the composite particle yields in a macroscopic approach [158]. Figure 2.53 shows the prediction of the strangeness phase-space factor ($S3$) from a thermal model [158]. It is interesting to note that the $S3$ from thermal models is relatively independent of energy at a value of about 0.6, while there is a strong beam energy depedence when feed-down from strong decays to Λ and protons are artifically left out [158]. Relative to the light quark content, more strange quark content populates in higher resonant baryon states at higher temperature (RHIC) than at lower temperature (AGS, FAIR) in this thermal model, resulting in an increasing $S3$ as shown in Fig. 2.53. On the other hand, AMPT simulations with and without string melting provide similar beam energy dependences [157].

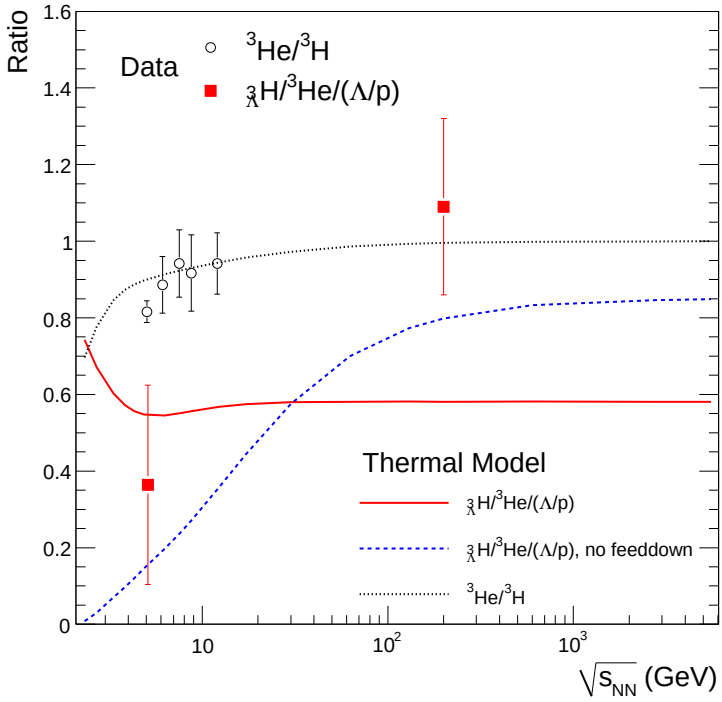

Figure 2.53: Ratio of the yields between hypertriton and ^3He scaled by the Λ/p ratio, or the strangeness phase-space factor. The data points are from STAR/RHIC and E864/AGS references. The curves show thermal model predictions for the ratios with and without strong decay feed-down to Λ and proton. Figure is taken from A. Andronic *et al.* [158].

However, the authors [157] argued that the increase is due to the strangeness phase-space population for the nucleus coalescence in a microscopic approach. It was stated that [158], "The discrepancy [of $S3$ between thermal model and data] at RHIC energy, if experimentally established, would point to a new production mechanism not contained in the thermal approach and not present at lower beam energies... The hyper-nuclei program, started by the STAR experiment at RHIC, has made these studies very topical. Although significant questions remain, it is clear that the study of the production of complex nuclei with and without strangeness in relativistic nuclear collisions can open a new chapter in the quest to understand the relation of particle production to the QCD phase boundary."

Hypernuclei provide the ideal lab for probing the hyperon-nucleon (YN) interaction, which is of fundamental interest in nuclear physics and nuclear astrophysics. For example, the YN interaction plays an important role in attempts to understand the structure of neutron stars. Depending on the strength of the YN interaction, the collapsed stellar core could consist of hyperons, strange quark matter, or a kaon condensate [159]. The decay rates of a hypernucleus depends on the strength of the YN interaction. Therefore, a precise determination of the decay rates of hypernuclei provides direct information on the YN interaction strength.

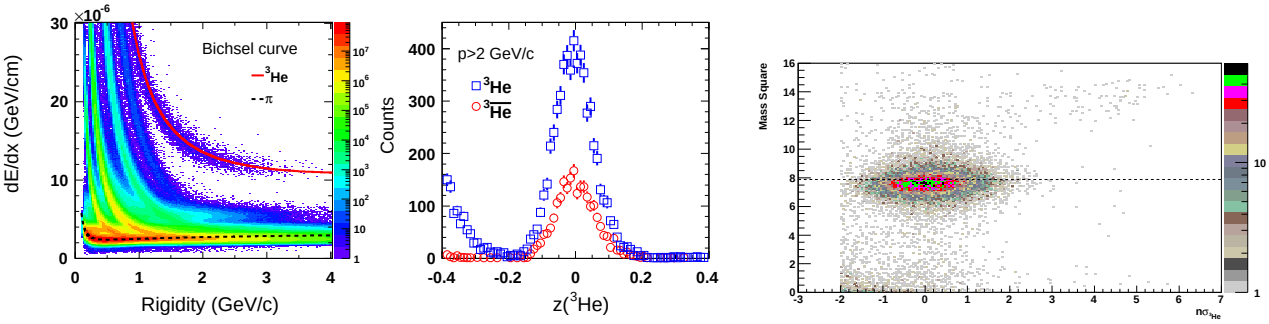

Figure 2.54: Left panel: dE/dx vs. rigidity distribution from Run 7 Au+Au data. Middle panel: ^{3}He statistics from Run 4 and Run 7 data; about 5800 ^{3}He candidates and 2200 $^3\bar{\text{He}}$ have been collected. Right panel: Preliminary $Mass^2$ from TOF vs $n\sigma$ from TPC dE/dx for charge $|q| = 2$ candidates with High-Level Trigger (HLT) data from Run 10 Au+Au collisions at $\sqrt{s_{NN}} = 200$ GeV.

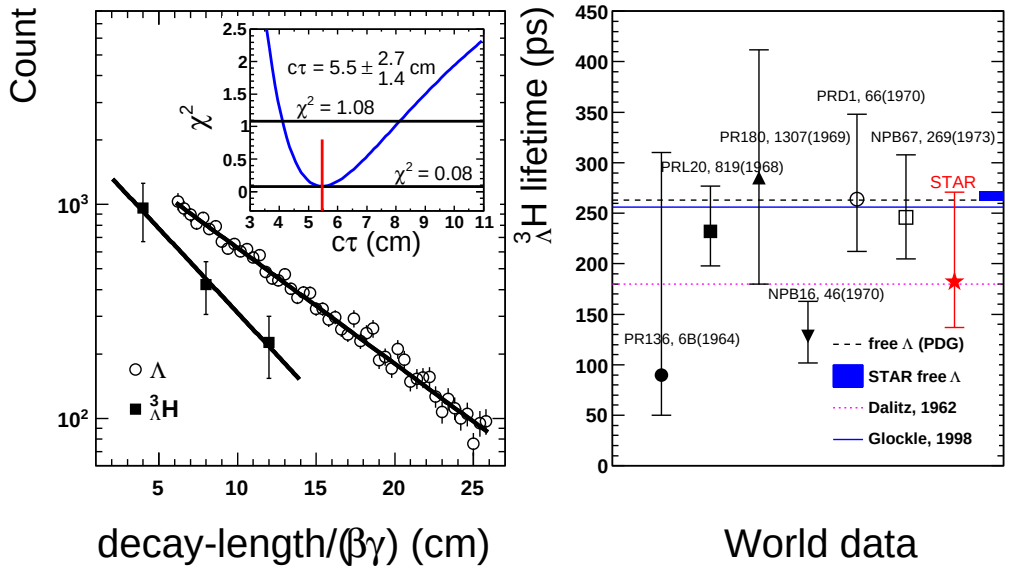

Figure 2.55: $^3_\Lambda$H lifetime measurement from STAR and in comparison with world data.

Testing coalescence mechanism with antinuclei and nuclei

One of the most important experimental findings at RHIC has been the signature of coalescence as the mechanism of hadron production. The differences in baryons and mesons at intermediate transverse momentum for observables like the nuclear modification factor and the elliptic flow parameter have been attributed to be signatures of quark coalescence as a mechanism of hadron

production [160]. However, the underlying mechanism for how this coalescence happens is difficult to study directly due to the inability of measuring the partonic momentum distributions in high energy heavy-ion collisions. In addition, due to the unique kinematics and approximately linear dependence of v_2 as a function of p_T at low p_T, the collective velocity effect and constituent quark scaling are indistinguishable for mesons and baryons.

Nuclei however are believed to be formed in the relativistic heavy-ion collisions through coalescence of nucleons, and we can study individual nucleon distributions. The binding energy for the nuclei are small and they are hence formed in a process that happens at a late stage of the evolution of the system. The coalescence probability is related to the local nucleon density. The advantage of nucleons over the partonic coalescence phenomena is that both the nuclei and the constituent nucleon space-momentum distributions are measurable quantities in heavy-ion collisions. These can then be used to understand the basic underlying process of coalescence, like effects of local density correlations and energy/entropy conservations [161]. By studying the spectra and elliptic flow of nuclei and comparing to those of their constituents, we can probe the properties of the medium in which the particles form. Fig. 2.6 left panel shows the systematics of v_2/n_q scaling for different hadrons including the nuclei and antinuclei. The preliminary data shows that even at low p_T, the nuclei are still produced by coalescence of individual nucleons and therefore their elliptic flow follows the constituent nucleon scaling.

Nuclei like deuterons, tritons, and helium will tell us about the effect of increasing the number of constituents on the coalescence process; studies with hypernuclei will provide a unique opportunity of studying the coalescence process with different types of constituents. The latter could be analogous to formation of strange quark and light quark carrying hadrons through partonic coalescence.

In the future, measurements involving high-statistics data sets characterized by excellent particle identification will allow:

- measurement of v_2 for deuteron, triton and helium
- measurement of v_2 for hypernuclei and comparison of v_2 for nucleons and hyperons.
- Comparison of phase-space correlation (interferomentry) results for nucleon-nucleon systems and nuclei-nuclei systems.

With the inclusion of the full TOF detector system along with the existing TPC, we are well suited for such studies in the coming decade. The proposed high-speed trigger with DAQ10K for TPC readout can enhance the statistics by orders of magnitude for this program.

Summary

In this project, we propose to carry out the following measurements in the near future:

1. Search for a $^4\overline{He}$ signal from high statistics heavy-ion data. As shown in Fig. 2.54, we have collected $\sim$ 2200 $^3\overline{He}$ from Run 4 and Run 7 data ($\sim$ 90M MB events plus 24M central trigger events). There will be a factor of 8 more statistics from Run 10 data, for a total 17K

$^3\overline{He}$ sample. The penalty factor is $\sim$ 1700 per anti-nucleon, so we can expect to observe 10 $^4\overline{He}$ candidates.

2. Search for A=4 or 5 unstable antinuclei. To improve the statistics for such searches, it is crucial to upgrade the trigger and DAQ rate to match the RHIC-II luminosity, and we propose to use high-tower threshold at $E_T > 2.5$ GeV at L0. From Run 10 preliminary data, the rejection on minbias Au+Au for such trigger at L0 is about 5, while the $^3\overline{He}$ trigger efficiency is greater than 60%. Altogether, these will provide a L0 rate of < 10 kHz in a sector-by-sector TPC readout with a factor of 100 enhancement for the antimatter search.

3. Improve the hypertriton lifetime measurement, and possibly determine anti-hypertriton and hypertriton lifetime difference. There is still large uncertainty in the $^3_\Lambda$H lifetime measurement (Fig. 2.55 right panel) and Ref. [151]. With an order of magnitude statistics increase, we will be able to improve the current measurement by a factor of 3.

4. Search for the possible Ξ-hypernuclei [162] from high statistics heavy-ion data. The Ξ production rate is about 10% of the Λ in Au+Au collisions at $\sqrt{s_{\rm NN}}$ =200 GeV [163], and we have seen $\sim$150 $^3_\Lambda$H candidates in the currently available data sample. There is good potential to detect any Ξ-hypernuclei with an order of magnitude statistics increase in the near future.

5. Detect the $\overline{p}$ ^{3}He atomcule [164] and study the anti-nucleus annihilation process. Search for the possible anti-deuteron, anti-triton, anti-helium atomcule. Rate estimation: the dN/dy for $\overline{p}$ is $\sim$30 in our case. We assume 3% of them will stop, and 3% of those stopped $\overline{p}$ will form a $\overline{p}$ atomcule [164]. Taking our luminosity, $20\,\text{kHz} \times 50\,\text{h} \times 3600\,\text{s} \times 10$ weeks $= 3.6 \times 10^{10}$, we will have $\sim 10^9$ $\overline{p}$, 10^6 $\overline{d}$ and 10^3 $\overline{t}$, and $^3\overline{He}$.

2.5.2 Glueball search

A process of unique interest in proton-proton collisions at RHIC is the central production process through the double-Pomeron exchange (DPE) mechanism $pp \rightarrow pM_Xp$, as shown in Fig. 2.56. Because of the constraints provided by the double Pomeron interaction, glueballs and other states coupling preferentially to gluons are expected to be produced with much reduced backgrounds compared to standard hadronic production processes [165]. The two protons stay intact after the interaction, but they lose momentum to the Pomeron and the Pomeron-Pomeron interaction produces a system M_X at mid-rapidity of the colliding protons.

The above process is commonly characterized by using the variables t, ξ, and M_X, where t is the squared four-momentum transfer between the incoming and outgoing protons, $\xi = \Delta p/p$ is the momentum fraction carried off by the Pomeron and M_X is the invariant mass of the centrally produced system. In the case of double Pomeron exchange, separate t and ξ variables exist for each proton-Pomeron vertex.

Two of the gluons in the DPE process, see Fig. 2.57, could merge into a mesonic bound state without a constituent quark, a glueball, in the central production $pp \rightarrow pM_Xp$. Lattice QCD calculations predict the lowest-lying scalar glueball state will have a mass in the range $1500 - 1700$ MeV/c^2, with tensor and pseudoscalar glueballs in the range $2000 - 2500$ MeV/c^2 [165].

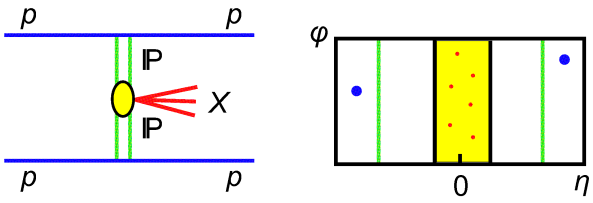

Figure 2.56: The diagram of the Central Production process through the DPE mechanism $pp \to pM_Xp$, and idealization of the associated rapidity gap. The Pomeron exchange is denoted by (IP).

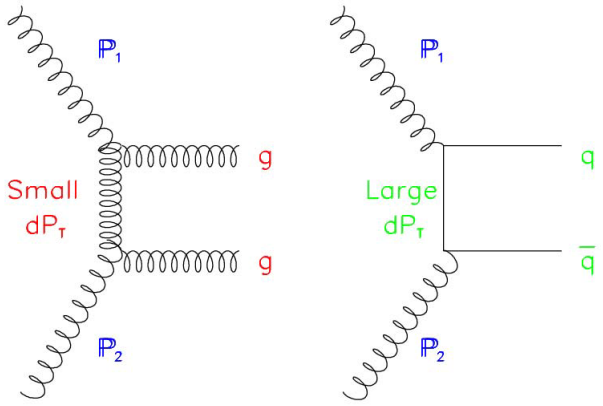

Figure 2.57: Schematic diagrams of the coupling of the exchanged particles into the final state meson for a) gluon exchange and b) quark exchange.

Experimentally measured candidates for the scalar glueball states are the f0(1500) and the $f_J(1710)$ in central production [166] as well as other gluon-rich reactions such as $p\bar{p}$ annihilation, and radiative J/ψ decay [167]. The spin of the $f_J(1710)$ is not yet confirmed; indications for both spin 2 and spin 0 have been reported. Glueballs are expected to be intrinsically unstable and decay in diverse ways, yielding typically two or more mesons. The $f_J(1710)$ dominantly decays into KK pairs, and f0(1500) into 4π.

One of the challenges in identifying a glueball state unambiguously lies in difficulties of isolating it from the conventional meson state that shares the same quantum numbers. To identify that the process is DPE rather than Reggeon exchange requires observing the suppression of $\rho(770)$ mesons, since the ρ cannot be formed in the DPE process due to isospin conservation. The other filter for enhancing glueball candidates in DPE is the dPT filter [168], in which small momentum transfer processes enhance gg kinematic configurations since the gluons can now directly bind into the final state (a glueball) in the process, see Fig. 2.57.

The idea that the production of glueballs is enhanced in the central region in $pp \to pM_Xp$ was proposed in [168]. The crucial argument here is that the pattern of resonances produced in the central region, when both forward protons are measured, depends on the vector difference of the transverse momentum of the final state protons $\overline{k_{T1}}$, $\overline{k_{T2}}$, with $dPT = \mid \overline{k_{T1}} - \overline{k_{T2}} \mid$. The so-called

dPT filter argument is that when dPT is large ($\geq \Lambda_{QCD}$), $q\bar{q}$ states are prominent, and when dPT is small the surviving resonances include glueball candidates.

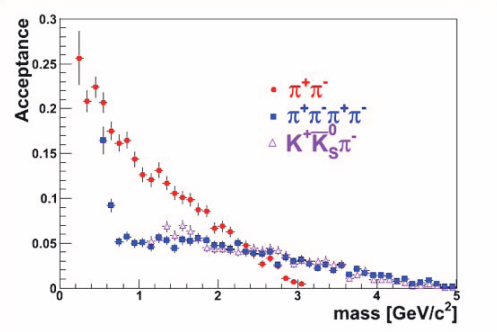

Figure 2.58: Accepted distributions of mass M_X decaying into a) $\pi^+\pi^-$; b) 4π and c) $K^+K_S\pi^-$- which are within acceptance of STAR TPC, using STAR particle ID and a phase-space decay of the M_X.

The technique for reconstructing resonances using the STAR detector system has been well established in p+p and A+A collisions. The current ongoing central photo-production program in ultra-peripheral A+A collisions at STAR is topologically similar to the DPE process, and the common available experimental machinery can be utilized for triggering and analyzing DPE processes. Figure 2.58 shows the acceptance of expected reconstructed kinematic phase-space distributions of a centrally produced mass decaying into $\pi^+\pi^-$, $K^+{K_s}^0\pi^-$, and into $\pi^+\pi^-\pi^+\pi^-$. Reconstruction of the tracks from the decay was simulated using the geometrical acceptance of the TPC (rapidity range $-1 < \eta < 1$ with full azimuthal coverage) and particle identification by the TPC and the TOF system, which can separate pions and kaons up to $p \sim 1.6$ GeV/c. The mass of the central system M_X will be reconstructed in the TPC using tracks of the decay products. The mass dependent partial wave analysis technique will be utilized to determine spin-parity of the reconstructed central system.

To implement this program, a new set of Roman Pot stations integrated with a new vacuum section between the DX-D0 magnets will be needed. At this location, the data taking will not require special beam optics; hence it will be done during normal RHIC operations. Thus we will be able to acquire a large data sample of central production events, necessary for the observation of glueball and exotic particle production. The double-Pomeron cross-section is not known at RHIC energies, so an estimate of 140 μb from Ref. [169, 170] was used in our simulations. Branching ratios as measured at $\sqrt{s} = 62.4$ GeV by the ISR experiment were also assumed. These give us trigger rates and expected data samples for various channels as shown in Table 2.6. During a twenty-week RHIC run, with luminosity of 1.5×10^{32} cm^{-2}sec^{-1} and assuming 60 DAQ hours per week at $\sqrt{s} = 500$ GeV, we can collect 10.4×10^6 $\pi^+\pi^-$, 2.7×10^6 $\pi^+\pi^-\pi^+\pi^-$, and 0.8×10^6 K^+K^- pairs (in $1 < M_X < 2$ GeV/c^2) for analysis. With such a data sample, the partial wave analysis necessary to identify exotic final states will be possible.

The assumed integrated luminosity can be easily achieved during the planned high luminosity spin program at RHIC. Furthermore, it is expected that the luminosity upgrade and a longer run

Table 2.6: Anticipated glueball search data sample.

Decay Channels	Event Rate (Hz)	Trigger Conditions	Event Yield for 20-week run
4π	27	≥ 2 tracks in TOF	2.7×10^6
2π	23	2 tracks in TOF	10.4×10^6
k^+K^-	2.3	2 tracks in TOF	0.8×10^6

can bring an order of magnitude higher statistics, which will enable differential kinematic sampling and spin-parity analysis.

2.5.3 Searches for di-baryon states with the STAR detector

Nucleus-nucleus collisions at RHIC have revealed two distinct features in particle production: 1) a large amount of strangeness production including a large yield of multi-strange hyperons per central AuAu collision [171] ; and 2) the hadronization of bulk partonic matter at RHIC seems to be through coalescence or recombination of constituent quarks [160]. The coalescence scheme predicts features in the particle type dependence for both the azimuthal angular anisotropy v_2 distributions and the transverse momentum distributions [172]. The observed quark number scaling supports the coalescence picture and is difficult to explain in traditional quark fragmentation models. RHIC can be a unique facility for investigating hadronic physics involving short-lived hadrons and for searches for exotic multi-strange particles.

In nucleus-nucleus collisions at RHIC, various particles are produced within a source size of typically 10 fm. Hadrons interact with each other on the time scale of several fm/c. For short-lived particles, hyperons for example, RHIC will be a unique facility to investigate hyperon-hyperon interactions through measurement of particle correlations. Because of the large number of strange quark pairs produced per nuclear collision at RHIC, particles with multiple strange quarks such as Ξ hyperons are produced with high yields, facilitating searches for exotic particles involving multiple strange quarks. The H di-baryon with a quark composition of $uuddss$ has inspired many searches since Jaffe proposed the possible existence of the 6-quark state in the framework of the MIT bag model [173]. The internal quark structure of the H particle could be a 6-quark single hadron if the H is deeply bound; or it could be a molecular structure of two hyperons similar to that of a deuteron if it is weakly bound. We use the notation of di-baryon or di-hyperon to refer to these particles with baryon quantum number of two without necessarily specifying the internal quark structure of the particle.

For a weakly bound H particle, the charged particle decay mode that is accessible to the STAR experiment is $H \rightarrow \Lambda + p + \pi^-$, where the proton and pion have too little energy to form a Λ hyperon. Ohnishi et al. proposed that $\Lambda - \Lambda$ correlation measurements in nucleus-nucleus collisions at RHIC can be sensitive to the Λ mutual attractive interactions with either positive or negative scattering length. This can be used to decide whether there is a stable H particle or an H resonance [174] . This sensitivity is due to the length scale involved, the source size for Λ production, and the allowed range of $\Lambda - \Lambda$ scattering parameters. Therefore RHIC could provide a definitive answer to the question of H particle existence, though the theoretical calculations require further improvement

and independent confirmations.

Other di-hyperons involving multi-strange hyperons have also been investigated theoretically. For example, Schaffner-Bielich, Mattiello and Sorge investigated di-hyperon stability and their weak non-leptonic decays using SU(3) symmetry [175]. The non-leptonic decay branching ratios depend strongly on the binding energy. Figure 2.59 shows the calculated branching ratios by Schaffner-Bielich et al. [155] for several di-hyperon candidates as a function of binding energy. We are only interested in the decay modes with charged particles in the final states. Possible di-hyperon decay candidates include:

- $\Sigma^+ p \rightarrow p + p$
- $\Xi^0 p \rightarrow p + \Lambda$
- $\Xi^0 \Lambda \rightarrow p + \Xi$ or $\Lambda + \Lambda$
- $\Xi^0 \Xi^- \rightarrow \Xi^- + \Lambda$

where the Λ hyperon may be detected from its $p+\pi^-$ decay mode. Miller has also argued, based on SU(3) flavor symmetry, for the existence of di-hyperon bound states of two Ξ particles [176]. Theoretical justifications for possible stable di-hyperons are largely based on symmetry principles and do not depend on detailed parameters of various calculations. Experimentally, there have been few results in the literature on searches for di-hyperons involving multi-strange hyperons, presumably due to the low multiplicity of multi-strange hyperon production in early nuclear collisions. STAR reported a measured rapidity density (dn/dy) for Ξ^- of 2.2 and for anti-Ξ^+ of 1.8 in the most central 5% Au+Au collisions at the top RHIC energy of 200 GeV [171]. Nucleus-nucleus collisions at RHIC with considerable production yield of multi-strange hyperons in each collision will provide the first viable experimental opportunity to search for these di-hyperons.

The production rate for di-baryons cannot be calculated reliably. It depends on both the collision evolution dynamics and the internal structure of the di-baryon. It is believed that the formation mechanism could be through coalescence of hadrons at the late stage of the evolution, similar to the formation of deuterons through $p-n$ coalescence. We will use deuteron production as a reference and take into account the strangeness suppression factor, decay branching ratios, and detection efficiency. The measured anti-deuteron production rate is about 0.02 per central Au+Au collision (most central 10% events) [177]. The strangeness suppression factor can be approximated from the anti-Λ to anti-p ratio of ~ 0.5. If the H particle has a similar coalescence probability as the deuteron, the H particle production rate would be $\sim 5 \times 10^{-3}$ per central collision. For the double-Ξ candidate, we use the anti-Ξ to anti-p ratio of 0.075 from STAR measurement, and anticipate $\sim 1 \times 10^{-4}$ per central collision. The branching ratio and the detection efficiency depend on the binding energy. The level of combinatorial background varies with the analysis geometrical cut. We do not have a solid estimate on these numbers. We expect to collect over 100 Million central Au+Au collision events in order to reach our desired sensitivity level for di-hyperon searches.

Zhang et al. [178] predicted that the di-Omega is the most stable di-hyperon using a chiral SU(3) quark model. The measured ratio of anti-Ω to anti-proton is approximately 0.01 based on STAR measurement. Therefore, the expected production rate for di-Omega will be $\sim 2 \times 10^{-6}$. Unless

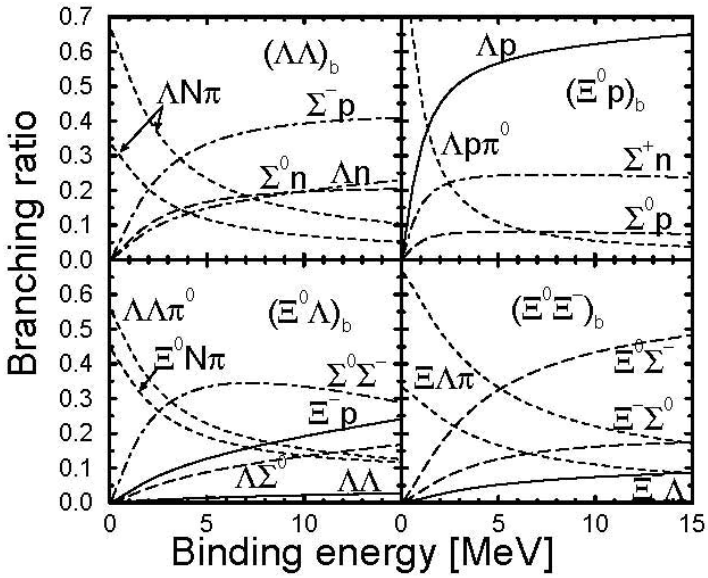

Figure 2.59: The calculated branching ratios for several di-hyperon candidates as a function of binding energy [155].

the di-Omega has a relatively long lifetime and the detection efficiency for its decay daughters is significantly enhanced due to the long di-Omega lifetime, searches for the exotic di-Ω state will be a challenge for STAR.

Exotic multiquark states with heavy quarks will also be a part of the STAR scientific program to explore physics beyond the current QCD framework once the Heavy Flavor Tracker upgrade is completed. Possible candidates include the tetraquark state TCC (ud,c,c) [179] and charmed pentaquark states [180]. The number of events required for sensitive searches for these heavy quark exotics will likely exceed 1 Billion. Searches for heavy quark exotics will remain a challenge for STAR. On the other hand, nucleus-nucleus collisions at RHIC will be the first major opportunity for possible production of these exotic particles. Experimental exploration of possible new physics in this area could be particularly worthwhile. STAR is well positioned to carry out these searches.

Chapter 3

What is the partonic structure of nucleons and nuclei?

Unraveling the quark and gluon substructure of nucleons and nuclei is one of the major goals in nuclear physics today. A great deal has been learned about the partonic structure of the nucleon at leading twist and with collinear factorization, but much is still unknown. Furthermore, new avenues have been opened during the past decade to explore the nucleon structure beyond leading twist and collinear factorization. The ability to collide polarized beams at RHIC provides unique information regarding these issues.

Ever since the low-x growth of the gluon density was discovered, it has been recognized that the gluon density must eventually saturate. However, the kinematic region where saturation occurs is an experimental question. Forward rapidity data indicate that the onset of saturation may be experimentally accessible at RHIC. Detailed studies of the onset region are essential to determine the dynamical mechanisms that lead to saturation. Furthermore, it is crucial to understand the partonic structure of heavy nuclei in order to separate initial-state effects from the novel features that arise in the dense medium in A+A collisions. The ability to perform detailed measurements in p+A collisions at RHIC represents a window to explore the partonic nature of cold nuclear matter.

Three of the key questions that the STAR Collaboration has identified for the coming decade involve these questions:

- What is the partonic spin structure of the proton?
- How do we go beyond leading twist and collinear factorization in perturbative QCD?
- What is the nature of the initial state in nuclear collisions?

In this chapter, we describe how STAR will address these questions at RHIC during the coming decade. In addition, we show how studies of e+p and e+A collisions during the early phase of eRHIC will provide an even more detailed understanding of the proton spin and cold nuclear matter.

3.1 What is the partonic spin structure of the proton?

3.1.1 Gluon Polarization

A major thrust of the proton spin physics program at RHIC [181] and in STAR is the precise determination of the gluon helicity distribution, $\Delta g(x)$, in the polarized proton over a wide and resolved range in the gluon longitudinal momentum fraction, $0.01 < x < 0.3$.

A number of reaction channels in collisions of longitudinally polarized protons are directly sensitive to $\Delta g(x)$. STAR has made significant progress since the previous Decadal Plan, in particular through measurement of differential cross sections and double beam-helicity asymmetries, A_{LL}, for the production of inclusive jets and pions in collisions at $\sqrt{s} = 200\,\text{GeV}$ center-of-mass energy. Significant performance advances in RHIC polarized proton operations, the completion of the STAR Barrel Electromagnetic Calorimeter, and improved trigger and rate capabilities in STAR underlie this progress.

Figure 3.1 shows the published differential cross sections for mid-rapidity inclusive jet and π^0 production versus transverse momentum p_T. The data are well described by next-to-leading (NLO) order perturbative QCD (pQCD) evaluations over many orders of magnitude and a wide range in p_T. The agreement of theory with data to within uncertainties thus supports the use of NLO pQCD techniques in extracting $\Delta g(x)$ from the corresponding measurements of A_{LL} [182, 183]. Gluon-gluon scattering contributions dominate the production cross section in the lower range of p_T, whereas quark-gluon scattering contributions dominate in the measured range at higher p_T. Measurements of the p_T dependence of A_{LL} for these probes are thus sensitive to a combination of scattering contributions and, by their inclusive nature, probe a broad range in x that is not explicitly resolved, although it can be assessed in simulations [183]. Figure 3.2 shows the most precise analyzed A_{LL} measurements for inclusive jet production to date.

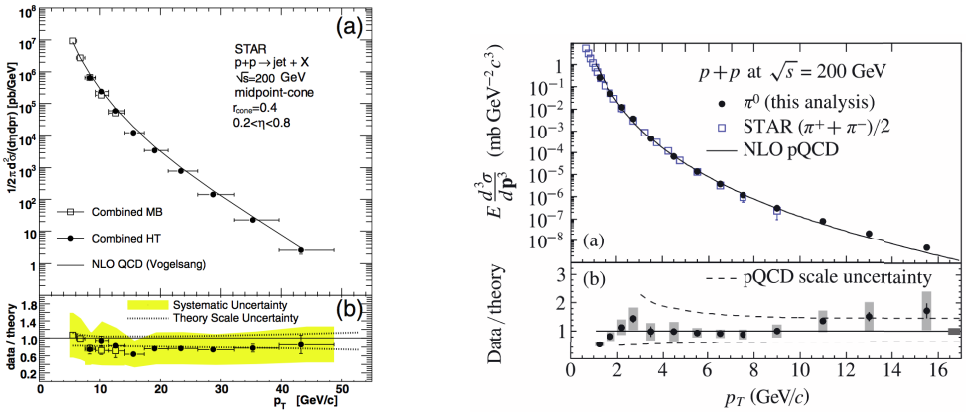

Figure 3.1: Differential cross sections for (left) inclusive jets and (right) inclusive pions produced at mid-rapidity in $\sqrt{s} = 200\,\text{GeV}$ proton collisions versus transverse momentum. The curves show NLO pQCD theory evaluations [184, 185].

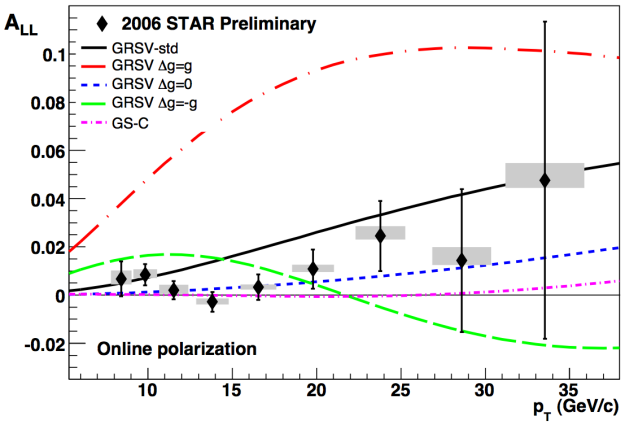

Figure 3.2: STAR inclusive jet A_{LL} from $\sqrt{s} = 200\,\text{GeV}$ longitudinally polarized proton collisions, with statistical uncertainty bars and systematic uncertainty bands. The curves show NLO pQCD evaluations for several sets of commonly used polarized parton distribution functions.

The STAR and PHENIX data on inclusive jet and π^0 production in polarized proton collisions have been analyzed, in conjunction with the body of inclusive and semi-inclusive data from deep-inelastic polarized lepton-nucleon scattering experiments, in a NLO pQCD simultaneous fit to extract the nucleon's polarized parton distributions [186, 187]. It is anticipated that this breakthrough analysis will be extended to other probes, eventually including future precision results from RHIC on coincident jet or hadron probes and W probes [188, 189].

Figure 3.3 shows preliminary results for the di-jet differential cross section and asymmetry A_{LL} versus the invariant mass of the jet pair. The cross section is well-described by NLO pQCD calculation, after corrections are made for the non-perturbative redistribution of energy into and out of the reconstructed jet cone by underlying event and out-of-cone hadronization. Two-to-two hard scattering processes are the dominant contributors and event-by-event measurement of correlations for jet and other probes thus provides sensitivity to the parton kinematics in the collision.

The analysis of 2009 STAR data on polarized proton collisions at $\sqrt{s} = 200\,\text{GeV}$ is in progress. As shown by the analyzed precision for inclusive jet A_{LL} in Figure 3.4, significant advances in precision over 2006 data are expected. Further improvements are expected from future data collection periods at this energy. At the present level of precision, the understanding and control of systematic effects and uncertainties is of paramount importance. Particularly pertinent is the measurement of the relative luminosities for collisions with different spin configurations. This involves continued analysis effort as well as necessary upgrades to the STAR scaler systems and signal routing, described in Chap. 4, and possibly also of the STAR beam-beam counters. Figure 3.5 shows the simulated precision that can be obtained from a $\sqrt{s} = 200\,\text{GeV}$ data set with an integrated luminosity of $50\,\text{pb}^{-1}$ and beam polarizations of 60% for four different topologies of di-jets reconstructed with the STAR Barrel and Endcap Electromagnetic Calorimeters and Time Projection Chamber.

The four di-jet topologies correspond to different regions in the center-of-mass hard-scattering

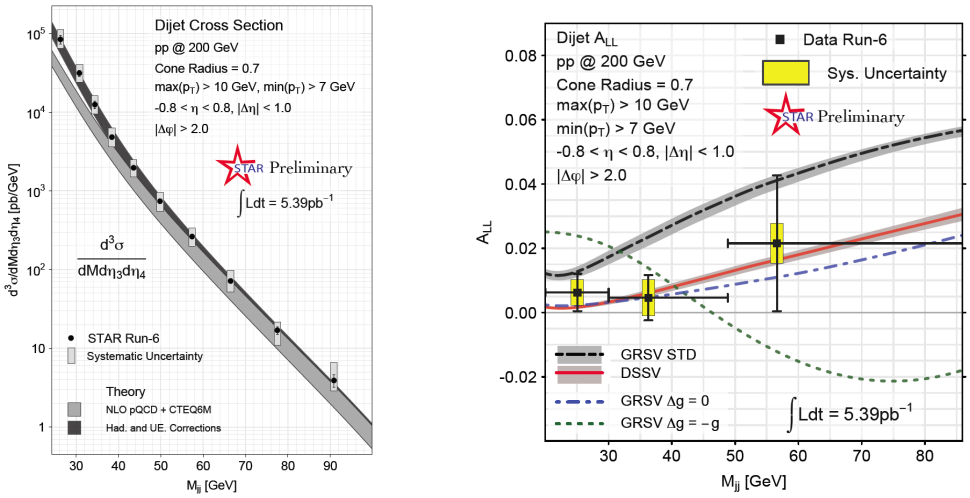

Figure 3.3: Differential cross sections (left) and double-helicity asymmetries (right) for the production of di-jets in $\sqrt{s} = 200\,\text{GeV}$ polarized proton collisions.

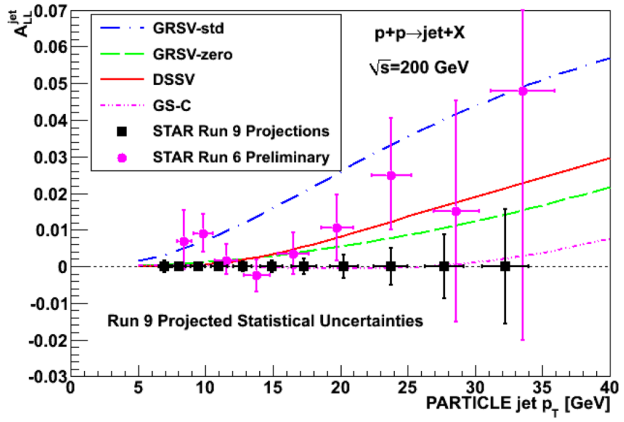

Figure 3.4: Projected precision for inclusive jet A_{LL} from 2009 data at $\sqrt{s} = 200\,\text{GeV}$. The preliminary results on A_{LL} from 2006 data are shown for comparison.

angle and different combinations of Bjorken-(x_1, x_2). Di-jets with opposite pseudorapidities probe equal momentum fractions, $0.12 < x_1 = x_2 < 0.37$. Backward scattering into the Endcap Calorimeter region gives access to the smallest x values, $x > 0.04$. The possible extension of the measurements to a topology with both jets in the acceptance of the Endcap Calorimeter is being investigated. The differences in hard-scattering kinematics and process contributions provide complementary sensitivities, as reflected clearly by the NLO pQCD evaluations of di-jet A_{LL} in Fig. 3.5 for different sets of polarized parton distributions.

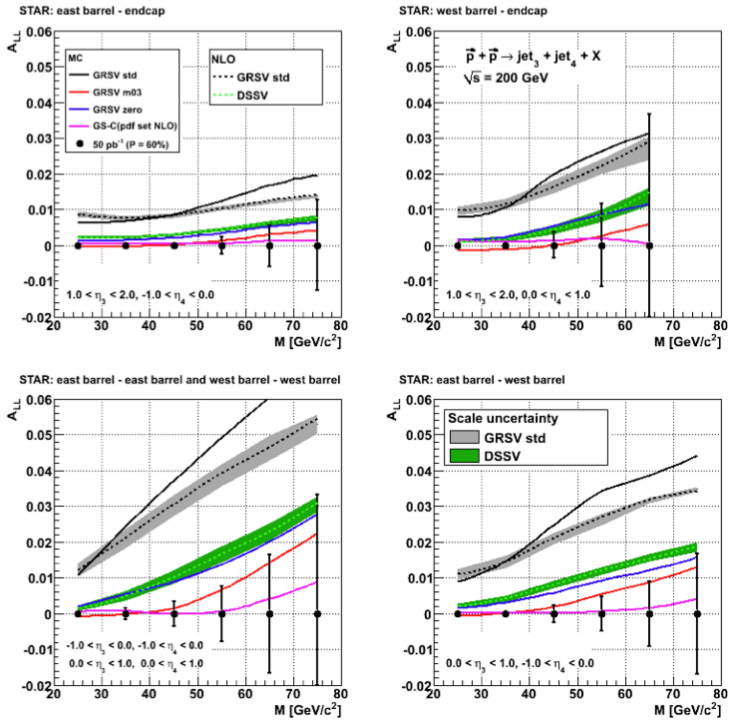

Figure 3.5: Simulated precision for di-jet A_{LL} versus invariant mass of the di-jet pair reconstructed in four combinations of STAR detector subsystem regions for an assumed integrated luminosity of $50\,\mathrm{pb}^{-1}$ with 60% beam polarization at a collision energy of $\sqrt{s} = 200\,\mathrm{GeV}$.

A start of $\sqrt{s} = 500\,\mathrm{GeV}$ polarized proton operations at RHIC was made in 2009. Jet measurements at equal scale, transverse momentum in the case of inclusive jets and invariant mass in the case of di-jets, are anticipated to provide sensitivity to $\Delta g(x)$ at smaller x at $\sqrt{s} = 500\,\mathrm{GeV}$ than at $\sqrt{s} = 200\,\mathrm{GeV}$. The observable asymmetries at $\sqrt{s} = 500\,\mathrm{GeV}$ are anticipated to be typically smaller than at $\sqrt{s} = 200\,\mathrm{GeV}$. Consequently, their measurement is statistically and systematically more challenging. Figure 3.6 compares the kinematic coverage and projected precisions for inclusive jet A_{LL} based on an assumed integrated luminosity of $300\,\mathrm{pb}^{-1}$ and 70% beam polarization at $\sqrt{s} = 500\,\mathrm{GeV}$. Projected sensitivities for di-jet measurements are shown in Fig. 3.7. STAR aims to pursue both measurements at this level of precision concurrently with the W measurements discussed below in Sect. 3.1.2. Their success relies on rapid development of $\sqrt{s} = 500\,\mathrm{GeV}$ collider performance, in particular polarization performance, two to three years of data collection, and advances in the understanding and control of relative luminosities and other systematic effects.

Besides the inclusive jet and di-jet measurements at $\sqrt{s} = 200$ and 500 GeV, STAR is pursuing measurements with other probes, including neutral [190, 191] and charged pions [192]. Of particular interest are event-by-event correlations of photons and jets. The production cross section of this

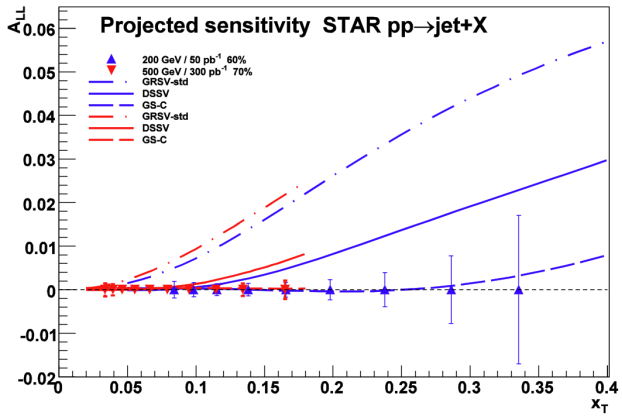

Figure 3.6: Comparison of projected sensitivities and kinematic ranges for inclusive jet A_{LL} vs. x_T ($= 2p_T/\sqrt{s}$) for assumed data samples of 50 pb^{-1} obtained at $\sqrt{s} = 200$ GeV with beam polarization of 60% and of 300 pb^{-1} at $\sqrt{s} = 500$ GeV with beam polarization of 70%.

experimentally challenging channel is dominated by quark-gluon scattering contributions. The event topology with the jet in the Barrel Electromagnetic Calorimeter and the photon in the Endcap ElectroMagnetic Calorimeter makes it possible, with good probability, to correctly correlate the reconstructed event kinematics with Bjorken-x of the hard scattered quark and gluon. This, in turn, makes it possible to pursue a direct leading-order extraction of $\Delta g(x)/g(x)$. Figure 3.8 presents the best current understanding, including simulated experimental efficiencies and purities, of the achievable sensitivity with STAR. These measurements would improve on the precision and extend the kinematic range to smaller x of existing leading-order extractions of $\Delta g(x)/g(x)$ from Deep-Inelastic-Scattering data [193, 194, 195, 196]. Photon+jet measurements would provide process selectivity and important complementarity, compared to the precision afforded by the inclusive jet and di-jet measurements. Continued data taking, beyond the 50 pb^{-1} indicated in Fig. 3.8, at $\sqrt{s} = 200$ GeV is foreseen for heavy quarkonia measurements and would further improve the precision of these measurements.

3.1.2 Quark Polarization

W probes

A second main goal of the proton spin physics program at RHIC [181] and in STAR is to delineate the u and d quark and anti-quark helicity distributions in the polarized proton, using the leptonic decays of W-bosons produced in collisions at $\sqrt{s} = 500$ GeV center-of-mass energy. The leptonic W decay modes are calculable and the mass of the W sets the scale for the measurements. Advanced theoretical frameworks exist to extract the quark helicity distributions from data [197, 189].

STAR has performed an initial measurement of the cross section and single beam-helicity asymmetry A_L in $p + p \rightarrow W^{\pm} + X \rightarrow e^{\pm} + X$, using 2009 data from the first beam operation period

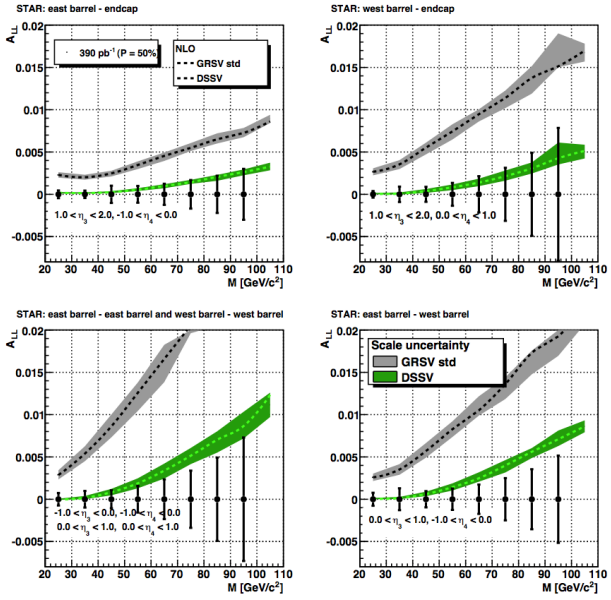

Figure 3.7: Simulated precision for di-jet A_{LL} versus invariant mass of the di-jet pair reconstructed in four combinations of STAR detector subsystem regions for an assumed sampled luminosity of $390\,\mathrm{pb}^{-1}$ with 60% beam polarization at a collision energy of $\sqrt{s} = 500\,\mathrm{GeV}$.

at RHIC with longitudinally polarized proton collisions at $\sqrt{s} = 500\,\mathrm{GeV}$ [198, 199, 200]. The dominant mechanism to produce a $W^{+(-)}$ in these collisions is through $u + \bar{d}$ ($\bar{u} + d$) interactions. The 11% decay branch for $W^{\pm} \rightarrow e^{\pm} + X$ provides a clean experimental signature of reasonably high efficiency. Events from these decays typically contain a highly energetic $e^{\pm}$ that is nearly isolated and an undetected neutrino at opposite direction in azimuth. The $e^{\pm}$ produced in decays of hadrons containing charm or bottom quarks typically have considerably lower energies. These and other QCD background processes, for example the production of di-jets, produce event signatures with balanced energy deposits that can, in many cases, be at least partially reconstructed in the large STAR acceptance afforded by the Barrel and Endcap Electromagnetic Calorimeters. Figure 3.9 shows the transverse energy spectra of the analyzed decay positrons and electrons, and the assessment of backgrounds. Tracking and charge separation is achieved with the Time Projection Chamber, and the initial measurement is at this time thus necessarily limited to mid-rapidity. The results for the asymmetry A_L are shown in Fig. 3.10.

STAR is upgrading its tracking capabilities in the forward acceptance region covered by the Endcap ElectroMagnetic Calorimeter. This acceptance region is essential to gain sensitivity separately to the polarization of quarks and anti-quarks. The addition of a Forward GEM Tracker, consisting of six GEM disks, together with the tracking capabilities of the existing STAR subsystems and a beam-line constraint, will allow charge-sign discrimination for $e^{\pm}$ from W decay. As described in Chap. 4, the Forward GEM Tracker is optimized specifically for this purpose and for

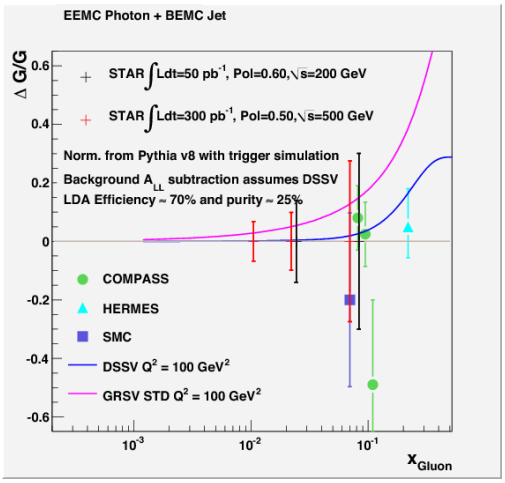

Figure 3.8: Simulated precision and kinematic range of leading-order extractions of $\Delta g(x)/g(x)$ from event-by-event correlation measurements of photons and jets at $\sqrt{s} = 200$ and 500 GeV, compared with similar extractions from polarized deep-inelastic scattering data.

the $\sqrt{s} = 500\,\text{GeV}$ $p+p$ collision environment. This upgrade is foreseen to be available for physics starting in RHIC Run 12.

STAR aims to sample $300\,\text{pb}^{-1}$ with 70% beam polarization following the commissioning of the Forward GEM Tracker in two to three RHIC beam operation periods with $\sqrt{s} = 500\,\text{GeV}$ longitudinally polarized proton collisions. The projected precision of the resulting A_L measurements is shown in Fig. 3.11, together with NLO pQCD evaluations of A_L for several sets of polarized parton distribution functions. The forward measurements, which rely crucially on the Forward GEM Tracker upgrade and on high integrated luminosity and polarization at $\sqrt{s} = 500\,\text{GeV}$, are seen to provide compelling precision. Since the asymmetries A_L are anticipated to be large, in absolute sense, the uncertainty in the measurement of absolute beam polarizations at RHIC is a particularly pertinent source of systematic uncertainty. Requests for further longitudinally polarized proton beam operation at $\sqrt{s} = 500\,\text{GeV}$ beyond $300\ \text{pb}^{-1}$, if any, will depend on the results of the above measurements and their comparison with data from semi-inclusive deep-inelastic scattering measurements.

Increases of the RHIC beam energies have been discussed in the context of a future Electron-Ion Collider, known as eRHIC. Collisions of the proton beams at center of mass energies of $\sqrt{s} = 650\,\text{GeV}$ with 70% beam polarization would offer some attractive electro-weak physics opportunities involving $W^{\pm}$ and Z^0 boson exchange in collisions. Such a 30% increase in the proton beam energy could be realized through either removing or changing the existing DX magnet configuration. Figure 3.12 shows the total $W^{\pm}$ cross section as a function of $\sqrt{s}$ in the range of 100 to 1000 GeV. The NLO calculations are based on the theoretical framework which has recently been published to extract polarized quark and antiquark distribution functions from $W^{\pm}$ production [189]. Also shown are measurements of the $W^{\pm}$ cross section from both RHIC experiments, PHENIX [204] and STAR

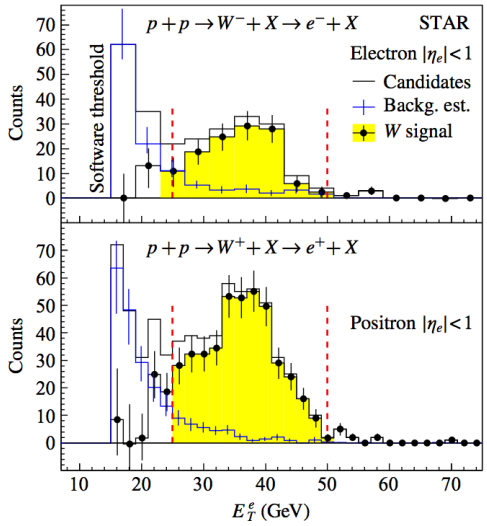

Figure 3.9: Transverse energy spectra for (top) W^- and (bottom) W^+ events showing the candidate histograms in black, the full background estimates in blue, and the decay positron and electron signal distributions in yellow.

[199, 198]. The cross section rises steeply in this energy region. A 30% increase in beam energy from 250 GeV to 325 GeV would provide an increase in the $W^{\pm}$ cross section by approximately a factor of two. This has clearly some appealing aspects for both a polarized and unpolarized program of $W^{\pm}$ and Z^0 boson production in proton-proton collisions as discussed by several authors in the past. It has been pointed out that a program of charm-associated W boson production would clearly benefit from an increase in the polarized proton beam energy to make a program of strange quark polarization at all possible.

In addition to the availability of a 325 GeV polarized proton beam for a future Electron-Ion Collider effort, the usage of a polarized Helium-3 beam has been discussed. The usage of such a uniquely polarized beam to study the spin structure of the neutron in polarized proton-Helium-3 collisions could be carried out prior to an EIC effort. Figure 3.13 shows a comparison of the longitudinal single-spin asymmetry A_L for $W^{\pm}$ boson production in polarized proton-proton collisions at $\sqrt{s} = 500$ GeV (left) and in polarized proton-Helium-3 collisions at 432 GeV (right). Such a program would provide complementary information on the polarization of u and d quarks and antiquarks, as well as on the polarization of gluons in the neutron.

Hyperon spin transfer

The polarization of strange quarks and anti-quarks is remarkably elusive. On the one hand, the spin structure function $g_1(x, Q^2)$ in longitudinally polarized inclusive DIS measurements is found to be smaller than expected. This observation, when combined with measured couplings in hyperon beta decay and the assumption of SU(3) flavor symmetry conservation or modest non-conservation,

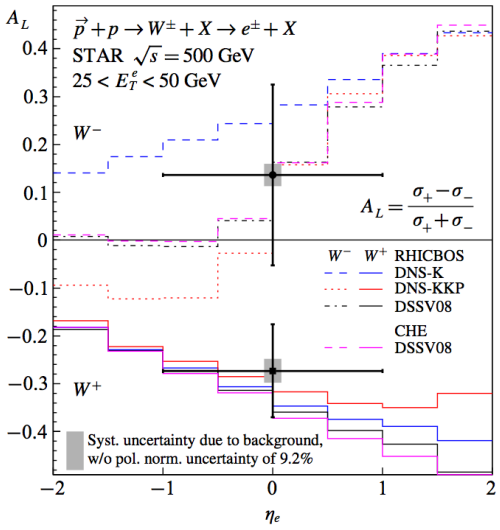

Figure 3.10: Longitudinal single-spin asymemtry, A_L, for $W^{\pm}$ events as a function of the leptonic pseudorapidity, η_e, for lepton transverse momenta, $25 < E_T^e < 50\,\text{GeV}$, together with theory evaluations.

implies that strange quark and anti-quark spins are preferentially aligned opposite to the proton spin. On the other hand, polarized semi-inclusive DIS measurements with identified Kaons in the final state have not confirmed this and, with input from unpolarized fragmentation functions, imply a vanishingly small contribution from strange quarks and anti-quarks to the proton spin [201, 202, 203]. Investigations with complementary techniques are thus called for.

For RHIC, it has been suggested to study the transfer of longitudinal beam spin in the production of hyperons [205]. Such measurements are sensitive to the parton helicity distributions and to polarized fragmentation. Hyperons are rather abundantly produced at RHIC, and their polarization can in many cases be measured from the azimuthal distribution of the decay hadrons. It is expected that the polarization of $\Lambda(\bar{\Lambda})$ hyperons is carried predominatly by strange(anti-strange) quarks [206]. Recent model calculations [207, 208] for Λ and $\bar{\Lambda}$ hyperon D_{LL} indeed show the expected sensitivity to differences in allowed fits of the strange quark and anti-quark distributions to DIS data. In the case of the $\bar{\Lambda}$, this sensitivity is found larger than the sensitivity to polarized fragmentation. Possible contributions from the decays of heavier hyperons could be studied with complementary measurements of, in particular, the Ξ and $\bar{\Xi}$ hyperons [208].

STAR has performed a first proof-of-concept analysis of D_{LL} for mid-rapidity Λ and $\bar{\Lambda}$ hyperons from about $2\,\text{pb}^{-1}$ of data collected at $\sqrt{s} = 200\,\text{GeV}$ in the year 2005 [209]. As shown in Fig. 3.14, the data currently have a precision that is similar to the spread in model expectations. Thus they do not yet discriminate between these models. The analysis of the tenfold larger data sample obtained in 2006 and 2009 is in progress.

The data are a subset of the jet samples collected to determine $\Delta g(x)$ and this mode of data

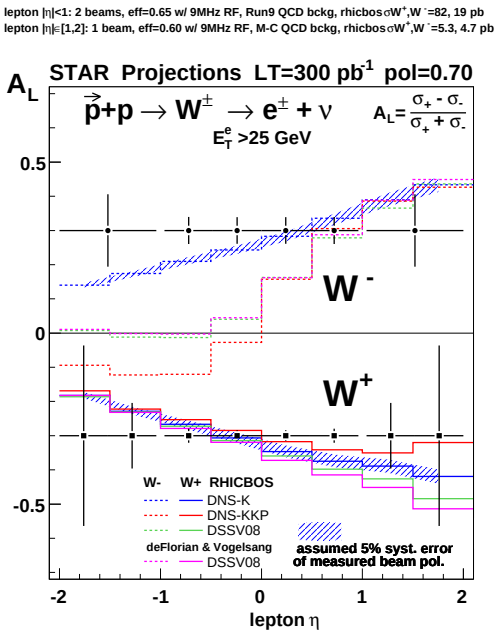

Figure 3.11: Simulated uncertainties of STAR measurements of the single-helicity asymmetries A_L of W bosons for an assumed integrated luminosity of 300 pb^{-1} with 70% beam polarization. The measurements at forward and backward pseudo-rapidity rely on charge-discrimination with the STAR Forward GEM Tracker upgrade.

collection is foreseen also for future hyperon and anti-hyperon measurements in the pseudo-rapidity region of the TPC. At more forward rapidities, it is practical to upgrade STAR with hadronic calorimetry in the form of the Forward Hadron Calorimeter (FHC), described in Chap. 4, that, in combination of the existing FMS, would enable direct triggering on $\Lambda \to n + \pi^0$ and $\bar{\Lambda} \to \bar{n} + \pi^0$ with relatively large transverse momenta. In this case, the π^0 would be measured in the FMS and the (anti-)neutron in FHC. Full simulations have started. Initial results indicate that adequate mass resolution can be achieved to extract $\Lambda + \bar{\Lambda}$ signal and that the FMS+FHC setup provides sufficient angular acceptance to enable hyperon polarization measurements. Model calculations for the forward region [210], reproduced in Fig. 3.15, predict a range of D_{LL} signal at the level of $\mathcal{O}(10^{-2})$ in the FMS+FHC pseudorapidity acceptance. Actual measurement is among the main motivations for the FHC upgrade. Other motivations are described in Sect. 3.2.

3.1.3 Quark Transversity

Transversity, δq, is the remaining leading twist quark distribution needed to characterize proton spin. It is defined, as a function of Bjorken x and Q^2, as the difference in probability of finding quarks with spin orientation parallel versus anti-parallel to the spin of a transversely polarized proton. Transversity is a chiral-odd property of the proton. Its determination thus requires ob-

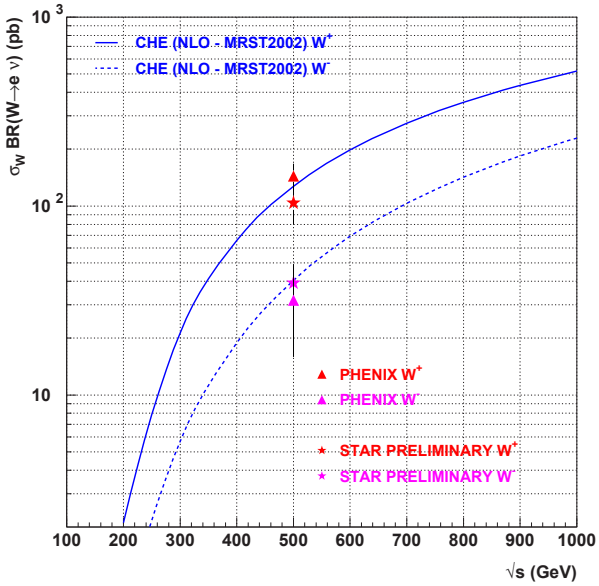

Figure 3.12: Total $W^{\pm}$ cross section as a function of $\sqrt{s}$ in the range of 100 to 1000 GeV.

servations that involve a second chiral-odd quantity, so that chirality is conserved in the hard scattering process.

For this reason, δq has only very recently been accessed in experiment. The most fruitful approach to date has been the measurements of the azimuthal asymmetries of hadrons produced in the semi-inclusive DIS of unpolarized leptons and transversely polarized nucleons. In this case, the observable, known as the Collins asymmetry, is a convolution of the chiral-odd quark transversity distribution in the initial state and a chiral-odd fragmentation function in the final state, known as the Collins fragmentation function. A crucial breakthrough has been made by the independent measurement of the convolution of two Collins fragmentation functions in $e^+e^- \to h_1h_2X$ unpolarized processes by the Belle Collaboration at the KEK B-factory [211]. This has made it possible to extract δq from data [212], rather than rely on positivity constraints [213].

Traditionally, the suggested observations at RHIC have been the measurements of double transverse beam spin asymmetries A_{TT} in the production of Drell-Yan lepton pairs ($p^\uparrow p^\uparrow \to ll$), inclusive jets ($p^\uparrow p^\uparrow \to$ jet(s)), and photon jet pairs ($p^\uparrow p^\uparrow \to$ photon + jet). Scattering contributions from gluons cause significant dilution and the expected A_{TT} at RHIC, using modern extractions of transversity distributions, are too small to be measured in practice. For example, at a center-of-mass energy of $\sqrt{s} = 500\,\text{GeV}$, A_{TT} is anticipated to be $\mathcal{O}(10^{-4})$ for inclusive jets with transverse momenta $p_T = 30\,\text{GeV}$ produced at mid-central rapidity and the statistical precision of its measurement is $\mathcal{O}(10^{-3})$, an order of magnitude larger, for 50% beam polarization and an integrated luminosity of $100\,\text{pb}^{-1}$. A similar conclusion is reached at $\sqrt{s} = 200\,\text{GeV}$ for realistic luminosities and polarizations. Estimates for $\sqrt{s} = 62\,\text{GeV}$, taking into account realistic trigger efficiencies and

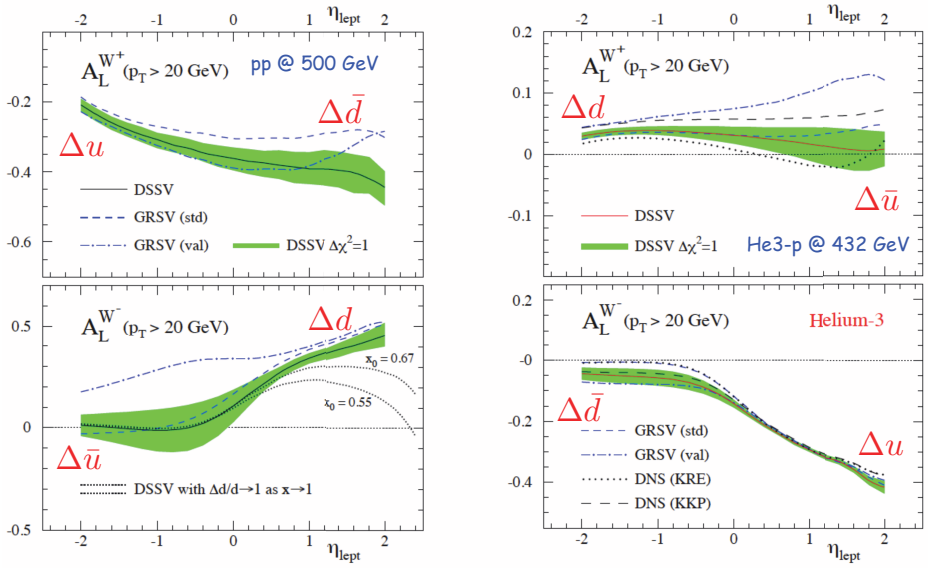

Figure 3.13: Comparison of the longitudinal single-spin asymmetry A_L for $W^{\pm}$ boson production in polarized proton-proton collisions at $\sqrt{s} = 500\,\text{GeV}$ (left) and in polarized proton-Helium-3 collisions at 432 GeV (right).

other factors in the measurements, have not currently been made.

More recently, it was noted that the Collins fragmentation function could provide the necessary second chiral-odd quantity needed to observe δq in single transversely polarized p+p scattering at RHIC through observation of the spin asymmetry in the azimuthal distribution of hadrons inside jets [214, 215]. The Collins fragmentation function, $\Delta D(z, k_\perp)$, represents the correlation between the transverse spin of the scattered quark and the transverse momentum of the fragmentation hadrons with respect to the momentum of the scattered quark (the jet axis). It is thus a correlation involving only the final state. The measurement requires observation of hadrons inside fully reconstructed jets to decouple any possible contributions from spin momentum correlations in the initial state, such as the Sivers effect (discussed below, in Sect. 3.2). A measurement of this type would be advantageous compared to measurements of A_{TT}, in view of the large values of $\Delta D(z, k_\perp)$ obtained from BELLE.

STAR has launched such an analysis, as a proof-of-concept, from about $1\,\text{pb}^{-1}$ of data collected with transversely polarized proton collisions at $\sqrt{s} = 200\,\text{GeV}$ in the year 2006. The measurement is based on STAR's jet reconstruction capability at mid-rapidity. The statistical precision from this initial data set is anticipated to be the limiting uncertainty and to be $\mathcal{O}(10^{-2})$ for an average quark momentum fraction $\langle x \rangle \simeq 0.2$ in each of four intervals for the hadron-jet momentum fraction z in the range $0.1 < z < 0.6$. This is to be compared with predicted asymmetries for charged pions at the level of $\mathcal{O}(10^{-3})$. Measurements with compelling precision would not benefit from currently foreseen new capabilities to trigger on leading charged pions, but would foremost require continued

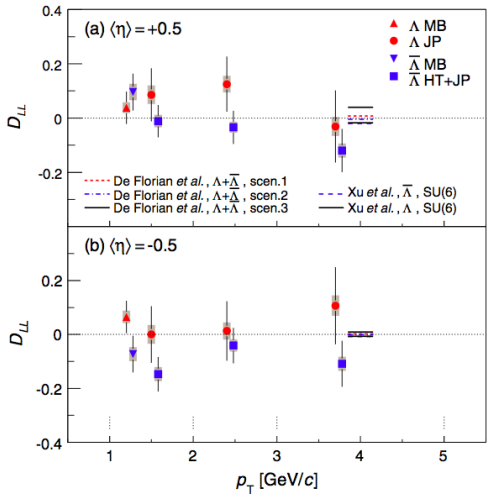

Figure 3.14: Spin transfer D_{LL} to Λ and $\bar{\Lambda}$ hyperons produced in polarized proton-proton collisions at $\sqrt{s} = 200\,\text{GeV}$ for (a) positive and (b) negative pseudorapidities, η, with respect to the polarized proton beam versus hyperon transverse momentum p_T. The data were obtained in 2005 and correspond to an integrated luminosity of about $2\,\text{pb}^{-1}$. The vertical bars and bands indicate the sizes of the statistical and systematic uncertainties, respectively. The dotted vertical lines indicate the p_T intervals of in the analysis of triggered data. The horizontal lines show model predictions evaluated at η and largest p_T of the data.

and significant operation with transversely polarized beams at $\sqrt{s} = 200$ GeV.

Asymmetries with substantially larger size have been observed in the forward region of STAR in collisions with transversely polarized proton beams. These asymmetries are sensitive to transversity in the proton, but potentially sizable contributions from other spin effects currently preclude quantitative determination of δq from these data. We thus defer their discussion to Sect. 3.2 below.

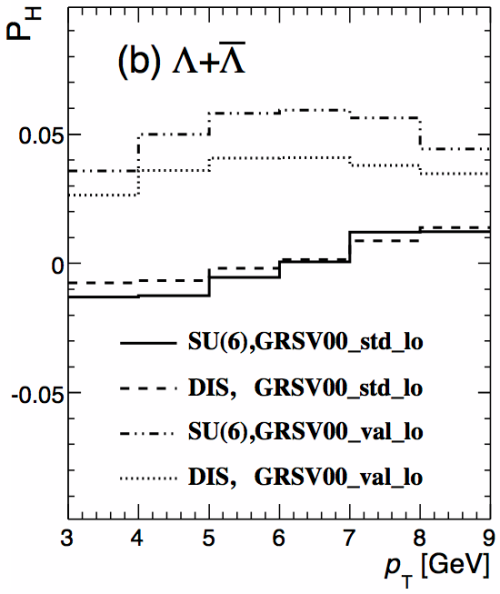

Figure 3.15: Model calculations of the longitudinal spin transfer D_{LL} for inclusive $\Lambda + \bar{\Lambda}$ at forward pseudorapidities in the range $2.5 < \eta < 3.5$ produced in $\vec{p} + p$ collisions at $\sqrt{s} = 500\,\text{GeV}$ versus transverse momentum. Reproduced from Ref. [210].

3.2 How do we go beyond leading twist and collinear factorization in perturbative QCD?

3.2.1 Transverse spin asymmetries

The traditional framework with which we visualize the quark and gluon nature of the nucleon is based upon perturbative QCD (pQCD) with collinear factorization. Within that framework, a relativistic nucleon is represented as a collection of partons that share the nucleon longitudinal momentum. Universal parton momentum distributions are introduced, but there is no attempt to account for parton transverse momentum. A large class of hard scattering observables can be numerically evaluated by folding these universal parton distributions with the standard pQCD interactions among the constituent partons. Factorization, the ability to calculate cross sections by folding universal parton distributions with hard QCD parton interactions, must be established for various processes on a case by case basis. The class of processes and kinematic regions for which factorization has been proven is large, but far from inclusive. Even for scattering processes where factorization has not been proven, the associated parton constituent interaction picture still serves as the starting point for extensions to new QCD calculational models. Exploring pQCD in the vicinity, near and beyond the established pQCD boundaries is an important goal for STAR.

For many years, it was believed that pQCD required transverse single-spin asymmetries to be vanishingly small [216]. Nonetheless, the E704 collaboration at Fermilab measured the transverse single-spin asymmetries for pion production in p+p collisions at $\sqrt{s} = 20$ GeV, and found them to be very large in the forward region [217]. Several different mechanisms were proposed to explain the E704, and similar lower energy, results. However, a question remained whether or not pQCD is the appropriate framework to discuss the asymmetries because the cross section for pion production was found to be much larger than expected by pQCD in the large-x_F region where the transverse single-spin asymmetries are large [218].

The first published spin physics result from RHIC was the STAR observation that the large transverse single-spin asymmetry, A_N, for inclusive π^0 production at large x_F persists to the ten-fold higher RHIC collision energy of $\sqrt{s} = 200$ GeV [219]. Furthermore, in contrast to lower energies, collinear, next-to-leading-order (NLO) pQCD calculations provide a reasonable description of the STAR spin-averaged differential production cross section [220], as shown in Fig. 3.16. An important conclusion is that the basic framework used to describe the process, a picture involving the hard scattering of a leading parton that fragments into a meson, is appropriate at RHIC energies.

Since the initial STAR results were reported, the existence of large transverse single-spin asymmetries at RHIC has been confirmed and amplified through further measurements by BRAHMS, PHENIX, and STAR. In parallel, sizable transverse spin effects have been established in semi-inclusive deep-inelastic scattering (SIDIS) measurements by HERMES and COMPASS. It is now generally accepted that one must go beyond a leading twist, collinear framework to describe the large asymmetries observed in forward transverse single-spin measurements. There is now a major theoretical thrust to explore the ways that collinear pQCD can be enriched and extended to include phenomena that would more naturally explain these effects. In a real sense, this has opened a new frontier in the study of QCD within the nucleon.

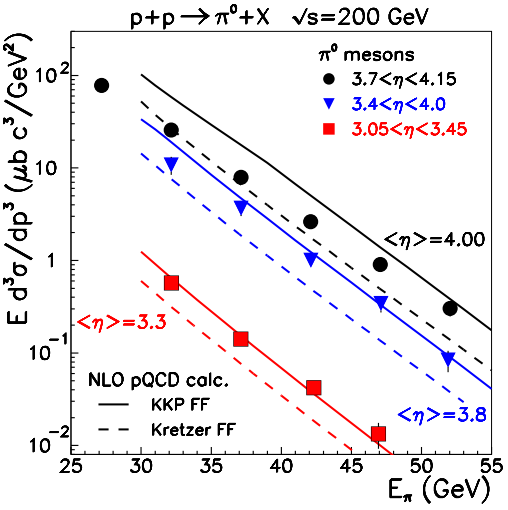

Figure 3.16: Cross section for inclusive π^0 production at forward rapidity in p+p collisions at $\sqrt{s}$ = 200 GeV versus π^0 energy. STAR measurements are compared to NLO pQCD calculations for two separate fragmentation functions [220].

3.2.2 Sivers and Collins effects

Various extensions of the collinear NLO pQCD framework are able to reproduce the large scale of measured values for A_N. Well-known extensions are the "Sivers effect" [221] and the "Collins effect" [222]. Both mechanisms introduce long-range, non-perturbative transverse momentum dependent objects to avoid the pQCD limit [216] on the magnitude of transverse single-spin asymmetries. The Sivers effect is an initial-state effect where spin-correlated transverse momentum dependent parton distributions within the proton lead to large A_N. The Collins effect is a final-state effect where quark transversity combines with spin-correlated transverse momentum dependent fragmentation functions to produce sizable A_N.

In the Sivers effect, the transverse momentum scale typically is assumed to be the same order as the intrinsic k_T of the partons within the proton. In the Collins effect, the transverse momentum scale is assumed to be the same order as the transverse broadening observed in jet fragmentation. These scales are comparable to $\Lambda_{\rm QCD}$. Thus, both the Sivers and Collins effects require a second hard scale for pQCD to be valid, making them formally two-scale phenomena. The large size of the measured values for A_N has also been reproduced in collinear, but higher twist, calculations. Twist-3 quark-gluon correlators have been identified [223, 224] that are closely related to the Sivers and Collins effects. They only involve a single hard scale. Two scales, Q^2 and p_T, occur naturally in SIDIS, where typically $p_T^2 << Q^2$. Two scales, one hard and one soft, also arise naturally in p+p scattering, when both of the outgoing jets in a di-jet event are observed [225]. In contrast, the twist-3 approach is perhaps a more natural way to describe inclusive single hadron production at RHIC, where the p_T of the outgoing hadron provides the scale, but only when that p_T is sufficiently large. However, the two approaches have been shown to be equivalent in the intermediate p_T region

where they are both valid [226, 227].

The STAR results for the x_F dependence of A_N for forward π^0s [228] can be described successfully using either approach, as shown in Fig. 3.17. While each of these pQCD models enjoyed success in describing the x_F dependence of the data, their p_T dependence is at variance with the data as shown in Fig. 3.18. The even larger forward A_N observed in the mass region of the η meson (Fig. 3.17) presents a non-trivial challenge to theoretical models. No evidence has been found for non-zero A_N at mid-rapidity at RHIC [229].

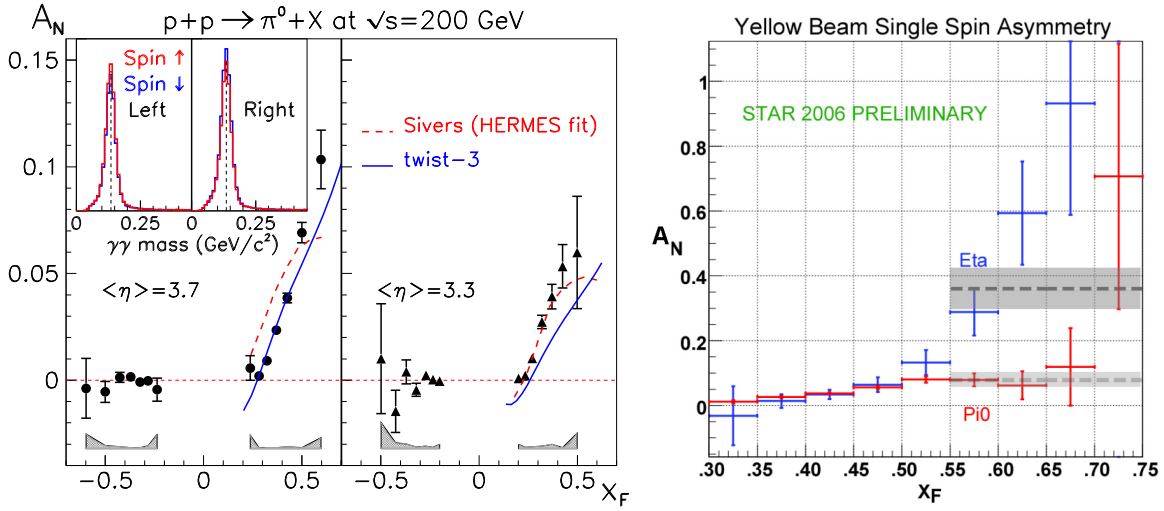

Figure 3.17: Left: Feynman-x (x_F) dependence of neutral pion A_N at fixed pseudo-rapidity [228]. Right: x_F dependence of A_N for η meson.

In the Sivers effect, the transverse spin of the proton is correlated with transverse orbital angular momentum of partons. Processes can be sensitive to these orbiting partons, exposing initial state orbital transverse parton motion (k_T) within the polarized proton. The most important idea in the Sivers effect is that the contributing part of the proton initial state parton distribution can have a bias in k_T, which is correlated with the spin of the proton.

For the Sivers effect to work, some absorption of the leading parton in field of the partner proton is required. This absorption breaks the symmetry nominally expected with orbits in a transverse plane, by emphasizing amplitudes associated with some k_T and suppressing amplitudes that would balance those k_T's. Critics of the Sivers model had argued that this symmetry, sometimes loosely referred to as a time reversal symmetry (T), was not broken in leading order or leading twist pQCD. This would have suggested that the Sivers effect could not have been an important source of single-spin asymmetries. Those questions have now been satisfactorily resolved [230, 231], and the Sivers approach is widely used in theoretical calculations.

To be non-zero, the Sivers effect requires a non-trivial phase. In modern QCD calculations, this phase is provided by the link that is required to preserve overall color neutrality and gauge invariance. This makes the Sivers function a highly non-trivial object, and places the Sivers model

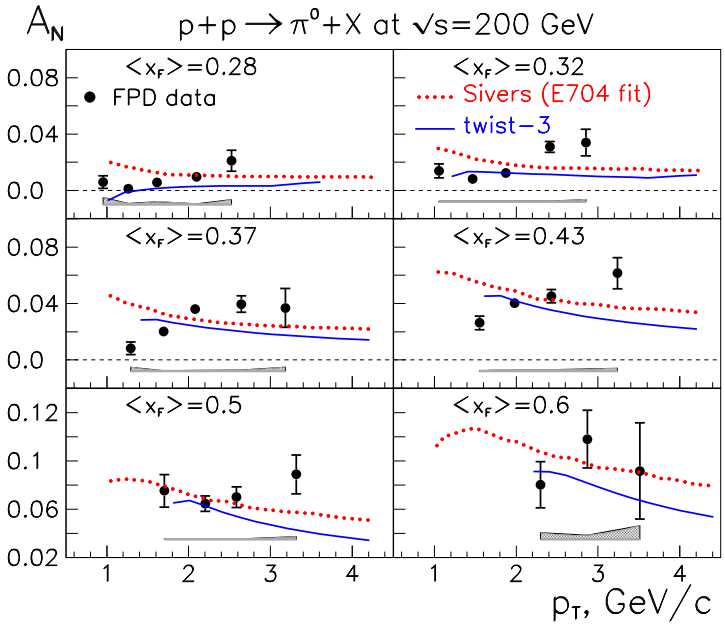

Figure 3.18: Transverse momentum dependence of neutral pion A_N at fixed x_F [228].

squarely at the boundary between between the regime of conventional pQCD application and regimes where more exotic QCD phenomena begin to dominate. The gauge link enters different calculations with different signs, so the Sivers function does not obey factorization in the conventional, naive form. Rather, for some processes, it appears with one sign; for other processes, the sign is opposite [231]. And in some processes, the color factors end up "entangled", leading to an ambiguous result in current calculations [232]. Theoretical studies of applicability or modifications of factorization will likely evolve in the next decade. An extensive set of measurements of forward transverse single spin asymmetries will be an important STAR contribution for input to these evolving QCD models.

The Sivers asymmetry is a "jet" asymmetry. If more of the jet fragments (more of the jet momentum) are observed, then the p_T spin dependence should grow, and it is expected that the asymmetry would increase. Within the Sivers model, a jet fragmenting to a single π^0 of energy 60 GeV should have the same asymmetry as the jet fragmenting to a pair of π^0s, each with 30 GeV. When two final state jets are observed, the combined p_T of the pair of jets would also show a spin-dependent p_T bias [225]. The asymmetry itself is caused by a proton spin dependent transverse momentum shift in an environment where the proton cross section is falling rapidly with p_T. The asymmetry can be understood by folding a proton spin dependent shift in p_T with a rapidly falling cross section. The observed A_N is proportional to both the average initial state transverse momentum $\langle k_T \rangle$ and the derivative of the cross section with respect to p_T. Because a surprising p_T dependence of A_N has been observed, precise measurements of the p_T dependence of

the spin averaged cross sections become very important and will be measured in STAR for each new asymmetry presented.

In the Collins effect, the transverse single spin asymmetry is the result of a dependence in the fragmentation of a quark jet on the transverse spin of the quark. Because the out of scattering plane transverse spin of the parton should be preserved in the hard scattering process, the Collins asymmetry directly reflects the transverse polarization of the parton in a transversely polarized proton, *i.e.* transversity. The Collins fragmentation function has now been measured by the BELLE collaboration and found to be sizable [233]. It is believed to be a universal function [234].

In this picture, there would be no asymmetry associated with the production of jets but only with the production of individual jet fragments. The asymmetry should vanish as we observe more jet fragments and include more of the initial parton momentum on the same side of the beam line as the highest energy pion. The recoil jet would usually come from a soft and unpolarized gluon from the "other" unpolarized proton. There should be no correlated asymmetry associated with the recoil jet or recoil jet fragment in the Collins model.

3.2.3 Planned measurements

Either the Collins or Sivers effects would introduce spin dependent transverse kicks to the observed forward particle or collection of jet fragments. Indeed, the observed asymmetries may arise from a combination of the two effects. It is very important to unravel the various contributions, as each one will tell us important information about the dynamics of the p+p interaction and the structure of the proton. The observed asymmetry for either should be proportional to the derivative of the cross section with respect to p_T at the observed value of p_T and should fall as $\frac{1}{p_T}$ for power law transverse momentum dependent cross sections. The published theoretical calculations with Collins or Sivers effects all predict that the asymmetry should fall with p_T at fixed x_F. The existing STAR results seem to contradict this out to p_T of about 4 GeV/c.

In the next decade, STAR transverse running will clarify this p_T question with measurements of the p_T dependence of the cross sections and the asymmetries with much greater precision, to much higher p_T. The final state cross sections and transverse asymmetries that will be studied in the forward region include the π^0 and η mesons, the single photons, and eventually electron-positron Drell Yan pairs. In each case, the determination of the global nature of the asymmetry by measurements of same side and opposite side correlated particles, or more generally the correlated jet structure of events, will be a major STAR objective.

In the nearest future, STAR will extend the existing asymmetry measurements to $\sqrt{s} = 500$ GeV p+p collisions. At this energy, the p_T reach of the FMS for π^0, η, and jet-like events should suffice to provide a clear indication whether or not the expected $1/p_T$ dependence is seen at high p_T.

An important near-term goal is the measurement of A_N for forward direct photon production in p+p collisions at $\sqrt{s} = 200$ GeV. This process involves no fragmentation, so the Collins effect can make no contribution. The measurement will test predictions that the single photon A_N has the opposite sign relative to the Sivers effect in SIDIS, due to the orderly factorization breaking expected from the analysis of the gauge link term for this particular process. The twist-3 approach makes the same prediction. In the FPD or FMS calorimeters, STAR reconstructs patterns of clusters as

photon candidates. The challenge will be to measure and distinguish single photons from isolated photon-like clusters from decays of π^0s and ηs. A key is the simultaneous measurement of cross sections and asymmetries for π^0s and ηs to fully understand their role as backgrounds for direct photons. Existing measurements indicate that, for 200 GeV p+p collisions, the source of isolated forward clusters of energy 50 GeV is about 50% real isolated photons and about 50% background mesons. We expect the value of A_N in the FMS region to be about 10% for π^0 and perhaps 30%-70% for the η. At 200 GeV, this measurement can be performed with the FMS as it currently exists.

Looking to the second half of the decade, STAR is planning a major upgrade of its forward instrumentation (see Chap. 4). Tracking will provide information about charged hadrons. A RICH will provide the ability to separate charged mesons from protons. Hadronic calorimetry will provide the ability to trigger on jets and energetic charged hadrons, and to reconstruct full jets. Preshower and shower maximum detectors for the FMS will provide e/h and γ/π^0 discrimination. Taken together, this upgrade will enable a broad range of important measurements to explore transverse spin dynamics at RHIC.

The enhanced γ/π^0 discrimination capabilities will extend STAR's ability to measure large-x_F direct photon and π^0 asymmetries to 500 GeV p+p collisions. Full jet reconstruction will aid in separating the Collins and Sivers effects in polarized proton collisions.

BRHAMS has found that the transverse spin asymmetries for forward π^+ and π^- production are opposite in sign and much larger in magnitude than the forward π^0 asymmetries [235]. In contrast, BRAHMS finds that A_N for forward proton production is quite small. The BRAHMS measurements, like the existing STAR measurements, are important first steps. They demand follow-up, including detailed correlation studies, to separate the underlying physics mechanisms. The STAR forward instrumentation upgrade will provide the ability to measure A_N separately for full jets with leading π^+ vs. π^-, facilitating the separation of Sivers effect into u and d quark contributions. In parallel, measurements of di-hadron correlations and the azimuthal asymmetries of π^+ and π^- within their parent jets will determine the contribution from the Collins effect, thereby providing information about quark transversity.

The most challenging measurement planned for the latter part of the decade is the study of Drell-Yan di-electron production. Like direct photon production, the Drell-Yan process does not involve fragmentation, so the Collins effect makes no contribution. The Drell-Yan process naturally contains two scales, the p_T and mass of the di-electron pair. Factorization has been proven for Drell-Yan production, and the color "entanglements" that complicate current calculations of the Sivers effect for hadronic final states are not an issue [232]. As such, the current theoretical framework based on transverse momentum dependent distributions **requires** A_N for Drell-Yan production to be equal in magnitude, but opposite in sign, of that seen in SIDIS [231]. This will provde a crucial test of the non-trivial factorization properties of the Sivers function.

Measurements with transversely polarized ^{3}He would be a very valuable complement to this suite of investigations, by providing direct information about the neutron. Current fits to SIDIS data find the Sivers function to be opposite in sign and larger in magnitude for down quarks than for up quarks [236]. Thus, Sivers effect spin asymmetries are expected to be larger in magnitude for polarized neutrons than for polarized protons [237]. The contribution from n+p scattering is

diluted in ^{3}He+p collisions by the (unpolarized) contribution from p+p collisions. Preliminary estimates indicate that the Roman Pots phase II upgrade (see Chap. 4) will provide significant acceptance for both spectator protons in n+p collisions with (polarized) ^{3}He beams. Once confirmed through detailed simulations, and possibly with further optimization of the detector configuration, this would create a means to tag the polarized neutron scattering events at STAR, which would dramatically enhance the statistical significance of polarized ^{3}He studies.

3.2.4 Spin asymmetries in diffractive phenomena

Large transverse single-spin asymmetries have also been observed in the production of very forward neutrons [238]. Azimuthal asymmetries have since been observed in the STAR Zero Degree Calorimeters (ZDC) [239, 240, 241] and are being used to complement polarimetry of transverse beam spin components at the STAR interaction region with charged particles in the Beam Beam Counters (BBC) [242]. The possible origins of these asymmetries remains to be understood, although the observations in the ZDC in combination with the BBC are qualitatively consistent with diffraction dissociation [243]. To quantitatively advance these correlation studies, it is proposed to equip the acceptance region of the BBC with additional detectors, described in Chap. 4, that provide spatial resolution at the level of 1 mm. This upgrade should also benefit local polarimetry and the determination of the reaction plane in heavy-ion collisions at low $\sqrt{s_{NN}}$.

Spin effects in elastic proton scattering are at the basis of the absolute measurement of beam polarization at RHIC. Roman Pot detectors have made it possible to study proton-proton elastic scattering and its transverse spin dependence at high $\sqrt{s} = 200\,\text{GeV}$ [244, 245, 246]. The analysis of considerably more precise data obtained with STAR in 2009 is in progress. STAR aims to extend these measurements to higher $\sqrt{s} = 500\,\text{GeV}$, either with the existing Roman Pot configuration and about a week of beam-time with dedicated beam-optics settings, or with the proposed Roman Pot upgrade, described in Chap. 4, that would forego the need for dedicated beam-time.

3.3 What is the nature of the initial state in nuclear collisions?

In the study of heavy ion collisions one has to distinguish between *final state* interactions, occurring in the plasma or in the later hadronic phase, and *initial state* interactions responsible for parton production in nucleus-nucleus collisions; this motivated the study of deuteron-gold collisions at RHIC, where the final state interactions are absent and the initial conditions are not wiped out by the evolving system as is the case in nucleus-nucleus collisions.

The d+Au program at RHIC serves a dual role. It is needed to calibrate the A+A measurements for a sounder interpretation. It also has intrinsic merits in the framework of a more profound understanding of QCD including nuclear effects such as shadowing and anti-shadowing and, more importantly, the understanding of higher twists, nonlinear QCD, and gluon saturation. The physics of deuteron-nucleus collisions at high energy has turned out to be very rich in new features when compared to p+p collisions as a baseline, for instance: high-p_T suppression at forward rapidities, Cronin enhancement (also observed at low energy), and the observed centrality dependence of spectra.

These results have been confronted with modern theories such as that of the Color Glass Condensate (CGC), which describes the nuclear wave function at high energy. The CGC extends small coupling QCD calculations to a region where high density effects do not allow one to apply the usual perturbative QCD, the so-called saturation regime that is characterized by a hard scale Q_s, the saturation scale. The understanding of this regime might also help us to shed light on one of the largest unexplained puzzles in heavy-ion physics, the rapid thermalization ($\tau c < 1$ fm) of the initial state created in A+A collisions at RHIC leading to the formation of a quark-gluon plasma. It is generally believed that the instability and consequent exponential growth of intense gluon fields would be the origin of early thermalization[1]. Saturation effects of these gluon fields will affect the early evolution of the system especially at low-x. Their spatial distribution governs the eccentricity of the collision volume in nucleus-nucleus collisions, and this affects our understanding of collective flow and its interpretation profoundly. However, the features of these gluon fields, their momentum and spatial distributions at energies relevant for RHIC, are only vaguely known.

Nuclear initial state effects such as shadowing and anti-shadowing are not well determined so far, but do affect the physics at RHIC even at the highest p_T scales [250]. Nuclear parton distribution functions (nPDFs) are an essential ingredient in understanding the magnitude of the nuclear effects on the factorized hard probe cross sections. While A+A collisions typically are too complex for detailed verification of the nPDF effects on the semi-hard probe cross sections, p+A (d+A) collisions provide a much cleaner environment for their study. p+A collisions can also probe to some extent the impact parameter dependence of nuclear effects.

In the rest of this section we discuss in more detail the two main physics drivers of a future p+A program at RHIC. In Sect. 3.3.3, we formulate the the key questions that will drive the program in the upcoming years. In Sect. 3.3.4, we present the measurements that will be needed to answer these questions and describe the upgrades to the STAR experiment that will be required to conduct these studies.

[1]The evolving picture of thermalization is that of the "Glasma" within the CGC framework [247, 248, 249], a transient stage between the initial CGC state and the thermalized plasma state.

3.3.1 Saturation and the Color Glass Condensate

A remarkable property of strongly interacting particles is that the small x part of their wave function is dominated by gluons. Since x is the ratio of the energy of a parton to that of the hadron in the reference frame where the hadron is fast moving, the smallest values of x are probed at the highest energies. It is this gluon-rich part of the hadron wave function that controls the high energy limit of QCD. The distribution of gluons as a function of x at $Q^2 = 10$ GeV^2 is shown in Fig. 3.19 for the proton. For $x < 0.01$ the proton wave function is predominantly gluonic. However, in sharp contrast to the proton, the gluonic structure of nuclei is not known for $x < 0.01$.

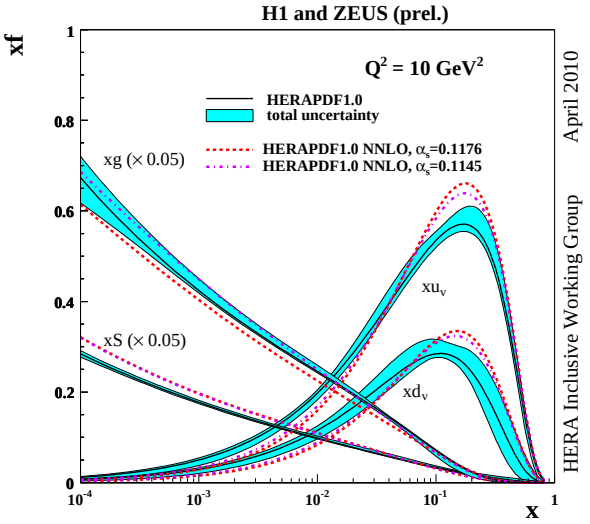

Figure 3.19: Parton distribution functions at the scale of $Q^2 = 10$ GeV^2 from a NNLO QCD fit analysis of the combined H1 and ZEUS measurement of the inclusive ep scattering cross-sections at HERA [251]. Note that the gluon distribution is scaled down by a factor 20.

Because the size of a proton grows at most like $\ln^2(E/E_0)$ at high energies, and because the gluonic contribution to a hadron is measured to grow much faster, like a power $1/x^\delta$ where $\delta = 0.2 - 0.3$, the gluons must form a high density state. The rapid growth in gluon densities with decreasing x is understood to follow from a self-similar Bremsstrahlung cascade where harder, large x, parent gluons successively shed softer daughter gluons. The coupling evaluated at such a high density scale is therefore weak. Weak coupling does not however mean weak interactions or the applicability of perturbative QCD (pQCD). Coherence amplifies the effects of an intrinsically weak interaction. The intensity of the chromo-electric and chromo-magnetic fields in the strong gluon field regime is of order $\mathcal{O}(1/\alpha_S)$, where the asymptotic freedom of QCD dictates that the fine structure constant $\alpha_S(Q_s^2) \ll 1$. These fields are therefore possibly the strongest fields in nature. Remarkably, the weak coupling suggests that the onset and properties of this regime may be computed systematically in a QCD framework. The high occupation numbers of gluons ensure

that their dynamics are classical and their piling up at a characteristic momentum scale (Q_s^A) is reminiscent of a Bose-Einstein condensate. Dynamical and kinematic considerations have led to a suggestion that the matter in nuclear wave functions at high energies is universal. This high energy density saturated gluonic matter is called the Color Glass Condensate (CGC) [252, 253, 254, 255].

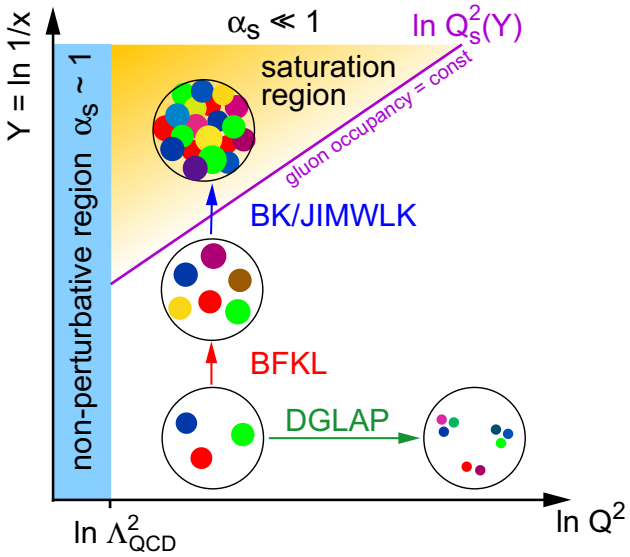

Figure 3.20: Regions of the nuclear wave function in the $\ln 1/x$ versus $\ln Q^2$ plane. The line indicating the saturation regime reflects a line of constant gluon density. It represents not a sharp transition but indicates the approximate onset of saturation phenomena.

Figure 3.20 depicts a schematic view of the regions of the hadronic wave function in the $\ln 1/x$ versus $\ln Q^2$ plane. At large x and at large Q^2, the properties of quarks and gluons are described by the linear evolution equations DGLAP [256, 257, 258] (along Q^2) and BFKL [259, 260] (along x). While these evolution schemes work well at large x and/or large Q^2, they fail to describe the low-x region at moderate Q^2 [261] violating unitarity in the high energy limit; they are a priori not applicable in the non-perturbative very low-Q^2 domain. The non-linear, small-x renormalization group equations, JIMWLK [253, 262, 263, 264] and its mean field realization BK [265, 266], solve these issues by propagating non-linear effects (*e.g.*, recombination into harder gluons) to higher energies, leading to saturation. The onset of saturation and the properties of the saturated phase are characterized by a dynamical scale Q_s^2 which grows with increasing energy (smaller x). The nature of gluon shadowing is terra incognita in QCD at high energies and represents an unique opportunity for RHIC.

The interaction of an external QCD probe with a nuclear target of atomic number A develops over longitudinal distances $l \sim 1/2m_N x$, where m_N is the nucleon mass. When l becomes larger than the nuclear diameter ($\sim A^{1/3}$), or equivalently when $x \ll A^{-1/3}$, the probe cannot distinguish between nucleons located on the front and back of the nucleus. All partons within a transverse area

$1/Q^2$, determined by the momentum transfer Q across the target, participate in the interaction *coherently*. A simple "pocket" formula to compare the saturation scale in heavy nuclei relative to the proton is

$$(Q_s^A)^2 \approx c\, Q_0^2 \left(\frac{A}{x}\right)^{1/3} \tag{3.1}$$

where c is a dimensionless constant. This dependence is supported by various more detailed studies [267, 268] based on saturation models and fits to NMC nuclear data. Therefore, collisions with nuclei probe the same universal physics as seen with protons at x's at least two orders of magnitude lower (or equivalently an order of magnitude larger $\sqrt{s}$). When $Q^2 \gg Q_s^2$, one is in the well understood "linear" regime of QCD. For large nuclei, there is a significant window at small x where $Q_s^2 \gg Q^2 \gg \Lambda^2_{\rm QCD}$ and where one is in the domain of strong non-linear gluon fields. Thus the nucleus is an efficient *amplifier* of the universal physics of high gluon densities.

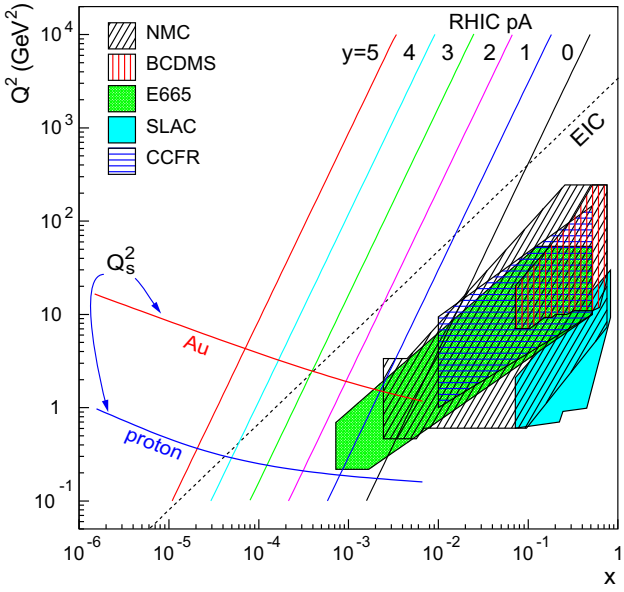

Figure 3.21: Kinematic acceptance in the (Q^2, x) plane for p+A collisions at RHIC. The diagonal lines indicate the acceptance at different rapidities given by $x = (Q/\sqrt{s})e^{-y}$. Also shown is the coverage of past nuclear DIS experiments. The dashed line indicates the kinematic limits of a future EIC. Lines showing the gluon saturation scale Q_s^2 for protons and Au nuclei are superposed on the kinematic acceptance.

The simple scaling of $Q_s^2 \propto (A/x)^{1/3}$ has considerable consequences at RHIC energies, as illustrated in Fig. 3.21. While saturation phenomena are essentially impossible to observe at RHIC energies in p+p collision due the small values of Q_s even at the lowest accessible x, the amplified Q_s scale in p+A collisions opens the experimentally accessible range where saturation effects become detectable. In a $2 \to 2$ process, the relation between rapidity y and transverse mass m_T of the

final partons/particles and their fractional momenta $x_{1,2}$ is $x_{1,2} = \frac{m_T}{\sqrt{s}} e^{\pm y}$. Hence, at mid-rapidity at RHIC, only particle production with very small p_T will be sensitive to the saturation region in parton densities while at the LHC, the region of transverse momenta will be much larger, making it very hard to disentangle initial- from final-state effects even at mid-rapidity. At RHIC, the situation is in general more favorable. We find ourself in the region where saturation effects are largely absent at central rapidities, but become measurable at large forward rapidities. It is this unique situation that allows to study the onset of saturation in a systematic fashion by varying the saturation scale Q_s through varying rapidity and nuclear mass number.

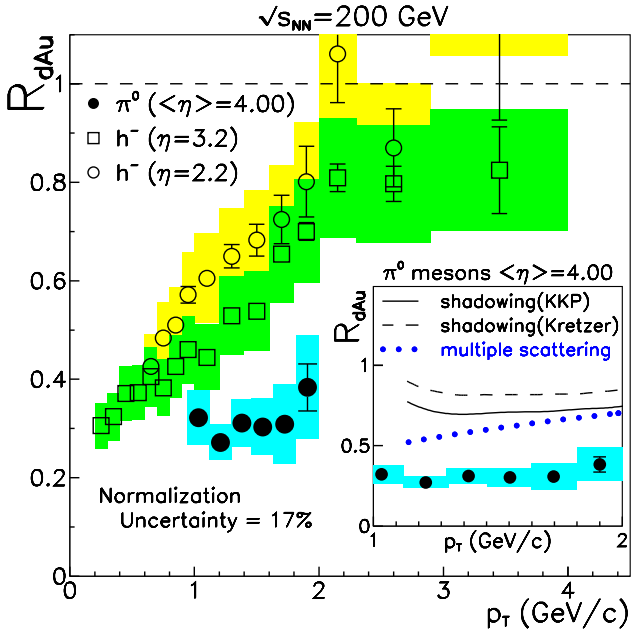

Figure 3.22: Nuclear modification factor (R_{dAu}) versus p_T for minimum bias d+Au collisions. The solid circles are for π^0 mesons measured by STAR [220]. The open circles and boxes are for negative hadrons [269] measured by the BRAHMS experiment. The error bars are statistical, the shaded boxes are point-to-point systematic errors. (Inset) R_{dAu} for π^0 mesons compared with pQCD calculations.

Strong hints for the onset of saturation have indeed been observed at RHIC, initially in studying the rapidity dependence of the nuclear modification factor, R_{dAu}, as a function of p_T for charged hadrons and π^0 mesons, and recently through forward-forward π^0-π^0 correlations.

Figure 3.22 shows R_{dAu} versus p_T for minimum bias d+Au collisions for charged hadrons measured by the BRAHMS experiment [269] and π^0 mesons by STAR [220]. While the inclusive yields of hadrons (π^0 mesons) at $\sqrt{s}$=200 GeV in p+p collisions generally agree with pQCD calculations, in d+Au collisions, the yield per binary collision is suppressed with increasing η, decreasing to ~30% of the p+p yield at $\langle\eta\rangle = 4$, well below shadowing and multiple scattering expectations. The p_T dependence of the d+Au yield is found to be consistent with the gluon saturation picture of

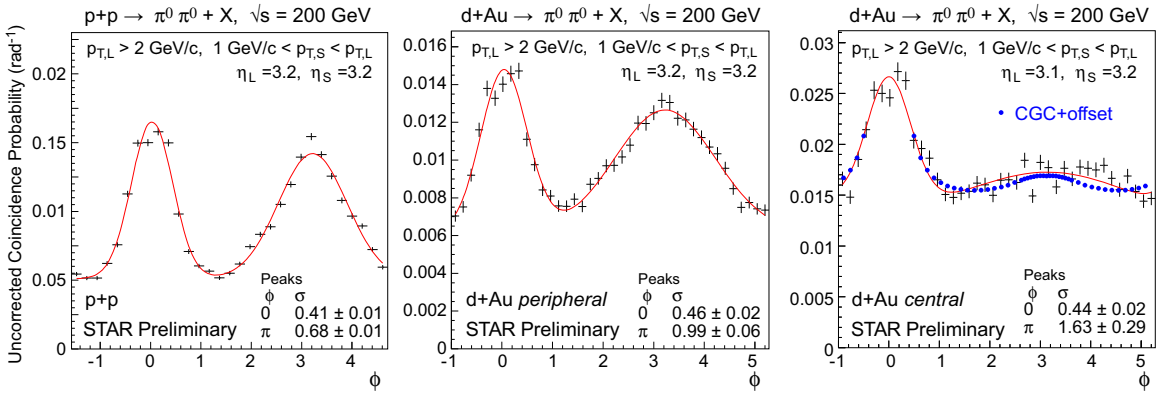

Figure 3.23: Uncorrected coincidence signal versus azimuthal angle difference between two forward neutral pions in p+p collisions (left) compared to peripheral (center) and central d+Au collisions (right) [270]. Data are shown with statistical errors and fit with a constant plus two Gaussian functions (in red). CGC expectations [271, 272] have been superimposed (in blue) on the data for central d+Au collisions.

the Au nucleus (*e.g.* CGC model calculations [273]), although other interpretations, such as the breakdown of factorization at large x_F, cannot be completely ruled out [274].

More powerful than single inclusive measurements are two particle azimuthal correlations. The systematic study of these correlations provides compelling insight into the transitional region between dilute and saturated partonic systems. In pQCD at leading order, particle production in high energy hadronic interactions results from the elastic scattering of two partons ($2 \rightarrow 2$ scattering). The scattered partons fragment to the observed hadrons. Although complexities arise in calculating two-particle correlations using pQCD, $2 \rightarrow 2$ partonic scattering leads to back-to-back jets. When high-p_T hadrons are used as jet surrogates, we expect the azimuthal correlations of hadron pairs to show a peak at $\Delta\phi = 0$ when $\Delta\eta$ between the two particles is smaller than a typical jet size ($R \sim 0.7$), and a peak at π. Transverse momentum effects will broaden these peaks in the azimuthal correlation function. When the gluon density increases, the basic dynamics for the particle production is expected to change. Instead of elastic $2 \rightarrow 2$ scattering, the particle production can proceed by the interaction of a probe parton from the proton (deuteron) beam with multiple gluons from the heavy-ion beam. At sufficiently high gluon densities, the transverse momentum from the fragments of the probing parton may be compensated by several gluons with lower p_T. Two particle azimuthal correlations are expected to show a broadening of the back-to-back peak (loss of correlation: $2 \rightarrow$ many processes) and eventually to disappear. In the CGC framework, the hadronic wave-function is saturated as a consequence of gluon recombination. At very low values of the longitudinal momentum fraction x of the probed gluons the occupation numbers become large and the probe scatters *coherently* off the dense gluon field of the target, which recoils collectively, leading to a modification in $\Delta\phi$.

Figure 3.23 shows the (efficiency uncorrected) probability to find an associated π^0 given a

trigger π^0, both in the forward region covered by STAR's Forward Meson Spectrometer (FMS). Shown is the coincidence signal versus azimuthal angle difference between the two pions in p+p collisions (left) compared to peripheral (center) and central d+Au collisions (right) [270]. The trigger and associated p_T ranges are indicated in the figure. All the distributions present two signal components, surmounting a constant background representing the underlying event contribution (larger in d+Au). The near-side peak represents the contribution from pairs of pions belonging to the same jet. It is not expected to be affected by saturation effects, therefore it is a useful tool to check the effective amount of broadening in the away-side peak. This away-side peak represents the back-to-back contribution to the coincidence probability, which should disappear in going from p+p to d+Au if saturation sets in. The data show that the width of the near-side peak remains nearly unchanged from p+p to d+Au, and particularly from peripheral to central d+Au collisions. Central d+Au collisions show a substantially reduced away side peak that is significantly broadened. Shown in the right plot of Fig. 3.23 is a comparison with theoretical expectations using the CGC framework. The calculation uses a fixed saturation scale Q_s and considers valence quarks in the deuteron scattering off low-x gluons in the nucleus with impact parameter $b = 0$ [271, 272]. This measurement represents the to-date **strongest hint for saturation** phenomena at RHIC and underlines the strength of forward-forward correlation measurements.

3.3.2 Nuclear Effects

The study of hard probes is a vital part of the RHIC program. The understanding of the production of high-p_T partons of any flavor in A+A collisions is mandatory for the interpretation of the final state spectra of hadrons and jets and their interaction with the medium. Other than for bulk matter, hard probes are calculable in perturbative QCD. However, pQCD calculations require the precise knowledge of two non-perturbative ingredients: the fragmentation function and the universal parton distribution function (PDF) of the colliding hadrons. In leading order, the PDF represents the probability of finding a parton of a given flavor with fractional momentum x at a scale Q^2. The PDFs of the proton are reasonably well known in the range of $10^{-4} < x < 0.3$, dominantly constrained by precision data on the $F_2(x, Q^2)$ structure functions from DIS experiments and a rich set of data from hadron colliders (see also Fig. 3.19). As a consequence pQCD calculations in p+p collisions at RHIC energies are quite precise, describing measured jets and meson spectra to within ~10%. Figure 3.24 shows the fractional contribution from gg, qg, and qq scattering processes to π^0 production at mid-rapidity for RHIC (black) and LHC (blue) in p+p collisions [275]. Note, the dominance of gg and qg processes up to $x_T = 2p_T/\sqrt{s} > 0.1$.

The fact that nuclear parton distributions in nuclei are different from the superposition of those of their constituents nucleons is a well known phenomenon since the early seventies. Typically one does not characterize the nuclear PDFs directly, but uses the ratio,

$$R^A(x, Q^2) = \frac{f_i^A(x, Q^2)}{A f_i^{\text{nucleon}}(x, Q^2)}, \qquad f_i = q, \bar{q}, g, \tag{3.2}$$

which can alternatively be expressed as the ratio of the nuclear structure function (F_2 for quarks, and F_L for gluons) per nucleon divided by the nucleon structure function.

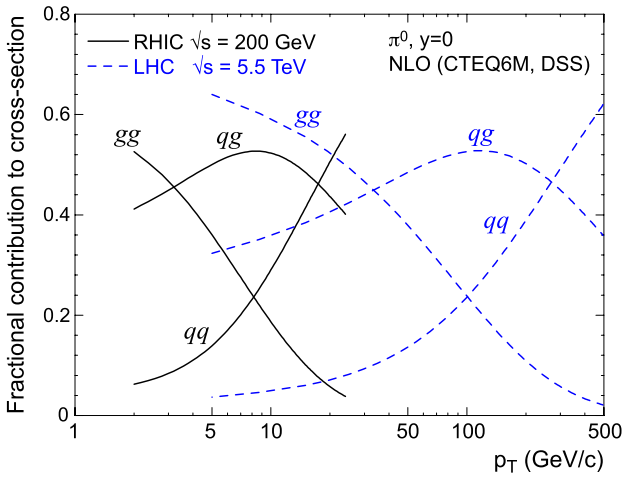

Figure 3.24: Fractional contribution from gg, qg, and qq scattering processes to π^0 production at mid-rapidity for RHIC (black) and LHC (blue) [275].

The behavior of $R^A(x, Q^2)$ as a function of x for a given scale Q^2 is typically divided into four approximate regions: (i) the Fermi motion region with $R^A > 1$ for $x > 0.8$, (ii) the EMC effect region with $R^A < 1$ for $0.25 < x < 0.8$, (iii) the anti-shadowing region with $R^A > 1$ for $0.1 < x < 0.25$, and (iv) the shadowing region with $R^A < 1$ for $x < 0.1$. While the EMC range is only relevant for the highest p_T observable at RHIC, shadowing and anti-shadowing effects can have a profound impact on the parton spectra from the initial scattering processes in A+A collisions.

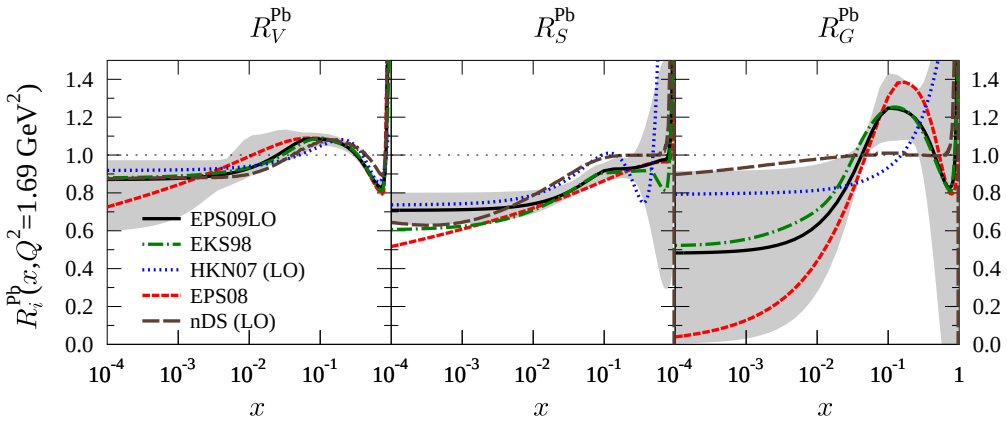

Figure 3.25: The nuclear modifications for the average valence (R_V) and sea quark (R_S), and gluon (R_G) at $Q^2 = 1.69$ GeV^2 for a Pb nucleus from LO global DGLAP analyses EPS09 [276] compared with distributions obtained by other other groups. The thick black lines indicate the best-fit results, the shaded areas depict the uncertainty band.

Figure 3.25 shows a leading-order DGLAP analysis of nuclear parton distribution functions (nPDFs) and their uncertainties from the EPS group [276] compared to other commonly used nPDFs. Nuclear PDFs as the one shown are typically based on data from deep-inelastic scattering experiments off nuclei and Drell-Yan dilepton production in p+A collisions. Recent works (e.g. EPS09) also used inclusive meson production data from d+Au and p+A collisions in order to retain sensitivity to the gluon distributions, providing evidence for shadowing and the EMC-effect in the nuclear gluons. The available experimental data are confined to a limited region of not very low x and small or moderate Q^2, with a strong kinematical correlation between small x and small Q^2. In general the data indicate that shadowing increases with decreasing x, it increases with the mass number of the nucleus, and decreases with increasing Q^2. Unfortunately, the existing data do not allow a determination of the dependence of shadowing on the centrality of the collision.

The differences among the various nPDFs are noticeable, even more when one considers that all approaches have been designed to reproduce available experimental data. Recent analyses put much emphasis in the complex analysis of the various systematic uncertainties as reflected by the gray shaded bands in Fig. 3.26. The large uncertainties in the gluon distributions pose an enormous problem for the interpretation of A+A collisions at RHIC, where the physics is dominantly driven by gluons. At $x \sim 10^{-3}$ the uncertainty in R_G is as large as 100%. Pinning down the nuclear gluon distributions is difficult in the absence of further stringent direct constraints. At $x > 0.2$, no experimental data are currently available, while for $x < 0.02$ no stringent experimental constraints exist yet. In the intermediate region, *i.e.*, around $0.02 < x < 0.2$, data from the NMC collaboration provides the tightest constraint.

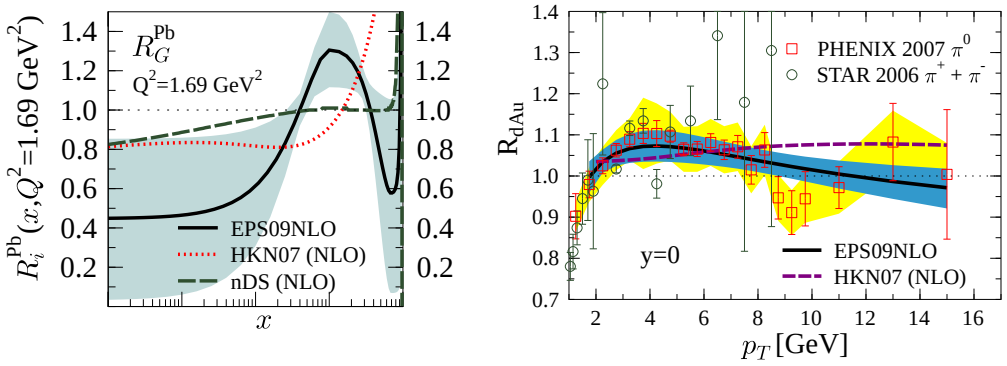

Figure 3.26: Left: The nuclear gluon modifications R_G at $Q^2 = 1.69$ GeV^2 from EPS09 in NLO compared to other common NLO distributions [277]. Right: The computed R_{dAu} for π^0's compared with the PHENIX and STAR data.

The comparison of the nuclear gluon modification R_G from EPS09 in NLO [277] with R_{dAu} measurements by PHENIX and STAR is plotted in Fig. 3.26. Note that the shape of the R_{dAu} spectrum – which in first approximation is a reflection of the similar shape in R_G – gets rather well reproduced. The left plot in Figure 3.26 also presents a comparison of the EPS09 gluon modifications R_G with the earlier NLO analyses that were extracted from the DIS and Drell-Yan

measurements. Consequently, the predictions for pion R_{dAu} differ significantly as is easily seen in the right plot. This provides evidence that more precise RHIC data may eventually discriminate between different proposed gluon modifications.

Hard probes in p+A(d+A) collisions at RHIC can provide us with very important constraints on the nPDFs, especially at scales where the DGLAP evolution is expected still to be applicable, i.e., at $Q > Q_s$. Given the kinematic constraints at RHIC, very forward hadron production measurements (low-x) are not well suited to study leading-twist shadowing since the Q^2 values are substantially too low. Typically nPDFs are calculated at most down to $Q^2 \sim 1.69$ GeV^2. Of special importance at RHIC will be measurements of correlated charm in p+A collisions at mid- or slightly forward rapidities, which will help to pin down the nuclear gluon distributions, while Drell-Yan pairs are expected to set further constraints on the nuclear effects for the sea quark distributions.

3.3.3 Summary of Key Questions

The topics discussed above show that the results and measurements in p+A collisions at RHIC will be critical in providing insight into one of the most urgent questions for our field:

What is the nature of the initial state in nuclear collisions? It is believed that the dense matter created in Au+Au collisions at RHIC evolves from an initial state involving the collision of soft gluon fields of each nucleus rapidly producing a thermalized state. These fields in the relevant region of small x are only vaguely known. Recent experimental measurements at RHIC (see above) indicate that the small-x gluon distribution in large nuclei exhibits saturation effects, a phenomenon that is described within the Color Glass Condensate framework. The detailed knowledge of the gluon density distributions and their dynamics is the source of all theoretical attempts to describe the evolution of the system. Without a deeper knowledge of the initial conditions, the most important fixed point in the theory of relativistic heavy-ion collisions will remain the biggest source of uncertainty.

However, the importance of our knowledge of the initial state reaches beyond the question of thermalization. The spatial distribution of the gluons in the nucleus governs the spatial eccentricity of the overlap region which, together with the observed elliptic flow, tells us to what extent the system approaches ideal hydrodynamics, thus providing a sensitive gauge for the viscosity-over-entropy ratio, η/s, one of the key properties of the sQGP [278, 279].

Hard probes are high energy (high momentum or large mass) probes of the QGP that are produced in the primary partonic collisions at a scale $Q \gg \Lambda_{\rm QCD}$. Such hard probes include the production of heavy quarks, prompt photons, and high-p_T partons observed as jets and high-p_T hadrons. It is well established that the inclusive cross sections of these processes can be computed through collinear factorization, *i.e.*, using short-distance cross sections of parton-parton scatterings and well-defined universal parton distribution functions (PDFs). While the partonic subcross sections and the scale evolution are calculable, the PDFs contain non-perturbative information which must be extracted from the measured cross sections of various hard processes. The state-of-the-art nuclear PDFs suffer from large uncertainties in the gluon density functions in the range relevant at RHIC energies. Further constraints from

p+A measurements are mandatory to improve the gluon PDFs, so that hard probes can be used as benchmark cross sections against which the signals and properties of the QGP can be extracted. Therefore, it is of extreme importance that the applicability of factorization be tested in p+A interactions.

We hence can divide the overarching question of the nature of the initial state into more specific questions, which can be directly related to a concrete p+A program of future measurements. Again, we emphasize that the p+A program at RHIC serves a dual role. It is needed to calibrate the A+A measurements for a sounder interpretation, but it also has intrinsic merits in the framework of a more profound understanding of QCD.

- What is the gluon density $xg(x, Q^2)$ in the x,Q^2 range relevant at RHIC energies?
- What role does saturation of gluon densities play at RHIC?
- What is the saturation scale Q_s at RHIC, and how does it scale with mass number A and x?
- What is the impact parameter dependence of the gluon density distribution?

A strong p+A program with special focus on large rapidity (forward) measurements in future RHIC running will have a significant impact on all of these questions. It will provide crucial input to further our understanding of heavy-ion physics and provide additional input to a better understanding of QCD. However, hadronic collisions also have their limitations. To fully answer all of the above questions with sufficient details will require an Electron-Ion Collider (EIC), a new facility with capabilities well beyond those currently existing.

In general, both p+A and e+A collisions, can provide excellent information on the properties of gluons in the nuclear wave functions. Only DIS, however, allows the direct model-independent determination of the momentum fraction x carried by the struck parton before the scattering and the momentum Q transferred to the parton in the scattering process, and thus a precise mapping of $G(x, Q^2)$. Deeply-inelastic e+A collisions are dominated by one photon exchange; they have a better chance to preserve the properties of partons in the nuclear wave functions because there is no direct color interaction between e and A. The photon could interact with one parton to probe parton distributions, as well as multiple partons coherently to probe multi-parton quantum correlations [280]. On the other hand, many observables in p+A collisions require gluons to contribute at the leading order in partonic scattering. Thus p+A collisions provide more direct information on the response of a nuclear medium to a gluon probe. However, soft color interactions between p and A before the hard collision takes place have the potential to alter the nuclear wave function and destroy the universality of parton properties [281]. The breakdown of factorization has already been observed in comparisons of diffractive final states in e+p collisions at HERA and p+p collisions at the Tevatron [282].

Ultimately it will be the combination of a strong p+A and e+A program, each providing complementary measurements, that will answer the questions raised above in full.

3.3.4 Proposed Measurements

In the following we describe the measurements needed to address the questions raised in the previous section. While some of these measurements can be conducted with the STAR experiment provided the ongoing upgrades are in place, many studies, especially those at large rapidities, will require further upgrading of the STAR detector. Improvements in the forward directions will also be necessary for STAR to participate in the e+p/e+A program should an Electron-Ion Collider at RHIC (eRHIC) become reality. Future upgrades need to be designed with both physics programs in mind. To stay within the scope of this document we limit ourselves to what type of detectors (acceptance, resolution) are needed without going into much detail on their conceptual design.

Measurements Constraining nPDFs

Correlated charm measurements

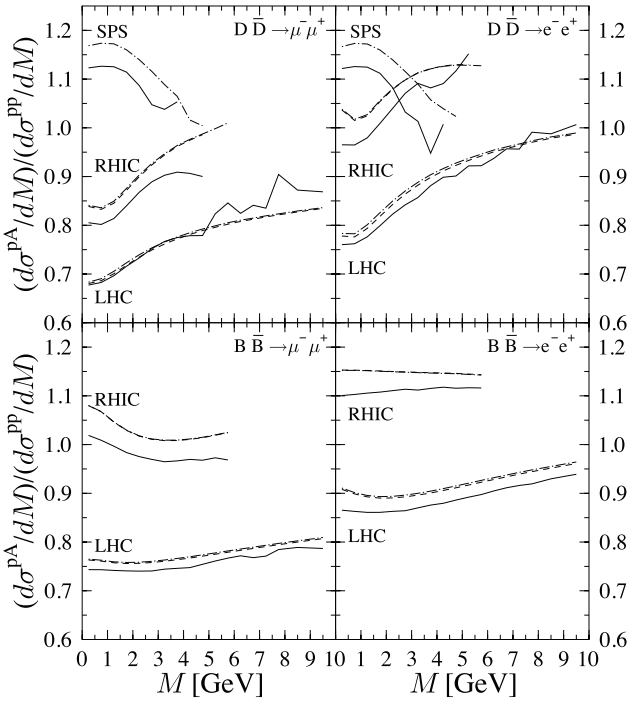

Figure 3.27: The calculated ratio of $e^{\pm}e^{\mp}$ and $\mu^{\pm}\mu^{\mp}$ pair cross-sections from correlated $D\bar{D}$ and $B\bar{B}$ decays in p+A and p+p collisions at SPS, RHIC, and LHC energies. The nuclear gluon distribution $R_g^A(x, Q^2)$ at $\langle x_2 \rangle$ and $\langle Q \rangle$ of each $M_{\ell\ell}$ bin is indicated by the dashed (dotted-dashed) curves. From [283].

Heavy quark production is dominated by gg fusion and is therefore sensitive to the initial gluon

distribution in the colliding hadrons. The ratio of correlated charm mesons ($D\bar{D}$ pairs) in p+A and p+p directly reflects the ratio $R_G^A = f_G^A/f_F^p$ [284, 283], and thus will allow us to provide constraints to the nuclear gluon distributions as depicted in Fig. 3.27 [283]. The average scale $Q^2 = \langle m_T^2 \rangle$ of open charm production is directly correlated with the average fractional momentum $x = x_2$ of the incoming nuclear gluon.

With the HFT, STAR has the capabilities to measure open charm pairs in p+A directly through their hadronic decay channels. Although this channel is the cleanest way to measure charm pairs, these studies are limited to the midrapidity region $|\eta| < 1$ and therefore only probe momentum fractions of $10^{-2} \leq x$. Nevertheless, already this measurement could provide substantial constraints as can be seen from Fig. 3.25 (right). Correlated charm can also be measured through their respective semileptonic decay leptons. When using non-photonic dilepton pairs (ee and also $e\mu$ using the MTD) we can extend our acceptance by using the endcap electro-magnetic calorimeter (EEMC) to $-1 < \eta < 2$. This improves the low-x reach to $4 \cdot 10^{-3} \leq x$. Additional detectors in the forward regions, such as a preshower detector in front of an upgraded FMS, possibly supported by additional tracking and PID, would allow us to measure out to $\eta \sim 2.5 - 3.5$ reaching $1 \cdot 10^{-3} \leq x$. The average values of $\langle Q^2 \rangle$ for the $c\bar{c}$ decay are around $9 < \langle Q^2 \rangle < 140$ GeV^2.

Saturation Physics

Drell-Yan

The Drell-Yan process, $q\bar{q} \rightarrow \gamma^* \rightarrow \ell^+\ell^-$, plays a special role among interactions with hadron beams. In contrast to hadronic final states, in Drell-Yan scattering the values of x_1, x_2, and Q^2 ($= M^2$) can be reconstructed on an event-by-event basis. In addition, factorization has been proven, rather than just assumed, for Drell-Yan di-lepton production. As such, for many years Drell-Yan cross sections have played a key role to constrain sea quark distributions in nucleon and nuclear PDF fits. (For example, see the discussions in [285, 286, 276].)

When measured in the forward direction, Drell-Yan di-lepton production in p+A collisions at RHIC can provide access to sea quark distributions in the nucleus at $x < 0.001$. This is nearly an order of magnitude lower x than the nuclear DIS data, and over an order of magnitude lower x than the Drell-Yan data, that form the primary inputs for EPS09. Furthermore, measurements of the Drell-Yan nuclear dependence at RHIC can also provide significant constraints on the nuclear gluon distribution at very low x via evolution [276]. As such, Drell-Yan measurements at RHIC will provide essentially model-independent information about the nuclear modifications of the gluon distribution well into the x regime where the π^0-π^0 correlation measurements indicate gluon saturation may be important.

STAR will measure forward Drell-Yan production in the e^+e^- channel. The FMS can trigger on the e^+e^- pairs and measure their energy. Significant upgrades are nonetheless essential to facilitate these measurements. The Drell-Yan cross section is very small, which makes control of backgrounds crucial. A suite of upgrades is described in the next chapter that will suppress the combinatorial backgrounds through e/h and charge-sign discrimination, as well as the identification of conversion electron pairs. The primary physics background arises from simultaneous semi-leptonic decays of $b\bar{b}$

pairs. PYTHIA calculations indicate that, in contrast to mid-rapidity, the $b\bar{b}$ background is small compared to the Drell-Yan yield in the region $2.5 < \eta < 4$ observed by the FMS. Isolation cuts can also be used to further suppress both the combinatorial and the physics backgrounds.

Forward J/ψ production will be measured concurrently with Drell-Yan scattering. J/ψ production in these kinematics is dominated by gg fusion, so this will provide complementary information about the gluon density at very low x.

C-AD projects a maximum delivered luminosity of ~ 130 nb^{-1}/week for p+Au collisions [287] in the latter part of the decade when the necessary forward instrumentation upgrades will be in place. This is sufficient to measure the forward Drell-Yan yield in p+A collisions for both a light and a heavy nucleus within a single RHIC running year.

Forward-forward correlations

The analysis of the angular dependence of two-particle correlations in hadronic collisions has proven to be an essential tool for testing the underlying QCD dynamics [288]. In forward-forward correlations facing the $p(d)$ one selects a large-x parton in the $p(d)$ interacting with a low-x parton in the nucleus. For $x < 0.01$ the low-x parton will be back-scattered in the direction of the large-x parton. Due to the abundance of gluons at small x, the backwards-scattered partons are dominantly gluons, while the large-x partons from the $p(d)$ are dominantly quarks. The presence of well pronounced back-to-back azimuthal correlations for high transverse momentum particles in p+p collisions at RHIC can be well understood within the standard leading-twist approach to QCD. Hadron-hadron measurements in d+Au at RHIC at mid-rapidity are consistent with the back-to-back structure seen in p+p, while recent measurements of di-hadron correlations in the deuteron fragmentation region display a strong suppression of the away-side peak. The presence of back-to-back correlations at mid-rapidity and the fact that total particle multiplicities decrease at forward rapidities rule out a final state interpretation of this novel phenomenon. Rather, they suggest an initial state effect. It argues that the broadening of the away-side provides evidence for the presence of saturation effects in RHIC data, and also that the CGC effective theory approximates QCD well in the saturation regime.

We therefore suggest to continue our program measuring forward-forward correlations with improved forward detectors in four channels: (i) h-h, (ii) π^0-π^0, (iii) γ-h, and (iv) γ-π^0 correlations. While the former two have substantially higher cross-sections and lower backgrounds, the latter two are theoretically easier to interpret [289, 290]. Two-hadron production is sensitive to the non-linear JIMWLK evolution equations described by the x evolution of n-point correlators of Wilson lines, which are unknown for $n > 2$ [271]. However, γ-π^0(γ-h) correlations are only sensitive to 2-point functions that are well studied and theoretically under control. Photon-jet correlations in the proton fragmentation region of p+A collisions have also been suggested as a direct probe of the nuclear unintegrated gluon distribution [291].

The study of γ-π^0(γ-h) as well as h-h correlations requires substantial upgrades to the STAR forward region. The unambiguous identification of photons requires improvements to FMS, a hadron calorimeter to allow for efficient isolation cuts to reject fragmentation photons, as well as a pre-shower detector to veto electrons. Hadron identification requires in addition tracking (GEM tracker) and modest PID (RICH) capabilities as detailed in Chapter 4.

The CGC predicts a very distinct mass (A) dependence of the saturation scale $Q_s^2 = c \cdot A^\lambda$. While p+p and d+Au alone provide only the scale exponent λ, measurement at varying A would also allow us to extract the constant, thus providing a full description of the saturation scale. We therefore foresee to conduct the forward-forward measurements in a wide mass range, with suitable candidates being p+O, p+Ca, and p+Cu.

Λ Polarization

A unique way to extract the x-dependence of the saturation scale in p+A collisions is the study of Λ polarization in the forward region where saturation of the gluon density is expected. The process $p(d) \rightarrow \Lambda\uparrow X$ is sensitive to saturation and could help to determine properties of this phenomenon.

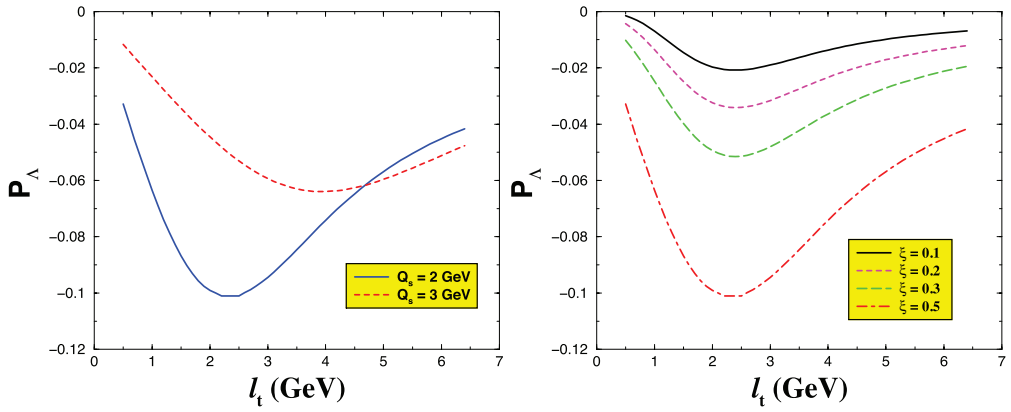

Figure 3.28: Transverse momentum distribution of the transverse polarization. Left: at fixed longitudinal momentum fraction $\xi = 0.5$ and varying target saturation scale, $Q_s = 2$, 3 GeV, respectively. Right: For $Q_s = 2$ GeV and various ξ. From [292].

The cross section of forward hadron production in the (near-)saturation regime is schematically of the form: pdf ⊗ dipole cross section ⊗ fragmentation function [293]. In the case of transversely polarized Λ production, one employs a so-called polarizing fragmentation function, which is an odd function of the transverse momentum of the Λ relative to the fragmenting quark. Due to this k_t-odd nature, the resulting Λ polarization is essentially proportional to the derivative of the quark-nucleus cross section with respect to transverse momentum, which peaks near the saturation momentum scale as depicted in Fig. 3.28.

This challenging measurement can be conducted in the $\Lambda \rightarrow n + \pi^0$ channel, which requires the installation of a hadronic calorimeter behind the FMS, or in the $\Lambda \rightarrow p + \pi^-$ channel, requiring additional tracking (GEM tracker) in the forward region augmented by particle identification capabilities (e.g. RICH) as detailed in Chapter 4.

Baryon Production at large x_F

The picture of baryon stopping deployed at RHIC (*e.g.* [294]) is coming increasingly under scrutiny (see for example [295]). The basic criticism is that a proton is in fact a very loosely bound, "fragile" state that would get destroyed, *i.e.*, the coherence of its valence quarks would be destroyed due to multiple scattering within a time interval shorter than the lifetime of its excited state. Here *multiple scattering* refers to scattering of two or more of the large-x quarks of the proton projectile. Multiple scattering becomes important in the high-energy regime of *coherent* scattering on a dense target. The valence quarks from the projectile scatter coherently from all the small-x gluons in the target, and each of the valence quarks scatters with a probability of order 1.

In other words the argument against proton stopping is that a fast, large-x quark in QCD cannot be stopped, but that the observed shift of baryon number at RHIC arises from shattering the beam proton into pieces, each of which carries only a part of the beam's momentum, and is hence shifted to lower x_F (or y).

In [296] the authors put together a practical calculation, combining these ideas with the CGC framework, based on the idea that the distribution of hadrons near the longitudinal light-cone in central high-energy p+A collisions is computable in weak coupling QCD. This is because, for a dense target, all incident proton constituents scatter and experience a large momentum transfer that is determined by the saturation scale of the target. Thus, the coherence of the projectile is destroyed completely, and the scattered quarks and gluons fragment independently.

The model predicts that the longitudinal distribution of (anti-)baryons and mesons steepens with increasing energy and atomic number of the target, and that the transverse momentum distribution broadens. As a consequence, the proton decays predominantly into a beam of leading mesons, with the baryon number shifted to small light-cone momentum fraction $z < 0.1$. What follows is that the p_T distributions of leading baryons and mesons closely reflect that of the scattered quarks, which is rather flat up to transverse momenta on the order of the square root of the density of gluons per unit area in the dense target.

Figure 3.29 shows the calculation for the resulting spectra. One finds that the transverse momentum distribution at large z flattens as the target density ($\propto Q_s$) increases. At the same time, the longitudinal z-distribution steepens, resulting in larger suppression of forward hadron production. Integrated over k_t, one is left with a convolution of the quark distribution in the proton with the fragmentation function, times the inelastic qA cross-section. This provides an expression for the "limiting curve" of hadron production from QCD in the high-density limit. The existence of such a scaling was confirmed by the PHOBOS collaboration at RHIC [297].

This model can be tested by measuring inclusive hadron production in the forward region of central p+A collisions at RHIC. Here the forward region is again defined as the fragmentation region of the $p(d)$ beam. Due to the baryon suppression, the resulting spectra are steep, making the measurement rather challenging. Candidates for measurements are mostly strange baryons (Λ) or strange hyperons [298]. Hadronic calorimetry would not provide sufficient energy resolution in the case of the neutron. This measurement requires additional tracking and PID capabilities in the forward region, augmented possibly by a dipole magnet between the STAR endcaps and the forward detectors.

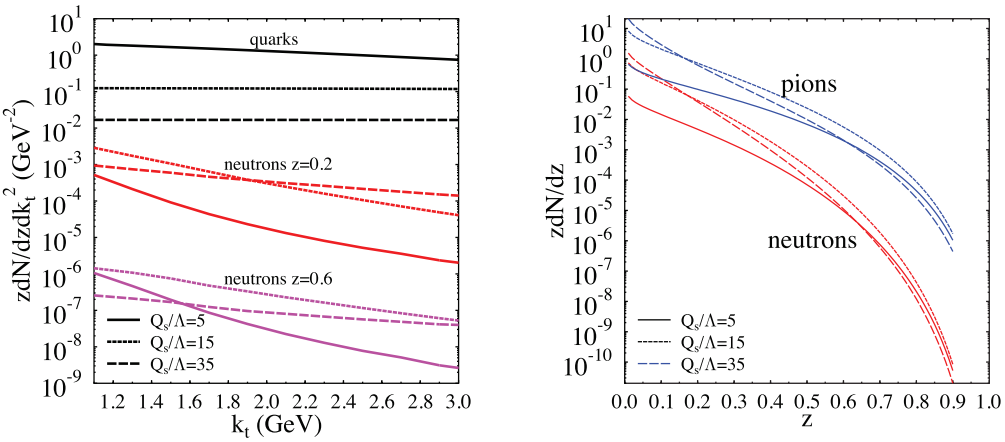

Figure 3.29: Left: Transverse momentum distribution of neutrons from the breakup of an incident proton at various longitudinal momentum fractions z and target saturation momenta Q_s (bottom six curves). The top three curves depict the underlying quark distributions. Right: Longitudinal distributions of n and π^0. From [296].

3.3.5 p+A or d+A?

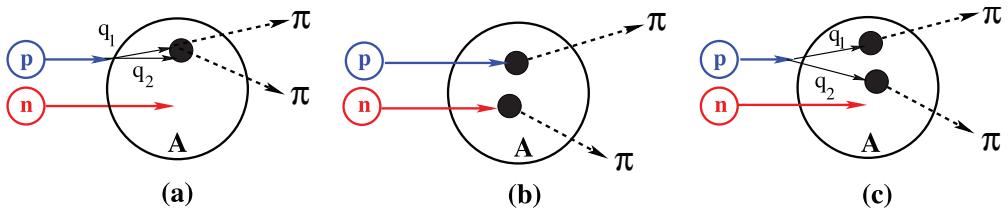

Figure 3.30: Contributions to two-pion production in d+A collisions through the double-interaction mechanism. From [299].

In a recent paper [299], the authors point out that the contributions from double-parton interactions to the cross sections for d+A $\rightarrow \pi^0\pi^0 X$ are not negligible. This mechanism is illustrated in Fig. 3.30. They find that such contributions become important at large forward rapidities, and especially in the the case for d+A scattering. Whether or not this meachnism provides an alternative explanation of the suppression of the away-side peak in π^0-π^0 is not settled. However, this new insight provides a ***strong*** argument for performing the proposed correlation studies in p+A, and not in d+A collisions. p+A collisions will also provide other benefits. They will facilitate cleaner centrality selections than possible in d+A, thus improving studies of the impact parameter dependence of nuclear and saturation effects. The Drell-Yan and photon correlation measurements described above involve an *electromagnetic* interaction of the high-x quark from the p or d, making

the cross sections sensitive to the valence quark charge. The use of proton beams will permit direct yield comparisons, not just between the heavy and light nuclear targets, but also vs. p+p. Furthermore, both the large transverse single-spin asymmetries seen in p+p collisions and the azimuthal de-correlation observed in central p+Au collisions arise from valence quark scattering off low-x gluon fields. Thus, scattering of transversely polarized protons off nuclei might open yet another window to explore the onset of gluon saturation. C-AD indicates that the proton beam in p+A collisions can be polarized [287], so theoretical work in this area would be extremely valuable.

3.4 STAR during the initial implementation of eRHIC

3.4.1 Introduction

Towards the end of the decade, the realization of a high-energy polarized Electron-Ion Collider (EIC) would present a program of physics measurements to advance the understanding of cold nuclear matter and spin in QCD with unprecedented precision. This physics program has been described in Ref. [300], and more recently in Ref. [301]. It is the topic of a recent INT workshop [302].

Recent developments in the conceptual design of an EIC at Brookhaven National Laboratory, eRHIC, envision the addition of an electron ring inside the RHIC tunnel with the possibility to collide the electron beam with one of the existing RHIC beams at STAR, after significant reconfiguration of the existing interaction region. Heavy ion and polarized proton capabilities at STAR would continue to exist, and switching between modes could occur with shutdown periods to allow for IR reconfiguration. Switching within running periods would not be possible. The electron beam would initially have 5 GeV energy and would collide with the existing hadron beams, which may by then be accelerated to modestly higher energies than have currently been achieved. Higher electron energies, up to 30 GeV, could be achieved in subsequent stages through collider upgrades. The luminosities are projected to be at the level of $10^{32}\,\mathrm{cm}^{-2}\mathrm{s}^{-1}$ in $e + A$ collisions and $10^{34}\,\mathrm{cm}^{-2}\mathrm{s}^{-1}$ in $e + p$ collisions.

The STAR collaboration has started to investigate if and how it could make productive use of such collisions. At the time of writing, the considerations are based on deep-inelastic scattering characteristics and fast simulations, rather than on full-fledged physics and detector simulations that will demonstrate capability and quantify impact. The center-of-mass energy of the collisions, even at the lowest electron beam energy, would exceed those achieved in the body of fixed target experiments, but remain below those achieved in unpolarized e+p collisions at HERA. The projected luminosities would present a substantial advance over prior measurements and are projected to be within STAR's capabilities in terms of rate and occupancy.

Figure 3.31 shows the kinematic plane in Bjorken$-x$ and the scale, Q^2, in collisions of 5 GeV electrons with proton or nuclear beams with 100 GeV energy per nucleon. These kinematics can be reconstructed by measuring the scattered electron energy and angle, the current-jet energy and angle, or a combination. STAR's strengths in mid-rapidity acceptance and particle identification capabilities are seen to be relatively well-matched to the initial eRHIC collision energies.

The scattered electron and current-jet angles for collisions with a proton beam at top-energy, as well as for collisions with an electron beam after its energy has been upgraded to 10 GeV, are shown in Fig. 3.32. The opportunities with STAR for the lower eRHIC center-of-mass energy are seen to largely carry over to higher proton energy. The effects of staging to higher electron beam energies underline the importance of dedicated detector development, which in STAR would focus on the forward region opposite the EEMC and FMS.

STAR proposes to reconfigure its Roman Pot system to forego the need for dedicated beam optics and enable concurrent data taking with the central detector in high-luminosity searches for exotics. Further reconfiguration, appropriate for the eRHIC interaction region design, should with good efficiency allow tagging of the spectator protons in scattering with deuteron and polarized ^{3}He beams. Roman Pot instrumentation will, in addition, be of importance to measurements of

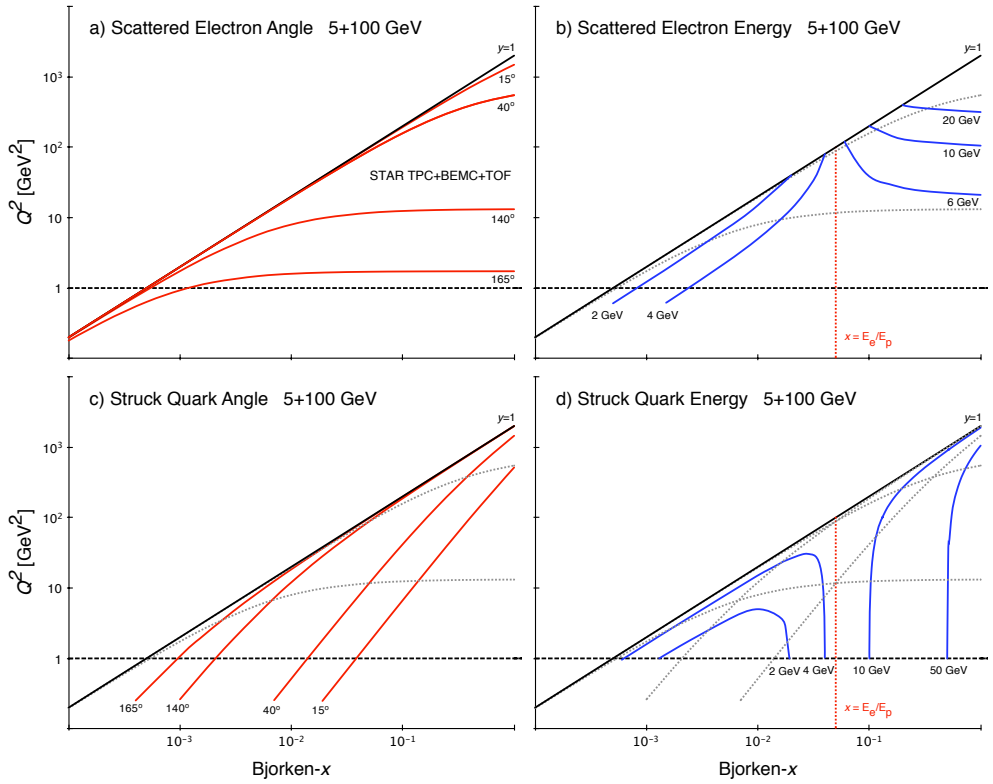

Figure 3.31: The (x, Q^2)-dependence of the laboratory angle and energy of the scattered electron and the struck quark (current jet) in Born-level deep-inelastic scattering of 5 GeV electrons off proton and nuclear beams with an energy of 100 GeV per nucleon. The angles are with respect to the nucleon beam direction. The geometrical acceptance of the existing TPC+BEMC+TOF for scattered electrons, shown in a), is replicated by the dotted grey lines in b), c), and in d), which also contains the acceptance for the struck quark.

diffraction and be essential to deeply-virtual Compton-scattering measurements aimed at nucleon and nuclear tomography.

Figure 3.33 outlines the eSTAR acceptance in Bjorken$-x$ and Q^2 for representative collision energies at eRHIC. The kinematic regions that can be accessed with the future 12 GeV electron beams at Jefferson Laboratory, as well as the kinematic region of the ongoing COMPASS deep-inelastic scattering experiment at CERN, are indicated for comparison. Combined, they cover nearly the entire range of existing polarized deep-inelastic scattering data and the existing data for nuclear targets. Measurements with eSTAR are seen to extend the measurements of the Jefferson Laboratory program to give perturbative access to considerably smaller values of Bjorken-x, where gluons dominate. High luminosities, well in excess of those achieved with the muon beam at COMPASS, are anticipated for the full range of collision energies. The indicated acceptance

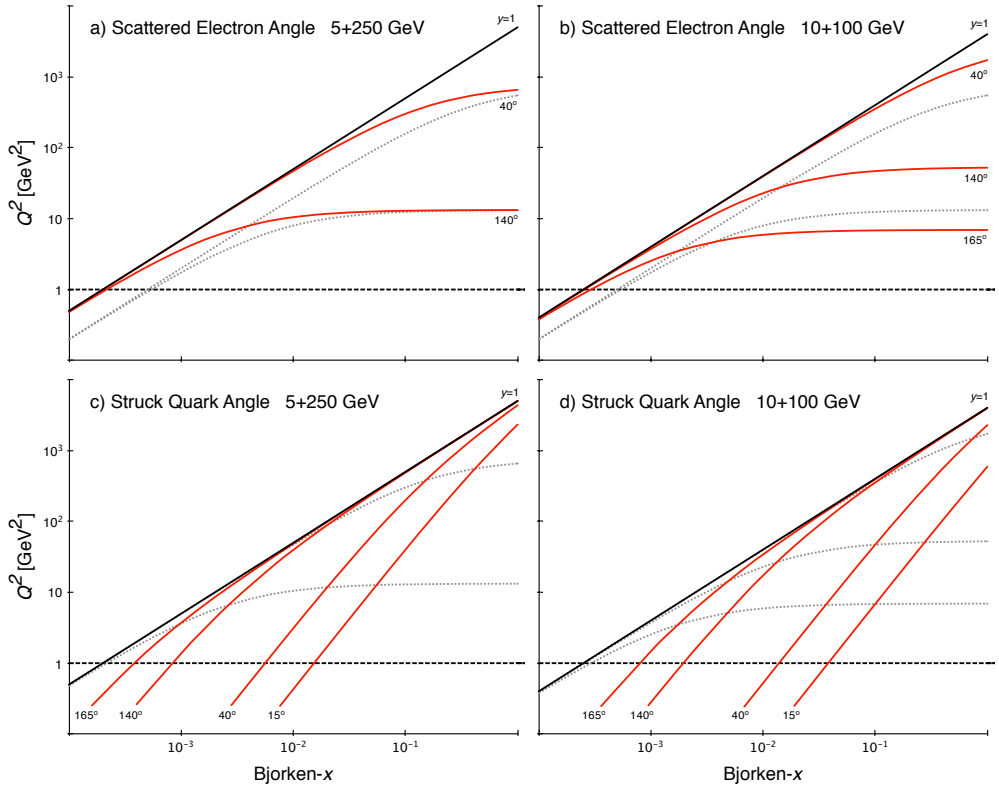

Figure 3.32: The (x, Q^2)-dependence of the laboratory angle of the scattered electron in Born-level deep-inelastic scattering of a) a 5 GeV electron beam off a 250 GeV proton beam and of b) of a 10 GeV electron beam off a nuclear beam with 100 GeV energy per nucleon as red continuous curves. The grey dotted curves replicate the dependences for 5 GeV electron beams (c.f. Fig. 3.31) and are shown for comparison. The corresponding angles of the struck quark are shown in c) and d), respectively. The grey dotted curves replicate the scattered electron acceptance curves at the indicated energies.

at highest collision energies assumes and depends crucially on new instrumentation covering two units in pseudo-rapidity beyond the mid-rapidity coverage offered by the existing Time Projection Chamber, Barrel ElectroMagnetic Calorimeter, and Time-of-Flight subsystems. The detector requirements, in terms of the all-important energy measurement, are quantified in Chap. 4. The detector concept remains to be worked out, although it is likely to combine low-mass tracking and calorimetry. Efficient electron identification capability is obviously of paramount importance. Hadron identification will be highly beneficial to semi-inclusive measurements. STAR's existing and proposed capabilities in the acceptance region of the existing EEMC and FMS calorimeters are optimized for high particle energies and are thus better matched to measurements of the current-jet than to requirements of good energy resolution in the scattered electron measurement to resolve

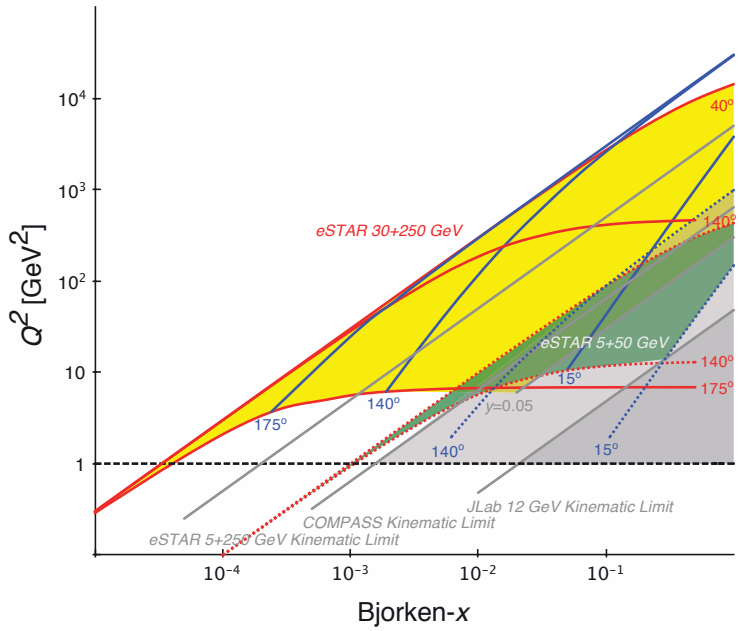

Figure 3.33: The kinematic acceptance of eSTAR for representative beam collision energies of 5 GeV (electron) and 50 GeV (hadron), and 30 GeV (electron) and 250 GeV (protons), as indicated. The kinematic limits of the COMPASS and future 12 GeV Jefferson Laboratory programs are indicated for comparison. The boundaries of electron acceptance are denoted in red, and those for the struck quark (current jet) in blue. The $5 + 50$ GeV acceptance is based on the current STAR acceptance, while the $30 + 250$ GeV assumes upgraded instrumentation over two units in pseudo-rapidity to identify and measure scattered electrons and produced hadrons.

Bjorken-x for this acceptance region. At this time, STAR proposes R&D aimed at a compact new forward arm with electron identification, measurement and trigger capability on the opposite side. This choice of beam directions is compatible with RHIC-CAD and PHENIX preferences.

Significant physics impact is expected, even with the initial 5 GeV electron beam energy at eRHIC, for integrated and unintegrated polarized and nuclear parton distributions, as well as for studies of energy loss in cold nuclear matter. Three important examples of the role eSTAR will play are outlined below. The essential upgrades to make productive use of collisions with this electron energy are focused on luminosity and polarization measurements, and are thus comparatively modest. Physics possibilities may exist also for selected studies of diffraction and tomography. Upgrades of the electron beam energy, which are essential to the definitive study of QCD matter in the regime of extreme gluon density and weak coupling, necessitate a commensurate upgrade of STAR in the forward region that entails significant R&D.

3.4.2 Nuclear parton distributions

Measurements with eSTAR in the initial stage of eRHIC should provide precision data on modification of the nuclear parton distributions over a wide region in Bjorken-x and Q^2. The impact of such data will likely be similar to the role of HERA data on proton structure. Data on the scale-dependence of the inclusive structure functions for different nuclei should reach a coverage and precision that should give meaningful sensitivity to the nuclear quark and gluon distributions. Semi-inclusive measurements should yield additional insights in the quark-flavor dependence. Figure

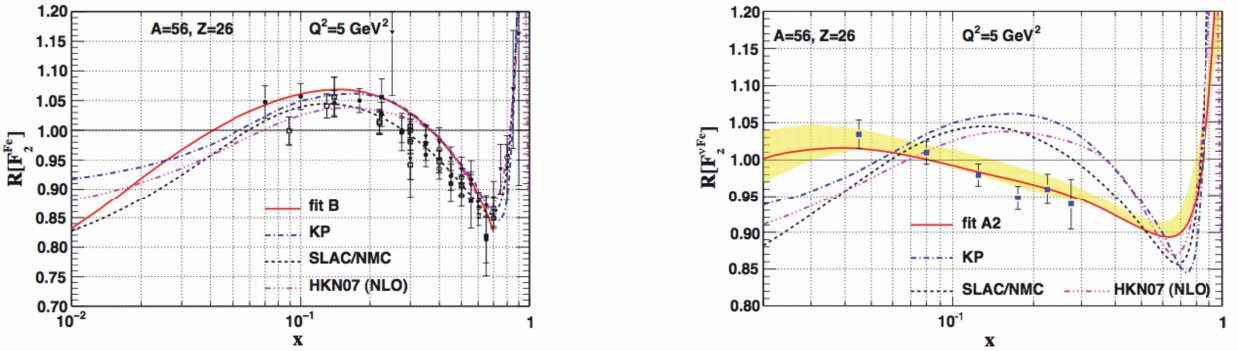

Figure 3.34: The nuclear correction ratio, $F_2^{\rm Fe}/F_2^{\rm D}$, as a function of Bjorken$-x$ for $Q^2 = 5\,{\rm GeV}$ from (a) electron- and muon-nucleus and Drell-Yan scattering data and (b) from neutrino-nucleus scattering data. The charged-lepton data are compared with the SLAC/NMC parametrization, as well as fits from Kulagin-Petti (KP) [305, 306] and Hirai (HKN07) [304] and fit B from Ref. [307]. The neutrino-nucleus data are compared with the same parametrizations and with fit A2 from Ref. [303].

3.34a) shows the nuclear correction ratio, $F_2^{\rm Fe}/F_2^{\rm D}$ in which F_2 denotes the unpolarized inclusive structure function, as a function of Bjorken$-x$ for $Q^2 = 5\,{\rm GeV}$ using lepton-nucleus and Drell-Yan data [307]. Figure 3.34b) shows a subset of recent neutrino-nucleus data from NuTeV [308], which have a qualitatively different behavior [307]. This behavior is not described by the parametrizations based on the charged-lepton data, although "fit A2" in Fig. 3.34 demonstrates that the data can be analyzed and parametrized independently in a very similar framework [303]. Each of the parametrizations has quantified or unquantified uncertainties, and it is thus conceivable that both $l^{\pm}A$ and νA data can be accommodated with a single parametrization that accounts for appropriate systematic and statistical uncertainties. Alternatively, the nuclear corrections for neutral and charged current interactions could differ. Measurements with eSTAR at the initial electron beam energy and the range of available hadron beam energies could yield precision data for a wide range of beam species over a wide range in Bjorken-x and Q^2 from a single experiment. Such precision insight in nuclear modification would be of interest in itself, and is expected to have broad impact on other areas of nuclear and high energy physics that rely on evaluation of reactions based on

collinear factorization. Staged upgrades to higher electron energies further extend the range of the measurements to higher Q^2 and to considerably smaller Bjorken$-x$, where the thus far essentially unknown nuclear gluon distributions are expected to dominate. At sufficiently high energies, such measurements would allow precision studies of QCD matter in the weak-coupling regime of extreme gluon density, where gluons self-interact.

3.4.3 Collins and Sivers asymmetries

The capability to collide longitudinally and transversely polarized beams is central to the eRHIC conceptual design. This flexibility affords measurements with eSTAR that span all combinations in polarized deep-inelastic scattering measurements. Impact, well exceeding that of RHIC and other data in terms of kinematic coverage and precision, is expected from measurements of gluon and quark polarization, including in particular the strange (anti-)quark polarization, using longitudinal beam polarizations. Semi-inclusive measurements of deep-inelastic scattering of unpolarized electrons and transversely polarized nucleons offer the attractive opportunity to simultaneously measure the Collins and Sivers asymmetries through observation of (current-) hadron azimuthal modulation with respect to the nucleon spin. The Collins asymmetries are related to quark transversity through convolution with independently measured Collins fragmentation functions. The Sivers asymmetries reflect a correlation between parton intrinsic transverse momentum and nucleon spin, and involve unpolarized fragmentation. Their quantitative relation to parton orbital momentum forms the topic of ongoing theoretical study. The HERMES collaboration has observed non-zero Collins and Sivers asymmetries in the production of identified hadrons in fixed-target deep-inelastic scattering of polarized protons [309]. Similar measurements have been made by the COMPASS collaboration [310], and are an integral part also of the spin physics program at Jefferson Laboratory. Figure 3.35 shows the HERMES data on the Sivers amplitudes for π^+ and K^+ versus Bjorken-x. The data are separated for each x-interval in high and low scales, Q^2. Data from eSTAR would span a by far wider range in Q^2, as illustrated in Fig. 3.33, which should yield qualitatively new insights through analysis of the Q^2 dependence, and would give unique access to the region of small Bjorken$-x$, where gluons dominate. The data, combined with Jefferson Laboratory measurements covering the valence quark region, should have definitive impact in global analyses [311] of transverse spin distributions.

3.4.4 Energy loss in cold nuclear matter with e+A

Energy loss has been studied in cold nuclear matter by a number of experiments on lepton-nucleus scattering, most recently HERMES at HERA and, at lower energies, CLAS at Jefferson Laboratory (for a recent comprehensive review, see [312]). These studies are highly complementary to studies in heavy ion experiments. The normal nuclear matter densities through which the partons must pass are lower than those in the hot and dense matter produced in high energy heavy ion collisions, and so the effects are not expected to be as striking. Despite this, significant and sizeable suppression patterns have been seen in these previous experiments.

There are two advantages of energy loss measurements in e+A collisions over their analog in A+A collisions. First, at leading order the kinematics of the initial outgoing quark are completely

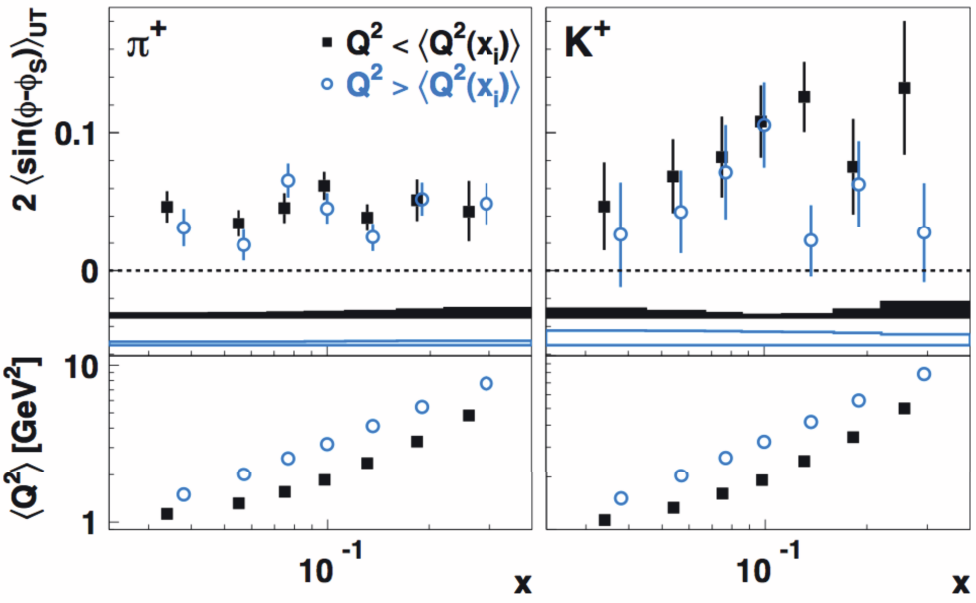

Figure 3.35: Sivers amplitudes for π^+ (top left panel) and K^+ (top right panel) versus Bjorken-x from HERMES data [309]. The lower panels show the corresponding average scales, Q^2.

determined by the measurement of the recoiling lepton. This process has its closest analogy to the γ-jet process in A+A collisions, in which the recoiling γ carries the kinematical information of the parton. Second, the properties of the medium through which the parton passes, the nucleus, are well understood, so that the measurements are sensitive primarily to the mechanism of energy loss in this medium, rather than the properties of the medium itself.

The simplest measurement is a semi-inclusive measurement, in which the energy and angle of the outgoing lepton serves as a tag of ν and Q^2 of the hard collision, and the fractional energy $z_h = E_h/\nu$ of the hadron is measured in coincidence with the lepton. At leading order, in the simple parton model, ν is the energy-loss of the lepton, and thus the energy of the recoiling parton, in the rest frame of the nucleus. The ratio R_A^h is formed between the multiplicities in a given kinematic bin in e+A collisions to the corresponding multiplicities in e+p (or e+D) collisions. More precisely,

$$R_A^h(\nu, Q^2, z, p_T^2) = \frac{\left(\frac{N^h(\nu,Q^2,z,p_T^2)}{N^e(\nu,Q^2)}\right)_A}{\left(\frac{N^h(\nu,Q^2,z,p_T^2)}{N^e(\nu,Q^2)}\right)_D} \tag{3.3}$$

with $N^h\left(\nu, Q^2, z, p_T^2\right)$ the number of semi-inclusive hadrons at a given $\left(\nu, Q^2, z, p_T^2\right)$ and $N^e\left(\nu, Q^2\right)$ the number of inclusive DIS leptons at $\left(\nu, Q^2\right)$. This quantity is closely analogous to a γ-triggered I_{AA} in heavy ion experiments. To first order this ratio factorizes out the modification of Parton

Distribution Functions in the nucleus, which should affect the ratio of $N^e(\nu, Q^2)$, but not the distribution of hadrons given that an electron is found.

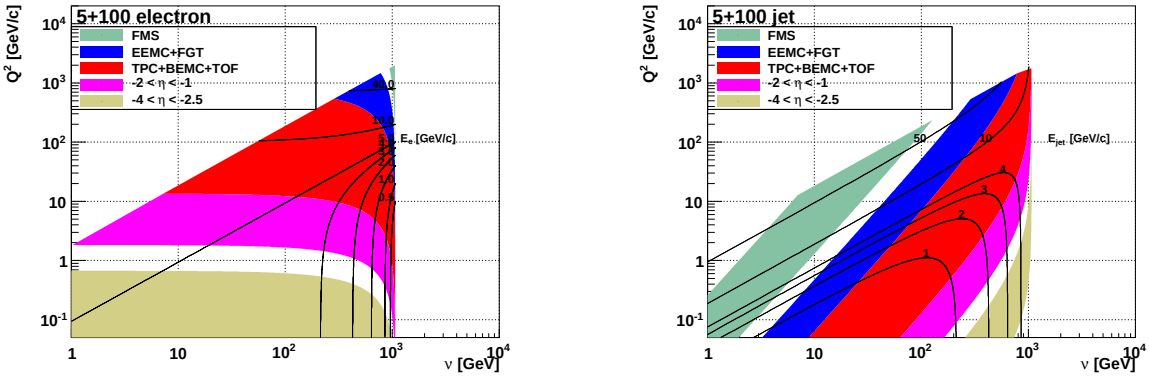

Figure 3.36: Kinematic coverage of the STAR detector in the (ν, Q^2) plane. Left: electron. Right: struck quark. Electron beam energy is 5 GeV, and nucleus beam energy is 100 AGeV. Lines of constant laboratory energy of the struck quark and electron are shown.

Figure 3.36 shows the kinematic coverage of the current STAR detector for the first stage of eRHIC, in which the electron has energy of 5 GeV and the nucleus energy of 100 GeV. The STAR detector as shown consists of the mid-rapidity detectors from $-1 < \eta < 1$, the Endcap Electromagnetic Calorimeter (EEMC) and Forward Gem Tracker (FGT) from $1 < \eta < 2$, and the Forward Meson Spectrometer (FMS) from $2.5 < \eta < 4$. The EEMC and FMS have been shown in two possible positions, one in which the electron heads towards them (hadron in yellow) and one in which the electron heads away from them (hadron in blue). The second case is preferable for measurements at high ν, and is better suited to the technology optimizations of the two calorimeters for high energy objects.

In order to make semi-inclusive measurements, one needs to cover approximately the same region in the (ν, Q^2) plane for both the struck quark and the outgoing electron. Figure 3.37 shows the reach for such a measurement, after choosing that the electron heads away from the EEMC. For hadrons, the energy and angle of the struck quark is used, which will be smeared by the fragmentation process, and provides an upper limit to the possible hadron energy. In the TPC region, electrons can be identified and their momentum and angles measured using the TOF, BEMC, and TPC, along with their full identification capabilities for hadrons. In the EEMC region, the combination of the Forward Gem Tracker (FGT) and the EEMC can be used to track and identify electrons at high energy. π^0 reconstruction and neutral jet reconstruction have been proven using the EEMC, while the FGT provides some charged hadron reconstruction capabilities, though not as extensive as at mid-rapidity. Neutral jet reconstruction provides good resolution in the angle of the jet, but poor resolution in energy.

HERMES has made precise measurements at a lower ν, differential in z and Q^2 and with identification of the hadrons. HERMES has the capability to identify hadrons, which is critical to the

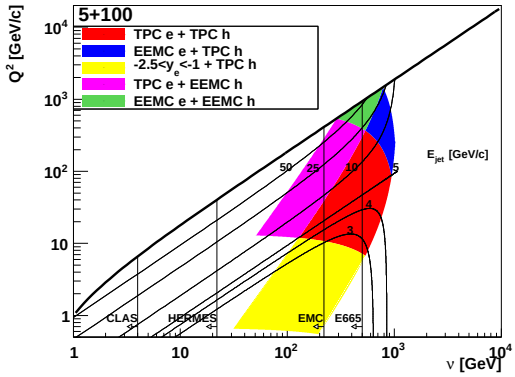

Figure 3.37: Reach in (ν, Q^2) for semi-inclusive DIS scattering with the existing STAR detector, and with additional electron detection capability at negative pseudo-rapidity. The electron has energy 5 GeV, in the direction away from the EEMC, while the nucleus has energy 100 AGeV. Regions in which the electron or hadron go to detector subsystems are identified. Lines of constant struck quark energy in the laboratory frame are shown (E_{jet}). Maximum ν reach of previous experiments is shown.

interpretation of the mechanism of energy loss, and the statistics to bin finely and doubly differentially in the relevant variables. Hadronic absorption, in which the hadron forms at least partially within the nucleus, and then interacts with the nucleus as a hadron, has been proposed as a competing mechanism to partonic energy loss for nuclear modification. The critical quantity is the formation length of the (pre-)hadron, which increases linearly with ν due to Lorentz dilation. For the kinematic region of the HERMES data, the formation length is estimated to be 1-10 fm, which, since it is on the order of the size of the nucleus, leads to appreciable attenuation within these approaches. Different hadron species will have different formation times, different hadronic interaction cross sections, and so different attenuation patterns. As shown in Fig. 3.38, phenomenologically, HERMES has distilled much of the behavior of the doubly differential suppression measurements by means of the scaling variable L_c, motivated to correspond to the formation length by the Lund string model.

$$L_c = z^{0.35}(1-z)\nu/(1GeV/fm) \tag{3.4}$$

At HERMES energies, disentangling partonic energy loss from hadronic absorption has therefore become a question of detailed comparison of theory and data [312].

In contrast, at the range of ν accessible by an eSTAR, for light quarks the formation times will be up to hundreds of fm, far beyond the size of the nucleus. Interpretation of the energy loss as partonic in origin is therefore quite clean. However, the size of suppression effects may be significantly smaller than those measured by HERMES, necessitating precision measurements as highly differential as possible. Of previous experiments, EMC [314] and E665 [315] reached the highest in ν, but without hadron identification. The nuclear modification factor R_A^h was found by both experiments to be unity within 5-10% for ν from 50 to 500 GeV, as shown in Fig. 3.39. As also

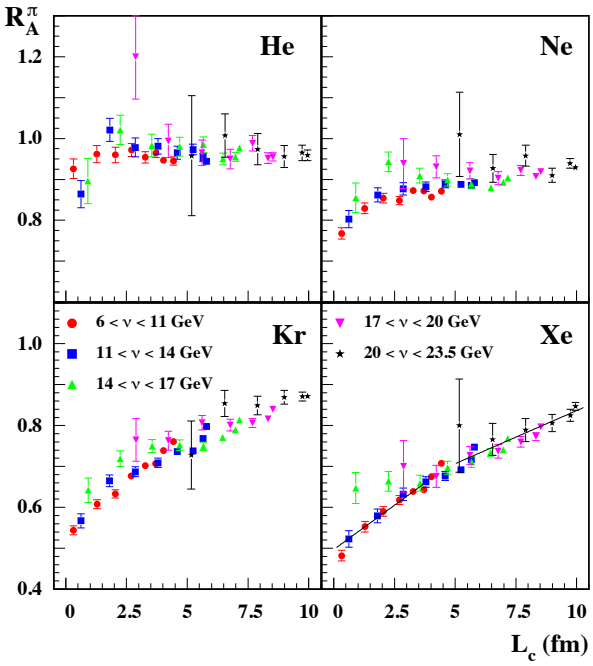

Figure 3.38: Measurements of R_A^h for charged pions as a function of the scaling variable L_c from HERMES [313].

shown in the figure, there is an indication of a modification of the p_T^2 distribution, with depletion at low p_T^2 and enhancement at high p_T^2, which has been attributed to an analogy to the Cronin effect, from multiple scattering of the outgoing parton in the nucleus. Neither experiment made measurements highly differential in z and ν. An eSTAR could greatly improve on these results, making differential measurements, at higher ν, with full hadron identification, though the ultimate limits on precision, relative to expected effects, require further study.

The interaction of heavy quarks with cold nuclear matter has been unexplored in nuclear deep inelastic experiments. The mass of the quark introduces an additional scale, which, especially for bottom, significantly reduces the formation time. Formation and hadronic dissociation of B mesons in the hot, dense matter at RHIC has been posited as a possible explanation for strong quenching of electrons from bottom decay at RHIC [316]. In this approach, for accessible energies of charm and bottom at RHIC, the formation time is estimated to be well within the size of the hot collision zone, reduced by up to two orders of magnitude relative to that of light quarks. A significant theoretical input to this explanation is the wavefunction of a bound heavy-light meson in hot nuclear matter [317], if such a state can survive. In the accessible kinematics of eSTAR, formation times for charm and bottom should also of the order of the size of the nucleus, so this picture can be tested in the very different environment of normal nuclear matter. With the Heavy Flavor Tracker, or its suitable upgrade at the time of eSTAR, such measurements will be possible in the region marked as TPC on Fig. 3.37.

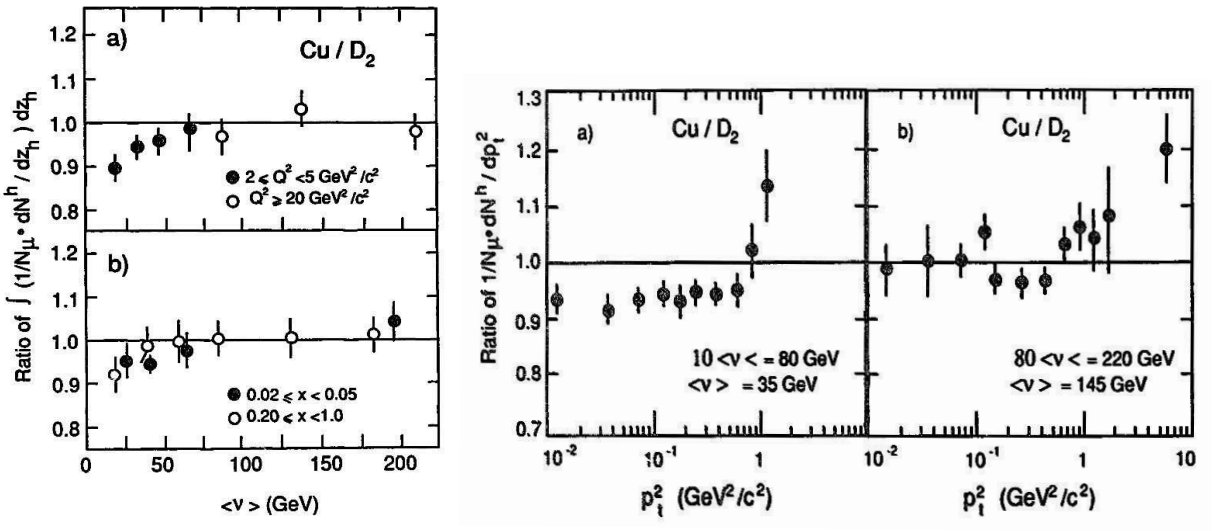

Figure 3.39: Measurements of R_A^h from EMC [314]

The reconstruction of jets has also not been attempted in nuclear deep inelastic scattering experiments. As shown in Fig. 3.37, in the laboratory frame the struck quark energy E_{jet} is appreciable, up to 50 GeV or more in the EEMC acceptance and up to 25 GeV in the TPC acceptance. This is well within the range of proven jet reconstruction in p+p collisions, which if anything overestimate the underlying event contribution in e+A collisions. As with the measurement of jets in A+A collisions, full jet reconstruction opens the possibility of detailed measurements of the flow of energy within and outside of the jet, with the added constraint that the total jet energy is constrained by the measurement of the lepton. Measurements of energy flow have been previously used in e+p collisions at HERA to precisely measure α_s, the techniques of which can be transferred to eSTAR.

Beyond the first stage of eRHIC, Figs. 3.40 and 3.41 show the kinematic reach of a higher energy machine, in which the electron has 30 GeV and the nucleus 130 AGeV. In this configuration, the acceptance moves to higher ν and Q^2, as do the struck quark energy. Depending on results from the first stage of eRHIC, whether significant and measurable suppression patterns can be seen at high ν, mid-rapidity coverage would remain useful for extending studies to even higher ν than can be achieved in the first stage of eRHIC. Forward instrumentation in the direction of the electron would allow for contact with the measurements at lower electron energy.

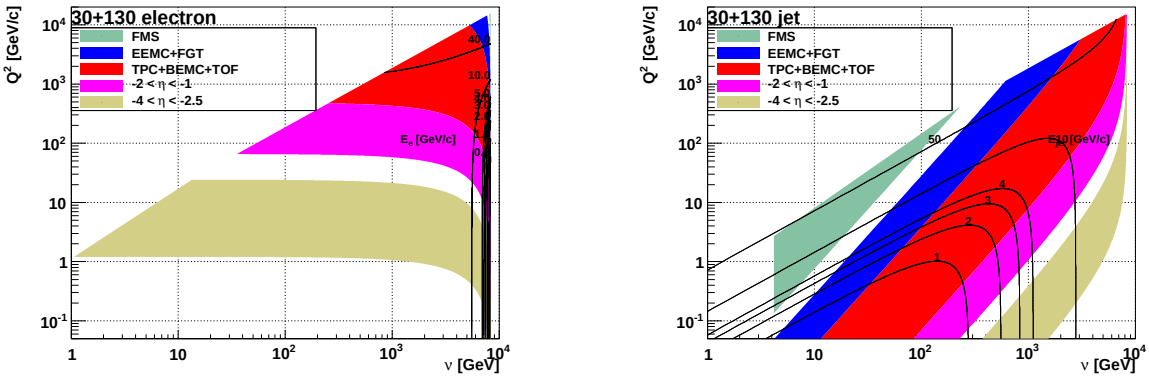

Figure 3.40: Kinematic coverage of the STAR detector in the (ν, Q^2) plane. Left: electron. Right: struck quark. Electron beam energy is 30 GeV, and nucleus beam energy is 130 AGeV. Lines of constant laboratory energy of the struck quark and electron are shown.

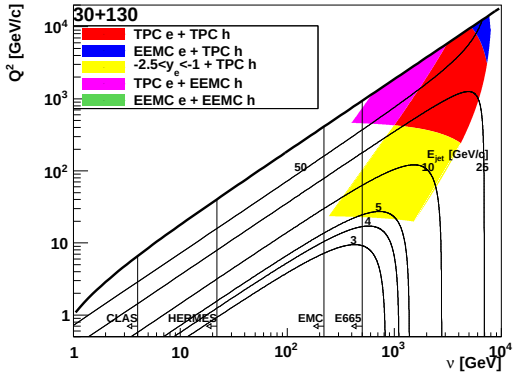

Figure 3.41: Reach in (ν, Q^2) for semi-inclusive DIS scattering with the existing STAR detector, and with additional electron detection capability at negative pseudo-rapidity. The electron has energy 30 GeV, in the direction away from the EEMC, while the nucleus has energy 130 AGeV. Regions in which the electron or hadron go to detector subsystems are identified. Lines of constant struck quark energy in the laboratory frame are shown (E_{jet}). Maximum ν reach of previous experiments is shown.

Chapter 4

STAR Upgrades for the Coming Decade

Since the beginning in 2000, STAR has had a strong upgrade program to take advantage of luminosity upgrades of the machine and to enhance the physics program. The latest upgrades installed were the DAQ1000 system, which was completed for Run 9, and the full azimuthal coverage with TOF for Run 10. This chapter of the decadal plan describes ongoing and planned upgrades in the near- to midterm in Sect. 4.1, and upgrades that would be implemented in the later part of the decade, including a transition to eSTAR, in Sect. 4.2. Several improvements to and maintenance of the STAR detector will also be required to ensure the continuous successful operation (Sect. 4.3).

The currently approved and ongoing upgrades are the Forward Gem Tracker (FGT), which will be available for Run 12, and the Heavy Flavor Tracker (HFT), a major MIE that has just received CD-1 approval and is projected to be ready for the STAR heavy flavor program with topological identification for Run 14. One of the other upgrades has reached the proposal stage. The Muon Telescope Detector (MTD) was just reviewed positively by BNL, and STAR aims to have it in place for Run 14, enabling a significant di-muon program along side the heavy flavor program with HFT. A number of additional proposals have been reviewed internally within STAR. One is to study central production in p+p collisions though an upgrade of the Roman Pots. This has great discovery potential for glueball states and would complement and compete with programs at Jefferson Laboratory. Another would install a Forward Hadron Calorimeter (FHC) behind the Forward Meson Spectrometer. This would enable measurements of Λ polarization in polarized p+p collisions to explore the strange quark helicity and transversity distributions.

As discussed in Chap. 3, there are very compelling reasons to upgrade the forward instrumentation specifically for p+p and p+A measurements. Conceptual ideas for these upgrades are described, but will clearly need substantial studies in the coming year to realistically assess performance as well as costs. The requirement for forward upgrade for electrons in eSTAR is also discussed.

By now the STAR detector is more than 10 years old, and spare parts are getting difficult to procure, so several sub-systems need attention and investment if they are to last for another 10 years. Of particular importance is the TPC, which is vital to all of the STAR physics programs. We present the status, as well as a plan how to deal with possible – but not yet materialized –

future failures. There are possibilities to increase the event rate by up to a factor of ten for certain physics programs that only require precise measurements of a few tracks. This will require modest upgrades to the TPC gating grid system. In addition, for STAR to reap the full potential of the RHIC-II luminosity upgrade, the trigger system through-put will have to be upgraded. A number of smaller proposals are also described. STAR has implemented the first stage of a High Level Trigger, which has capabilities to select events of interest. It may be desired to upgrade this system. It will not increase sampled lumonisity, but would make off-line data analysis much more efficient through selection of events of interest. An additional upgrade of the BBC could open opportunities to study diffractive polarization.

Improvements to the RHIC accelerator complex will also be required to address the key physics questions discussed in this Plan. We mention the improvements that we have identified, which will likely require significant resources in terms of either cost or manpower, in Sect. 4.4.

The future will enable collection of large data sets, and computing resources are clearly needed. These are not described here, but recently STAR prepared a detailed computing plan for the coming years. It can be found at: `http://drupal.star.bnl.gov/STAR/starnotes/public/csn0474` .

4.1 Near- and Mid-term Upgrades

4.1.1 The Forward GEM Tracker

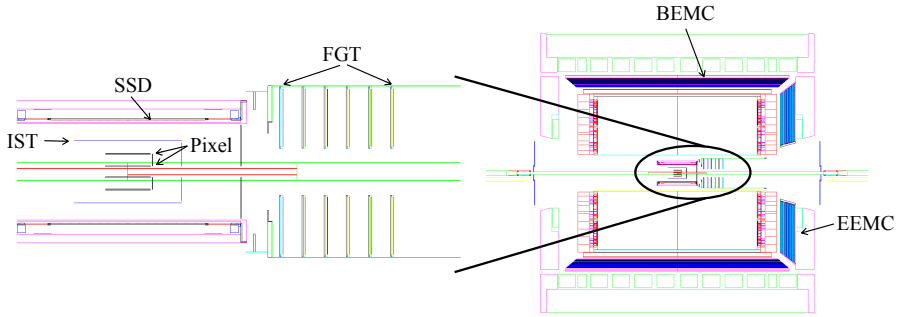

Figure 4.1: Side view of the STAR experiment with the location of six-triple-GEM detectors referring to the FGT.

The Forward GEM Tracker (FGT) will focus on novel spin physics measurements in high-energy polarized proton-proton collisions at a center-of-mass energy of 500 GeV, determining the flavor dependence of u and d anti-quarks of the polarized proton sea [181]. STAR plans to probe these polarized distribution functions using parity violating W production in the electron (positron), $e^{-(+)}$, decay mode. See also Sect. 3.1. The discrimination of u and d anti-quark combinations requires distinguishing between high-p_T $e^{-(+)}$ through their opposite charge sign, which in turn requires precise tracking information. At forward rapidity, new tracking capabilities will be provided by the FGT, consisting of six triple-GEM detectors [318] currently under construction.

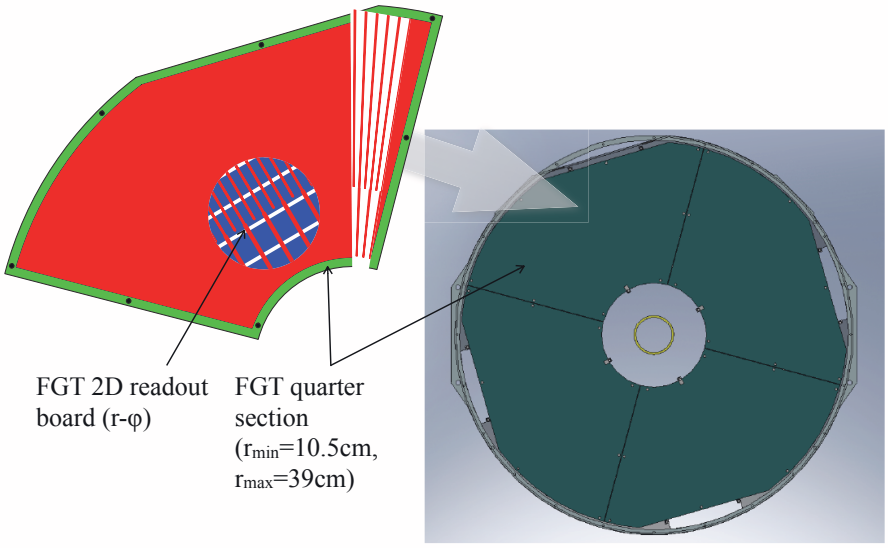

Figure 4.2: FGT quarter section (left) indicating the r-φ two-dimensional readout board together with the layout of a full disk (right) based on a honey-comb support material.

Figure 4.1 shows a side view of the STAR experiment with the location of six triple-GEM detectors. Also shown is the location of the new Heavy-Flavor Tracker consisting of an existing single layer silicon strip detector (SSD), a new Inner Silicon Tracker (IST) based on conventional silicon strip/pad technology along with a novel design of a two layer active pixel sensor detector (Pixel). The FGT covers the pseudo-rapidity range of the Endcap Electromagnetic Calorimeter (EEMC) of $1.1 < \eta < 2$.

The layout of a single FGT disk providing support for four independent triple-GEM detectors referred to as quarter sections is shown in Fig. 4.2. The inner radius of each quarter section is approximately 10.5 cm; the maximum outer radius is approximately 39 cm.

The quarter section layout takes into account the current size limitations of GEM foils from the Tech-Etch Inc. production facility of approximately $50 \times 50\,\mathrm{cm}^2$. A GEM foil is subdivided into nine sectors with a total area per sector of approximately $100\,\mathrm{cm}^2$ The production of GEM foils by Tech-Etch Inc. profits enormously from a dedicated SBIR[1] proposal between Tech-Etch Inc. and BNL, MIT and Yale University. Each disk will be installed inside a carbon fiber support cone which provides at the same time the necessary support for the new inner silicon-based tracking system. The readout board is based on a laser-etched two-dimensional strip readout as shown in Fig. 4.2, with strips running in the radial and azimuthal directions. The radial strips are on top of the azimuthal strips with a vertical separation of $50\,\mu$m. Each quarter section has 1274 readout strips with 948 radial strips and 326 azimuthal strips. The readout system of the FGT is employing the APV25-S1 front-end chip [319]. A total of 10 readout chips are used for each quadrant, with

[1]Small Business Innovative Research, US-DOE funded program to foster collaboration of small companies and research institutions.

five readout chips glued and bonded onto a readout module (APV module). Two APV modules are connected to a single quadrant using multi-pin connectors and are mounted on the borders between quarter sections. The performance of smaller 10×10 cm^2 prototype detectors has been evaluated in a testbeam experiment at FNAL [320]. The detectors showed stable performance with high efficiency and good spatial resolution at the level of $\sim 70\,\mu$m. Efficiencies between 95% and 98% were observed.

The FGT is currently under construction, with a system test scheduled in late Spring 2011 and full installation in STAR by late summer. It will be ready for operation beginning with Run 12.

4.1.2 The Heavy Flavor Tracker

The Heavy Flavor Tracker (HFT) is a state-of-the-art micro-vertex detector utilizing active pixel sensors and silicon strip technology. The HFT will significantly extend the physics reach of the STAR experiment for precision measurements of the yields and spectra of particles containing heavy quarks. This will be accomplished through topological identification of mesons and baryons containing charm quarks, such as D^0 and Λ_c , by the reconstruction of their displaced decay vertices with a precision of approximately 50 μm in p+p, d+A, and A+A collisions. The combined measurements of directly identified charm hadrons and of the total non-photonic electrons will enable us to identify the bottom production at RHIC, including the bottom production cross section and $R_{\rm AA}$ and v_2 of the decay electrons. See Sects. 2.1 and 2.2 for more detailed physics discussions.

The HFT consists of 4 layers of silicon detectors grouped into three subsystems with different technologies, guaranteeing increasing resolution when tracking from the TPC towards the vertex of the collision. The Silicon Strip Detector (SSD) is an existing detector with double-sided strip technology. It forms the outermost layer of the HFT. The Intermediate Silicon Tracker (IST), consisting of a layer of single-sided strip-pixel detectors, is located inside the radius of SSD. Two layers of silicon pixel detector (PXL) are inside the IST. The pixel detectors have the resolution necessary for a precision measurement of the displaced vertices. With the HFT, the TOF detector, and the TPC, we will study the physics of mid-rapidity charm and bottom production. The layout of the HFT detector system within STAR is shown in Fig. 4.3.

The pixel detector will use CMOS Active Pixel Sensors (APS), an innovative technology never used before in a collider experiment. The APS sensors are only 50 μm thick with the first layer at a distance of only 2.5 cm from the interaction point. This opens up a new realm of possibilities for physics measurements. In particular, a thin detector (0.37% of a radiation length per layer) in STAR makes it possible to do the direct topological reconstruction of open charm hadrons down to very low transverse momentum by the identification of the charged daughters of the hadronic decay.

The HFT is a DOE MIE project with a scheduled new funding of M$15.2. It has received CD-0 and CD-1 approval and is proceeding with detailed design and engineering. It is planned to have at least the PXL and SSD installed for Run 14, with the IST possibly installed for Run 15.

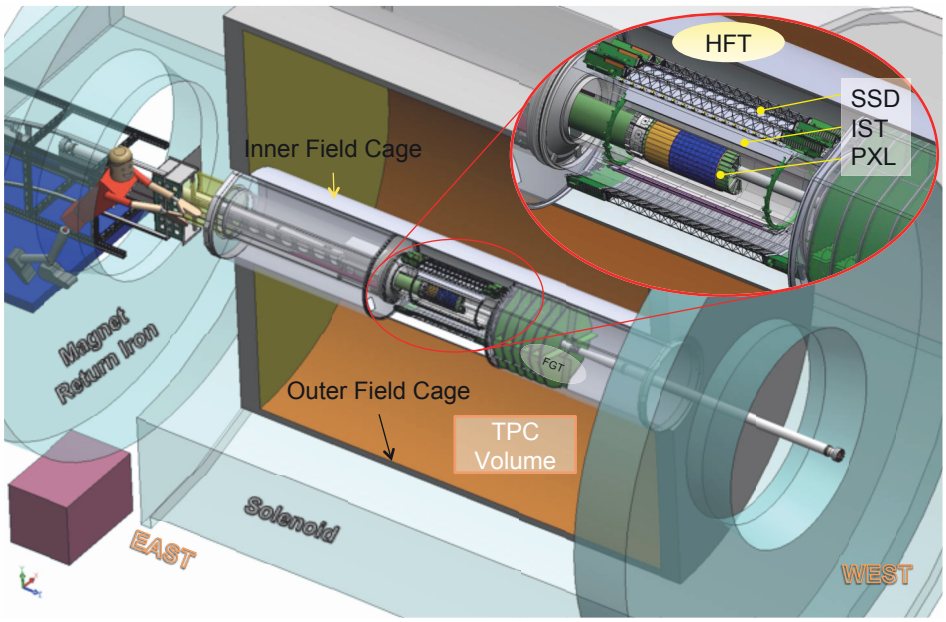

Figure 4.3: HFT detector within the STAR TPC.

4.1.3 The Muon Telescope Detector

The precise measurement of transverse momentum distributions of quarkonia for different centralities, collision systems, and energies will serve as a thermometer of the QGP. A large-area detector identifying muons with momenta of a few GeV/c at mid-rapidity allows for the detection of di-muon pairs from QGP thermal radiation, quarkonia, light vector mesons, possible correlations of quarks and gluons as resonances in the QGP, and Drell-Yan production. For more physics discussions, see Sects. 2.1 and 2.2. Among the many exciting perspectives, the proposed Muon Telescope Detector (MTD) will enable us to collect a large sample of J/ψ events with its trigger capabilities, to separate different $\Upsilon \to \mu^+\mu^-$ decay channels due to the reduced Bremsstrahlung radiation and Dalitz decay background, and to provide a unique measurement of $\mu - e$ correlations from heavy-flavor decays.

In addition, the proposed MTD will enable the study of the rare decays (e.g. $\Sigma^+ \to p\mu^+\mu^-$) and exotic states, such as the muonic atoms of $\mu\pi$, μK and $\mu\bar{p}$.

This novel muon detector, providing precise timing and hit position information, is different from the conventional muon detector, consisting of a sandwich of tracking stations, trigger detectors, and absorbers, in high-energy particle and nuclear physics experiments. The proposed large-area MTD, based on Multi-gap Resistive Plate Chamber (MRPC) technology, covers $\sim 45\%$ in azimuth and $|\eta| < 0.5$ behind the return iron bars of the STAR magnet system. The MRPC utilizes the same technology as used in the TOF system. The layout of the MRPC module is shown in Fig. 4.4. Five modules will be assembled on the outside of each of the STAR magnet return bars in the configuration illustrated in Fig. 4.5. A total of 118 modules will be used to instrument the MTD.

It will provide excellent muon trigger and identification capabilities at mid-rapidity in the high-

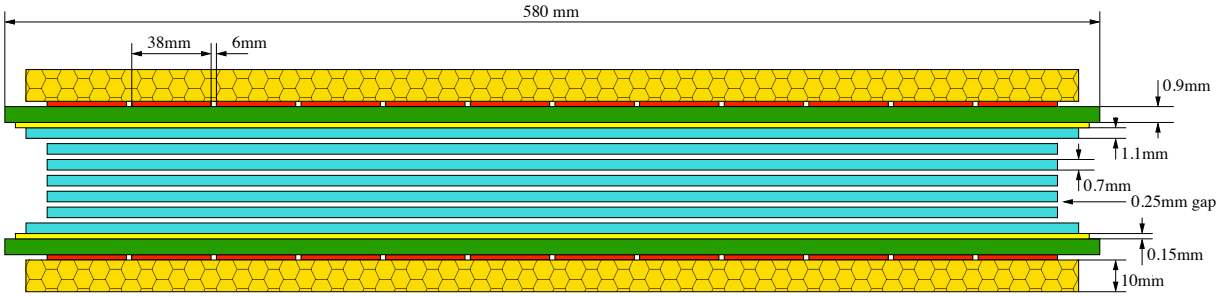

Figure 4.4: Cross section and dimensions of the MRPC module for the MTD.

Figure 4.5: MRPC module mounting layout.

luminosity era of RHIC.

The project will be a joint effort by two institutions from China (USTC and Tsinghua University) funded by NSFC, one institution from India (VECC), and several institutions from the United States (BNL, UC Berkeley, UC Davis, Rice, UT Austin, and Texas A&M) funded by DOE and NSF. The Chinese and Indian institutions will fabricate the long MRPC modules, while the US institutions are responsible for the electronics, the assembly of the trays, and the operation of the detector. It is proposed to start the project in FY2011, complete the construction by the end of FY2013, and finalize the system during Run 14. This is contingent on a 3 year funding schedule.

4.1.4 The Roman Pots Phase II

The main focus of this program is a glueball search in the Double Pomeron Exchange (DPE) process (see Sect. 2.5). The program we propose will naturally include many other topics like: a) search for the Odderon; b) spin dependence of the elastic and diffractive scattering in polarized p+p collisions in the center of mass energy range $\sqrt{s}$ up to 500 GeV; c) polarized proton on polarized ^{3}He scattering, and d) a possibility of new physics of sphaleron production in DPE.

The system proposed here could also be used to determine how well coherent diffractive production of vector mesons in electron+nucleus collisions, e+A $\rightarrow eV$A, could be tagged. These reactions

are considered one of the golden measurements at the future EIC, e.g. in its implementation at the Relativistic Heavy Ion Collider (eRHIC).

A set of exploratory benchmark measurements may be developed at RHIC, with its heavy ion beams, utilizing ultra-peripheral collisions (UPC) of heavy ions. In these reactions, if the nucleus breaks up into several or many fragments in the collisions, it may be possible to observe them with a detector system placed beyond the DX magnet.

The detector system for those measurements will be located between the DX and D0 magnets at RHIC. To implement this program, a new set of Roman Pot stations integrated with a new vacuum section between the DX-D0 magnets will be needed. At this location, the data taking will not require special beam optics; hence it will be done during normal RHIC operations. The conceptual design of the DX-D0 vacuum chamber has been developed in the context of integrating the existing Roman Pot design, as shown in Fig. 4.6.

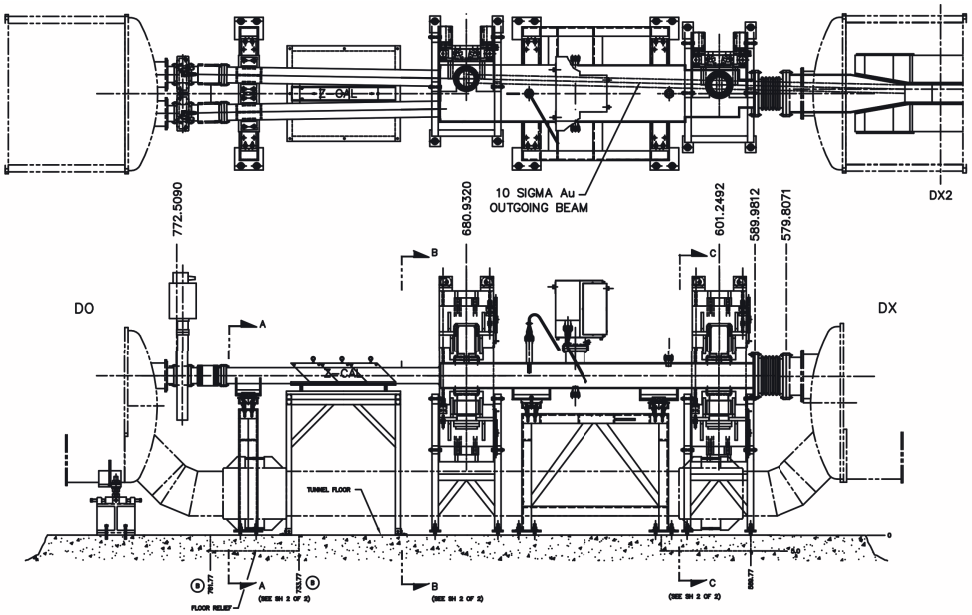

Figure 4.6: The Roman pots of the pp2pp experiment in the STAR interaction region.

A technically driven, two-year design and construction schedule would allow completion before Run 13, thus allowing the program to be run in parallel with the high luminosity W spin program.

4.1.5 The Forward Hadron Calorimeter

We have proposed to add existing hadron calorimeter modules behind the STAR Forward Meson Spectrometer (FMS), as shown in Fig. 4.7. The Forward Hadron Calorimeter (FHC) will facilitate measurement of transverse single spin asymmetries for inclusive jet production at large rapidity ($\eta \sim 2.7$), and reconstruction of hyperons produced at large rapidity to study polarization observables for hyperon production at medium to large Feynman-x.

The jet program is made possible by triggering on the sum of electromagnetic energy detected by the FMS and hadronic energy detected by the FHC. Offline jet reconstruction would be accomplished from electromagnetic energy deposited in the FMS and hadronic energy deposited in the FHC. The hadronic energy is required to obtain an accurate measurement of the energy of the forward jet. Hyperons such as the Λ can be reconstructed from their decay to $n\pi^0$. Identification requires reconstruction of the π^0 from its decay photons observed in the FMS, which also point to the Λ decay vertex. The neutron is identified in conjunction with the π^0 through its energy deposit in the FHC and the absence of a charged particle signal in the BBC. The constrained π^0 fit with the n signal provides invariant mass on which the Λ identification is based.

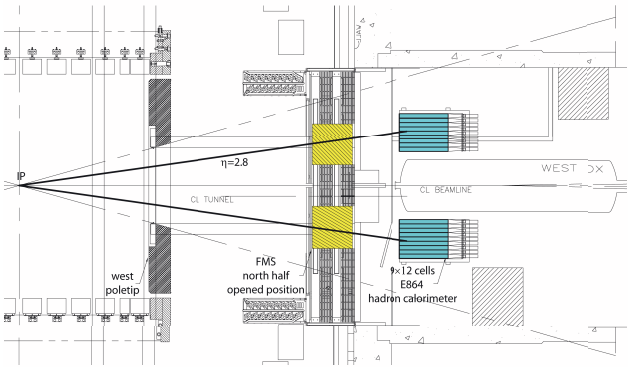

Figure 4.7: Layout of FHC modules behind FMS.

The two modules will use existing symmetric enclosures that are large enough to house arrays of 9 columns by 12 rows of hadronic calorimeter modules.

4.2 Long Term Upgrades

4.2.1 The Forward Instrumentation Upgrade

Chapter 3 describes a broad program of forward measurements to elucidate the dynamics that underlie the observed large transverse single-spin asymmetries in polarized p+p collisions and explore the onset of gluon saturation in p+A collisions. Important components of this program will require the ability to measure large rapidity identified hadrons (π^0, η, Λ, ...), unidentified charged hadrons, direct photons, e^+e^- pairs from Drell-Yan and J/ψ production, and jets, as well as di-hadron and γ+hadron correlations.

The Forward Meson Spectrometer provides STAR with the capability to measure electromagnetic final states in the pseudorapidity range $2.5 < \eta < 4$. Once the Forward Hadron Calorimeter (FHC), see Sect. 4.1.2, is installed behind the FMS, these capabilities will be expanded to include measurements of jets and (unseparated) $\Lambda + \bar{\Lambda}$, as well as the ability to trigger on high-energy charged hadrons in the forward direction.

The FMS, independently and in conjunction with the FHC, will suffice to embark on the program of measurements, but significant upgrades of STAR's forward detection capabilities will be required

for the full suite of measurements to become practical. The single most challenging requirement is the ability to identify Drell-Yan di-electron pairs amidst the far more intense backgrounds from conversion electrons and mis-identified hadrons. Another significant challenge is γ/π^0 separation at high energies. Recent analyses of Run 9 FMS small cell data have demonstrated that single photons can be separated from π^0s with good efficiency to at least 75 GeV, which is 25% higher than had previously been expected. This is sufficient for measurements at $\sqrt{s} = 200$ GeV, but not at 500 GeV. Several spin physics measurements would also profit significantly from an ability to distinguish charged mesons from protons and anti-protons. For example, the sensitivity of the forward hyperon measurements to the strange quark helicity and transversity can be enhanced by focusing on polarization transfers to $\bar{\Lambda}$. The $\bar{\Lambda}$s can only be separated from the more intense Λs by identifying the $\bar{p}\pi^+$ decay channel. In addition, BRAHMS has found that A_N is quite small for forward protons [321], which provides a strong motivation to separate mesons from baryons when examining hadron correlations.

At present, STAR is exploring two conceptual schemes that we believe will serve these purposes. Both begin with fast tracking in the forward direction. This is needed for charge-sign determination, momentum resolution, and to enhance our ability to apply isolation cuts during the Drell-Yan measurement. In STAR, forward charged particles are first deflected by the 0.5-T solenoidal magnetic field. The radial magnetic field in the vicinity of the effective field boundary then deflects the particles through about half as large an angle in the opposite direction. The net effect is to produce an overall deflection

$$\Delta\phi \sim \frac{0.25 \text{ rad GeV}/c}{p_z}.$$

To date, forward tracking in STAR has been accomplished with the Forward Time Projection Chambers (FTPCs). The FTPCs provide charge-sign determination and modest momentum resolution, comparable to that required for the forward physics programs. This has been demonstrated in the analysis of Run 8 data where FTPC tracks have been extrapolated and matched to FMS cluster locations. However, the FTPCs are not well matched to the requirements for high-luminosity p+p and p+A running because they experience significant pile-up from out-of-time collision backgrounds. Furthermore, the FTPCs will be removed from STAR after Run 11 to make room for the FGT and HFT. The addition of $\sim$6 GEM disks in the region between the FGT and the effective field boundary, together with an addtional space-point measurement near the front of the FMS, will provide momentum resolution comparable or better than that of the FTPCs, without the complications from pile-up. If the space-point at the front of the FMS is provided by an array of high-granularity GEMs, single electrons can also be discriminated from high-energy conversion electron pairs, which will produce two closely-spaced clusters.

Both schemes also include a low-mass RICH, capable of meson/baryon discrimination, installed in the open region between STAR and the FMS. This would provide the ability to distinguish π^+ from p and Λ from $\bar{\Lambda}$, as discussed above.

In one scheme, 2 to 3 radiation lengths of Pb and a final GEM plane would be installed in front of the FMS to assist with γ/π^0 and e/h discrimination. The two photons from a 200 GeV π^0 are separated by at least 9 mm at the FMS, so the final GEM plane can have a coarse read-out pitch.

The FMS would then measure the final-state electromagnetic energy and a fraction of the hadronic energy, and the FHC would measure the remainder of the hadronic energy.

In the second scheme, a Forward Spaghetti Calorimeter (FSC) with full azimuthal coverage and pseudo-rapidity coverage over the range $2 < \eta <\sim 4$ is being considered as an alternative to the FMS and FHC. This calorimeter will serve the p+Au and polarized p+p programs in the latter part of the decade, as well as jet physics in the eSTAR era. The FSC tower granularity should be adequate to provide $\pi^0 - \gamma$ discrimination. Charged particle tracking, as described above, would provide separation of electrons/positrons from photon showers and of neutrons from charged hadrons. The proposed technology is a transversely segmented and compact compensating calorimeter. Such spaghetti calorimeters have demonstrated performance advantages in jet energy measurements and shower identification for both hadrons and electrons [322, 323, 324]. An R&D program for our application will be needed, and will benefit the STAR spin physics and cold nuclear matter physics programs, leading into the eSTAR era.

Detailed simulations of these schemes are needed in order to match their performance to the requirements of the planned p+p and p+A measurements. Once those simulations are completed, a cost-benefit analysis will be necessary to choose between the two schemes. In either case, it is foreseen that some R&D will be required to optimize the detector system.

4.2.2 Preparing STAR for the eRHIC Era

STAR mid-rapidity acceptance and particle identification capabilities, paired with more forward instrumentation aimed at high (total) energies, form key strengths into the EIC era. R&D is needed to adapt p+p, d+A, A+A luminosity measurements and $\vec{p} + \vec{p}$ polarimetry capabilities to the $\vec{e} + \vec{p}(^3\vec{H}e$, A) environments. Significant effort is needed also for the interaction region.

The STAR mid-rapidity region with the existing TPC, BEMC, and TOF and future MTD is relatively well matched to the demands of inclusive and semi-inclusive deep-inelastic scattering measurements at hard scales $Q^2 > 10$ GeV^2 for the initially low electron beam-energies foreseen at an EIC.

The extension of this coverage to smaller scales requires forward instrumentation, in particular to identify and measure the forward scattered electron with good efficiency, purity, and resolution. Coverage over the region $-3 < \eta < -1$ (on the east end of STAR, opposite to the EEMC) would expand the Q^2 range of inclusive and semi-inclusive measurements accessible to STAR to cover essentially the entire conventional deep-inelastic regime, $Q^2 > 1$ GeV^2. The small-x region, below $x = E_e/E_h$ with $E_{e(h)}$ the electron (hadron) beam energy, is of particular interest. In this region, the scattered electron energies range up to the electron beam energy. This holds also for the energies of the hadrons produced at backward angles in scattering of small-x partons. The identification of hadrons with these energies is of particular importance to semi-inclusive measurements. For the initial 5 GeV electron beam energy, these characteristics thus point to track-based momentum measurements using low-X_0 technology. At higher electron beam energies, this would need be complemented with calorimetric measurements.

The requirements of such a spectrometer are illustrated in Fig. 4.8, which shows the scattered electron (total) energies for different (fixed) detector angles at representative combinations of eRHIC beam energies versus Bjorken-x. The curves in the lower panel are shown for $Q^2 > 1$ GeV^2, the deep-

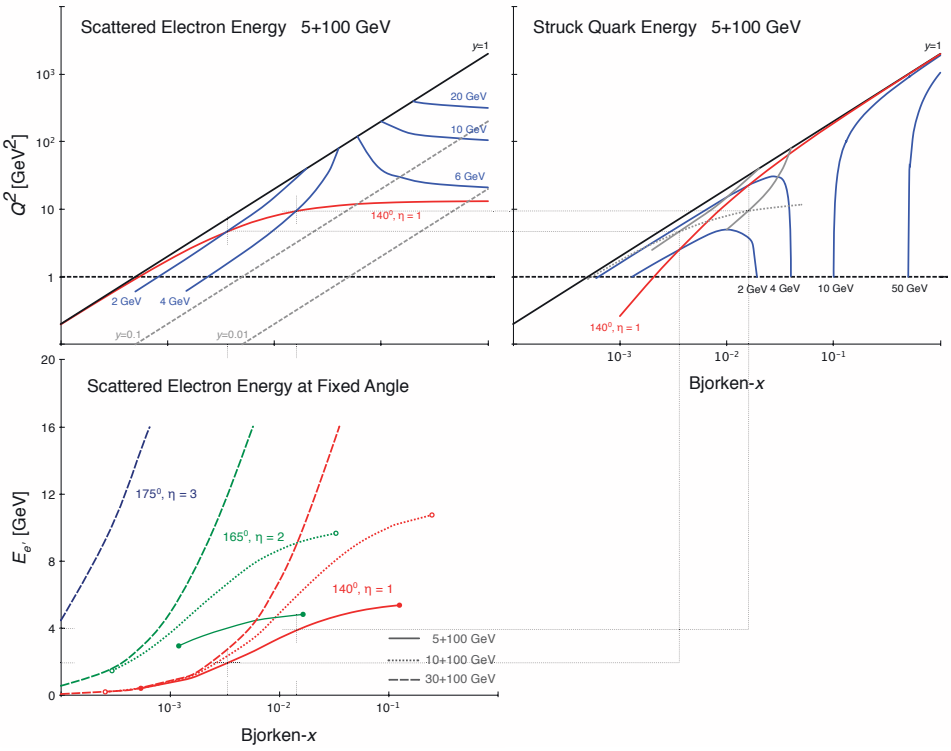

Figure 4.8: Contours of constant energy in x and Q^2 for the scattered electron (top left panel) and struck quark (top right panel) in collisions of a 5 GeV electron beam with a 100 GeV hadron beam. The lower panel shows the total energy of the scattered electron versus Bjorken-x for different scattered electron angles and collision energies.

inelastic scattering region, and for $y > 0.05$. The reconstruction of Bjorken-x imposes increasingly stringent demands on energy resolution with decreasing y.

The kinematics of the struck quark, which is not directly observable, are related to the kinematics of the scattered electron and follow from collision symmetries. At fixed Bjorken-x, the combinations of angle and energy for the scattered electrons are identical to those for the struck quarks, that is, $(\theta_{e'}, E_{e'}) \leftrightarrow (\theta_q, E_q)$ at fixed x. However, scattered electrons and current jets with equal angles and energies probe collisions at different scales, Q^2.

Significant R&D is required to develop a suitable forward spectrometer with adequate electron identification, factoring in the hadron detection requirements and constraints imposed by existing subsystems (including, in particular, spatial constraints imposed by the magnet return yoke and the mid-rapidity tracking subsystems).

The EEMC and FMS, and the future FGT and FHC, have been optimized primarily for the measurement of particles with high (total) momenta and energies. This instrumentation is thus best suited for the detection and measurement of backward-scattered electrons and jets produced in

the forward region, which are of particular interest in studies of energy-loss in cold nuclear matter.

4.3 Detector Enhancements and Maintenance

4.3.1 The Time Projection Chamber maintenance

The STAR Time Projection Chamber (TPC) has performed exceptionally well over the past decade. More than 1.8 billion events were collected in the TPC in the most recent run alone. The TPC is currently functioning in an environment with peak luminosities in the range of $8 \cdot 10^{31}$ cm^{-2}s^{-1} for p+p at 500 GeV and $2 \cdot 10^{27}$ cm^{-2}s^{-1} for Au+Au at 200 GeV. Results from the TPC have been constantly improved over that period due to efforts in the TPC group to understand and provide corrections for observed distortions in the raw data. These effects include residual space charge present in the chamber, leakage of positive ions through the gap in the gating grid between the inner and outer sector segments (grid leak), $\vec{\mathbf{E}} \times \vec{\mathbf{B}}$ effects, as well as small differences in the relative alignments of the various sub-sectors.

Efforts in support of TPC operation are currently centered around two issues, that of anode wire aging and that of high voltage channel tripping in the high luminosity running environment. Aging of anode wires is a well-known and intensely studied effect in which polymerization occurs in the plasma that is present in the avalanche region around a given wire. Layers of deposits build up on the wire surfaces as a result and over time reduce the gain on a wire. Work in the TPC group has recently been focused on characterizing the degree of anode wire aging already present in the TPC and determining the best approach to minimizing this effect in future running. Tripping of the high voltage channels can eventually result in permanent loss of that channel (*i.e.* no longer able to hold the nominal voltage).

Both effects are currently within tolerable ranges but will present significant long-term risks to TPC operations if left unchecked. The following section is therefore devoted to an explanation of the work needed to mitigate these effects and allow the TPC to continue operation through the next decade.

Polymerization of the anode wires appears to be largely unavoidable without the addition of potentially corrosive components to the TPC gas mixture. The TPC group is therefore pursuing the option of rewiring the entire TPC anode grid. This task must proceed in several stages, the first of which is modifying the existing TPC sector removal tool to allow removal and replacement of sectors while the TPC remains mounted in the STAR magnet. First steps in this plan are already underway. Current plans are to remove two sectors of the TPC in Summer 2011 or 2012 and replace them with existing spares. The degree to which deposits have formed on the wires, as well as the composition of those deposits, can then be determined by scanning electron microscope. Depending on what is concluded from these studies, a schedule and plan for the complete rewiring of all TPC anode sections would be developed.

It should be noted that ground plane shields could be installed at the outer edges of the inner sectors during the rewiring process to mitigate the grid leak problem mentioned above.

The second challenge to long-term operation of the TPC is the frequency of tripping of the high-voltage channels. High voltage channel trips in the TPC may have many different sources.

The precise cause of the frequent trips in the high-luminosity p+p environment has yet to be determined. At present, a working solution has been found in lowering the voltages on the inner sectors. Adverse effects on data reconstruction have been shown to be absent for voltages lowered by no more than 70 V from nominal. Also, modified ground cards will be installed on the inner sectors to reduce the energy released in a given trip event. The rewiring of the anode sections described above will allow the recovery of channels that have already been lost, while running at lower voltages in the future will prolong the life of all channels by reducing trips.

GEM Monitoring

With increasing luminosity, space charge distortions have become the major correction to TPC tracking. As the luminosity increases, exciting new physics opportunities are available in STAR, many of which rely on precision tracking in the TPC. At present, a model of the accumulated charge in the TPC is used to correct distortions. The validity of the model can be checked at the inner radius by using the interaction vertex and, in the future, by using the HFT silicon detectors. We note however that the DCA distribution at the interaction vertex is used to adjust the model.

At present, there is no check for the corrected tracks at the outer radius of the TPC. We plan to install 10 cm x 10 cm GEM based chambers (GMT) in 8 locations outside the TPC barrel to provide precision points at large radius for tracks crossing those locations. The plan is to place the chambers near $\eta \sim 0$ and $\eta \sim 1$, in two azimuthal locations on the East and West sides at the same radius as the STAR TOF. The chambers will be based on the GEM technology and readout system developed for the FGT upgrade. Using the Fermilab test beam, prototype chambers have been demonstrated to have a spatial resolution of 70 μm for normal incident tracks, degrading to 300 μm for tracks at 30 degrees to the normal. Simulations including all material show that the projection accuracy of a TPC track to the GMT chambers is 750-1000 μm depending on track momentum. The installation of the GMT chambers will allow testing of the distortion corrections with tracks constrained at both ends. Further, since there will be chambers in two known Z locations on both the East and West sides, there will be a running monitor of the TPC drift velocity.

4.3.2 The High Level Trigger

To cope with the high collision rates at RHIC, STAR has upgraded its data acquisition system. The improved data taking capability imposes a challenge for STAR's computing resources in terms of CPU time and tape storage. By implementing a High-Level Online Tracking Trigger (HLT) it will be possibly to reduce the amount of data written to tape by selecting desired events, while still maintaining a high sampling rate to fully utilize the delivered luminosity for a wide range of triggers. STAR will be able to address a suite of compelling physics topics efficiently. Examples include: i) the study of the heavy flavor production and especially its collective flow, ii) the study of hard process , iii) the study of anti-matter production, and iv) exotic particle search (for example, strangelets).

The HLT is designed to issue trigger decisions based on information combined from all related subsystems. During the RHIC run in 2010, a HLT prototype was deployed with online tracking on every triggered event from level 0 triggers. The 24 Sector Level 3 (SL3) machines, which are

used for the data acquisition and cluster finding for STAR's TPC, are also used in sector-by-sector tracking. Tracks, tower information from the Barrel EMC, and time of flight information from the TOF are sent to Global Level 3 (GL3) machines, in which the complete event is reconstructed and a trigger decision is made.

The performance of the HLT prototype during Run 10 is encouraging. It has successfully selected di-electron, high p_T and charge-2 events, all together with an acceptance rate of no more than 2%. Figure 4.9 shows that the di-electron events flagged by the HLT show a clear J/ψ signal. During the Beam Energy Scan (BES) of 2010, the HLT prototype was used as an online monitoring

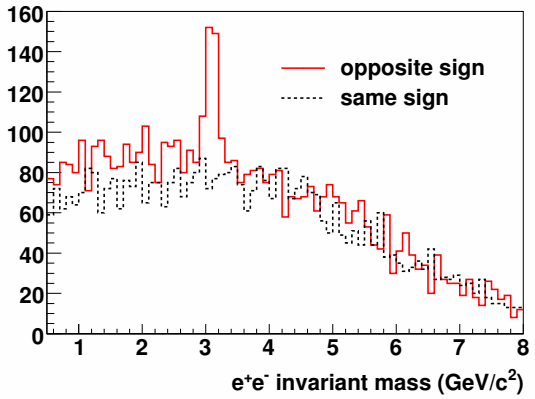

Figure 4.9: e^+e^- invariant mass (solid) line with background (dashed line), for $p_T > 5$ GeV/c. This plot is based on data taken by the HLT during Run 10.

device to reconstruct good collision events amidst large background. This role was crucial for the BES, as usually only 1-10% of events taken were good collisions at $\sqrt{s_{\rm NN}}$=7.7 GeV.

In the future, the plans for the HLT are to 1) implement a R&D program with expanded capabilities for the GL3 machines with Graphics Processing Units to develop fast reconstruction of secondary vertices. 2) possibly upgrade of the SL3 machines depending on the future load of DAQ machines during RHIC-II era. 3) Develop a robust routine for fast online self-calibration and integrate the HLT deeper into the STAR system. 4) Improve the Monte-Carlo environment for the HLT. All these developments, if completed successfully, will allow the HLT to reach its full potential in the RHIC-II era.

4.3.3 Trigger overview

The physics goals of STAR require measurements using p+p collisions at rates > 10 MHz, and using A+A collisions at rates > 100 kHz. The trigger goal is to provide nearly deadtimeless operation taking data at event rates > 20 kHz for "fast detector" events, and > 1 kHz for "slow" (TPC) events. The trigger operates at 10 MHz, examining each RHIC crossing for events of interest.

The current 4-level trigger system is fully pipelined at Levels 0, 1, and 2, and allows data taking at rates up to ∼3 kHz for "fast" and ∼0.5 kHz for "slow" events at overall STAR detector deadtimes of ∼10%. Events are selected at Level-0 and then either aborted or passed on to higher trigger

levels. Triggers are issued at Level-0 within 1.5 μs of the occurrence of the collision, followed by further analysis for accept/reject decisions at Level-1 ($\approx$20 μs later) and Level-2 ($\approx$1 ms later). The rate limit for fast events is set by readout of the various fast detector electronics. The data from individual subsystems (BEMC, TOF, etc.) is not correlated for individual detector cells until Level-2 in the trigger, meaning many triggers from Level-0 must be rejected at higher levels to meet overall bandwidth limits, leading to "unnecessary" deadtime.

There are natural growth paths for the trigger to accommodate new detector subsystems. The small size of the HFT leads to a requirement for a more precise vertex selection at Level-0. The MTD will form summary hit information and will fit neatly into the current trigger complement. A Forward Hadron Calorimeter (FHC) will also be added. These detectors will fit into the trigger scheme like the other calorimeters, providing hadronic and electromagnetic information at Level-0 to complement our existing electromagnetic information and leading to significantly better jet definition.

The upgrades discussed here are aimed at increasing the inter-subsystem communication at Level-0, to allow more constrained correlation triggers, and at increasing the readout speed of the fast detector electronics, to increase overall throughput. Modifications to the readout of all detectors may be required to meet a 20 kHz rate requirement. The plan is to stage the development to match the capabilities of RHIC, concurrently developing the increased cross-subsystem communication at Level-0 and decreasing the time required to read individual detector electronics into the data stream.

The STAR collaboration has established an internal review committee to evaluate the proposed trigger upgrades, and how these match the proposed detector upgrades, and the operations. Here we summarize briefly the upgrades; additional details are available in internal STAR documentation.

1. RHIC Clock and Control system (RCC-II): The STAR Trigger provides the principal clock for the experiment, which is derived from RHIC timing signals and distributed to all STAR subsystems through the RCC system. This upgrade is designed to make addition of dispersed systems simpler and more robust. The plan for FY10 and FY11 is to produce essentially identical boards for all VME crates, with each board providing active local signal regeneration, including clock and control signals.

2. Scaler-II: The STAR Scaler system is responsible for luminosity and polarization and correlation monitoring for each RHIC bunch, as well as for monitoring individual subsystem deadtimes. These monitor tasks require correlation among at least 24 individual signals. Four of these boards are to be tested in Run 11, with the remaining boards being implemented for Run 12 and beyond.

3. Routing And Throughput board (RAT-II): The RAT board is designed to facilitate signal routing for the trigger and the scaler systems. A RAT-II board may prove handy in interfacing subsystems into the DSM tree to allow interconnecting different DSM-II boards without cabling changes for different runs. We expect to begin a design of the RAT-II board in FY12, producing a new board for Run 13.

4. Data Storage and Manipulation (DSM-II): Trigger decisions at Level-0 are made in a tree

of data storage and manipulation (DSM) boards. The two driving requirements for DSM-II are to increase the I/O bit count and to decrease the readout time, thereby increasing the sophistication of the local calculation and raising the fast-detector trigger rate to > 20 kHz. This will also allow us to have dynamic boundaries for cluster definition for our calorimeters, significantly reducing the bias for jet triggers in A+A collisions. The ability to mix data from BEMC with TOF will also allow us to make Level-0 trigger decisions for anti-matter tracks, allowing us to trigger individual sectors of the TPC in our rare particle search. We expect to make use of the readout scheme we are developing for the Scaler-II boards to increase the speed of DSM-II readout by more than an order of magnitude. We expect to replace the ≈ 30 Layer-1, 2, and 3 DSM boards with DSM-II boards in FY12 and FY13. We will replace the ≈ 30 Layer-0 DSMs with DSM-II in FY14 as part of a general upgrade as we retire our older electronics.

5. QT Readout board (QTR): Detector subsystems have typically several charge- and time-digitizing QT boards in each of multiple VME crates. The current readout scheme through the VME backplane to the local CPU limits readout rates to $\approx$ 3kHz. To achieve a 20 kHz rate goal, we will need to engineer a new readout scheme for these boards. Development of this board will overlap with network concepts we expect to develop as discussed in the next bullet. An intelligent back-of-crate card can receive data from the current QT boards and include a driver to push data packets into a Linux memory. The QT output is already zero-suppressed in readout, so that each board produces a small number of bytes for an event.

6. Network: When we convert our DSM tree to DSM-II, we will have a different network topology. Level-0 will continue to impose the most severe time constraint. The Level-2 machines will need to pass data off to DAQ event builders. Bookkeeping will be taken care of by the token concept implemented as it is today, with the Trigger Control Unit (TCU) handling all accounting. Since this development is not likely to get implemented before Run 15, we can wait to see how the market evolves low-latency multi-CPU communication in the next three years. However, we anticipate that our needs for connecting and controlling data streams in 20 or more CPUs may involve special engineering solutions which we will begin developing in FY13.

7. Vertex Position Detectors (VPD): The current interaction diamond at STAR has a FWHM > 60 cm in length along the beamline (Z). Several detectors, most notably the HFT, are most effective when the vertex position is within 10 cm. At present, our Level-0 vertex selection capability is limited to resolutions of ≈ 30 cm for p+p and peripheral A+A collisions and ≈ 6 cm for central Au+Au collisions. Determining the vertex position at Level-0 requires a detector and electronics capable of position measurement within $<$400 psec. Fast enough PMT-based detectors allow vertex position determination by taking the arrival time difference between particles detected on the East and West sides of the interaction at STAR. We are pursuing two options to improve this.

   (a) The current Level-0 Z measurement is based on the BBC or μVPD detectors, using QT discriminators feeding TAC boards whose output current is digitized in QT boards.

We will construct a new detector based on PMT/Cherenkov technology to feed TDC QT-daughter cards developed.

(b) Pursuing a SBIR program to develop electronics capable of feeding an appropriate digital signal to Level-0 in < 1 μs. This is based on the succesful TOF development.

4.3.4 The DAQ 10k upgrade

We propose a sparse readout scheme for the TPC that would enable STAR to acquire events at rates of 10 kHz for classes of physics where only one or two TPC sectors contain all the necessary particle information. The scheme relies on existing detectors (i.e. Barrel Calorimeter (BTOW) or planned Muon Telescope Detector (MTD)) coupled with additional logic to provide the selection of the required sectors.

Physics Motivation

There exist physics topics where enough tracking information is naturally contained within only one or two TPC sectors. Such physics topics are usually addressed with one- or two-arm spectrometer-type detectors and include:

1. High rate trigger with a low barrel EMC (BTOW) threshold for antimatter and dielectrons

   (a) Dielectrons at an intermediate mass range and from J/ψ and Υ decays are important measurements for the understanding the color-screening effect in QGP, thermalization of heavy quarks, and temperature. The high threshold in the EMC trigger provides low rate for dielectrons. However, the efficiency for J/ψ and Υ at low and intermediate p_T is very low in both p+p and A+A collisions. A dedicated trigger with two-sector TPC readout with low EMC high-tower energy of (>1.5 GeV) will enable us to take all the luminosity of RHIC-II p+p and A+A collisions with high efficiency for J/ψ and Υ.

   (b) As discussed in Sect. 2.5, RHIC is a very suitable facility for antimatter production and detection. To go beyond A=4 and to take advantage of the high RHIC-II luminosity, a dedicated trigger to enhance the antimatter detection in STAR is necessary. The energy deposition of an antinucleus in the Barrel EMC calorimeter is significantly higher than that of mesons or nuclei. A single high-tower trigger with threshold at around 2 GeV will provide a high efficiency (>60%) for antimatter detection with ($|A| >= 3$).

2. High rate trigger with MTD for dimuons (J/ψ, Υ) and muonic atoms

   (a) The dimuon from quarkonia and continuous dilepton invariant mass spectra at the intermediate mass range provide complementary measurements to the dielectron measurements. $e - \mu$ correlations provide a unique measurement of open heavy flavor contributions to the dilepton spectra. In p+p or peripheral Au+Au collisions, the dimuon rates are very low, and full TPC readout would be acceptable for such study. In central Au+Au collisions, the dimuon rate is in the order of hundred Hz, and becomes a sizable

dataset. An optional approach is to read out the full TPC at a prescaled rate (e.g., a prescale=10) and to read out the two-sector TPC with the two muon hits for the remaining events. Similarly, $e-\mu$ correlation events can be read out by a combination of a TPC sector corresponding to EMC HT and another with MTD hit.

(b) Muonic atoms carry information about the direct thermal lepton production in QGP. The dissociation at the beam pipe makes it look like a V0 decay with one muon and one hadron (pion) at the same velocity. Single muon trigger rates are quite high (thousand Hz). However, since the muon and pion are at the same velocity and very close in momentum, we can read out only the one sector which has both muon and pion at high rates with a MTD single muon trigger.

Implementation

We envision logic within the BTOW or MTD Trigger decision (DSM) tree where, at some point in time before a trigger decision is made, the one or two particle hits in BTOW or MTD are translated via phi-to-sector maps into a bit pattern of requested TPC sectors. The particle which enters the MTD or BTOW at a specific slat/cell is assumed to be fully contained in the corresponding TPC sector.

This sector bit pattern would be passed to a TPC-specific electronics board, which would control both the issuing of a Level-0 trigger (readout) to the TPC sectors and the generation of the gating grid (GG) control signal. Depending on the bit pattern, some sectors would be required to open the GG and start the read-out, while most sectors would simply be ignored. Note that the current TPC trigger and gating grid distribution system is already segmented into sectors, so this approach does not require any changes to the core read-out and GG electronics.

In this way, due to the random distribution of required sectors event-to-event, the per-sector gating grid rate (and thus also the space charge and general TPC aging) and DAQ readout rate would be 1/12 of the 2-particle trigger rate. Assuming that the currently possible TPC rates are almost 1 kHz, this would in turn enable this physics trigger type to run at approximately 10 kHz.

Two new electronics boards and associated interconnectivity need to be designed and built. Those would be the logic board, which translates the BTOW/MTD cell/slat hit information into a TPC sector bit pattern (presumably sitting within the Trigger System), and the control board that interprets this information and issues read-out commands to the TPC.

The whole DAQ and Trigger system together with the required detectors needs to be able to take data at 10 kHz. While this does not seem to be a problem for most required systems (i.e. DAQ, TPC, MTD, BTOW, ETOW, ESMD) it is not currently possible for BSMD (due to hardware limits) and the Trigger data itself. While BSMD is not necessary for the proposed physics triggers and can simply be ignored, some effort needs to be spent on designing a way to acquire Trigger data at these high rates, as discussed in the previous subsection.

The proposal is targeting RHIC Run 12 and beyond, with an initial test in Run 11 to assess the feasibility. The cost of the hardware implementation is modest, but to reach the full potential several of the trigger upgrades discussed above will also be needed.

4.3.5 STAR Barrel SMD Readout Upgrade

The Barrel Shower Max Detector (BSMD) is necessary for discrimination between photons and π^0, and for high purity electron identification. As such, it is necessary for the non-photonic electron and the γ-hadron programs outlined in the section on the mechanism of energy loss. These programs are not possible without this readout.

There are several considerations driving plans for a BSMD readout upgrade/replacement in the near future. First, there are overall operational issues (e.g., impacting the efficiency and quality of data taking) which are in large part determined by the FEE failure rate as well as availability of spare parts to repair the failures that occur during every running period. The current BSMD readout implementation is also somewhat problematic, for instance in regards to serviceability and diagnostics. Second, there are inherent overall performance issues, such as a limited dynamic range and significant dead time compared to other major STAR detector subsystems, which continue to limit the most effective use of the detector in STAR. In any case, something must be done soon since, given current projections, we will be without spare chips to repair FEE cards after Run 12, and portions of the BSMD without readout will accrue. A major upgrade to the BSMD readout could address all the above operational and performance issues and is the proposed best path.

Details:

1. Spare parts. The pool of spare parts is almost empty. In particular, there are two ASICs in the BSMD FEE cards for which we will run out of spares in ~ 2 years. The batch of amplifier shapers (SAS), a modification of the original STAR TPC SAS, was produced once in 2000. The fabrication process is now obsolete. The average rate of repairs recorded during 2006-2010 was about 30 SAS chips per year. There was a spike in 2009 (45 chips were replaced), perhaps related to the increased radiation environment during the 500 GeV p+p run. The failure mode is not understood, although it is not likely due to radiation effects alone since it is largely confined to the "U1" and "U6" chip locations. With the current projections, after Run 12 we will be left without spare SAS chips. The second ASIC is a Storage Capacitor Array (SCA) chip, for which we have seen roughly the same rate of repairs as for the SAS, but with considerably more fluctuation. After Run 12, we may be without spare SCA chips also. For the SCA, extra ("good batch", see below) wafers exist which can be re-packaged to produce the needed SCAs for the next ten years of operation. The bottom line is, without spare ASICs for FEE repair, every year after Run 12 will see about a 5% decrease (3% from SAS alone) of the BSMD working readout coverage.

2. The efficiency of data taking at present depends largely on the reliability of the FEEs. Although still somewhat problematic, several of the past issues with readout crate operation, which are located on the STAR magnet backlegs, have been resolved with a series of modifications and upgrades carried out during 2007-2011. However, the failure rate of the FEEs has remained basically the same for the past five years. The early hopes that, after initial high mortality rate the failure rate would decrease with time, are so far not clearly realized, although the most recent 2010 SCA repair rate is at a new low point. The main reasons for this are defective ASICs ("bad batch" SCA on the east side) and the SAS failures described above.

3. The limited dynamic range of the present design is another factor which limits effectiveness of data taking. The BSMD readout design was borrowed from the original SVT implementation. While it was clear from day one that the 10-bit ADC was quite marginal, the compromise was made because of a budget constraint for the whole BEMC project. At the present nominal working point, saturation of a BSMD central strip (e.g., at channel $\sim$ 850) is in the range 4-7 GeV (depending on detector plane and location), as deduced from extrapolation of a recent calibration using electrons in the range from 2-6 GeV. At the lower end this corresponds to electrons of total energy $\sim$ 6.5 GeV assuming 62% of the energy in the central strip. With a pedestal of nominal 150 channels and width of several channels, the present configuration has a dynamic range of roughly 425. The desired dynamic range is given by a requirement to go as low as possible in measuring the energy deposition for strips in the tails of the electromagnetic showers on the one hand, and by the desire to have reasonable/non-saturated response of the central strip for γ/π^0 characterization up to a scale of order $\sim$ 25 GeV (central strip $\sim$ 15 GeV) on the other. This means increasing the dynamic range over the present by a factor $\sim$ 4 while retaining approximately the current channel dispersion over shower shape (there should also be significant extra margin added for the detector resolution). Any major readout rework will certainly use 12-bit ADCs. Then the combination of a change of HV working point, shift (by new design) of preamplifier gain, and careful matching to the detector characteristics may allow us to approach a desired $\sim$ 2000 dynamic range. Detailed tests with a spare BSMD module are planned to evaluate what is possible. More modest incremental performance gains may be possible by "tuning" the present configuration.

4. Dead time. In the past two years we have incrementally decreased the dead time for the BSMD from 100% dead at 350 Hz to 15% dead at 500 Hz. At present the readout requires a fixed 326 μsec per event, although this could be reduced to 220 μsec if the "bad batch" SCAs would be replaced. Still, the BSMD readout makes it the slowest detector in STAR at present, and hence continues to influence the decision whether or not to include BSMD for a given trigger whose processing or analysis requires BSMD transverse shower profile information (direct photons , e/h rejection, etc.). The increasing sophistication of HLT algorithms, and somewhat separately the desire to increase DAQ speeds (DAQ 10k) for selected triggers, drives the need for lower BSMD dead time. A rebuild of the readout could significantly reduce the dead time ultimately reaching $\sim$ 10% at 10 kHz.

At present we are considering two options:

1. Continue maintaining the present readout system without significant gains in performance. This option will require designing and fabricating a pin-for-pin operational replacement for the current SAS chip. Option one will also require production of the SCA chips from existing wafers. It is estimated that the cost of this option will be in the 200-300 k$ range and be highly dependent on how one might be able to leverage existing chip designs, what unexpected issues arise, etc. (Note: It is possible to replace all the "bad batch" SCA chips in the system. This should increase SCA reliability as well as allow increased clock speeds and further reduction of dead time. This task, however, is too large for a usual RHIC shutdown (120 east side FEEs refurbished), and probably requires $\sim$1 year of integrated calendar time work.)

2. Upgrade the readout of the BSMD significantly to boost both its reliability and performance. This will require a new FEE designed essentially from scratch. It may be possible to utilize some components of the existing readout crates to keep the cost down, but much will need to be changed to accommodate the new FEE and to increase reliability and overall readout performance. A more promising approach may be to design the new FEE to work seamlessly with an existing back-end readout system, in particular the FGT/IST readout could work for BSMD with a new flavor of "APV" front end ASIC. With any new design the dead time will be significantly reduced and the dynamic range increased as much as feasible. An accurate cost estimate for this option will require significant FY11 engineering efforts. However, it is believed that an "almost all new readout" for BSMD will cost somewhere between $1-2M.

4.3.6 Improved spatial resolution for the inner BBC tiles

There are ideas to implement a small detector which would provide roughly 1 mm resolution over the small BBC tiles. It would be used for local polarimetry for the spin physics program, to learn about the physics in Diffractive Dissociation, and to help in finding the reaction plane in heavy ion measurements. The original motivation was a follow-up on a STAR data analysis and Monte-Carlo of events with correlated BBC and ZDC hits. These have kinematics consistent with diffraction dissociation, and show enhanced spin asymmetries compared to single detector asymmetries. It is hypothesized that these events consists of a neutron into the ZDC and a single (or a few) charged pions in the BBC.

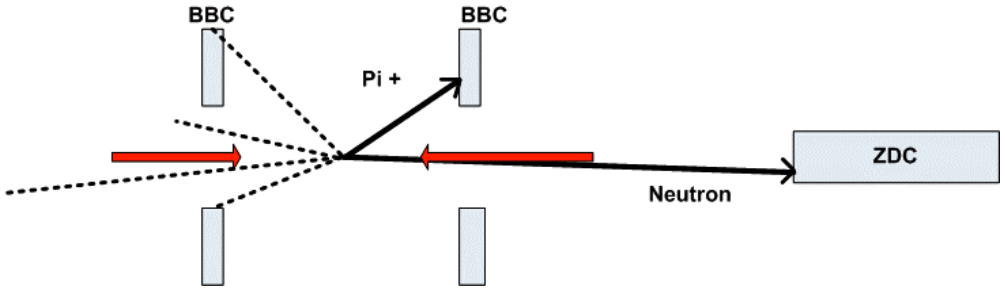

Figure 4.10: Example of a 2-body event with correlated hits in ZDC and BBC. The innermost BBC counters are at approximately rapidity of 4 to 5 , and are 8.3 cm wide. The effective $(n\pi^+)$ mass resolution with this position resolution for the pion is several GeV/c^2.

The current BBC has insufficient resolution to reconstruct the mass of the $n\pi^+$, so a better resolution detector is warranted. It is considered to use a new technology of Thick GEMs, which could use the electronics being developed for the FGT upgrade. The number of channels of the proposed set of 12 small detectors would be 5% of the FGT channels. We are investigating the best way to build a prototype, and the options for layouts are being investigated. A resolution of roughly 1 mm at the inner BBC would improve mass resolution greatly, so that it would be limited by other factors such as the ZDC spatial and energy resolution. Strips can be used over the 8.3 cm detector size since the multiplicity is very low .

4.4 RHIC accelerator improvements

The experimental measurements described in this Decadal Plan will make full use of the flexibility of the RHIC facility to collide beams ranging from protons to uranium, including both symmetric and asymmetric systems, over a broad range of energies. Many of the measurements also depend crucially on the increased heavy ion luminosity that will be available upon completion of the RHIC-II upgrade, as well as the increased proton luminosity that is anticipated when electron lenses are installed. In addition, some of the anticipated measurements require – or will profit greatly from – further improvements to the RHIC accelerator complex beyond this baseline. The list includes:

- Higher luminosity for proton beams
- Low-energy electron cooling for heavy-ion beams
- Availability of p+A collisions
- Increased beam energies, up to 325 GeV for protons
- Polarized ^{3}He beams

The available proton beam luminosities play a critical role in the STAR physics program. Measurements of the longitudinal single-spin asymmetry for W production in polarized p+p collisions are currently underway. Measurements are planned of the transverse single-spin asymmetry for Drell-Yan production in polarized p+p collisions. Future measurements might also explore the transverse single-spin asymmetries for W or Z production. Measurements of the cross section for Drell-Yan production in p+A collisions for at least a couple of different "target" nuclei are also planned. These processes involve very small cross sections. The available p+p luminosities also represent the primary limit on STAR's ability to measure R_{AA} for γ+jet and Υ production. All of these investigations would profit greatly from additional increases in proton beam luminosities beyond those anticipated from electron lenses, such as might be achieved with coherent electron cooling.

The STAR program to search for the QCD critical point and the associated first-order phase transition line is discussed in Sect. 2.3. The first, survey phase of this program is underway now. The measurements during this phase are being performed at a coarse sequence of energies spanning the full range available at RHIC. If the results from the first phase provide indications that the QCD critical point is accessible at RHIC, a second phase will explore the critical point region with considerably higher precsion. If the region of interest ends up near the lower end of the survey energies, we will require electron cooling for the heavy-ion beams in order to perform the second-phase measurements in a practical time period. If the region of interest ends up at higher energies, the currently available luminosities should suffice, and electron cooling won't be required. STAR should be able to provide a definitive statement on this point within a year after the completion of the current survey phase.

Section 3.3 emphasizes the importance of performing future investigations of the partonic structure of heavy nuclei with p+A collisions, for example to explore the onset of gluon saturation. Formally, this capability has been available at RHIC since it first turned on. However, it requires

realignment of the DX magnets in order to compensate for the large difference in the beam rigidities. C-AD indicates that essentially the entire period of a standard RHIC shut-down would be required to perform this realignment [287]. A second comparable period would be needed to move the DX magnets back to their conventional locations before returning to p+p and A+A collisions. RHIC Runs 3 and 8 studied d+Au collisions as a compromise, which both minimized the effort required by C-AD and permitted p+p collisions to be investigated during the same running periods. STAR believes it will be essential to perform future exploration of the initial state with p+A collisions, combining studies with light and heavy nuclear beams into a single running period to minimize the necessary overhead.

Most of the RHIC magnets could support a 30% increase in the beam energy, but new DX magnets would be required to make this possible. Increasing the p+p center-of-mass energy from 500 GeV to 650 GeV would double the cross section for W production, as noted in Sect. 3.1. It would also lead to a significant increase in the cross section for Drell-Yan production in the forward direction. In both cases, the higher energy would also extend the kinematic reach to lower x. Higher beam energies would also provide access to higher energy densities in heavy-ion collisions, especially for U+U. STAR urges C-AD to investigate the cost and effort required to achieve such an increase.

To date, the RHIC spin program has focused solely on p+p collisions. During the coming decade, STAR expects to expand this to include p+A collisions with transversely polarized proton beams. Polarized ^{3}He is another attractive option, as it provides effective access to polarized neutrons. This could open additional avenues for future study, involving both transversely and longitudinally polarized beams. Polarized ^{3}He beams will also be quite valuable for further future experiments with eRHIC. It is believed that polarized ^{3}He beams should be available with the new EBIS source. R&D will will needed to make this a reality.

4.5 Upgrade Schedule and Projected Costs

Tables 4.1 and 4.2 show the estimated cost range and when the various STAR upgrades in fact could technically be implemented. The future upgrades that will support the physics program in the latter part of the decade and in the initial part of an eRHIC era need significant development of the concepts, followed by R&D for detector technology, particular for the forward upgrades in the electron forward region. It is too early to give an estimate for such upgrade. STAR is establishing a task force with the goal of strengthening the physics case for eSTAR, developing the forward detector upgrade concepts, and identifying the R&D needed for them.

Table 4.1: STAR detector upgrades.

upgrade	category	status	years	cost (k$)
HFT	MIE	on-going	FY10-FY14	15,200
MTD	capital	proposal/BNL reviewed	FY11-FY13	1,600
RP-II	capital	proposal	FY11-12	850
FHC	ops.	proposal	FY11/12	80
Forward Upgrade	MIE	Concept (R&D)	FY14-18	8,000-
eSTAR Forward e-Upgrade	MIE	Concept (R&D)	FY17-	?

Table 4.2: STAR detector improvements. The range of cost indicates the range of considered options, and in case of the TPC the high range is the cost if all sectors must be replaced.

Improvement	category	status	years	cost (k$)
TPC	ops+capital	planning	FY11-	300-1,900
HLT	ops+capital	in use+conceptual	FY11-FY14	100-500
BSMD	ops + capital	planning	FY11-FY12	300-2,000
Trigger	capital	plans & concepts	FY11-FY14	1,850
DAQ10K	ops	R&D	FY11-FY12	100

Chapter 5

Evolution of the STAR Collaboration

At the present time, the STAR Collaboration consists of 540 collaborators from 52 institutions and 12 countries. About 390 of them are scientific authors. (See `http://www.star.bnl.gov/` for more details about the STAR Collaboration.) The proportional composition from US, European, and Asian institutions is 48%, 22%, and 28%, respectively. The major physics programs within the collaboration are research topics related to proton spin physics and relativistic heavy ion physics.

Although a few groups have shifted their attention to the LHC program, major national laboratories (ANL, BNL, LBNL) and universities remain committed to the STAR/RHIC physics program. The RHIC Beam Energy Scan program, which is searching for the critical point in the QCD phase diagram and is being carried out with enhanced particle identification capabilities in STAR via the inclusion of the barrel Time-of-Flight detector, has led to increased participation from the Asian and European groups at the level of 5-10%. Since 2008, three groups have joined the STAR Collaboration. The applications from three more groups, who have expressed keen interest in joining the collaboration, are being discussed in the STAR Council. Some of these groups have expertise in lepton-hadron and photon-hadron scattering, relevant to STAR's future physics programs.

We expect this strong participation to continue, especially in the areas of heavy flavor and spin physics, due to the inclusion of the Heavy Flavor Tracker, Muon Telescope Detector, and Forward GEM Tracker in STAR in the near future. This should ensure sufficient manpower to carry out STAR's scientific programs.

The management of the collaboration has drawn up an action plan to boost efforts for detector R&D and physics analysis in the forward rapidity region. Currently, there are only a few participating institutions with a primary focus on forward physics. In the near future, we shall establish a task force, eSTAR, to focus on guiding the forward rapidity related projects, including the detector R&D and physics analyses discussed in this plan. Our goal is to gradually expand the collaboration to harvest the rich physics possibilities that are available at forward rapidities, while maintaining the STAR experiment's physics strengths at mid-rapidity. In addition, we plan to work on attracting more colleagues with a knowledge of lepton-hadron and/or photon-hadron scattering physics to join the STAR experiment. They will certainly enhance the physics case planned by the collaboration for eSTAR, which is needed for the development of the future EIC physics program. In order achieve this goal, we will organize annual workshops, make forward physics discussions a

regular feature of our collaboration meetings, and encourage members of the eSTAR task force to discuss the program laid out in this document with prospective new collaborating institutions.

Bibliography

[1] N. Borghini *Eur. Phys. J.* **A 29**, 27 (2006).

[2] T. Biro and B. Muller, *Phys. Lett.* **B 578**, 78 (2004), and references therein.

[3] J. M. Maldacena, *Adv. Theor. Math. Phys.* **2**, 231 (1998).

[4] M. Muller *et al., Phys. Rev. Lett.* **103**, 025301 (2009).

[5] J. E. Thomas, *Nucl. Phys.* **A 830**, 665c (2009).

[6] A. Andronic, P. Braun-Munzinger, J. Stachel and H. Stoecker, arXiv:1010.2995 [nucl-th].

[7] A. Andronic, P. Braun-Munzinger and J. Stachel, *Phys. Lett.* B **673**, 142 (2009) [Erratum-ibid. B **678**, 516 (2009)] [arXiv:0812.1186 [nucl-th]].

[8] J. Adams *et al.*, *Phys. Rev. Lett.* **92**, 112301 (2004).

[9] E.Schnedermann, J.Sollfrank and U.Heinz, *Phys. Rev.* **C 48**, 2462 (1993).

[10] Z. Tang *et al.*, *Phys. Rev.* **C 79**,051901 (2009).

[11] A. Adare *et al.*, arXiv:1005.3674v1.

[12] J. Adams *et al.*, *Phys. Rev. Lett.* **98**, 62301 (2007).

[13] B. Abelev *et al.*, *Phys. Rev. Lett.* **99**, 112301 (2007); B. Abelev *et al.*, *Phys. Rev.* **C 79**, 064903 (2009).

[14] M. Shao *et al.*, *J. Phys.* **G37**, 085104 (2010).

[15] H. van Hecke, H. Sorge, and N. Xu, *Phys. Rev. Lett.* **81**, 5764 (1998).

[16] J. Adams *et al.*, *Nucl. Phys.* **A757**, 102 (2005).

[17] P. Kolb and U. Heinz, arXiv:nucl-th/0305084v2.

[18] T.Trainor *Int. J. Mod. Phys.* **E 17**, 1499 (2008).

[19] H. Sorge, *Phys. Lett.* **B 402**, 251 (1997).

[20] H. Sorge, *Phys. Rev. Lett.* **82**, 2048 (1999).

[21] J. Adams *et al.*, *Phys. Rev. Lett.* **92**,052302 (2004).

[22] P. Huovinen, P.F. Kolb, U. Heinz, P.V. Ruuskanen and S.A. Voloshin, *Phys. Lett.* **B 503**, 58 (2001).

[23] P. F. Kolb and U. Heinz, in Quark Gluon Plasma 3, eds. R.C. Hwa and X.N. Wang (World Scientific, Singapore, 2003); nucl-th/0305084.

[24] M. Gyulassy, nucl-th/0403032.

[25] A. Adil *et al.*, *Phys. Rev.* **C 74**, 044905 (2006); T. Hirano *et al.*, *Phys. Rev.* **B 636**, 299 (2006); H. Song *et al.*, *Phys. Rev.* **C 78**, 024902 (2008); T. Hirano, *J. Phys.* **G 36**, 064031 (2009).

[26] M. Luzum *et al.*, *Phys. Rev.* **C 78**, 034915 (2008).

[27] G. Policastro *et al.*, *Phys. Rev. Lett* **87**, 081601 (2001).

[28] A. Tang, *Nucl. Phys.* **A 830**, 673c (2009).

[29] R. Ryblewski (2010) arXiv:1007.4718 [nucl-th].

[30] T. Hirano, *Phys. Rev.* **C 65**, 011901 (2002).

[31] R. Andrade, F. Grassi, *et al. Eur. Phys. J.* **A 29**, 23 (2006).

[32] B. Abelev *et al.*, *Phys. Rev.* **C 77**, 54901 (2008).

[33] P. Huovinen and P.V. Ruuskanen, *Ann. Rev. Nucl. Part. Sci.* **56**, 163 (2006).

[34] D. Kettler *et al.*, *Eur. Phys. J.* **C 62**, 175 (2009).

[35] R. C. Hwa and C. B. Yang, *Phys. Rev.* **C 70**, 024904 (2004); R. C. Hwa and C. B. Yang, *Phys. Rev.* **C 75**, 054904 (2007).

[36] C. Nonaka, R.J. Fries and S.A. Bass, *Phys. Lett.* **B 583**, 73 (2004); C. Nonaka *et al.*, *Phys. Rev.* **C 69**, 031902 (2004).

[37] V. Greco, C. Ko and P Levai, *Phys. Rev.* **C 68**, 034904 (2003).

[38] R. Fries, *J. Phys. G: Nucl. Part. Phys.* **30**, S85 (2004).

[39] J. Jia and C. Zhang, *Phys. Rev.* **C 75**, 031901 (2007).

[40] S.S. Shi, et al. (STAR Collaboration), QM2009 proceedings, arXiv: 0907.2265.

[41] C. Chiu and R. Hwa, *Phys. Rev.* **C 76**, 024904 (2007).

[42] J. Adams *et al.*, *Phys. Rev. Lett.* **95**, 152301 (2005).

[43] B.I. Abelev *et al.*, *Phys. Rev.* **C 80**, 064912 (2009).

[44] N. Armesto *et al.*, *Phys. Rev. Lett.* **93**, 242301 (204); P. Romatschke, *Phys. Rev.* **C 75**, 014901 (2007); A. Majumder, B. Muller, S.A. Bass, *Phys. Rev. Lett.* **99**, 042301 (2007); C.Y. Wong, *Phys. Rev.* **C 76**, 054908 (2007); C.B. Chiu, R.C. Hwa, *Phys. Rev.* **C 72** 034903 (2005); E.V. Shuryak, *Phys. Rev.* **C 76**, 047901 (2007).

[45] M. Schroedter, R. L. Thews and J. Rafelski, *Phys. Rev.* **C 62**, 024905 (2000).

[46] F. Becattini, *Phys. Rev. Lett.* **95**, 022301 (2005).

[47] I. Kuznetsova and J. Rafelski,*Eur. Phys. J.* **C 51**, 113 (2007).

[48] V. Greco *et al., Phys. Lett.* **B 595**, 202 (2004).

[49] T. Matsui *et al., Phys. Lett.* **B 178**, 416 (1986).

[50] R.L. Thews *et al., Phys. Rev.* **C 63**, 054905 (2001); H. van Hees *et al., Phy. Rev.* **C 73**, 034913 (2006).

[51] A. Mocsy, P. Petreczky, *Phys. Rev.* **D 77**, 014501 (2008).

[52] R. G. de Cassagnac *J. Phys.* **G 35**, 104023 (2008).

[53] L. Ruan *et al. J.Phys.* **G 36**, 095001 (2009).

[54] A. Frawley, T. Ullrich and R. Vogt, *Phys. Rep.* **462**, 125 (2008).

[55] Phys.Rev.Lett. **37**, 249 (1976).

[56] S. Aronson *et al.*, Phys.Rev.Lett. **48**, 1078 (1982).

[57] G. Baym *et al.*, Phys.Rev D **48**, R3957 (1993).

[58] Joseph I. Kapusta and Agnes Mocsy, Phys.Rew.C **59**, 2937 (1998).

[59] Acta Phys. Pol. 10 (1979) 635

[60] J. Adams *et al.,* [the STAR Collaboration], *Phys. Rev. Lett.* **95**, 152301 (2005); M. M. Aggarwal *et al.,* (the STAR Collaboration), arXiv:1004.2377.

[61] B.I. Abelev *et al.,* [the STAR collaboration], *Phys. Rev. Lett.* **102**, 052302 (2009).

[62] B. Alver *et al., Phys. Rev.* **C 81**, 054905 (2010); H. Petersen *et al.,* arXiv:1008.0625 [nucl-th]; H. Agakishiev *et al.,* [the STAR Collaborations], arXiv:1010.0690v1 [nucl-ex].

[63] C. Adler *et al.* [STAR Collaboration], Phys. Rev. Lett. **89**, 202301 (2002) [arXiv:nucl-ex/0206011].

[64] C. Adler *et al.* [STAR Collaboration], Phys. Rev. Lett. **90**, 082302 (2003) [arXiv:nucl-ex/0210033].

[65] J. Adams *et al.* [STAR Collaboration], Phys. Rev. Lett. **91**, 072304 (2003) [arXiv:nucl-ex/0306024].

[66] R. Baier, and D. Schiff and B.G. Zakharov Ann. Rev. Nucl. Part. Sci., **50**, 37 (2000).

[67] M. Gyulassy, I. Vitev, X. N. Wang and B. W. Zhang, arXiv:nucl-th/0302077.

[68] Y. L. Dokshitzer and D. E. Kharzeev, Phys. Lett. **B 519**, 199 (2001) [arXiv:hep-ph/0106202].

[69] B. I. Abelev *et al.* [STAR Collaboration], Phys. Rev. Lett. **98**, 192301 (2007) [arXiv:nucl-ex/0607012].

[70] A. Adare *et al.* [PHENIX Collaboration], Phys. Rev. Lett. **98**, 172301 (2007) [arXiv:nucl-ex/0611018].

[71] M. M. Aggarwal *et al.* [STAR Collaboration], Phys. Rev. Lett. **105**, 202301 (2010) [arXiv:1007.1200 nucl-ex]].

[72] B. I. Abelev *et al.* [STAR Collaboration], Phys. Rev. **C 82**, 034909 (2010) [arXiv:0912.1871 [nucl-ex]].

[73] M. Ploskon [STAR Collaboration], Nucl. Phys. **A 830**, 255C (2009) [arXiv:0908.1799 [nucl-ex]].

[74] M. Cacciari and G. P. Salam, Phys. Lett. **B 641**, 57 (2006) [arXiv:hep-ph/0512210].

[75] M. Cacciari, G. P. Salam and G. Soyez, JHEP **0804**, 063 (2008) [arXiv:0802.1189 [hep-ph]].

[76] M. Cacciari and G. P. Salam, Phys. Lett. **B 659**, 119 (2008) [arXiv:0707.1378 [hep-ph]].

[77] J. Putschke [STAR Collaboration], proceedings of Hard Probes 2010.

[78] O. Barannikova [STAR Collaboration], J. Phys. **G 35**, 104086 (2008).

[79] S. A. Bass, C. Gale, A. Majumder, C. Nonaka, G. Y. Qin, T. Renk and J. Ruppert, J. Phys. **G 35**, 104064 (2008) [arXiv:0805.3271 [nucl-th]].

[80] S. A. Bass, C. Gale, A. Majumder, C. Nonaka, G. Y. Qin, T. Renk and J. Ruppert, Phys. Rev. **C 79**, 024901 (2009) [arXiv:0808.0908 [nucl-th]].

[81] Theory-Experimental Collaboration on Hot Quark Matter [TECHQM], https://wiki.bnl.gov/TECHQM/index.php/Main_Page .

[82] Topical collaboration on Jet and Electromagnetic Tomography of Extreme Phases of Matter in Heavy-ion Collisions [JET Collaboration], http://jet.bnl.gov .

[83] B. Muller, arXiv:1010.4258 [hep-ph].

[84] T. Renk, Phys. Rev. **C 80**, 014901 (2009) [arXiv:0904.3806 [hep-ph]].

[85] C. A. Salgado and U. A. Wiedemann, Phys. Rev. **D 68**, 014008 (2003) [arXiv:hep-ph/0302184].

[86] H. Zhang, J. F. Owens, E. Wang and X. N. Wang, Nucl. Phys. **A 830**, 443C (2009) [arXiv:0907.4816 [hep-ph]].

[87] G. Y. Qin, J. Ruppert, C. Gale, S. Jeon and G. D. Moore, Phys. Rev. **C 80**, 054909 (2009) [arXiv:0906.3280 [hep-ph]].

[88] W. Fischer *et al.,* , http://www.agsrhichome.bnl.gov/RHIC/Runs/RhicProjections.pdf .

[89] W.A. Horowitz *et al., J. Phys.* **G 35**, 104152 (2008).

[90] J. Adams, et al., (STAR Collaboration), Nucl. Phys. **A 757**, 102 (2005) and references therein.

[91] F. Karsch, et al., Nucl. Phys. Proc. Suppl. **129**, 614 (2004); M. Cheng, et al., Phys. Rev. **D 79**, 074505 (2009) and references therein.

[92] M. Stephanov, Prog. Theor. Phys. Suppl. **153**, 139 (2004); Int. J. Mod. Phys. **A 20**, 4387 (2005); Z. Fodor and S.D. Katz, JHEP **0404**, 50 (2004).

[93] R. V. Gavai and S. Gupta, Phys. Rev. **D 78**, 114503 (2008); Phys. Rev. **D 71**, 114014 (2005); arXiv:1001.3796; S. Gupta, arXiv:0909.4630.

[94] M. A Stephanov, arXiv:0911.1772.

[95] J. Cleymans, H. Oeschler, K. Redlich, and S. Wheaton, Phys. Rev. **C 73**, 034905 (2006).

[96] STAR Note: SN0493; http://drupal.star.bnl.gov/STAR/starnotes/public/sn0493.

[97] M.M. Aggarwal, et al. (STAR Collaboration), arXiv: 1007.2613.

[98] B. I. Abelev, et al., (STAR Collaboration), Phys. Rev. **C 81**, 024911 (2010).

[99] A. Adare, et al., (PHENIX Collaboration), Phys. Rev. Lett. **104**, 132301 (2010); M. M. Aggarwal et al., (WA98 Collaboration), Phys. Rev. Lett. **85**, 3595 (2000).

[100] M. Asakawa et al., Phys. Rev. Lett. **101**, 122302 (2008).

[101] M. Asakawa, S. A. Bass, B. Muller, and C. Nonaka, Phys. Rev. Lett. **101**, 122302 (2008).

[102] M. Stephanov et al., Phys. Rev. **D 60**, 114028 (1999).

[103] M. Asakawa, et al., Phys. Rev. Lett. **103**, 262301 (2009).

[104] M.M. Aggarwal, et al. (STAR Collaboration), Phys. Rev. Lett. **105**, 22302 (2010).

[105] B. Berdnikov and K. Rajagopal, Phys. Rev.**D 61**, 105017(2000); M. Asakawa and C. Nonaka, Nucl. Phys. **A 774**, 753 (2006).

[106] S.S. Shi, et al. (STAR Collaboration), QM2009 proceedings, arXiv: 0907.2265.

[107] M.M. Aggarwal, et al. (STAR Collaboration), Phys. Rev. Lett. **103**, 251601 (2009) and references therein.

[108] F. Karsch and K. Redlich, arXiv:1007.2581.

[109] D. H. Rischke and M. Gyulassy, Nucl. Phys. **A608**, 479(1996).

[110] F. Retiere and M. A. Lisa, Phys. Rev. **C70**, 044907(2004).

[111] M. A. Lisa, U. W. Heinz, and U. A. Wiedemann, Phys. Lett. **B489**, 287(2000).

[112] U. W. Heinz and P. F. Kolb (2002), hep-ph/0204061.

[113] B. I. Abelev *et al.* [STAR collaboration], Phys. Rev. Lett. **103**, 251601 (2009).

[114] B. I. Abelev *et al.* [STAR collaboration], Phys. Rev. **C 81**, 054908 (2010).

[115] E. V. Shuryak and T. Schafer, Ann. Rev. Nucl. Part. Sci. **47**, 359 (1997).

[116] D. Diakonov, Prog. Part. Nucl. Phys. **51**, 173 (2003).

[117] D. Kharzeev, Phys. Lett. **B 633**, 260 (2006).

[118] D. E. Kharzeev, L. D. McLerran and H. J. Warringa, Nucl. Phys. **A 803**, 227 (2008).

[119] P. V. Buividovich, M. N. Chernodub, E. V. Luschevskaya and M. I. Polikarpov, Phys. Rev. **D 80**, 054503 (2009).

[120] M. Abramczyk, T. Blum, G. Petropoulos and R. Zhou, arXiv:0911.1348 [hep-lat].

[121] P. V. Buividovich, E. V. Lushchevskaya, M. I. Polikarpov and M. N. Chernodub, JETP Lett. **90**, 412 (2009).

[122] C. Nepali, G. Fai and D. Keane, Phys. Rev. **C 76**, 051902 (2007); Erratum, ibid. **76**, 069903 (2007).

[123] S. A. Voloshin, arXiv:1003.1127 [nucl-ex].

[124] S. A. Voloshin, arXiv:1006.1020 [nucl-th].

[125] B. Hong *et al.* [FOPI Collaboration], Phys. Rev. **C 66**, 034901 (2002).

[126] B. Hong *et al.* [FOPI Collaboration], Nucl. Phys. **A 721**, 317 (2003).

[127] B. I. Abelev *et al.* [STAR collaboration], STAR Note SN-0493; M. M. Aggarwal *et al.* [STAR collaboration], arXiv:1007.2613 [nucl-ex].

[128] L. Foà, Phys. Rep. **22**, 1 (1975).

[129] D. M. Ostrovsky, G. W. Carter and E. V. Shuryak, Phys. Rev. **D 66**, 036004 (2002).

[130] E. Shuryak and I. Zahed, Phys. Rev. **D 68**, 034001 (2003).

[131] W. Guryn, Acta. Phys. Polon. **B 40**, 1897 (2009); STAR pp2pp Phase II Proposal http://drupal.star.bnl.gov/STAR/system/files/STARPhaseIIupdate04142010.pdf .

[132] G.E. Brown and M. Rho, Phys. Rev. Lett. **66**, 2720 (1991).

[133] R. Rapp and J. Wambach, Adv. Nucl. Phys. **25**, 1 (2000); also references therein.

[134] G. David, R. Rapp and Z. Xu, Phys. Rept. **462**, 176 (2008).

[135] L. McLerran and T. Toimela, Phys. Rev. **D 31**, 545 (1985).

[136] NA60 Collaboration, Phys. Rev. Lett. **96**, 162302 (2006).

[137] NA45 Collaboration, Phys. Lett. **B 422**, 405 (1998).

[138] PHENIX Collaboration, Phys. Rev. **C 81**, 034911 (2010); arXiv:0706.3034.

[139] NA60 Collaboration, Phys. Rev. Lett. **100** 022302 (2008).

[140] M. Shao *et al.*, Nucl. Instrum. Meth. **A 558**, 419 (2006).

[141] NA60 Collaboration, Eur. Phys. J. **C 59**, 607 (2009).

[142] A.E. Dorokhov, arXiv:0905.4577.

[143] J.D. Bjorken *et al.*, Phys. Rev. **D 80**, 075018 (2009).

[144] M.J. Savage, M.E. Luke and M.B. Wise, Phys.Lett. **B 291**, 481 (1992).

[145] L. Bergstrom, Z. Phys. **C 14** 129 (1982); L. Bergstrom *et al.*, Z. Phys. **C 37**, 281 (1988).

[146] Muon (g-2) Collaboration, Phys. Rev. **D 73**, 072003 (2006).

[147] KTeV Collaboration, Phys. Rev. **D 75**, 012004 (2007).

[148] HyperCP Collaboration, Phys. Rev.Lett. **94**, 021801 (2005).

[149] L. G. Landsberg, Phys. Reports **128**, 301 (1985).

[150] CLEO Collaboration, Phys. Rev. **D 56**, 5359 (1997); CELSIUS/WASA Collaboration, arXiv:0711.3531, Phys. Rev. **D 77**, 032004 (2008).

[151] B. I. Abelev et al., *Science* **328**, 58 (2010).

[152] E864 Collaboration, T.A. Armstrong *et al.*, *Phys. Rev. Lett.* **83**, 5431 (1999).

[153] W. Greiner, Int. J. Mod. Phys. **E 5**, 1 (1996).

[154] C. Greiner *et al.*, Phys. Rev. **D 38**, 2797 (1988).

[155] J. Schaffner *et al.*, Phys. Rev. **C 46**, 322 (1992).

[156] J. Schaffner *et al.*, Annals Phys. **235**, 35 (1994).

[157] S. Zhang et al., *Phys. Lett.* **B 684**, 224 (2010).

[158] A. Andronic, P. Braun-Munzinger, J. Stachel and H. Stoecker, arXiv: 1010.2995.

[159] J. M. Lattimer, M. Prakash, *Science* **304**, 536 (2004).

[160] R. Fries *et al.*, Ann. Rev. Nucl. Part. Sci. **58**,177 (2008).

[161] H. Sato and K. Yazaki, Phys. Lett. **B 98**, 153 (1981).

[162] D. J. Millener, C. B. Dover and A. Gal, Prog. Theor. Phys. Suppl. **117**, 307 (1994).

[163] J. Adams et al., *Phys. Rev. Lett.* **98**, 062301 (2007).

[164] M. Iwasake at al., *Phys. Rev. Lett.* **67**, 1246 (1991).

[165] For a review, see F.E. Close, Rep. Prog. Phys. **51**, 833 (1988), and C. Amsler and N.A. Tornqvist, Phys. Rept. **389**, 61 (2004).

[166] S. Abatziz *et al.*, Phys. Lett. **B 324**, 509 (1994).

[167] V. Crede and C.A. Meyer, Prog. Part. Nucl. Phys. **63**, 74 (2009).

[168] F.E. Close and A. Kirk, Phys. Lett. **B 397**, 333 (1990).

[169] K.H. Streng, Phys. Lett. **B 166**, 443 (1986).

[170] Yu.A. Simonov, Phys. Lett. **B 249**, 514 (1990).

[171] J. Adams *et al.*, Phys. Rev. Lett. **98**, 62301 (2007).

[172] JH Chen et al, Phys. Rev. **C 78**, 034907 (2008).

[173] R.L. Jaffe, Phys. Rev. Lett. **38**, 195 (1977); Erratum ibid, **38**, 617 (1977).

[174] A. Ohnishi et al, Nucl. Phys. **A 670**, 297c (2000).

[175] J. Schaffner-Bielich, R. Mattiello and H. Sorge, Phys. Rev. Lett. **84**, 4305 (2000).

[176] G.E. Miller, arXiv: nucl-th/0607006.

[177] STAR Collaboration, B.I.Abelev *et al.*, arXiv: nucl-ex/0909.0566.

[178] Z.Y. Zhang et al, Phys. Rev. **C 61** 065204, 2000.

[179] S.H. Lee *et al.*, Eur. Phys. J. **C 54**, 259 (2008).

[180] D. Diakonov, arXiv: 1003.2157 [hep-ph].

[181] G. Bunce, N. Saito, J. Soffer, and W. Vogelsang, Ann. Rev. Nucl. Part. Sci. **50** (2000), 525.

[182] B. I. Abelev et al. (STAR Collaboration), Phys. Rev. Lett. **97** (2006), 252001.

[183] B. I. Abelev et al. (STAR Collaboration), Phys. Rev. Lett. **100** (2008), 232003.

[184] B. Jäger, M. Stratmann, and W. Vogelsang, Phys. Rev. **D70** (2004), 034010.

[185] B. Jäger, A. Schafer, M. Stratmann, and W. Vogelsang, Phys. Rev. **D67** (2003), 054005.

[186] D. de Florian, R. Sassot, M. Stratmann, and W. Vogelsang, Phys. Rev. Lett. **101** (2008), 072001.

[187] D. de Florian, R. Sassot, M. Stratmann, and W. Vogelsang, Phys. Rev. **D80** (2009), 034030.

[188] D. de Florian, Phys. Rev. **D79** (2009), 114014.

[189] D. de Florian and W. Vogelsang, *Helicity Parton Distributions from Spin Asymmetries in W- Boson Production at RHIC*, (2010).

[190] B. I. Abelev et al. (STAR Collaboration), Phys. Rev. **D80** (2009), 111108.

[191] S. W. Wissink et al. (STAR Collaboration), Proceedings of the 18th International Spin Physics Symposium (2008).

[192] A. Kocoloski et al. (STAR Collaboration), Proceedings of the 18th International Spin Physics Symposium (2008).

[193] A. Airapetian et al. (HERMES Collaboration), *Leading order determination of the gluon polarization from high p_T hadron electroproduction*, (2010).

[194] B. Adeva et al., Phys. Rev. **D70** (2004), 012002.

[195] E. S. Ageev et al., , Phys. Lett. **B633** (2006), 25.

[196] M. Alekseev et al., Phys. Lett. **B676** (2009), 31.

[197] P. M. Nadolsky and C. P. Yuan, Nucl. Phys. **B666** (2003), 31.

[198] M. M. Aggarwal et al. (STAR Collaboration), *Measurement of the parity-violating longitudinal single- spin asymmetry for $W^{\pm}$ boson production in polarized proton-proton collisions at $\sqrt{s} = 500\,GeV$*, (2010).

[199] J. Stevens et al. (STAR Collaboration), APS Spring Meeting 2010 (2010).

[200] J. Seele et al. (STAR Collaboration), *The STAR W Program : New Results and Future Measurements*, arXiv:1006.0445 [hep-ex], (2010).

[201] A. Airapetian et al., Phys. Rev. **D71** (2005), 012003.

[202] A. Airapetian et al., Phys. Lett. **B666** (2008), 446.

[203] M. Alekseev et al., Phys. Lett. **B680** (2009), 217.

[204] A. Adare et al. (PHENIX Collaboration), *Cross Section and Parity Violating Spin Asymmetries of $W^{\pm}$ Boson Production in Polarized $p + p$ Collisions at $\sqrt{s} = 500\,\mathrm{GeV}$* (2010).

[205] D. de Florian, M. Stratmann, and W. Vogelsang, Phys. Rev. Lett. **81** (1998), 530.

[206] C. Boros and Z.-T. Liang, Phys. Rev. **D57** (1998), 4491.

[207] Q.-H. Xu, Z.-T. Liang, and E. Sichtermann, Phys. Rev. **D73** (2006), 077503.

[208] Y. Chen, Z.-T. Liang, E. Sichtermann, Q.-H. Xu, and S.-S. Zhou, Phys. Rev. **D78** (2008), 054007.

[209] B. I. Abelev et al. (STAR Collaboration), Phys. Rev. **D80** (2009), 111102.

[210] W. Zhou, S.-S. Zhou, and Q.-H. Xu, Phys. Rev. **D81** (2010), 057501.

[211] K. Abe et al., Phys. Rev. Lett. **96** (2006), 232002.

[212] M. Anselmino et al., AIP Conf. Proc. **1149** (2009), 465.

[213] J. Soffer, Phys. Rev. Lett. **74** (1995), 1292.

[214] F. Yuan, Phys. Rev. **D77** (2008), 074019.

[215] F. Yuan, Phys. Lett. **B666** (2008), 44.

[216] G.L. Kane, J. Pumplin, and W. Repko, Phys. Rev. Lett. **41**, 1689 (1978).

[217] D. L. Adams et al., Z. Phys. **C56** (1992), 181.

[218] C. Bourrely and J. Soffer, Eur. Phys. J. C **36**, 371 (2004).

[219] J. Adams et al. (STAR Collaboration), Phys. Rev. Lett. **92** (2004), 171801.

[220] J. Adams *et al.* [STAR Collaboration], Phys. Rev. Lett. **97**, 152302 (2006).

[221] D. W. Sivers, Phys. Rev. **D41**, 83 (1990).

[222] J. C. Collins, Nucl. Phys. **B396**, 161 (1993).

[223] J.-W. Qiu and G. F. Sterman, Phys. Rev. Lett. **67**, 2264 (1991).

[224] Y. Koike, AIP Conf. Proc. **675**, 449 (2003).

[225] D. Boer and W. Vogelsang, Phys. Rev. D **69**, 094025 (2004).

[226] D. Boer, P. J. Mulders, and P. Pijlman, Nucl. Phys. **B667**, 201 (2003).

[227] X. Ji, J. Qiu, W. Vogelsang, and F. Yuan, Phys. Rev. Lett. **97**, 082002 (2006).

[228] B. I. Abelev et al. (STAR Collaboration), Phys. Rev. Lett. **101** (2008), 222001.

[229] B.I. Abelev *et al.* (STAR Collaboration), Phys. Rev. Lett. **99**, 142003 (2007).

[230] S. J. Brodsky, D. S. Hwang, and I. Schmidt, Phys. Lett. B **530**, 99 (2002).

[231] J.C. Collins, Phys. Lett. **B536**, 43, (2002).

[232] T.C. Rogers and P.J. Mulders, Phys. Rev. D **81**, 094006 (2010).

[233] R. Seidl *et al.* (BELLE Collaboration), Phys. Rev. D **78**, 032011 (2008).

[234] F. Yuan, Phys. Rev. D **77**, 074019 (2008).

[235] I. Arsene et al., Phys. Rev. Lett. **101**, 042001 (2008).

[236] M. Anselmino *et al.*, arXiv: 0807.0166.

[237] Z. Kang, *Some Theory Predictions for Polarized* ^{3}*He*, RHIC Spin Collaboration Meeting - Ames, IA (2010).

[238] A. Bazilevsky et al., Phys. Lett. **B650** (2007), 325.

[239] D. Grosnick et al., *Local Polarimetry for Proton Beams with STAR ZDC Calorimeters*, DNP Fall Meeting 2008 (2008).

[240] O. Grebenyuk et al., *Local Polarimetry with the Zero Degree Calorimeters at STAR*, RHIC-AGS Users' Meeting 2009 (2009).

[241] A. Bridgeman et al., *Local Polarimetry at STAR Using the Zero Degree Calorimeter Shower Maximum Detector*, APS Spring Meeting 2010 (2009).

[242] J. Kiryluk et al., *Local polarimetry for proton beams with the STAR beam beam counters*, (2005).

[243] D. Underwood et al., *Looking for Diffraction Dissociation at RHIC*, RHIC Spin Collaboration Meeting - Ames, IA (2010).

[244] S. L. Bueltmann et al., Phys. Lett. **B579**, 245 (2004).

[245] S. Bultmann et al., Phys. Lett. **B632**, 167 (2006).

[246] S. Bultmann et al., Phys. Lett. **B647**, 98 (2007).

[247] T. Lappi and L. McLerran, Nucl. Phys. A **772**, 200 (2006) [arXiv:hep-ph/0602189].

[248] F. Gelis, S. Jeon and R. Venugopalan, Nucl. Phys. A **817**, 61 (2009) [arXiv:0706.3775 [hep-ph]].

[249] F. Gelis, T. Lappi and R. Venugopalan, Nucl. Phys. A **820**, 111C (2009) [arXiv:0810.1610 [hep-ph]].

[250] N. Armesto, J. Phys. G **32**, R367 (2006) [arXiv:hep-ph/0604108].

[251] H1 and ZEUS Collaborations, H1 prelim-10-044, ZEUS prelim-10-008 [www-h1.desy.de/publications/H1preliminary.short list.html].

[252] L. D. McLerran and R. Venugopalan, Phys. Rev. D **49**, 2233 (1994) [arXiv:hep-ph/9309289].

[253] J. Jalilian-Marian, A. Kovner, A. Leonidov and H. Weigert, Phys. Rev. D **59**, 014014 (1999) [arXiv:hep-ph/9706377].

[254] E. Iancu and R. Venugopalan, (2003), arXiv:hep-ph/0303204.

[255] H. Weigert, Prog. Part. Nucl. Phys. **55**, 461 (2005), arXiv:hep-ph/0501087.

[256] V. N. Gribov and L. N. Lipatov, Sov. J. Nucl. Phys. **15**, 438 (1972).

[257] G. Altarelli and G. Parisi, Nucl. Phys. **B126**, 298 (1977).

[258] Y. L. Dokshitzer, Sov. Phys. JETP **46**, 641 (1977).

[259] E. A. Kuraev, L. N. Lipatov, and V. S. Fadin, Sov. Phys. JETP **45**, 199 (1977).

[260] I. I. Balitsky and L. N. Lipatov, Sov. J. Nucl. Phys. **28**, 822 (1978).

[261] F. Caola, S. Forte and J. Rojo, Phys. Lett. B **686**, 127 (2010) [arXiv:0910.3143 [hep-ph]].

[262] J. Jalilian-Marian, A. Kovner, and H. Weigert, Phys. Rev. **D59**, 014015 (1999).

[263] E. Iancu, A. Leonidov, and L. D. McLerran, Nucl. Phys. **A692**, 583 (2001), arXiv:hep-ph/0011241.

[264] E. Ferreiro *et al.* Nucl. Phys. **A703**, 489 (2002), arXiv:hep-ph/0109115.

[265] I. Balitsky, Nucl. Phys. **B463**, 99 (1996), arXiv:hep-ph/9509348.

[266] Y. V. Kovchegov, Phys. Rev. **D61**, 074018 (2000), arXiv:hep-ph/9905214.

[267] H. Kowalski, T. Lappi and R. Venugopalan, Phys. Rev. Lett. **100**, 022303 (2008) [arXiv:0705.3047 [hep-ph]].

[268] N. Armesto, C. A. Salgado and U. A. Wiedemann, Phys. Rev. Lett. **94**, 022002 (2005) [arXiv:hep-ph/0407018].

[269] I. Arsene *et al.* [BRAHMS Collaboration], Phys. Rev. Lett. **93**, 242303 (2004) [arXiv:nucl-ex/0403005].

[270] E. Braidot for the STAR Collaboration, arXiv:1008.3989 [nucl-ex].

[271] C. Marquet, Nucl. Phys. A **796**, 41 (2007) [arXiv:0708.0231 [hep-ph]].

[272] J. L. Albacete and C. Marquet, arXiv:1005.4065 [hep-ph].

[273] A. Dumitru, A. Hayashigaki and J. Jalilian-Marian, Nucl. Phys. A **765**, 464 (2006) [arXiv:hep-ph/0506308].

[274] B. Z. Kopeliovich, J. Nemchik, I. K. Potashnikova, M. B. Johnson and I. Schmidt, Phys. Rev. C **72**, 054606 (2005) [arXiv:hep-ph/0501260].

[275] W. Vogelsang, private communications (2008).

[276] K. J. Eskola, H. Paukkunen and C. A. Salgado, JHEP **0904**, 065 (2009) [arXiv:0902.4154 [hep-ph]].

[277] K. J. Eskola, H. Paukkunen and C. A. Salgado, Nucl. Phys. A **830**, 599C (2009) [arXiv:0906.4231 [hep-ph]].

[278] R. S. Bhalerao, J. P. Blaizot, N. Borghini and J. Y. Ollitrault, Phys. Lett. B **627**, 49 (2005) [arXiv:nucl-th/0508009].

[279] M. Luzum and P. Romatschke, Phys. Rev. C **78**, 034915 (2008) [Erratum-ibid. C **79**, 039903 (2009)] [arXiv:0804.4015 [nucl-th]].

[280] J. w. Qiu and I. Vitev, Phys. Rev. Lett. **93**, 262301 (2004) [arXiv:hep-ph/0309094].

[281] J. C. Collins, D. E. Soper and G. F. Sterman, Adv. Ser. Direct. High Energy Phys. **5**, 1 (1988) [arXiv:hep-ph/0409313].

[282] F. P. Schilling [H1 Collaboration], Acta Phys. Polon. B **33**, 3419 (2002) [arXiv:hep-ex/0209001].

[283] K. J. Eskola, V. J. Kolhinen and R. Vogt, Nucl. Phys. A **696**, 729 (2001) [arXiv:hep-ph/0104124].

[284] Z. w. Lin and M. Gyulassy, Phys. Rev. Lett. **77**, 1222 (1996) [Heavy Ion Phys. **4**, 123 (1996)] [arXiv:nucl-th/9510041].

[285] H.L. Lai et al., Eur. Phys. J. **C12**, 375 (2000).

[286] A.D. Martin, R.G. Roberts, W.J. Stirling, and R.S. Thorne, Eur. Phys. J. **C4**, 463 (1998).

[287] W. Fischer, private communication (2010).

[288] J. Jalilian-Marian, arXiv:1011.1601 [hep-ph].

[289] F. Gelis and J. Jalilian-Marian, Phys. Rev. D **66**, 014021 (2002) [arXiv:hep-ph/0205037].

[290] J. Jalilian-Marian, Eur. Phys. J. C **61**, 789 (2009) [arXiv:0808.2769 [nucl-th]].

[291] W. Schafer, Nucl. Phys. Proc. Suppl. **198**, 59 (2010) [arXiv:0909.4684 [hep-ph]].

[292] D. Boer and A. Dumitru, Phys. Lett. B **556**, 33 (2003) [arXiv:hep-ph/0212260].

[293] D. Boer, A. Utermann and E. Wessels, Phys. Lett. B **671**, 91 (2009) [arXiv:0811.0998 [hep-ph]].

[294] I. G. Bearden *et al.* [BRAHMS Collaboration], Phys. Rev. Lett. **93**, 102301 (2004) [arXiv:nucl-ex/0312023].

[295] Y. L. Dokshitzer, arXiv:hep-ph/0306287.

[296] A. Dumitru, L. Gerland and M. Strikman, Phys. Rev. Lett. **90**, 092301 (2003) [Erratum-ibid. **91**, 259901 (2003)] [arXiv:hep-ph/0211324].

[297] B. B. Back *et al.*, Phys. Rev. Lett. **91**, 052303 (2003) [arXiv:nucl-ex/0210015].

[298] M. Strikman, private communication (2010).

[299] M. Strikman and W. Vogelsang, arXiv:1009.6123 [hep-ph].

[300] A. Deshpande, R. Milner, R. Venugopalan and W. Vogelsang, Ann. Rev. Nucl. Part. Sci. **55**, 165 (2005).

[301] E. Aschenauer *et al.*, "A High Luminosity, High Energy Electron-Ion-Collider – A White Paper Prepared for the NSAC LRP 2007".

[302] INT, "Gluons and the Quark Sea at High Energies: Distributions, Polarization, and Tomography", http://www.int.washington.edu/PROGRAMS/10-3/ (2010).

[303] I. Schienbein *et al.*, Phys. Rev. D **77**, 054013 (2008).

[304] M. Hirai, S. Kumano, and T.H. Nagai, Phys. Rev. C **76**, 065207 (2007).

[305] S.A. Kulagin and R. Petti, Nucl. Phys. A **765**, 126 (2006).

[306] S.A. Kulagin and R. Petti, Phys. Rev. D **76** 094023 (2007).

[307] I. Schienbein *et al.*, Phys. Rev. D **80**, 094004 (2009) and references therein.

[308] M. Tzanov *et al.* [NuTeV Collaboration], Phys. Rev. D **74**, 012008 (2006).

[309] A. Airapetian *et al.* [HERMES Collaboration], Phys. Rev. Lett. **103**, 152002 (2009).

[310] M.G. Alekseev *et al.* [COMPASS Collaboration], Phys. Lett. B **673**, 127 (2009); ibid. B **692**, 240 (2010).

[311] see e.g. M. Anselmino *et al.*, AIP Conf. Proc. **1149**, 465 (2009).

[312] A. Accardi, F. Arleo, W. K. Brooks, D. D'Enterria and V. Muccifora, Riv. Nuovo Cim. **32**, 439 (2010) [arXiv:0907.3534 [nucl-th]].

[313] A. Airapetian *et al.* [HERMES Collaboration], Nucl. Phys. B **780**, 1 (2007) [arXiv:0704.3270 [hep-ex]].

[314] J. Ashman *et al.* [European Muon Collaboration], Z. Phys. C **52**, 1 (1991).

[315] M. R. Adams *et al.* [E665 Collaboration], Phys. Rev. D **50**, 1836 (1994).

[316] A. Adil and I. Vitev, Phys. Lett. B **649**, 139 (2007) [arXiv:hep-ph/0611109].

[317] R. Sharma, I. Vitev and B. W. Zhang, Phys. Rev. C **80**, 054902 (2009) [arXiv:0904.0032 [hep-ph]].

[318] M. C. Altunbas et al., Nucl. Instrum. Meth. **A490**, 177 (2002).

[319] M. J. French et al., Nucl. Instrum. Meth. **A466**, 359 (2001).

[320] F. Simon et al., Nucl. Instrum. Meth. **A598**, 432 (2009).

[321] JH. Lee and F. Videbæk, Cross-sections and Single Spin Asymmetries of Identified Hadrons in p+p at sqrt(s) = 200 GeV , Proc. of XVII Int. Workshop on Deep-Inelastic Scattering and Related Topics, Madrid, Spain, April 2009, `http://dx.doi.org/10.3360/dis.2009.196`

[322] D. Acosta et al., Nucl. Instrum. Meth. **A308**, 481 (1991).

[323] D. Acosta et al., Nucl. Instrum. Meth. **A316**, 184 (1992).

[324] R. Wigmans, "Calorimetry Energy Measurement in Particle Physics", International series of monographs on physics, ISBN 978-0-19-850296-8.

Appendix A

Decadal Plan Charge Letter

Dear Barbara and Nu,

As we have discussed in Spokespersons Meetings, I am herein charging the PHENIX and STAR Collaborations with generating new decadal plans that lay out your proposed science goals and detector upgrade paths for the period 2011-2020. The decadal plans generated in 2003 have been extremely useful for RHIC and both experiments. Now that we have received (or are on the verge of receiving) funding to carry out most of the upgrades described in those earlier reports, it is timely to develop a clear roadmap for what comes next. With current funding profile guidance from DOE, it appears that the STAR Heavy Flavor Tracker may be completed in FY2015, and the suite of significant PHENIX upgrades are likely to be completed sooner. We also anticipate that the various RHIC machine luminosity upgrades under way (six planes of stochastic cooling, 56 MHz SRF rebunching, electron lenses) or contemplated (low-energy electron cooling) will be completed by 2015. Not unexpectedly, then, we are being asked by DOE what plans we have for RHIC beyond 2015.

I am therefore asking you to generate a document for each Collaboration, to be delivered to me by August 1, 2010, that provides the following information:

1) A brief summary of the detector upgrades already (or soon to be) in progress, the timelines for completing them, the new science capabilities each adds in combination with upgraded RHIC luminosity, and your best current estimates (informed by the current strawman 5-year run plan for RHIC) of when you will be able to acquire the data that addresses the relevant science goals. This can even be summarized in tabular form, and should be consistent with the latest RHIC Midterm Plan.

2) The compelling science goals you foresee for RHIC A+A, p+p, and d+A collisions that can only be carried out with additional upgrades (or replacements) of detector subsystems or machine capabilities (e.g., further luminosity or diamond size improvements). For each such goal, provide some explanation of why RHIC is the appropriate facility (e.g., in competition with LHC or FAIR) to pursue that science, and preferably some simulations that demonstrate the need for new detector

or machine capabilities to address the compelling questions. If the pursuit of some science goals is conditional on results to be obtained over the next several years, try to outline the decision points you foresee for deciding future paths.

3) Prioritized, or at least time-ordered, lists of the major (above $2M total project cost) and more modest (below $2M total project cost) new detector upgrades your Collaboration foresees, together with R&D milestones that may have to be passed to demonstrate their technical feasibility. Also provide whatever information you have on the indicated timescale concerning probable costs of each upgrade. I understand these will likely be very preliminary in most cases.

4) Any plans or interest your Collaboration has in adapting your detector or detector subsystems (or detector R&D) to study electron-nucleon and electron-ion collisions with an eventual eRHIC upgrade. This is relevant only near the end of the decade addressed here, but will be important for planning purposes. (We may well be forced by financial or environmental considerations, even for a first MeRHIC stage, to consider options in which acceleration of the electron beam is carried out around the RHIC tunnel, requiring some scheme for getting an electron beamline through or around PHENIX and STAR. So its worth considering if there is some way you could make use of the e-p and e-A collisions if we provided them.)

5) The envisioned evolution of your Collaboration through the decade: institutions that may leave, others that might join, any plans to keep your Collaboration healthy and vibrant as RHIC becomes a "mature" facility.

Having been involved heavily myself in the preparation of the previous decadal plan for STAR, I understand how much work is involved in this exercise. But we also now have an existence proof of how important it can be in providing a future program. Please let me know if you foresee difficulty in meeting the above timeline. I imagine convening a special PAC (or perhaps overlapping "red team") review of the decadal plans after they are prepared, to help advise me on priorities. It continues to be made clear to us by DOE that they want higher standards applied in the internal vetting of the compelling science goals that are actually technically achievable with proposed upgrades.

I know that both of you have already launched the intensive discussions within your Collaborations that are necessary to inform these plans. I will need an update (not necessarily written) from each of you before our annual ONP budget briefing (scheduled for February 10, 2010) of the upgrades and new science goals you already foresee, so that we can intelligently answer questions that we are likely to get regarding the RHIC science program beyond 2015.

Please let me know if you have questions about this charge.

Cheers,

Steve